THE UNIVERSITY OF MANCHESTER

Ultrasonic Welding of Aluminium to Titanium: Microstructure, Properties, and Alloying Effects

A thesis submitted to the University of Manchester for the degree of Doctor of Philosophy in the faculty of Engineering and Physical Sciences

By Chaoqun Zhang

June 2015

Supervisors: Dr. Joseph Robson, Prof. Philip Prangnell

Contents

List of Figures

Chapter 2

Chapter 3

Chapter 4

Chapter 6

List of Tables

List of Abbreviations

ADF	Annular Dark Field
Al	Aluminium
BF	Bright Field
BSE	Back-scattered Electron
CGZ	Coarse Grain Zone
CP	Commercially Pure
EBSD	Electron Backscatter Diffraction
EDS	Energy-dispersive X-ray Spectroscopy
EELS	Electron Energy Loss Spectroscopy
FE-SEM	Field Emission Scanning Electron Microscope
FIB	Focused Ion Beam
FSW	Friction Stir Welding
GB	Grain Boundary
GP	Guinier–Preston
GTAW	Gas Tungsten Arc Welding
HAADF	High-Angle Annular Dark Field
HAZ	Heat Affected Zone
HP-USW	High Power Ultrasonic Spot Welding
HPD	Highest Packing Density
Hv	Vickers Hardness
ID	Interface Direction
IMC	Intermetallic Compound
IPF	Inverse Pole Figure
ND	Normal Direction
OPS	Oxide Particle Suspension
PAW	Plasma Arc Welding
PB	Phase Boundary
RSW	Resistant Spot Welding
S/TEM	(Scanning) Transmission Electron Microscopy
SAD	Selected Area Diffraction
SDD	Silicon Drift Detector
SEM	Scanning Electron Microscope
TD	Transverse Direction
TEM	Transmission Electron Microscopy
Ti	Titanium
USW	Ultrasonic Spot Welding
WD	Working Distance
XRD	X-Ray Diffraction

Ultrasonic Welding of Aluminium to Titanium: Microstructure, Properties, and Alloying Effects

by Chaoqun Zhang June 2015

For the degree of Doctor of Philosophy

Abstract

Use of welded titanium alloy to aluminium alloy structures in the aerospace industry has a number of potential benefits for both cost and weight saving by enabling titanium to be used only in the most critical parts, with the cheaper and lighter aluminum alloy making up the rest of the structure. However, due to the formation of brittle intermetallic compounds (IMC) at interface and the enormous gap in melting point, the welding of titanium to aluminium remains a major challenge. Solid state welding processes are most likely to be successful since they do not involve any melting, and so issues associated with the large difference in melting point and the high reaction rate of the liquid phase are avoided.

In this study, an emerging low energy input solid state welding process - high-power ultrasonic spot welding (USW) was applied to weld Al and Ti (AA6111-T4/Ti6Al4V and AA2139-T8/Ti6Al4V combinations). No obvious intermetallic reaction layer was observed on the Al/Ti interface even using transmission electron microscopy. As a result, the maximum joint strength measured reached the same level as similar Al-Al (AA6111) welds and greatly exceeded those observed in Al-Fe and Al-Mg joints made using the same technique, in which a brittle reaction layer forms rapidly. However, the Al/Ti welds always failed at the weld interface after natural ageing, which is not desirable due to the low fracture energy associated with interfacial fracture mode. By using high resolution STEM-EDS, residual oxides and Si segregation were detected on the as-welded Al/Ti interface, which are thought to be factors that result in the no reaction layer Al/Ti interface. The Si segregation is predicted to be able to increase the weld interface cohesion through thermodynamic calculation.

A series of prolonged heat treatment experiments were performed to understand the Al-Ti reaction layer growth kinetics and to explain the lack of reaction layer in as-welded Al-Ti joint. Al_3Ti ($D0_{22}$ structure) was the only Al-Ti intermetallic phase observed in the reaction layer (IMC layer). In pure Al/Ti joints, it is found that the very long slow-growth stage of IMC layer is probably caused by the residual oxides on the interface. Calculations show that grain boundary (GB) diffusion makes the major contribution to the effective diffusion coefficient in the Al_3Ti layer. In AA2139/Ti joints, the IMC layer growth is significantly slower than that in pure Al/Ti joints. The effects of alloying elements on the IMC layer growth was studied in detail. Cu was observed to segregate on both the Al_3Ti grain boundaries and the Al_3Ti/Ti interface. Si also segregated on the the Al_3Ti/Ti interface and enriched in the Al_3Ti layer. Both Cu and Si are thought to retard IMC layer growth. Interestingly small patches of Al were found trapped in the IMC layer; its formation mechanism is discussed. In pure Al/Ti6Al4V joints, the IMC layer growth rate did not change significantly. The presence of V greatly retarded the Al_3Ti grain growth at high annealing temperature (630 ℃) and suppressed the anisotropic growth of Al_3Ti at 600 ℃.

Overall this study successfully joined Al/Ti by USW and systematically investigated the grain size effect and alloying effects on the Al_3Ti layer growth. The present study for the first time: (a) observed the no-IMC-layer Al/Ti weld interface; (b) observed Cu segeration on Al_3Ti GBs; (c) quantitatively studied the grain size effect on Al_3Ti layer growth kinetics; (d) observed the orientation relationship between trapped Al islands and the adjacent Al_3Ti grains; (e) observed that V greatly retarded the anisotropic growth of Al_3Ti grains.

Declaration

No portion of the work referred to in this thesis has been submitted in support of an application for another degree or qualification of this or any other university or institute of learning**.**

Copyright Statement

The following four notes on copyright and the ownership of intellectual property rights must be included as written below:

I. The author of this thesis (including any appendices and/or schedules to this thesis) owns certain copyright or related rights in it (the "Copyright") and s/he has given The University of Manchester certain rights to use such Copyright, including for administrative purposes.

II. Copies of this thesis, either in full or in extracts and whether in hard or electronic copy, may be made only in accordance with the Copyright, Designs and Patents Act 1988 (as amended) and regulations issued under it or, where appropriate, in accordance with licensing agreements which the University has from time to time. This page must form part of any such copies made.

III. The ownership of certain Copyright, patents, designs, trademarks and other intellectual property (the "Intellectual Property") and any reproductions of copyright works in the thesis, for example graphs and tables ("Reproductions"), which may be described in this thesis, may not be owned by the author and may be owned by third parties. Such Intellectual Property and Reproductions cannot and must not be made available for use without the prior written permission of the owner(s) of the relevant Intellectual Property and/or Reproductions.

IV. Further information on the conditions under which disclosure, publication and commercialisation of this thesis, the Copyright and any Intellectual Property and/or Reproductions described in it may take place is available in the University IP Policy (see http://documents.manchester.ac.uk/DocuInfo.aspx?DocID=487), in any relevant Thesis restriction declarations deposited in the University Library, The University Library's regulations (see http://www.manchester.ac.uk/library/aboutus/regulations) and in The University's policy on Presentation of Theses.

List of Publications

1. C. Q. Zhang, J. D. Robson, O. Ciuca, and P. B. Prangnell, Microstructural Characterization and Mechanical Properties of High Power Ultrasonic Spot Welded Aluminum Alloy AA6111–Ti6Al4V Dissimilar Joints, Materials Characterization, 97 (2014), 83-91.

2. C.Q. Zhang, J.D., Robson, P. B. Prangnell, Mechanical Properties and Microstructure Analysis of High Power Ultrasonic Spot Welded AA2139-Ti6Al4V Dissimilar Joints, 25th Advanced Aerospace Materials and Processes (AeroMat) Conference and Exposition (June 16-19, 2014).

3. C.Q. Zhang, J.D. Robson, P. B. Prangnell, Dissimilar ultrasonic spot welding of aerospace aluminium alloy AA2139 to titanium alloy Ti6Al4V, Journal of Materials Processing Technology, In preparation for submission, 2015.

4. J. D. Robson, A. Panteli, C.Q. Zhang, D. Baptiste, E. Cai, P. B. Prangnell, Interfacial Reaction During Dissimilar Joining of Aluminum Alloy to Magnesium and Titanium Alloys. Proceedings of the 13th International Conference on Aluminum Alloys. 2012. 761-770.

Acknowledgements

My PhD study would have been impossible to complete without the strong support and guidance from my supervisors, Dr. Joseph Robson and Professor Philip Prangnell. I am much indebted to them for their long-term help.

This work was funded by the EPSRC through LATEST2, Light Alloys towards Environmentally Sustainable Transport (EP/G022402/1) and Friction Joining—Low Energy Manufacturing for Hybrid Structures in Fuel Efficient Transport Applications (EP/G022402/1.JLR).

I would like to thank Dr. Sarah Haigh for her help in performing high resolution STEM-EDS analysis.

I would like to thank Dr. Octav Ciuca for his help in preparing high quality EBSD samples and other microscopy analysis.

I am very grateful to all the PhD students and post-doctoral researchers in C7 and C10, past and present, for their useful discussion and help.

I am grateful to all the stuff and students in the School of Materials who helped me in my PhD study.

I would like to thank Novelis UK, Constellium, Airbus UK and Prof. Frank Balle for the provision of materials.

I gratefully acknowledge the China Scholarship Council (CSC, 2011612001) for financially supporting my PhD study.

Finally, I thank my family for their love, encouragement and moral support.

Chapter 1

Introduction

1. Introduction

In this chapter, the background information and the motivation for this work are given. The objectives of this study are introduced. The chapters in this thesis are overviewed.

Background and the motivation

Weight and cost reduction is a critical challenge in the aerospace industry so as to reduce fuel consumption and enhance aircraft performance. Light-weight, lower cost design, by replacing monolithic titanium components with multi-material parts produced from titanium and aluminium alloys, has been considered as a promising route to achieve this objective [1]. This requires the joining of structures made of titanium alloys and aluminium alloys.

The dissimilar joining of aluminium to titanium is problematic due to the enormous difference in melting point and the brittle intermetallic phases at the weld interface.

Many welding processes have been attempted to weld aluminium and titanium, but brittle intermetallic phases are still often found on the weld interface. Low energy input solid-state welding processes are believed to be able to retard the intermetallic phase growth.

Objectives

The important tasks of this study are: (1) to find out whether the low energy input welding process selected for the present study, ultrasonic spot welding, can successfully join aluminium and titanium and in the meantime control the brittle intermetallic layer growth; (2) to understand in detail the interface structure using high resolution transmission electron microscopy.

To control Al-Ti intermetallic layer growth and to understand how to limit layer thickness, it is vital to understand its growth kinetics. However, so far the growth kinetics of reaction layer between aluminium and titanium are still not well understood, especially the influence of alloying elements in both aluminium alloys and titanium, such as copper and vanadium, and the influence of intermetallic phase grain size evolution during annealing. Thus, a series of static annealing experiments were performed using different Al/Ti combinations containing different alloying elements. Afterwards, electron microscopy analysis was applied to characterize the reaction layer grain size evolution and the distribution of alloying elements so as to understand how they affect the Al-Ti intermetallic layer growth.

Thesis overview

Chapter 2: Literature review

Literature relevant to this study is reviewed in this chapter to summarize the current understanding over the subject and identify knowledge gaps.

Chapter 3: Experimental methods

Experimental details and the materials used in this study are described in this chapter.

Chapter 4: Microstructural characterization and mechanical properties of HP-USWed AA6111/Ti6Al4V and AA2139/Ti6Al4V dissimilar joints

In this chapter, ultrasonic spot welding (USW) of AA6111/Ti6Al4V combination and AA2139/Ti6Al4V combination was performed. The effect of welding time, which is the only variable parameter in this study, on the weld peak load and

fracture energy was studied. The weld interface structure was investigated using SEM and TEM, to check if there is brittle intermetallic compound formed on the interface. Because the mechanical properties of welded aluminium alloy changes significantly with aging time, the influence of post-weld natural ageing (of the aluminum alloy) on the joint performance is also examined. The mechanical properties of welds produced using two different welding tips with different geometry are compared. The residual oxides and the alloying elements segregation on the Al/Ti interface were investigated as well.

Chapter 5: Static Growth Kinetics of IMC layer in CP-Al/CP-Ti joints

In this chapter, the growth kinetics of the IMC layer in CP-Al/CP-Ti joints was studied through a series of static heat treatment experiments. The reaction product on the CP-Al/CP-Ti interface was identified by TEM Selected Area Diffraction (SAD). The effect of grain size and the residual oxides on the growth rate of the IMC layer was investigated.

Chapter 6: Static Growth Kinetics of IMC layer in AA2139/CP-Ti joints and CP-Al/Ti6Al4V joints

On the basis of Chapter 5, the growth kinetics of the IMC layer on Al/Ti interface with the presence of alloying elements in Al and Ti base metals was studied in this chapter. The distribution of the alloying elements was investigated in detail using STEM-EDS (Scanning transmission electron microscopy - Energy-dispersive X-ray spectroscopy); and the effect of alloying elements on IMC layer microstructure evolution was studied, with the aim of gaining insight into how the alloying elements influence the IMC layer growth.

Chapter 2

Literature review

2. Literature review

Literature relevant to the present study is reviewed in this chapter. Al-Ti dissimilar welding technologies, such as laser welding, gas tungsten arc welding, friction stir welding, diffusion welding, friction welding and ultrasonic welding, are reviewed.

In the subsequent section, the basic properties and features of the base metals used in this study, including commercially pure aluminium (CP-Al), AA6111 aluminium alloy, AA2139 aluminium alloy, commercially pure titanium (CP-Ti) and Ti6Al4V titanium alloy, are addressed.

Next, a significant portion of this chapter is devoted to dissimilar interface structures and reactions, including no-reaction-layer interface structures, segregation of alloying elements on the dissimilar interface, reaction products in Al-Ti and Al-Ti-X systems, growth kinetics of reaction layer in Al-Ti couples, effect of alloying elements on reaction layer growth.

2.1 Al-Ti dissimilar welding technologies

2.1.1 Laser welding and laser brazing

Compared with traditional fusion welding methods, such as gas tungsten arc welding (GTAW), resistant spot welding (RSW) and plasma arc welding (PAW), laser welding is a promising technology for welding dissimilar metals due to its high energy density, low energy input and fast cooling rate, which is beneficial for controlling the interfacial reaction [2].

For example, Chen et al. [3] successfully welded 1.5 mm thick Ti6Al4V titanium sheet and 1.5 mm thick Al 5A06 sheet together by laser brazing with a filler wire

made from aluminium alloy, as shown in Figure 2.1. Cross-section of a typical Al-Ti weld produced by laser brazing is shown in Figure 2.2. The laser beam was offset to aluminium side during welding to minimize the interfacial reaction. The optimized tensile strength exceeded 290 MPa, which is 80% of the base aluminium alloy. However, this laser brazing process has some disadvantages. Both the Al and Ti base metals need to be prebevelled before welding. Also, because the aluminium base metal is melted, shielding argon gas need to be applied on both sides (upper side and lower side) of the sheets to prevent severe oxidation. These disadvantages lead to low efficiency and high cost (compared with ultrasonic welding, a solid state welding process). Both $Ti_7Al_5Si_{12}$ and Al_3Ti phases were observed in the reaction layer. The thickness of the reaction layer varies from a few microns to around 50 μm depending on the welding parameters [3].

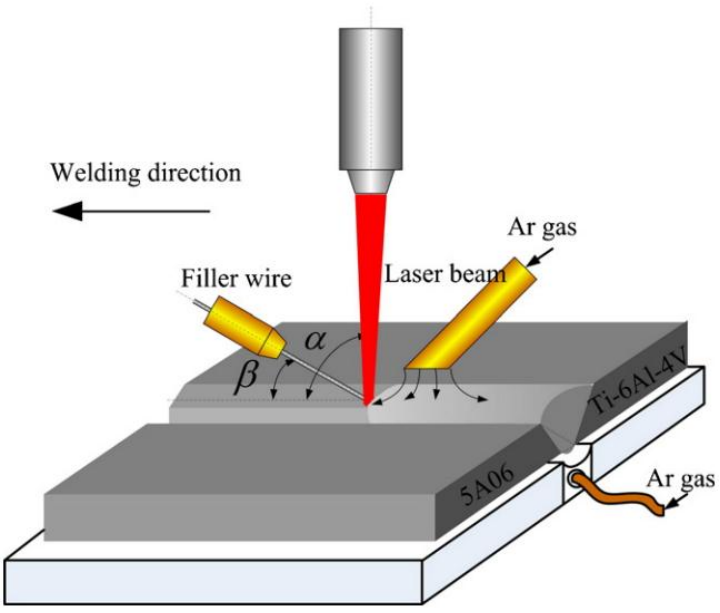

Figure 2.1 Laser brazing of aluminium and titanium sheets [3].

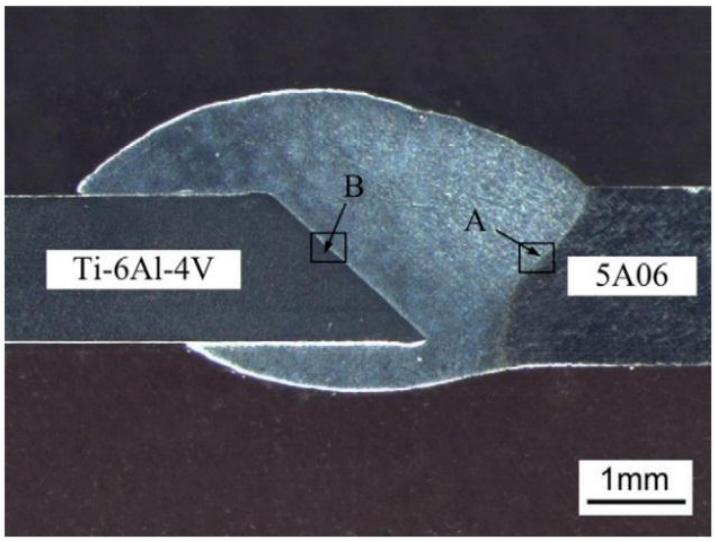

Figure 2.2 Cross-section of a typical Al-Ti weld produced by laser brazing [3].

In butt joints, the offset of laser beam from the joint line is broadly considered to be an important technique for successful welding [4-7]. For example, Song et al. [7] investigated the effect of laser offset on the reaction layer thickness and the joint mechanical properties of A6061-Ti6Al4V dissimilar welds. It was found that with an increase of laser offset distance the Al-Ti intermetallic reaction layer thickness decreased and thus the tensile strength increased. The highest average tensile strength reached 203 MPa, which is 64% of the base Al metal, when the laser offset is 1 mm. Al_3Ti was found to be the reaction product on the Al/Ti interface.

2.1.2 Gas Tungsten Arc Welding

Gas Tungsten Arc Welding (GTAW) is an arc welding process that uses a non-consumable tungsten electrode shielded with an inert gas, to protect both the electrode and the melted metals. The arc is generated between the electrode and the weldment to melt the metal being welded and the filler metal, as shown in Figure 2.3. The reason for performing welding in a chamber with argon atmosphere is that both Al and Ti are very active metals and can be oxidized easily. The cross-section

of a typical Al-Ti weld produced by GTAW using Al-based filler metal is shown in Figure 2.4.

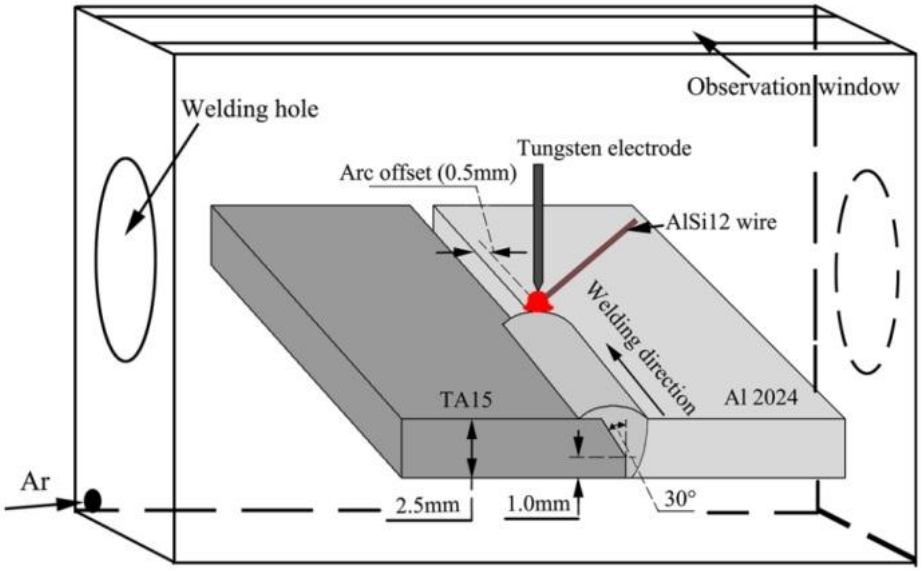

Figure 2.3 Schematic drawing of the GTAW welding set up [8].

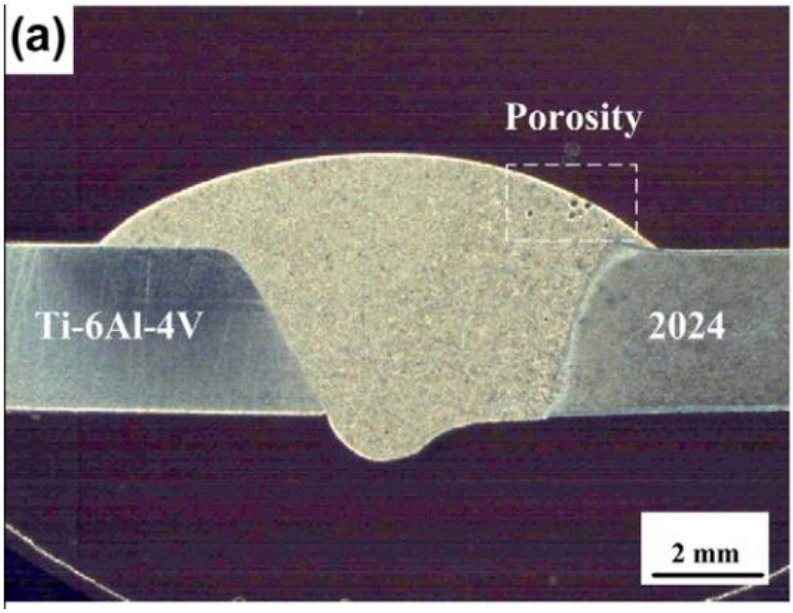

Figure 2.4 The cross-section of a typical Al-Ti welding produced by GTAW using Al-based filler metal [9].

Sambasiva Rao et al. [10] butt welded pure aluminium to Ti6Al4V titanium alloy using AA 4047 Al–Si filler material by GTAW. Tensile tests showed that the

ultimate tensile strength of the weld is 70 MPa (with a large elongation of 10%), which is in a similar level with the pure Al base metal**.** $(AlSi)_3Ti$ intermetallic compound was found on the interface between Ti and the weld by selected area electron diffraction patterns using transmission electron microscopy.

Ma et al. [9] butt joined AA2024 aluminum alloy and Ti6Al4V titanium alloy in 3 mm sheet form by GTAW using an Al-Si filler wire. The highest tensile strength is 158 MPa. The reaction layer thickness is from 2 to 5 um. A SEM image of the reaction layer is shown in Figure 2.5. Both Al_3Ti and $Ti_7Al_5Si_{12}$ intermetallic phases were found on the weld interface.

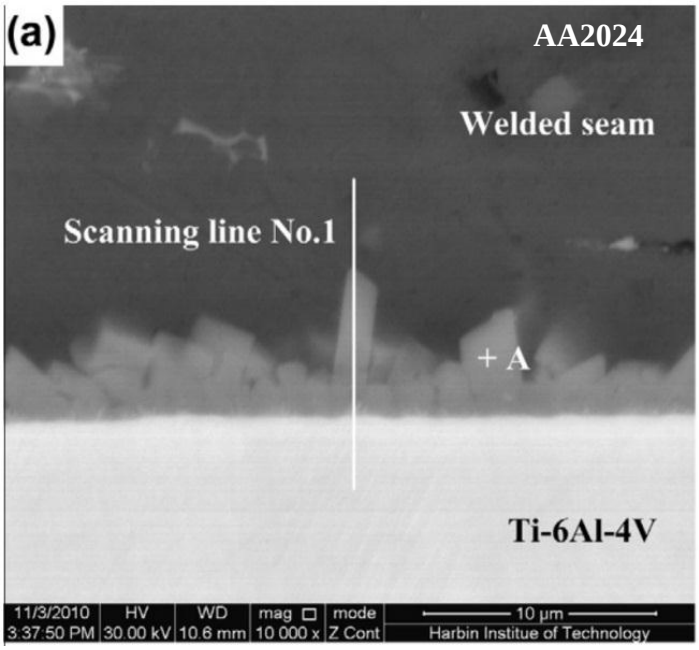

Figure 2.5 SEM image of the Al-Ti weld interface [9].

Wei et al. [8] also butt welded 2.5 mm thick AA2024 aluminum alloy and TA15 titanium alloy by pulsed current GTAW using AlSi12 filler wire. Ti_3Al, Ti_5Si_3, TiAl, $TiAl_3$ phases were detected in the weld.

In summary, GTAW process using filler wire is able to butt weld aluminium sheets and titanium sheets. However due to its high welding temperature brittle intermetallic phases were found in the weld, which could reduce joint mechanical properties. Generally speaking, the tensile strength of GTAW Al-Ti joint is lower that than of laser welding joint due to its higher heat input. Similar to laser welding, shielding inert gas is also required and metal sheets need to be bevelled before welding, which makes the welding process complex and expensive.

2.1.3 Friction stir welding

Friction stir welding (FSW) is a solid state welding process that uses a third body rotating tool to weld two clamped plates. The rotating tool is inserted into the plates to be joined and traverses along the line of joint [11]. A schematic diagram of typical FSW process is shown in Figure 2.6. It has a much lower welding temperature than fusion welding methods such as laser welding and GTAW. Hence, it is believed that by using FSW the interfacial reaction between aluminium and titanium can be reduced.

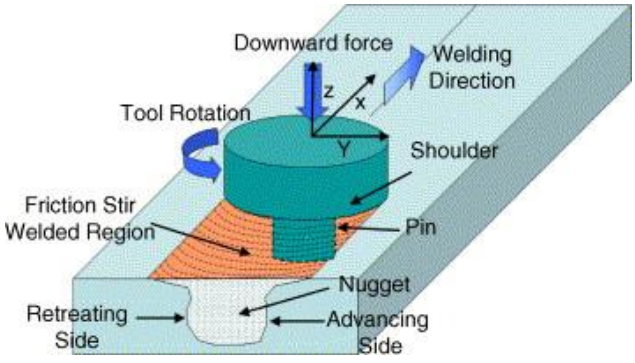

Figure 2.6 Schematic diagram of typical friction stir welding process [11].

Chen and Nakata [12] have lap welded 4 mm thick ADC12 cast aluminum alloy sheet and a 2 mm thick commercially pure titanium sheet by FSW. The maximum

failure load of lap joints reached 62% that of the aluminium base metal. Al_3Ti phase was detected on the weld interface by X-ray diffraction. A fractured Al-Ti friction stir lap weld is shown in Figure 2.7.

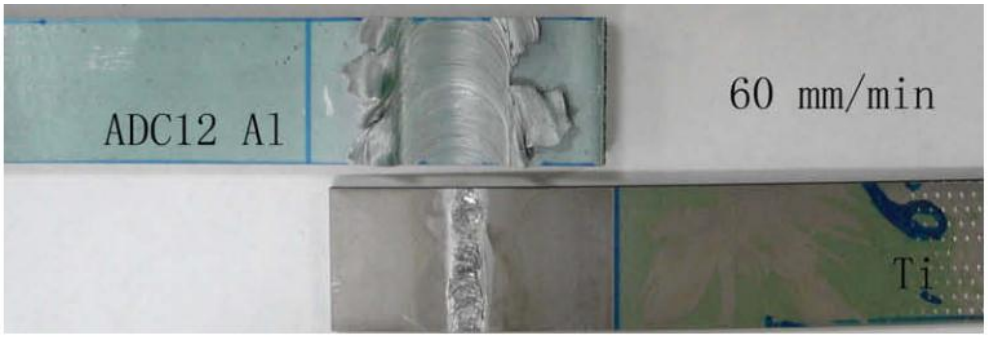

Figure 2.7 A typical fractured Al-Ti friction stir lap weld [12].

Aonuma et al. [13] butt welded 2024-T3 and 7075-T651 aluminium alloy to pure titanium and Ti-6Al-4V alloy by FSW. The tool probe was also shifted to the aluminium side. A schematic diagram of the friction stir butt welding process with tool probe shifting is shown in Figure 2.8. In these joints, pure Ti/2024 joint has the highest average tensile strength 311 MPa. Al_3Ti intermetallic phase was detected by XRD on the fracture surface of the weld. No other intermetallic compounds were detected using XRD and SEM-EDS.

Dressler et al. [14] butt welded 2 mm thick AA2024-T3 aluminium alloy and Ti6Al4V titanium alloy using FSW by shifting the tool pin towards the aluminium side. The joint ultimate tensile strength reached 73% of the AA2024-T3 base material. The authors do not discuss any interfacial reaction product in this paper.

Bang et al. [15] also has butt joined 5 mm thick 6061-T6 aluminum alloy and Ti6Al4V Alloy using FSW. The tool pin was also offset towards the aluminium side. The authors also have not discussed the intermetallic reaction product on the

weld interface. The ultimate tensile strength of the joints reached 134 MPa, which is 35% by of the aluminium alloy base metal. Besides, the elongation of the joints is lower than that of the base Al alloy metal.

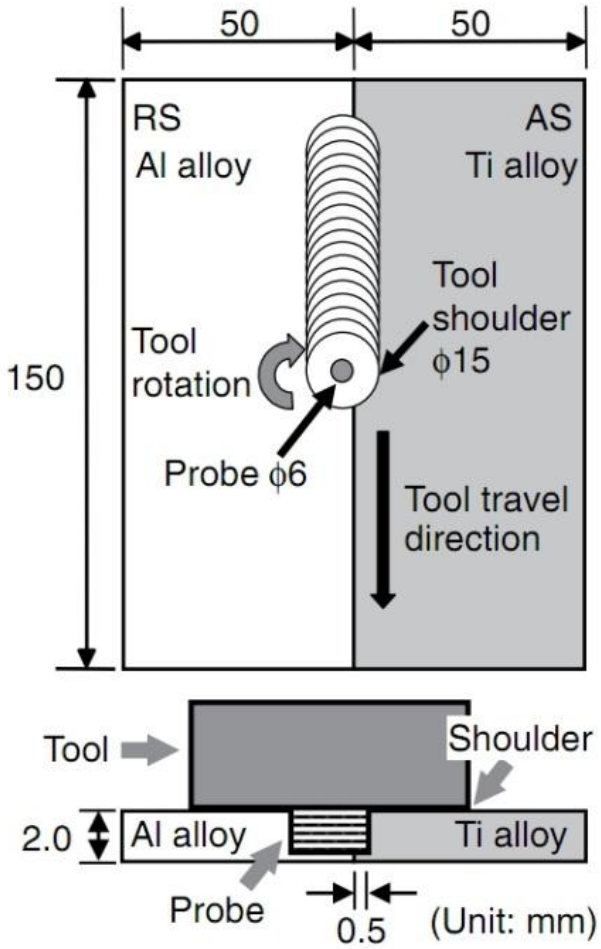

Figure 2.8 A schematic diagram of the friction stir butt welding process with tool probe shifting to Al side [13].

Chen et al. [16] also butt welded 2 mm thick TC1 Ti alloy and LF6 Al alloy (an Al-Mg alloy) plates by FSW adding a Zinc middle layer between Al and Ti. It was found that by adding Zinc interlayer the joint became more brittle because of the formation of Al_3Ti and $Zn_{0.69}Ti_{0.31}$ intermetallic compounds on the interface.

Wei et al. [17] lap welded 3 mm thick Aluminum 1060 and titanium alloy Ti6Al4V plates by FSW using a cutting stir pin made of tungsten carbide with 6 mm diameter. This special pin was slightly plunged into the titanium plate and can increase the mechanical mixing on the weld interface, which is beneficial for the joint strength. The failure load of the joint reached 1910 N, which was nearly equal to that of 1060Al base metal, and the fracture occured in HAZ of Al base metal.

Very recently, Song et al [18] researched the influence of probe offset distance on the mechanical properties and interfacial microstructure of the Al/Ti dissimilar FSW butt joint, as shown in Figure 2.9. A6061 aluminium alloy and Ti6Al4V alloy were used. Here the offset distance (OD) denotes the distance that the edge of the probe inserts into the titanium side. It was found that when the OD is not enough, a kissing bond or no bond is formed in the joint, which leads to poor tensile strength. (A kissing bond is a common defect in friction stir welds, which means that two surfaces lying extremely close, but not close enough for the majority of the original surface in contact for forming atomic bonds [19].) When the OD is too much, lots of intermetallics (Al_3Ti) formed on the joint interface, leading to brittle fracture along the interface. The element (Al, Ti, V) distribution in the weld interface region is shown in Figure 2.10. When the OD is optimized, sound welds can be made, which have high tensile strength and fracture at the HAZ of the aluminium base metal. The tensile strength reached 193 MPa.

In summary, FSW can successfully join aluminium and titanium alloys both in lap weld and in butt weld configurations. During butt friction stir welding, the welding tool pin always needs to be shifted to the aluminium side. One disadvantage of

FSW of Al/Ti is that the welding tool can be easily damaged and worn because the most commonly used titanium alloy (Ti6Al4V) is very hard.

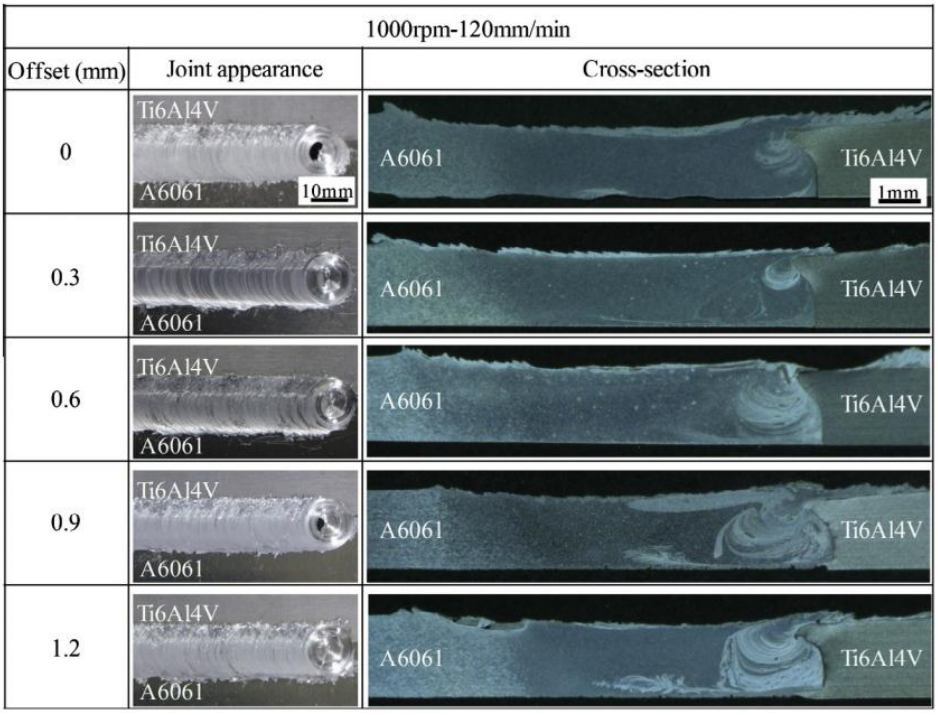

Figure 2.9 Surface appearance and cross-section images of Al-Ti friction stir welds produced by various probe offset distances [18].

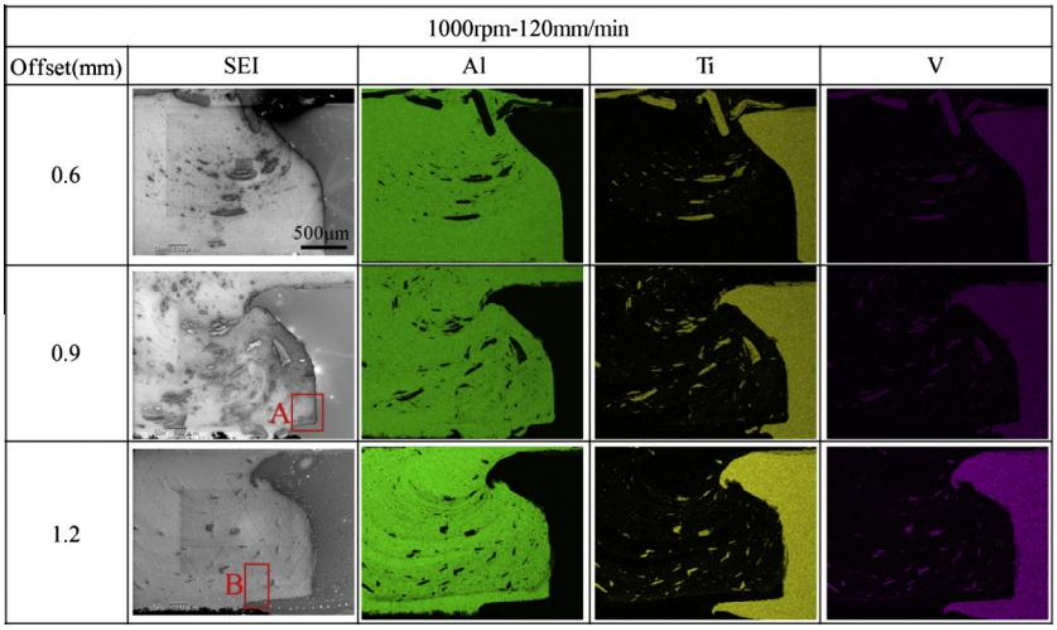

Figure 2.10 The elements distribution in the weld interface region (different probe offset distance) [18].

2.1.4 Rotational friction welding

Rotational friction welding is solid-state welding process, which is realized by applying both high pressure and rotational friction between two workpieces. During the welding process, one of the materials to be welded is fixed and another material rotates. The materials near the joint line are heated and softened by the friction and are joined in a thermoplastic state. A photograph of the rotational friction welding process is shown in Figure 2.11. A typical Al-Ti joint made by friction welding is shown in Figure 2.12.

Kimura et al. [20] successfully friction welded Ti6Al4V alloy and an Al–Mg alloy (AA5052). AA5052 in 2 different heat treatment conditions were used, H112 and H34. AA5052–H34 has a much higher tensile strength (275 MPa) than AA5052–H112 (194 MPa). For both AA5052–H34/Ti6Al4V and AA5052–H112/Ti6Al4V joints, the joint strength reached the same as the base Al metals and fracture occurred in the base Al side. An intermetallic compound layer ($Ti_2Mg_3Al_{18}$) was formed on the joint line when the friction time was long.

Figure 2.11 A photograph of rotational friction welding process [21].

Figure 2.12 Al-Ti joint made by direct drive rotational friction welding [20].

Katoh et al. [22] friction welded 5052 aluminum alloy to pure titanium. The effect of an insert metal on the joint microstructure and mechanical properties was researched. The insert metal was a 15 μm thick pure aluminum foil. The IMC layer in the weld without the insert metal is more irregular and thicker than in the weld with the insert metal. All the joints with insert metal fractured at the softened region of the base 5052 aluminum alloy during tensile testing. The highest tensile strength of the joints with the insert metal reached 92% of 5052 aluminum alloy. The highest tensile strength of the joints without the insert metal reached 78% of 5052 aluminum alloy.

Fuji et al. [23] investigated the effect of post weld heat treatment and the silicon in aluminium on the Al/Ti joint mechanical properties produced by friction welding. It is found that both the tensile strength and the bend test property dropped drastically by post weld heat treatment due to the formation of the intermetallic layer on the joint line. This dramatic drop occurred when the reaction layer thickness exceeded 10 μm. The maximum tensile strength and bend angle can

reach more than 90 MPa, which is at the same level with the pure Al base metal, and 90 degree, respectively.

Overall, the friction-welded Al/Ti joint strength can reach a very high level which is equal or nearly equal to the strength of base Al metal. However, friction welding has some disadvantages which limit its popular application. It is only feasible for workpieces with round cross section or other simple and small cross sections. It cannot be used for producing a long or curved seam weld. Also the cost of friction welding equipment, tooling and setup is expensive.

2.1.5 Diffusion welding

Diffusion welding is a solid-state welding process, which can be used for joining both similar materials and dissimilar materials, and is usually implemented by applying certain pressure and high temperature to the materials to be welded. During diffusion welding, the atoms move across the welding interface due to the chemical potential gradients. It is especially useful for joining dissimilar materials, because of the easy-to-be-controlled interfacial reaction.

Wei et al. [24] diffusion welded commercially pure Ti and commercially pure Al. A 5 MPa static pressure was applied on the Al and Ti being welded. The welding temperature varied from 500 ℃ to 650 ℃. Al_3Ti was found to be the only interfacial reaction product in this study by XRD. The interfacial microstructure of an Al/Ti diffusion weld is shown in Figure 2.13. The joint shear strength can reach the strength of base pure aluminium when an Al_3Ti layer formed on the interface.

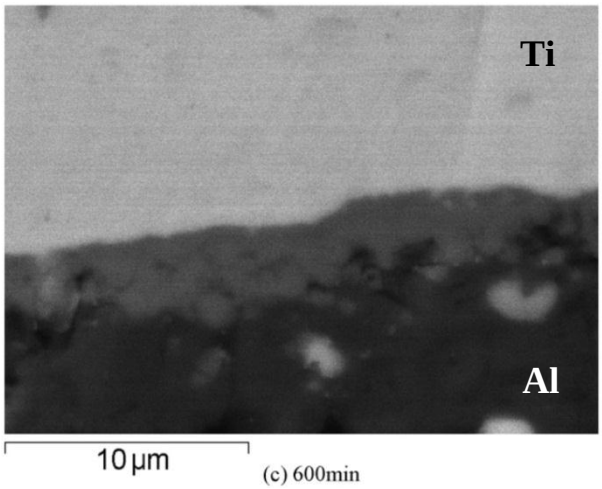

Figure 2.13 Interfacial microstructure of an Al/Ti diffusion weld, dark side is Al, bright side is Ti and the gray layer is the reaction layer [24].

Wei et al. [25] also researched the influence of a Nb diffusion-retarding layer on the mechanical properties and interfacial reaction of an Al-Mg alloy and commercially pure Ti diffusion weld. It is found that in the weld without the Nb layer, $Al_{18}Ti_2Mg_3$ intermetallic easily formed on the interface, which is detrimental for the joint shear strength. When the Nb layer was added, the diffusion of Mg atoms was impeded because Nb and Mg are nearly mutually insoluble in the solid state, also the diffusion of Ti atoms was retarded. As a result, $Al_{18}Ti_2Mg_3$ intermetallic growth was retarded. The highest shear strength of Al/Ti joint with an Nb interlayer reached 105 MPa.

Ren et al. [26] successfully diffusion welded commercially pure Al and commercially pure Ti at 640 ℃ with a holding time of 90 min. The surface of Ti was aluminized before welding. Intermetallics AlTi and Al_3Ti were detected in the transition zone on Ti substrate by XRD. No intermetallic was found in the transition zone on Al substrate. The authors did not study the tensile strength of the weld.

Kenevisi et al. [27] bonded Al7075 aluminium alloy and Ti6Al4V titanium alloy by inserting a 50 μm thick Sn–10Zn–3.5Bi interlayer at the temperature of 500 ℃ under vacuum. The highest lap joint strength reached 30 MPa. Various intermetallics were detected on the welding interface by XRD, such as AlTi, $AlTi_3$, Cu_3Ti_2, $CuZn_5$, Mg_2Sn, Al_2Cu, Sn_3Ti_5 and $MgZn_2$.

Diffusion welding (DW) can avoid the problem of the huge melting point gap between Al and Ti during fusion welding methods. However, the surface of the weldments needs to be very carefully smoothed and cleaned before diffusion welding. Also, the production of large workpieces is limited by the size of furnace. A vacuum environment is required for the diffusion process to avoid oxidation. DW is also not suitable for mass production, because both the diffusion process and the high quality sample surface preparation need a long time to finish.

2.1.6 Ultrasonic welding

Ultrasonic welding is also a solid state welding process which applies high frequency ultrasonic vibration and high pressure on the materials to be welded. The materials are joined together by the friction heat and the high pressure applied during welding. A typical ultrasonic welding system is shown in Figure 2.14. Ultrasonic welding is usually used for spot welding. It has a very good energy efficiency, only using ~2% of the energy of resistance spot welding (RSW) [28].

It is traditionally used for joining thin Cu wires and plastics. In recent years, with the progress of power ultrasound technologies, it has been used for welding structural metal sheets, both similar and dissimilar combinations, such as Al/Al, Al/Mg, Al/Fe and Al/Ti.

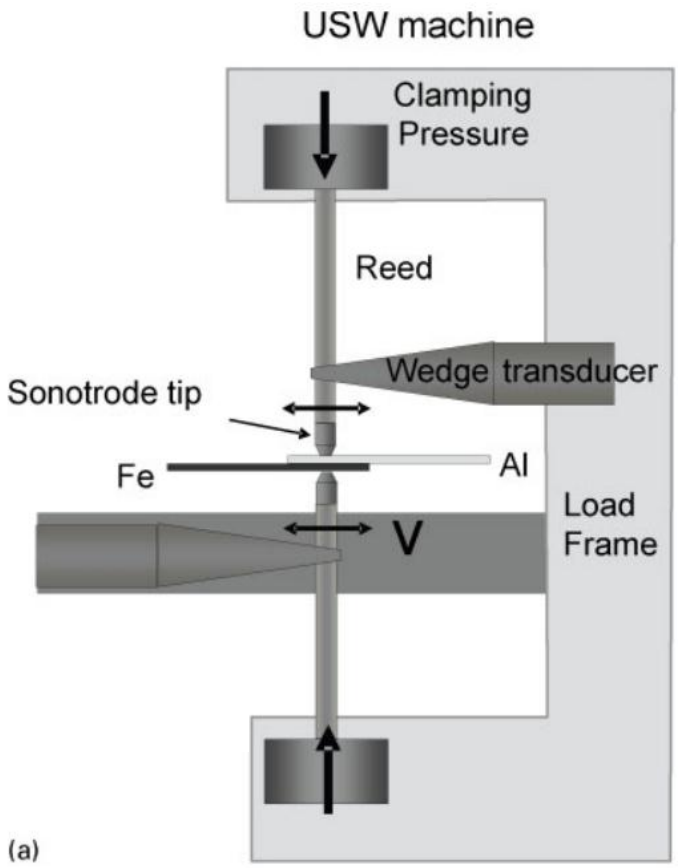

Figure 2.14 A typical set-up of USW system [29].

Prangnell et al. [29] successfully joined 1 mm thick 6111 aluminium and DC04 steel automotive sheet together by ultrasonic spot welding (USW). The highest lap shear load reached 2.8 kN. A thin reaction layer (less than 2 um) of $FeAl_3$ and Fe_2Al_5 formed at the joint line. The joint fracture mode changed from interfacial debonding to weld nugget pullout, at peak load, and back to interfacial cleavage with increasing weld energy.

Panteli et al. [30] have ultrasonic spot welded aluminium (AA6111) to magnesium (AZ31). The optimum peak failure loads reached ~2 kN, which is similar to that of a similar Mg-Mg weld. Fracture always occurred on the weld interface. A thick reaction layer ($Al_{12}Mg_{17}$) formed on the weld interface, which is detrimental for joint mechanical properties. To prevent the fast growth of the detrimental reaction

layer, a 100-μm-thick Al coating was cold sprayed on the Mg surface prior to welding [31]. This reduced the reaction layer growth by by 50 to 70 pct. As a result, the optimum fracture energy increased ~33% from 1.2 kN·mm (uncoated weld) to 1.6 kN·mm (coated weld).

Patel et al. [32] also have investigated the USW of Al (Al5754, 1.5 mm thick) to Mg (AZ31, 2 mm thick). The reaction product on the weld interface was also determined as $Al_{12}Mg_{17}$. Fracture also occurred on the interface due to the brittle reaction product. The maximum lap shear strength was 36 MPa, which is much lower than the shear strength of the base metals (Al5754 and AZ31).

Very recently, Balle and Magin [33] investigated the USW of CP-Al/CP-Ti and AA7075/Ti6AlV4. It is worth noting that they have used a very different ultrasonic source compared with the other USW investigations above-mentioned and the present study, i.e. a rotational oscillation generation system. In their system, the welding tool performs a high frequency rotational oscillation when performing welding. In most other investigations, a linear oscillation ultrasonic source was used. The optimized tensile shear strength for the CP-Al/CP-Ti joint and AA7075/Ti6AlV4 joint respectively reached 15.2 MPa and 41.4 MPa (peak load: 1.2 kN and 3.2 kN respectively). All the welds fractured on the weld interface.

The influence of welding tool geometry:

For solid state welding, tool geometry is very important for the microstructure and mechanical performance of welds, since welding energy and plastic deformation are transmitted and driven by the welding tool [34-36]. The influence of the friction stir welding tool geometry on weld geometry and mechanical properties has been studied extensively due to its high importance [36, 37]. However, only a small

number of studies have investigated tool geometry in the case of USW, as application of USW to joining structural metals only has been developed in recent years [38, 39]. Watanabe et al [39] studied the effect of two types of welding tip, one is labelled as C-tip with a cylindrical contact face and the other one is labelled as K-tip with a flat contact face (Figure 2.15). It was demonstrated that C-tip welds have less unwelded regions on the interface (Figure 2.16 and Figure 2.17) and have better mechanical performance [39] compared with the K-tip welds.

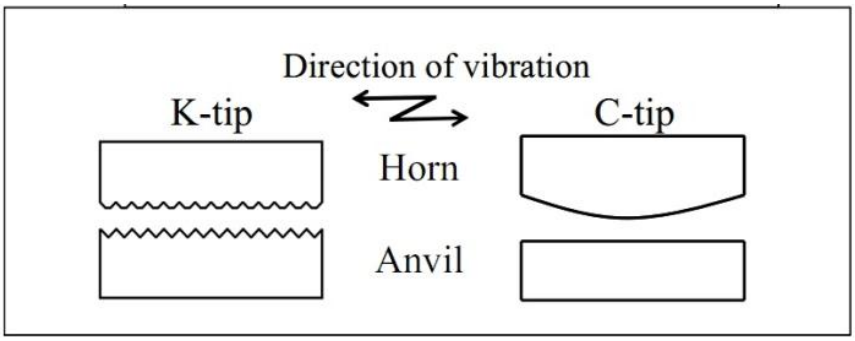

Figure 2.15 Schematic diagram for the K-tip and C-tip welding tools [39].

In summary, USW is a very energy-saving and low heat input solid-state welding process, which is currently mainly used for spot welding. Due to the low heat input, it has the potential for reducing the interfacial reaction rate and then increasing the weld mechanical properties.

2.1.7 Summary of the weld mechanical properties and the advantages and disadvantages of various welding processes

To make the comparison between various welding processes used for joining Al/Ti more clearly, some typical mechanical property results from previous investigations were collected and listed in Table 2.1. The advantages and disadvantages of various welding processes were summarized in Table 2.2.

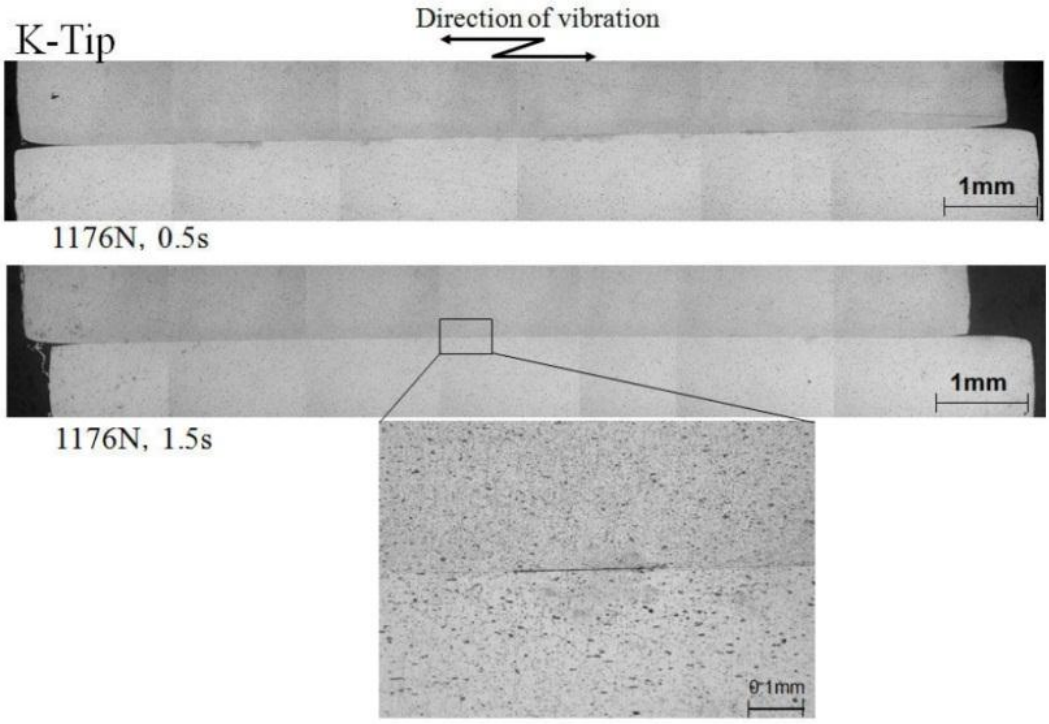

Figure 2.16 Al-Al welds produced using K-tip welding tool [39].

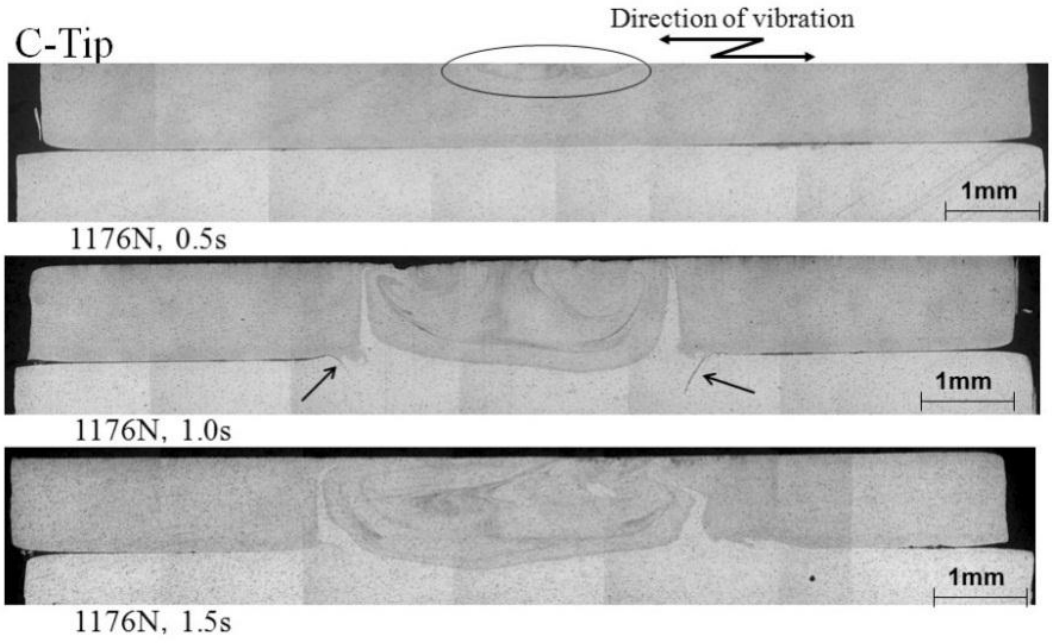

Figure 2.17 Al-Al welds produced using C-tip welding tool [39].

2.2 Base metals

2.2.1 Role of Al and Ti in the aerospace industry

In World War I, aluminum became essential in aircraft design due to its light weight. In World War II, the use of aluminium increased dramatically. More than half of all aircraft were made primarily from aluminium [40]. Recently though, the dominant position of aluminium is challenged by the rise of composites, 20% of the latest Boeing 787 was made from aluminium (by weight) [41], as shown in Figure 2.18.

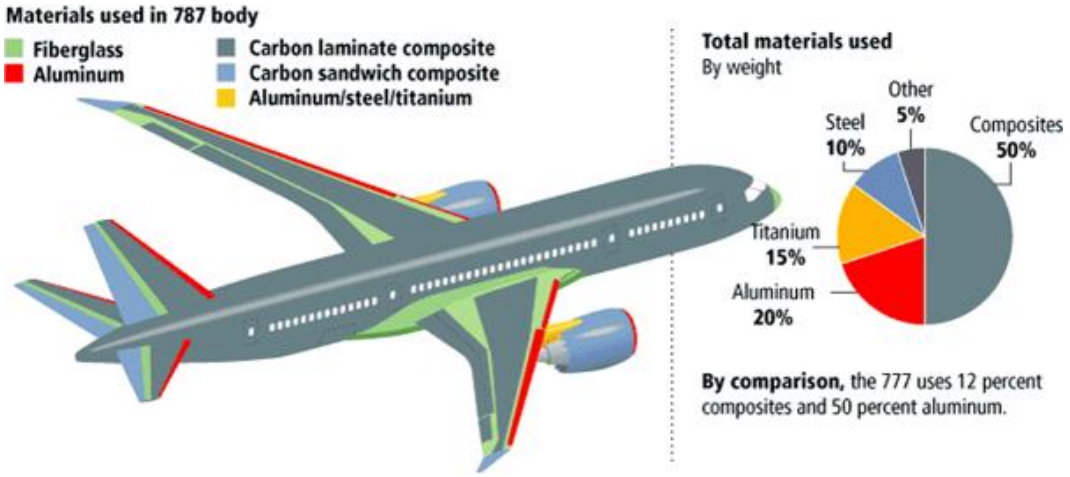

Figure 2.18 Use of Al and Ti in Boeing 787 [42].

In 1940's, titanium was selected by the US Department of Defence as a "metal of choice" for making military aircraft due to its high strength/weight ratio and the superior corrosion resistance as well as its ability to perform at high temperatures. In the fifth-generation jet fighter F/A-22, titanium is the primary material used (39% by weight). Also, as shown in Figure 2.18, in the Boeing 787 titanium is the second most used metal (15% by weight) after aluminium.

Table 2.1 Summary of the mechanical properties of Al-Ti joints produced by various welding processes.

	Welding process	**Materials**		**Max strength (MPa)**		**Max elongation**	**Fracture position**	**Ref**
		Al	Ti		Comparison with Al base metal			
Butt joint	Laser welding	AA6061-T6	Ti64	203	64%	N/A	in Al	[7]
	Laser brazing	Al 5A06 (5xxx series)	Ti64	290	80%	N/A	N/A	[3]
	GTAW	AA2024-T6	Ti64	158	37% *	6.3%	weld interface	[9]
	FSW (butt weld)	AA2024-T3	CP-Ti	311	64% *	N/A	weld interface	[13]
		AA2024-T3	Ti64	348	73%	1.0%	weld interface	[14]
		AA6061-T6	Ti64	134	35%	1.7%	near interface	[15]
		AA6061-T6	Ti64	197	62%	N/A	HAZ of Al	[18]
	Friction welding	AA5052-H34	Ti64	275	~100%	N/A	in Al	[20]
		AA5052	CP-Ti	237	92%	N/A	HAZ of Al	[22]
Lap joint	FSW (lap weld)	ADC12 (a cast aluminum alloy)	CP-Ti	9.39 kN** (shear)	62%	N/A	weld interface	[12]
	Diffusion welding	Al 5A06 (5xxx series)	CP-Ti	105 (shear)	N/A	N/A	in Al, near interface	[25]
		AA7075	Ti64	30 (shear)	N/A	N/A	weld interface	[27]
Spot joint	Ultrasonic welding	AA7075-T6	Ti64	41.4 (shear)	N/A	N/A	weld interface	[33]

Note: CP-Al/Ti welds strength data are not listed in this table, CP-Al/Ti welds usually have similar strength as the CP-Al base metal and large elongation but are rarely used for structural applications; *calculated using the Al base metal strength data from other sources; ** no bonding area data available, thus only maximum load was presented here.

Table 2.2 Summary of the advantages and disadvantages of various welding processes used for joining Al/Ti.

Welding process	Advantages	Disadvantages
Laser welding	1. High welding speed; 2. High energy density.	1. Need inert gas protection; 2. Fast brittle intermetallic phase formation;
Laser brazing	1. High welding speed;	1. Need inert gas protection; 2. Need filler wire; 3. Need to be prebevelled before welding; 4. Fast brittle intermetallic phase formation.
GTAW	1. High welding speed;	1. Need inert gas protection; 2. Need filler wire; 3. Need to be prebevelled before welding. 4. Fast brittle intermetallic phase formation.
FSW	1. Do not need inert gas protection; 2. Slow brittle intermetallic phase formation.	1. The welding tool can be easily damaged and worn because the most commonly used titanium alloy (Ti6Al4V) is very hard.
Rotational friction welding	1. Do not need inert gas protection; 2. Slow brittle intermetallic phase formation; 3. Excellent weld mechanical properties.	1. Only feasible for workpieces with round cross section or other simple and small cross sections. 2. Not suitable for producing a long or curved seam weld. 3. Expensive.
Diffusion welding	1. Slow brittle intermetallic phase formation.	1. Carefully surface preparation; 2. Weldment size limited by the size of furnace; 3. A vacuum environment or inert gas protection is required; 4. Very long welding time; 5. Expensive.
Ultrasonic welding	1. Do not need inert gas protection; 2. Slow brittle intermetallic phase formation; 3. High welding speed.	1. Only capable of welding thin materials;

2.2.2 Aluminium

2.2.2.1 Commercially pure aluminium

Commercially pure (CP) aluminum, i.e. 1xxx series aluminium alloy, contains at least 99.0% Al. Fe and Si (both less than 1 %) are the main impurity elements in CP-Al. Fe can slightly improve the strength and creep characteristics at moderately elevated temperatures, for instance for electrical conductors. Fe also can control the grain size [43].

Compared to other Al alloy series, CP aluminum has the following properties [43]:

(1) Very low strength. As there is almost no solute or precipitates in CP aluminium, dislocation motion has little resistance. As a result, CP aluminum shows excellent formability and workability.

(2) Non-heat-treatable but strain hardenable. This is because there is no precipitate but the grain size can be reduced by plastic working. Also, plastic working can increase dislocation density and density of other crystal defects.

(3) Excellent corrosion resistance. As there are nearly no precipitate phases containing other elements, very little anodic/cathodic reaction sites exist both on the surface and in the base metal. So there is not enough inducement and driving force for corrosion reactions.

(4) Very high thermal and electrical conductivities. Because impurities and alloying additions scatter electrons, which are the carrier of electric current and heat flow, both the electrical conductivity and thermal conductivity drop with the

increase of solute concentration. Pure aluminium has little solute in it, so it has very high thermal and electrical conductivities.

Because of the good combination of the above-mentioned properties, pure aluminium is very suitable for electronic devices, heating equipment and packaging.

2.2.2.2 AA6111 aluminium alloy

6xxx series aluminium alloys are developed for automotive application and are mainly alloyed with silicon and magnesium. The concentration of Si and Mg are mostly in the range of 0.3–1.5 wt% [44]. They can be strengthened by precipitation hardening through heat treatment. They are not as strong as 2xxx series and 7xxx series alloys. But they have better formability and weldability [45].

Magnesium and silicon form Mg_2Si precipitates, which makes the 6xxx series strong alloys. Besides, silicon can improve the corrosion resistance of aluminium alloys, also can improve the fluidity of liquid aluminium alloys and reduce the possibility of hot cracking during welding and casting process. As a result, 6xxx series show good weldability, castability and corrosion resistance.

Because 6xxx series Al-Mg-Si-Cu aluminum alloys combine high strength, formability, corrosion resistance and weldability very well, they are quite popular for many applications such as: automotive body-panels, doors, windows, offshore structures and so on.

The 6xxx series alloys generally contain excessive Si. Its content is more than enough to form Mg_2Si. The hardening of these alloys are principally controlled through precipitation produced by ageing [44].

Because AA6111 alloy has a complicated chemical composition, including Mg, Si, Cu, Fe and Mn, its precipitation path is also complicated and has attracted lots of attention. According to previous studies [46-51], the most probable precipitation route is :

$$\alpha_{(sss)} \rightarrow Mg + Si \text{ clusters} \rightarrow Mg - Si \text{ co-clusters} \rightarrow \text{GPZ}_S \rightarrow \beta'' + Q' \rightarrow \beta + Q$$

where

$\alpha_{(sss)}$: the supersaturated Al solid solution;

Q: equilibrium quaternary ($Al_4Cu_2Mg_8Si_7$) [52, 53];

β: binary (Mg_2Si) phases [52, 53];

β": has a composition of Mg_5Si_6 [54];

Q': has a composition close to $Al_4Cu_2Mg_8Si_7$ (Q) but has different coherency with matrix.

2.2.2.3 AA2139 aluminium alloy

AA2139, mainly alloyed by Cu, Mg and Ag, was originally developed from a NASA funded project with the aim of engineering a high strength, high fracture toughness 2xxx alloy [55]. In traditional 2xxx Al alloys, strengthening phases are nucleated heterogeneously, i.e. precipitates tend to nucleate on grain boundaries, which can limit the damage tolerance capabilities since it can lead to the intergranular failure of the material. Though 7xxx Al alloys are less influenced by this problem, as they rely on homogenous nucleation of the precipitates, which results in both high strength and high fracture toughness, they are prone to stress

corrosion cracking (SCC) in the high strength temper. Thanks to the work of Polmear [56, 57], Cho and Bes [58] the new 2139 alloy was developed by adding small amounts of magnesium (Mg) and silver (Ag) into Al-Cu alloy. In 2139 alloy, Ω phase (which precipitates along the Al {111} planes, Figure 2.19) forms homogeneously within Al grains [59]. The homogeneously distributed Ω phase leads to lower propensity for intergranular fracture. Ω phase also can effectively hinder dislocation activity due to its precipitating along the Al {111} slip planes, thus shows high strength. Besides, Ω phase exhibits better coarsening resistance than other strengthening precipitates, such as θ' phase （Al_2Cu）and S' phase, when aged at elevated temperatures. Hence 2139 alloy has good thermal stability [55]. The 2139 alloy also does not rely on a large amount of cold deformation to obtain maximum strengthening, which allows for producing thick plates without much loss in strength.

All the above makes AA2139 a leading strong candidate for aeronautical and military armour applications, where high strength, good corrosion resistance, good thermal stability and high damage tolerance are required.

2.2.3 Titanium

For pure titanium, an hcp (α) to bcc (β) phase transformation occurs when the temperature reaches 882 °C. For alloyed titanium, the phase transformation temperature varies with alloying elements and their contents [60]. The unit cell of α phase and unit cell of β phase are shown in Figure 2.20.

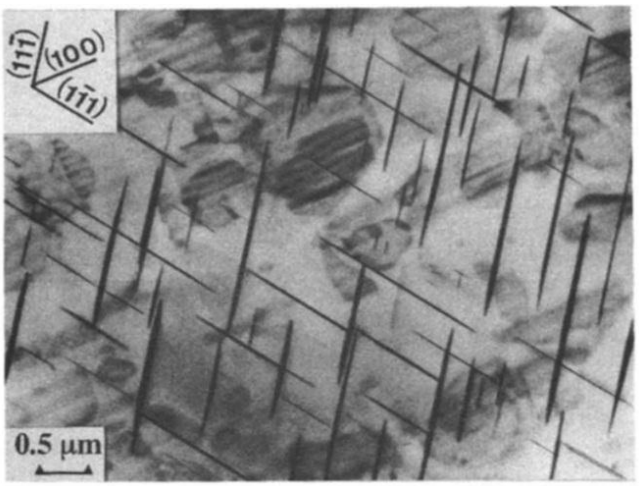

Figure 2.19 Ω phase which precipitates on the Al {111} planes [59].

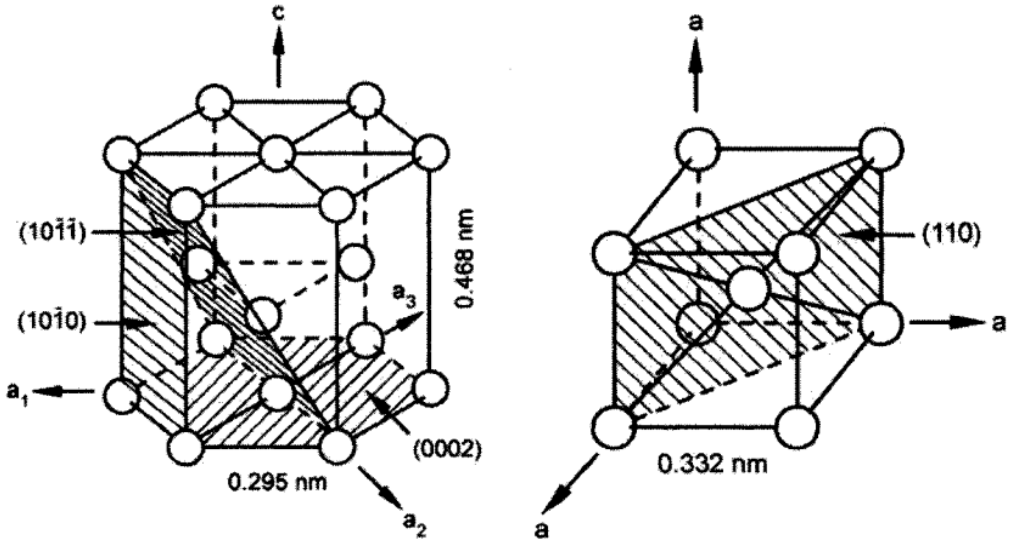

Figure 2.20 Unit cell of α phase (left) and unit cell of β phase (right) [60].

2.2.3.1 Commercially pure titanium

Chemical composition:

Commercially pure (CP) titanium contains at least 99.0% Ti. Other significant elements are Fe, O and N. Chemical composition (maximum allowed O and Fe content) and minimum yield stress of different grades of CP-Ti are listed in Table 2.3.

Table 2.3 Chemical composition and minimum yield stress for CP titanium and α titanium alloys [60].

Grade or Alloy	O (max.)	Fe (max.)	Other Additions	$\sigma_{0.2}$ (MPa)
CP Titanium				
CP Titanium Grade 1	0.18	0.20		170
CP Titanium Grade 2	0.25	0.30		275
CP Titanium Grade 3	0.35	0.30		380
CP Titanium Grade 4	0.40	0.50		480
Ti-0.2Pd (Grade 7)	0.25	0.30	0.12-0.25Pd	275
Ti-0.2Pd (Grade 11)	0.18	0.20	0.12-0.25Pd	170
Ti-0.05Pd (Grade 16)	0.25	0.30	0.04-0.08Pd	275
Ti-0.05Pd (Grade 17)	0.18	0.20	0.04-0.08Pd	170
Ti-0.1Ru (Grade 26)	0.25	0.30	0.08-0.14Ru	275
Ti-0.1Ru (Grade 27)	0.18	0.20	0.08-0.14Ru	170

Microstructure:

Due to existence of Fe in all grades of CP-Ti and the low solubility of Fe in α phase, there is always a small amount of β phase in CP-Ti. CP titanium of higher grade number contains a higher amount of Fe. Fe is added to CP titanium deliberately to control grain size, as the small β phase can pin α-Ti grain boundaries (Figure 2.21, Figure 2.22) [60].

Mechanical properties:

The mechanical properties of CP-Ti strongly depend on both contents of Oxygen and Fe and the processing history, which determines the grain size and the texture. Both Oxygen and Fe additions and small grain sizes limit the deformation twinning and then reduce formability [61]. It is also possible to increase strength by the means of texture, which however is highly directional.

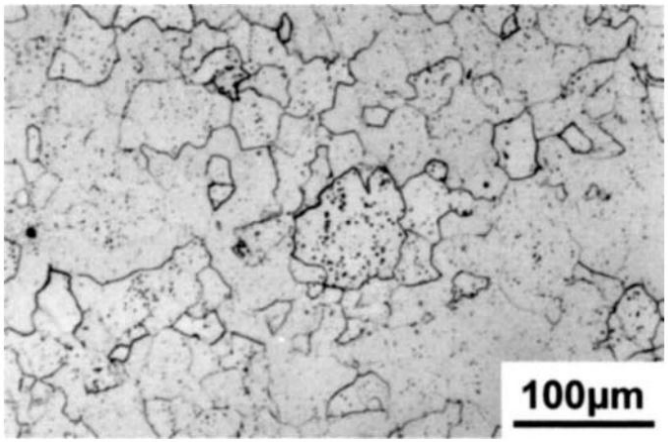

Figure 2.21 Dispersion of iron stabilized β phase in Grade 3 CP-Ti (containing 0.15% Fe) [60].

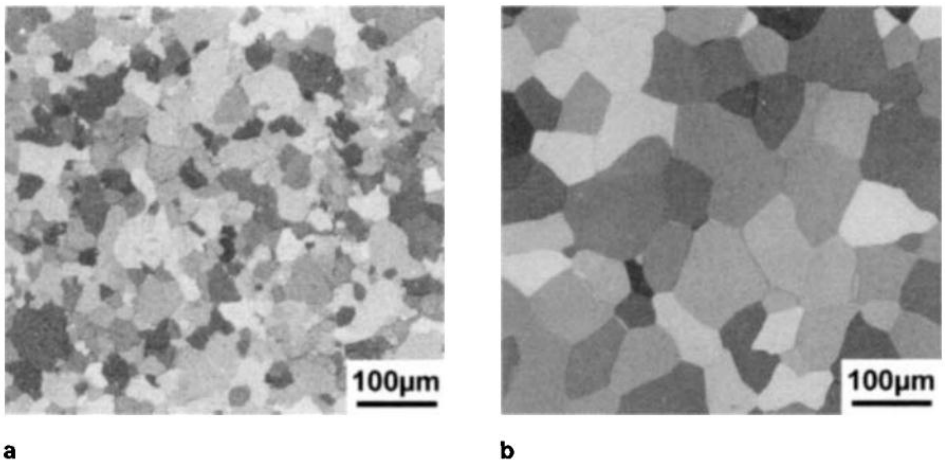

Figure 2.22 Comparision of the grain size of CP-Ti with different Fe content: (a) 0.15% Fe, (b) 0.03% Fe [60].

Oxygen is a very strong strengthener for CP titanium. This very pronounced effect of Oxygen is reflected by the increase of ultimate tensile strength with the increasing grade numbers of CP titanium (Oxygen content increases with the grade numbers of CP titanium). Therefore, in CP titanium, the contents of Oxygen and Fe are strictly controlled during the manufacturing process [60].

Like most polycrystalline materials, grain size strengthening is also a very effective means to increase strength of CP titanium. The relationship between grain size and

yield strength of CP titanium can be described by the Hall-Petch equation [60].

2.2.3.2 Ti6Al4V

Application:

Ti6Al4V was developed in the 1950s and is the most frequently used titanium alloy, which accounts for more than 50% of the titanium usage amount in the world [62]. 80% of Ti6Al4V is used for aerospace applications. Medical devices are the second largest application, which takes up 3% of the market. Ti6Al4V products are supplied in wrought, cast and power metallurgy forms. Among them, wrought products account for more than 95% of the market. In aerospace applications, Ti6Al4V was initially applied to compressor blades in gas turbine engines. Now, it is also widely used for airframe components [62].

Chemical composition:

The chemical compositions of Ti6Al4V vary slightly depending on the specific application. The oxygen content may vary in the range of 0.08% to more than 0.2% (wt.%), the nitrogen content can be changed up to 0.05 wt.%, the aluminium and vanadium content may respectively reach 6.75 wt.% and 4.5 wt.%. Increase of these elements content, especially O and N, results in better strength. Conversely, lower content of the alloying elements enhance the ductility, stress corrosion resistance and fracture toughness [62].

Most alloying elements in Ti alloys either stabilize the α phase to higher temperatures or stabilize the β phase to lower temperatures. In Ti6Al4V, Al and oxygen are typical alpha-stabilizing elements, and vanadium (V) is a beta-stabilizing element.

Microstructure and mechanical properties:

Ti6Al4V is most commonly used in mill-annealed condition. In this condition, it combines good strength, toughness, ductility and fatigue properties. Its minimum yield strength varies from 760 to 895 MPa, depending on the processing, chemical composition, heat treatment and section size. A phase diagram of Ti-6Al and V is shown in Figure 2.25. As shown in this figure, different percentage of alpha and beta phase can be achieved by cooling the Ti6Al4V from different temperatures, which affects the mechanical properties of Ti6Al4V. As shown in Figure 2.26, various microstructures can be formed by using different cooling rates and different quenching temperatures [63].

Phase transformation in Titanium:

There are two approaches that the bcc β phase transforms to α phase: (1) Martensite transformation; (2) Nucleation and diffusional growth [60].

(1) Martensite transformation

Martensite transformation usually occurs with high cooling rate. It is a diffusionless transformation, which involves the cooperative movement of atoms by a shear type process [60]. As a result of the diffusionless transformation, the α' martensite is supersaturated in β stabilizers, when annealing in the $\alpha+\beta$ phase field, it will decompose to $\alpha+\beta$ phases.

(2) Nucleation and diffusional growth

When Ti alloys are cooled slowly from the β phase field to $\alpha+\beta$ phase field, the α phase firstly nucleates on β grain boundaries. During continued cooling process the

α plates grow into the β matrix as parallel plates. The individual α plates are seprated by the retained β matrix. The resulting microstructure shows a lamellar feature; an example of this microstructure is shown in Figure 2.23.

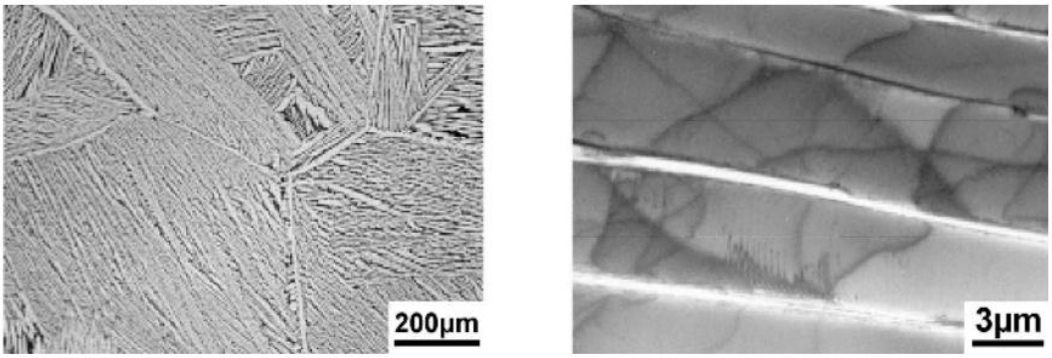

Figure 2.23 Lamellar $\alpha+\beta$ microstructure in Ti6Al4V slowly cooled from the β phase field, (a) Light microscope image, (b) TEM image [60].

Burgers orientation relationship:

The crystallographic relationship between bcc α phase and hcp β phase has first been studied by Burgers in zirconium [64]. The following relationship (Figure 2.24) was found:

$$(110)_\beta \,||\, (0002)_\alpha$$
$$[\bar{1}11]_\beta \,||\, [11\bar{2}0]_\alpha$$

Later it was also confirmed for titanium. This orientation relationship is named Burgers relationship. The Burgers orientation relationship exists both for the martensite transformation and for the nucleation and diffusional growth process.

Effect of aging and oxygen content:

When aluminium concentration is high enough (about 6%), Ti_3Al (α2) phase is able

to precipitate in α phase by an ageing process, which can strengthen α phase. Besides Al, oxygen can promote the Ti_3Al (α2) phase formation as well. The precipitated α2 particles can improve the yield strength of titanium alloy, because they boost the resistance of dislocation movement. At the same time, because they are sheared by moving dislocations, intense and planar slip bands form at the α2 particle sites, which leads to easy crack nucleation and lower ductility [60].

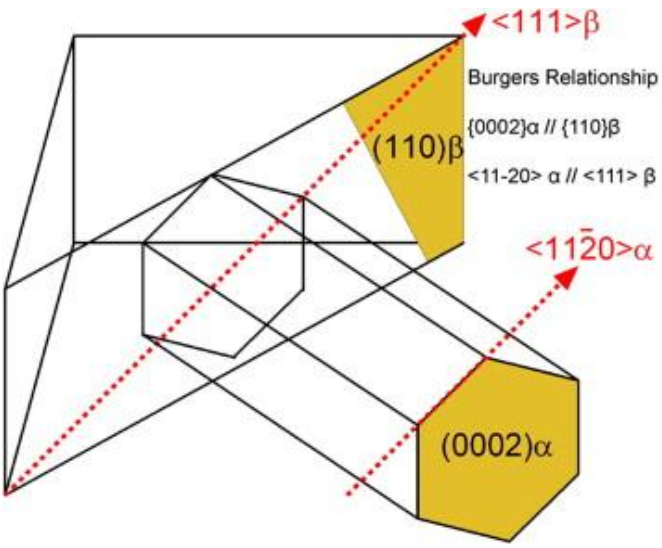

Figure 2.24 The burgers orientation relationship [65].

Effect of α-Ti grain size:

The mechanical properties of fully equiaxed Ti6Al4V titanium alloy also depends on the α grain size, because the slip length depends on the α-Ti grain size and the smaller the slip length is the higher the yield strength is [60].

This is the end of literature review on base metals. The following sections will turn to dissimilar metal interfacial structure and reactions.

2.3 Metal-metal no-reaction-layer interface

As mentioned in Chapter 1, the brittle intermetallic phase layer (reaction layer) on weld interface is a great challenge for welding dissimilar metals. On most dissimilar weld interfaces, there is always a reaction layer between the dissimilar materials. However, occasionally it has been observed that there is no reaction layer on the interface.

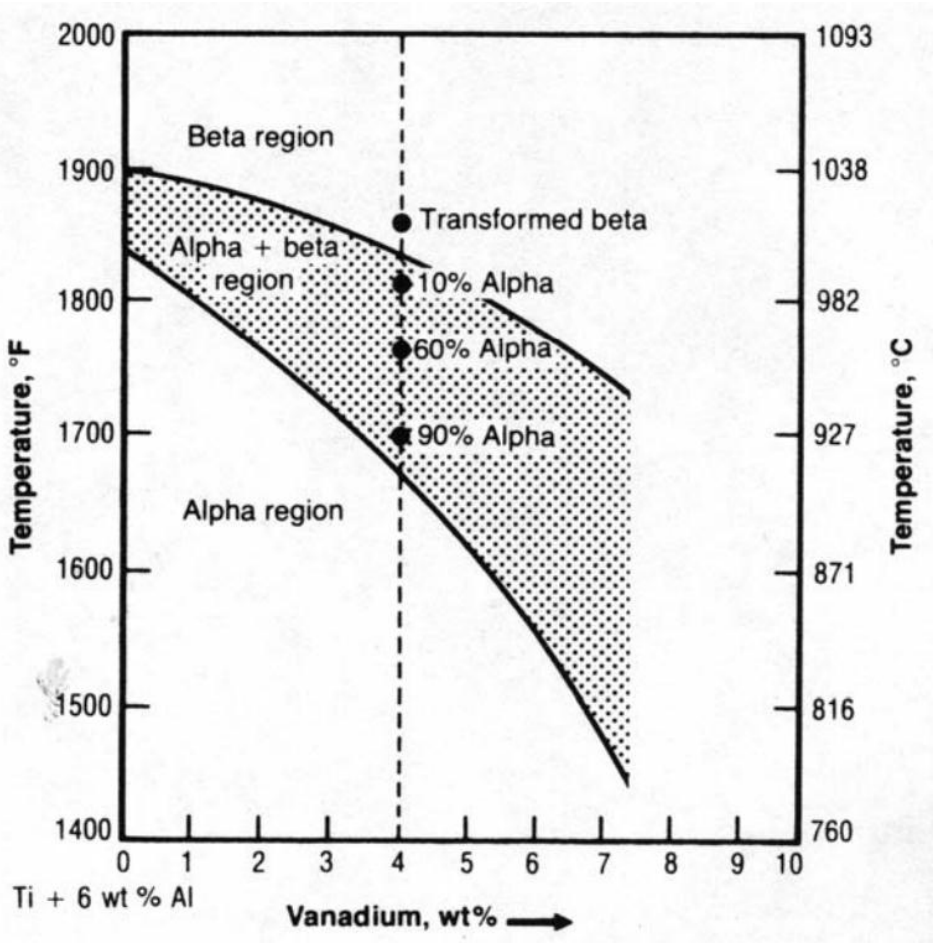

Figure 2.25 Phase Diagram of Ti-6Al and V [63].

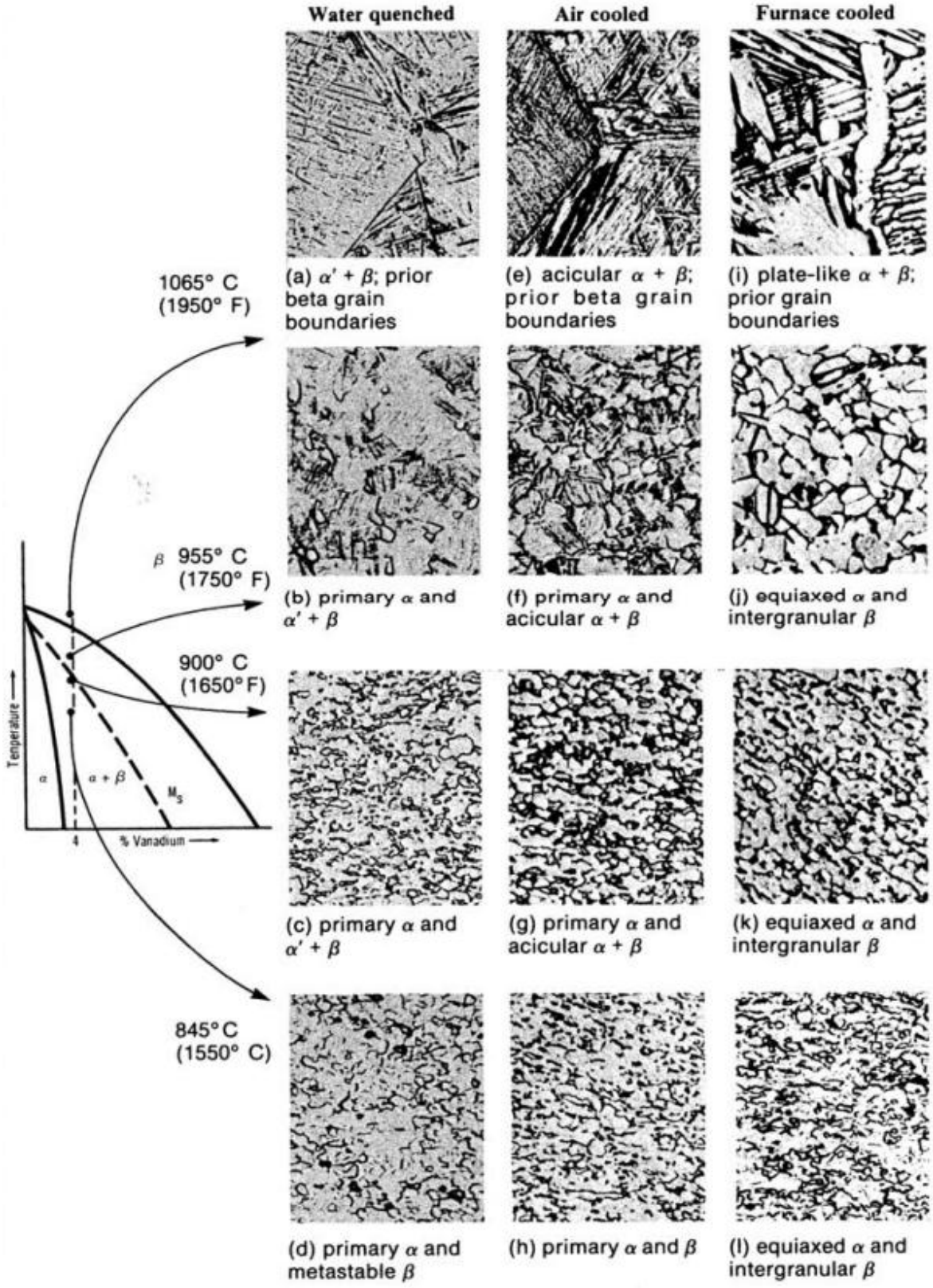

Figure 2.26 Different microstructures of Ti6Al4V achieved by different cooling rates and different quenching temperatures [63].

In the dissimilar metal-metal case, the no-reaction-layer interface was formed either due to a very low welding energy [66] or owing to two metals having complete solid solubility, such as the Cu-Ni combination [67]. The complete solid solubility between Cu and Ni is because they share the same face-centred cubic (FCC) crystal structure, and have similar atomic radii, electronegativity and valence state.

In electronic industry, the ultrasonic power used for dissimilar wire bonding is usually very low in the range of 10^{-2} watt (W) to 10^{-1} W, and the bonding time used is also very short, in the range of tens of milliseconds [68-70]. This leads to a very low welding energy, which results in insufficient interfacial reaction for forming IMCs. For example, Kim et al. [66] investigated the interface between Cu bonding wire and Au pad after bonding. No Cu-Au IMCs were detected on the interface, only a 4 ± 1 nm thick Cu–Au diffused layer was found on the interface by transmission electron microscopy, as shown in Figure 2.27.

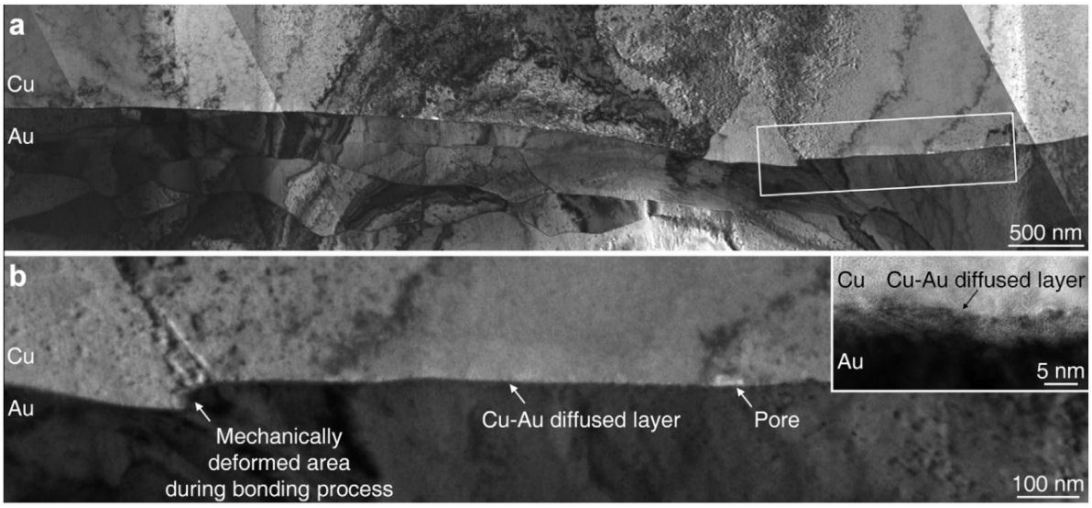

Figure 2.27 (a) Bright field TEM image of the interface between the Cu bonding wire and the Au pad after bonding and (b) magnified image of the area marked with a white rectangle in (a) [66].

Besides, on the aluminium/Mo-coated glass substrate interface, produced by ultrasonic wire welding, Iwamoto et al. [71] reported a no-reaction-layer Al-Mo interface, on which Al and Mo lattices were directly connected, as shown in Figure 2.28 and Figure 2.29.

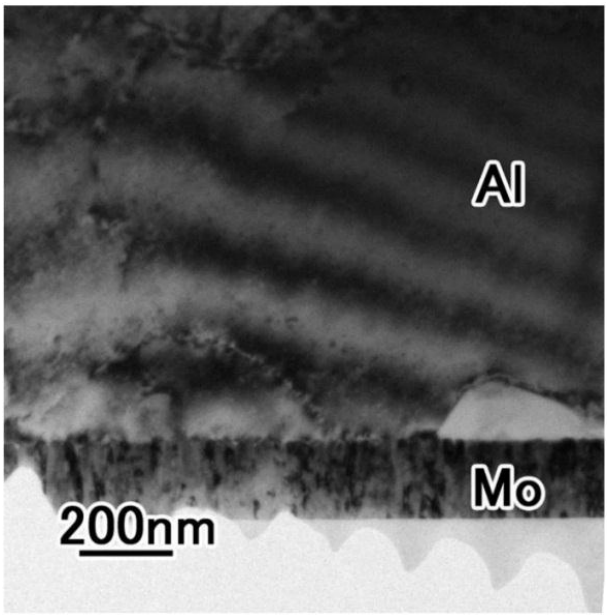

Figure 2.28 Bright field TEM image of interface between Al and Mo [71].

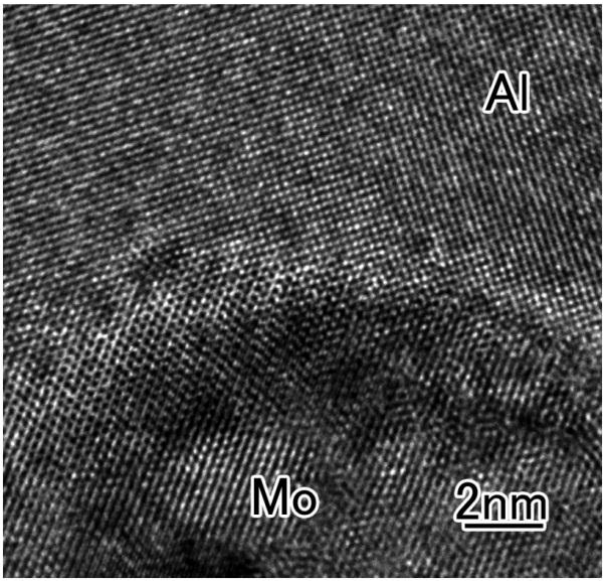

Figure 2.29 HR-TEM image of Al-Mo interface [71].

2.4 Segregation of alloying elements on dissimilar interface

Segregation of elements to the interface can markedly affect the mechanical properties, corrosion properties and other properties. Segregation is very common in crystalline materials due to the lattice disorder at interfaces. One example is the segregation of additional elements to a dissimilar metal weld interface [23]. However this kind of segregation has not been extensively studied. Grain boundary segregation is the most commonly studied segregation and most theories on segregation, including segregation driving force theory and the influence of segregation on the interface cohesion, were developed from research on grain boundary segregation. The fundamental driving force of segregation is the total free energy change associated with solute atoms segregation. Simplest models for grain boundary segregation assumed that the total free energy change is dominant by elastic strain energy change caused by solute atoms movement when the solute atom size and the matrix atom size difference is big enough [72].

As the present study focuses on Al-Ti dissimilar interface, a previous study on the segregation of alloying elements on interphase boundaries in Al-Ti system will be reviewed in this section. (There is very little literature on the segregation of alloying elements on the dissimilar interfaces in Al-Ti diffusion couple.)

Segregation on Al_3Ti-Ti interface

As mentioned in section 2.1.5, Fuji et al. [23] friction welded titanium to aluminium containing silicon and an Al_3Ti reaction layer formed on the weld interface. In the meantime more than 20 at.% Si were found segregated on the interface between the Al_3Ti intermetallic phase and the titanium base metal by

using TEM-EDS, as shown in Figure 2.30. The authors considered that the Si segregation on the interface retarded the growth of Al_3Ti layer by acting as a barrier layer for diffusion.

Alloying elements segregation to heterophase interfaces is not only theoretically possible but also has been verified by the above mentioned experimental observation. The system energy drop caused by interatomic interactions between the alloying element atom and the atoms in the other phase could be an important driving force for the segregation.

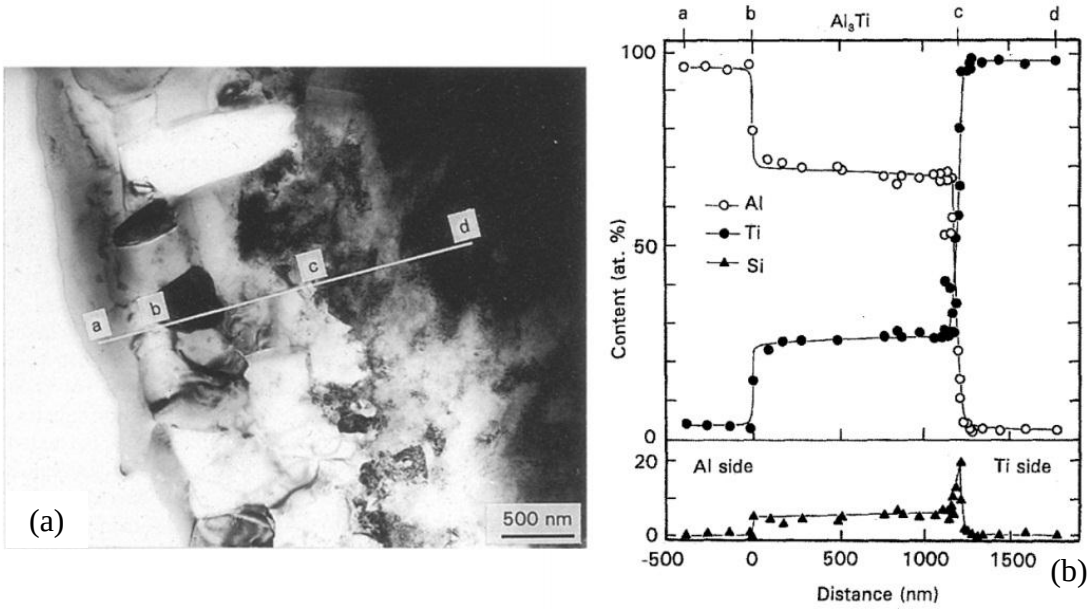

Figure 2.30 TEM bright field image of the (0.12 wt.% Si)/Ti weld interface (a), Al, Ti and Si concentration profile across the Al-Al_3Ti-Ti interfaces (b) [23].

2.5 Reaction products in Al-Ti and Al-Ti-X systems

In this section, the reaction products in Al-Ti binary system and in Al-Ti-X ternary systems are reviewed. Reaction products at low temperatures are the main concerns. X, here, mainly refers to the alloying elements used in AA2139 aluminium alloy

and Ti6Al4V titanium alloy, including dominant alloying elements Cu and V, and minor alloying elements Mn, Mg, Ag and Si.

2.5.1 Reaction products in Al-Ti binary system

As shown in the Al-Ti binary phase diagram (Figure 2.31), there are lots of possible reaction products between Al and Ti, including Ti_3Al, TiAl, $TiAl_2$ and Al_3Ti. Depending on welding or heat treatment temperatures, different reaction products form on the Al-Ti interface.

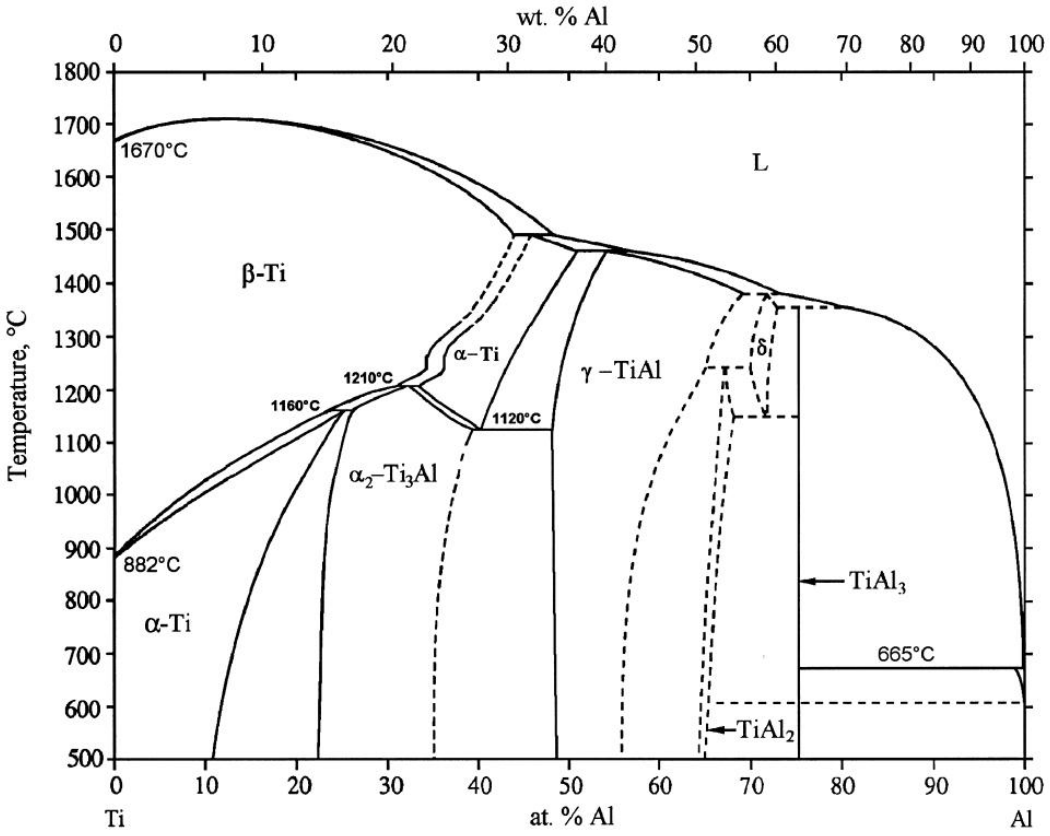

Figure 2.31 Al-Ti binary phase diagram [73].

When the welding or heat treatment temperature is high (higher than the melting point of aluminium), all Ti_3Al, TiAl, $TiAl_2$ and Al_3Ti phases can form on the Al-Ti interface. For example, Oh et al. [74] fabricated titanium aluminide sheets by hot rolling and heat treatment. As shown in Figure 2.32, Ti_3Al, TiAl, $TiAl_2$ and Al_3Ti

phases formed after multilayer Ti/Al sheets were hot rolled at 500 °C and then annealed at 1000 °C. An example from welding has showed that in an aluminum alloy AA5754 to titanium alloy Ti6Al4V weld produced by laser welding, Ti_3Al, TiAl, Al_3Ti phases were detected on the weld interface by XRD [75].

However, when the welding or heat treatment temperature is low (in solid-state welding conditions), Al_3Ti phase is the dominant (in most cases the only) titanium-aluminium binary compound formed on the Al-Ti interface [76-84]. Several examples have been given in section 2.1.3 on friction stir welding of Al-Ti.

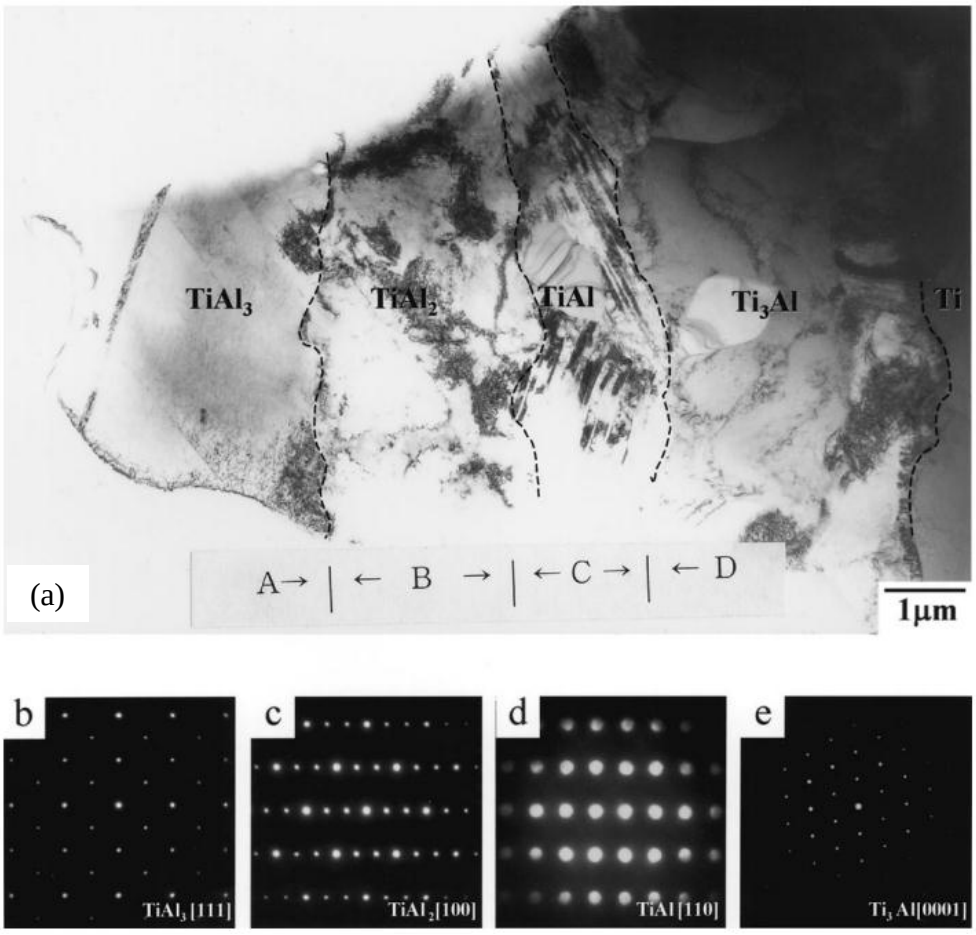

Figure 2.32 (a) TEM bright field image of the interface region between Al and Ti of the multilayer Ti/Al sheet produced by hot rolling and heat treatment. (b)-(e) Selected area diffraction pattern of A, B, C and D regions respectively [74].

Occasionally, some other variations of the Al_3Ti structure can form in Al-Ti binary diffusion couples at very low annealing temperatures. For example, $Al_{24}Ti_8$ super structure was observed at 350 °C annealing temperature [85]. Metastable $L1_2$ structure of Al_3Ti was observed in an in-situ annealing experiment in TEM at 350 °C and started to transform to equilibrium $D0_{22}$ phase when the temperature rose to 400 °C [86].

2.5.2 Al_3Ti

Crystal structures of Al_3Ti:

Al_3Ti has 2 different crystal structures, tetragonal $D0_{22}$ structure and cubic $L1_2$ structure, as shown in Figure 2.33. Previous first principles calculations of the lattice stability of the Al_3Ti showed that the $D0_{22}$ structure has a lower energy than the $L1_2$ structure by 0.05 ev/atom [87]. That is to say, the $D0_{22}$ structure is the thermally stable one [88]. As a result, it is the majority structure of Al_3Ti reaction product detected in previous studies of Al-Ti bonding and welding [76-84] at relatively low temperatures. However, the $L1_2$ structure is often preferred to improve ductility because it has a higher symmetry structure which increases the independent slip systems and then allows accommodation of plastic deformation [87]. The $L1_2$ structure of Al_3Ti can be stabilized by adding some ternary elements when casting. Experimental works found that Fe, Ni, Cu and Zn are effective elements for stabilizing $L1_2$ structure.

Basic properties of Al_3Ti

The lattice parametres of Al_3Ti ($D0_{22}$) are a=b=0.3848 nm, c=0.8596 nm [88]. Its density is calculated as 3.36 g/cm^3. While having a very low density, only 24%

higher than pure aluminium, it also has a high melting point (1350 °C) and high Young's modulus (215.7 GPa) compared with 69 GPa of aluminium and 116 GPa of titanium [88]. However, a serious problem of Al_3Ti is its poor ductility owing to the lack of crystal symmetry and hence lack of slip systems to deform [89].

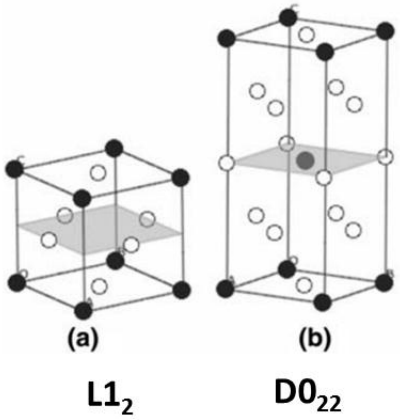

Figure 2.33 $D0_{22}$ and $L1_2$ structures of Al_3Ti [90].

Besides, Al_3Ti is believed to have the best oxidation resistance in all binary Al-Ti compounds; it is the only compound in Al-Ti system that can form protective Al_2O_3 scales in air [88]. It shows good corrosion resistance and has been proved to be able to improve the corrosion resistance of stainless steel 316 and 304 base metals when it is used as the coating layer [91].

Plastic deformation of Al_3Ti

Yamaguchi et al. [92] investigated the plastic deformation of polycrystalline Al_3Ti with $D0_{22}$ structure at different temperatures from 25 °C to 860 °C. At temperatures lower than 620 °C, Al_3Ti fractures at very small strain. At temperatures higher than 620 °C, it showed good compression ductility. Twinning of the type (111)[112], which does not disturb the $D0_{22}$ symmetry of Al_3Ti lattice, is observed as the major deformation mode. At high temperatures, the four (111)[112]-type twinning

systems are complemented by slip of the types [110], [100] and [010], which was suggested to be the reason for the good compression ductility at temperature above 620 °C. Examples of deformation twinning observed at both low and high temperatures are shown in Figure 2.34 and Figure 2.35. Besides, Morris et al. [93] observed significant deformation occurring by single $\frac{1}{2}[110]$ dislocation motion on (001) planes.

Figure 2.34 Deformation twins observed in a Al_3Ti specimen deformed at 25 °C [92].

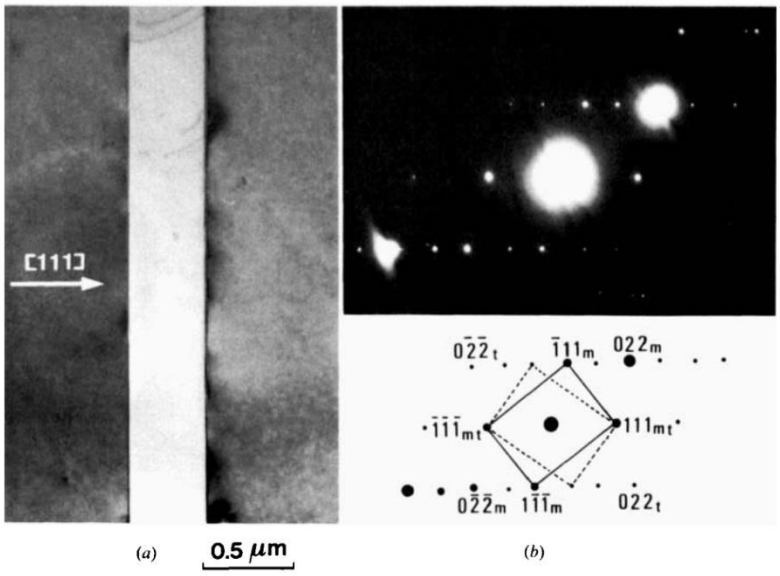

Figure 2.35 A deformation twin observed in an Al_3Ti specimen deformed at 760 °C [92].

(a) TEM bright field image, (b) the diffraction pattern of the deformation twin.

2.5.3 Reaction products in Al-Ti-X ternary system

2.5.3.1 Al-Ti-V ternary system

As mentioned previously, Ti6Al4V takes up more than 80% of titanium market. When welding titanium alloys containing vanadium to aluminium alloys, vanadium will participate in the Al-Ti reaction and may affect the reaction product. The Al-Ti-V ternary system has been investigated by several groups. $Ti_3Al(\alpha_2)$, $TiAl(\gamma)$, $(Ti,V)Al_3(\xi)$, Al_8V_5, TiAl are all established intermetallic phases in Al-Ti-V system [94]. Their formation depends on the specific temperature and composition [94]. A isothermal section phase diagram of Al-Ti-V system at 873 K is shown in Figure 2.36.

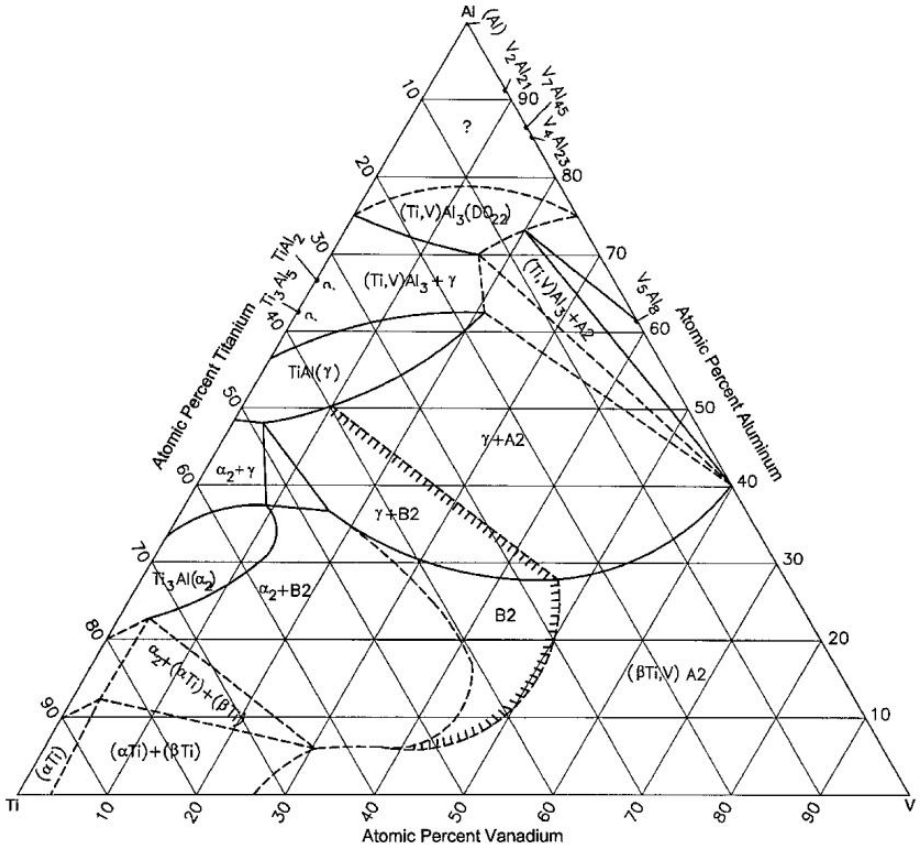

Figure 2.36 Al-Ti-V isothermal section at 600 ℃ [95].

$Al_3(Ti,V)$ (ξ) phase

As Al_3Ti is the dominant reaction product in solid state conditions (which are the conditions used in the present study), $Al_3(Ti,V)$ (ξ) phase, in which some Ti atoms are substituted by V atoms, should be the Al-Ti-V ternary phase most related with this study. Thus, $Al_3(Ti,V)$ (ξ) phase is the focus of this section.

Lee et al. [96] investigated the effect of vanadium on the lattice parameters of Al_3Ti phase. It is found that substitution of titanium atoms by vanadium atoms resulted in slight increase of lattice parameters along both a- and c- axes. Takahashi et al. [97] found that the 0.2% proof stress of $Al_3(Ti,V)$ increased with increasing vanadium content up to ~10 at. %, and then decreased toward that of Al_3V both at room temperature and at elevated temperatures.

Takahashi et al. [98] found that the lattice parameters increased linearly with increasing vanadium content as a fourth element in $L1_2$ structure $Al_3(Ti,Cr)$ or $Al_3(Ti,Fe)$. The yield strength of $Al_3(Ti,Cr)$ or $Al_3(Ti,Fe)$ also increases with vanadium addition. The strengthening effect of vanadium can be retained to high temperatures (like 1200 K). The strengthening mechanism was thought to be solid solution strengthening of vanadium.

2.5.3.2 Al-Ti-Cu ternary system

TiCuAl (C14, $MgZn_2$-type hexagonal), $TiCu_2Al$ ($L2_1$, $MnCu_2Al$-type cubic), and Ti_2CuAl_5 ($L1_2$, $AuCu_3$-type cubic) are established ternary phases in Al-Ti-Cu system [99].

Al-Cu phases, including $CuAl_2$, CuAl, Cu_3Al_2, Cu_9Al_4, and **Cu-Ti phases** including Cu_4Ti, Cu_2Ti, Cu_3Ti_2, Cu_4Ti_3, CuTi, $CuTi_2$ and $CuTi_3$, and **Al-Ti phases**

including $TiAl_3$ (D022-type tetragonal), Ti_5Al_{11}(tetragonal), $TiAl_2$ ($HfGa_2$-type tetragonal), $Ti_{1-x}Al_{1+x}$(AuCu-type tetragonal), Ti_3Al_5(tetragonal), TiAl(γ)(AuCu-type tetragonal), and Ti_3Al (α2)($D0_{19}$,Ni_3Sn-type hexagonal) are all possible binary phases in the Al-Ti-Cu system [99]. An Al-Ti-Cu isothermal section at 850 °C is shown in Figure 2.37.

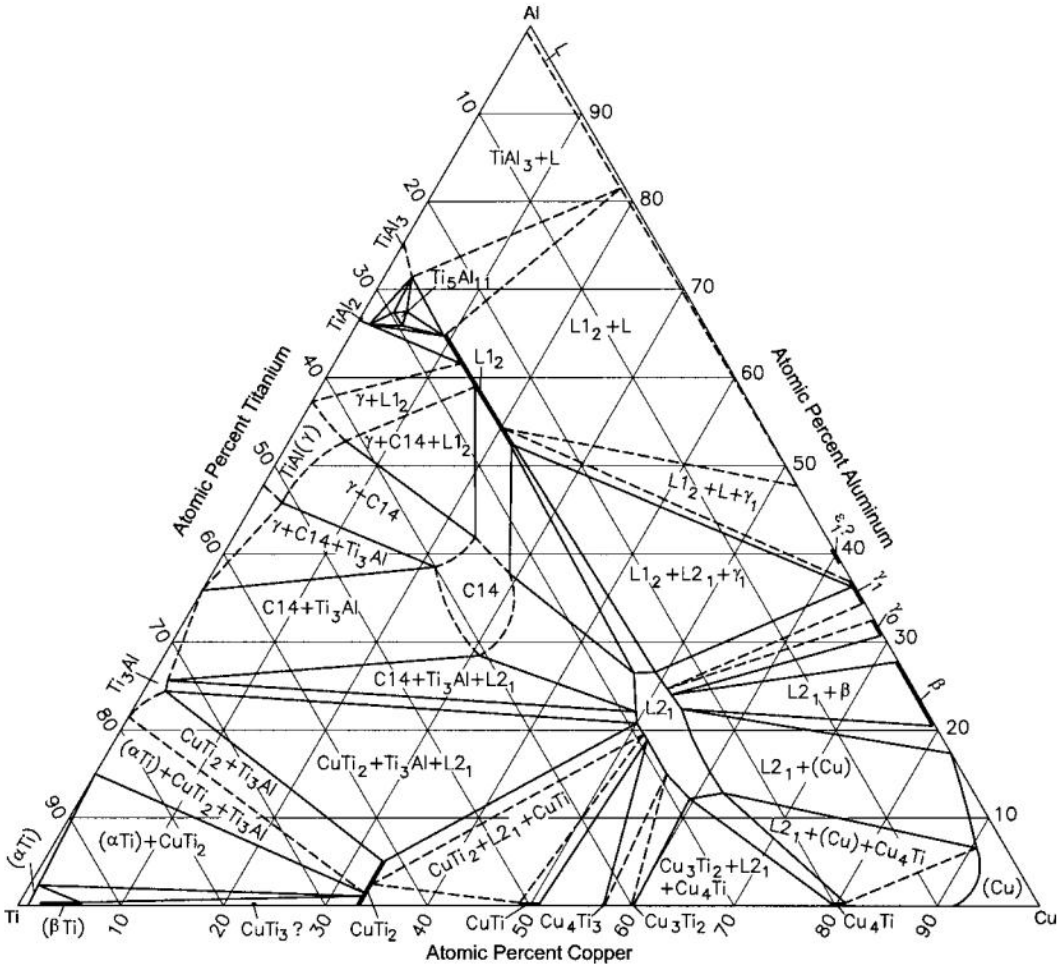

Figure 2.37 Al-Ti-Cu isothermal section at 850 °C [99].

Hong and Freeman [100] investigated the effect of Cu addition on the structural stability and electronic structure of Al_3Ti intermetallic compounds by first principles calculation. It is found that Cu atoms are strongly favourable to sit on Al

sites and can improve the stability of the $L1_2$ Al_3Ti phase, which is in agreement with experimental study.

Senying et al.'s [101] first-principles study also found that alloying element Cu strongly favours the sites of Al atoms in Al_3Ti and can promote the stability of cubic $L1_2$ structure. Frazier et al.'s [102] experimental study confirmed this, adding copper resulted in the transformation of Al_3Ti (made by rapid solidification) from $D0_{22}$ structure to $L1_2$ structure. Due to the transformation to the more symmetric cubic $L1_2$ structure, the adding of copper to Al_3Ti also significantly reduced the alloy's hardness and its crack susceptibility during microhardness testing [102].

2.5.3.3 Al-Ti-X ternary system (X=Mg, Mn, Ag, Si):

Mg, Mn and Ag are all minor alloying elements in AA2139 aluminium alloy. Si is an impurity element for AA2139, its content is controlled at a very low level, ~ 0.03 weight %, but it is still present and may affect the Al-Ti reaction.

Ag:

Ag is a minor but important alloying element in AA2139 aluminium alloy. Hence it is necessary to review the role of Ag on the Al-Ti reaction.

When Ag is added to Al-Ti reaction system, Ag_2Al phase was observed by some researchers [103, 104].

For example, in a study using Al-30Ag-10Cu filler metal to weld Al/Ti, Takemoto and Okamoto detected both Al_3Ti and Ag_2Al on the weld interface by XRD [103]. Ag also can stabilize Al_3Ti $L1_2$ structure and was often used as an additional

element to produce $L1_2$ Al_3Ti. It was found that Ag atoms occupy preferentially the Al sites in Al_3Ti [104].

Mg:

There is no binary intermetallic compound between Mg and Ti, but the addition of Mg to Al-Ti system can lead to the formation of cubic $Al_{18}Ti_2Mg_3$ phase coexisting with Al_3Ti phase [105]. First principles calculation showed that $Al_{18}Ti_2Mg_3$ phase has better ductility and lower elastic anisotropy than stable Al_3Ti phase [106].

Sometimes, $Al_{18}Ti_2Mg_3$ phase was the only phase formed on Al-Mg/Ti diffusion interface. Wei et al. only observed $Al_{18}Ti_2Mg_3$ phase by XRD on the fracture surfaces of diffusion welds between 5A06 aluminium alloy (containing 6.23 wt.% Mg and 92.30% Al) and titanium produced at bonding temperatures 525 °C, 550 °C and 565 °C [107].

Mn:

Like Ag, Mn was also widely used as an additional element to produce and stabilize the $L1_2$ structure Al_3Ti [108, 109]. Similar to Ag, Mn atoms also prefer to occupy Al sites in Al_3Ti [110].

Si:

The phases that can form in Al-Ti-Si are summarized in Table 2.4 [111]. Li et al [112] studied the Al-rich corner of the Al-Si-Ti system at 500 ℃ and found that Al, Si, $Ti_7Al_5Si_{12}$ and $Ti(Al,Si)_3$ phases co-exist at 500 ℃. Ternary phase $Ti_7Al_5Si_{12}$ was also observed in an Al-Ti joint brazed using a Zn-Si filler metal [113].

Table 2.4 Compounds in Al-Ti-Si ternary system [111].

Compound	Pearson symbol	Space group	Structure type	Lattice parameters.(pm)		
				a	b	c
Al	*cF*4	*Fm-3m*	Cu	404.96	…	…
$TiAl_3$	*tI*32	*I4mmm*	$TiAl_3$(r)	387.7	…	3382.8
$TiAl_2$	*tI24*	*I4$_1$/amd*	$HfGa_2$	397.0	…	2497.0
Ti_3Al_5	*tP*32	*P4/mbm*	Ti_3Al_5	1129.3	…	403.3
TiAl	*tP*4	*P4/mmm*	AlCu(I)	400.0	…	407.5
Ti_3Al	*hP*8	*P6$_3$/mmc*	Ni_3Sn	580.6	…	465.5
α-Ti	*hP*2	*P6$_3$/mmc*	Mg	295.06	…	468.35
Ti_3Si	*tP*32	*P4$_2$/n*	Ti_3P	1039.0	…	517.0
Ti_5Si_3	*tP*16	*P6$_3$/mcm*	Mn_5Si_3	744.5	…	514.6
Ti_5Si_4	*tP*36	*P4$_1$2$_1$2*	Zr_5Si_4	713.3	…	1297.7
TiSi	*oP*8	*Pnma*	FeB	654.4	363.8	499.7
$TiSi_2$	*oF*24	*Fddd*	$TiSi_2$	825.3	478.3	854.0
(Si)	*cF*8	*Fd-3m*	C	543.06	…	…
τ_1	*tI*24	*I4$_1$/amd*	$Zr_3Al_4Si_5$	357.6	…	2715
τ_2	*oC*12	*Cmcm*	$ZrSi_2$	358.33	1355.2	357.93

Besides $Ti_7Al_5Si_{12}$ phase, the other two ternary phases τ_1 and τ_2 were often observed as well. Both of them have fixed crystal structures, τ_1 ($I4_1/amd$, $Zr_3Al_4Si_5$-type) and τ_2 (Cmcm, $ZrSi_2$-type) respectively, but their chemical compositions varies depending on the conditions [111]. At 700 ℃, Li et al found the composition region of τ_1 and τ_2 were $Al_{6.2\text{-}9.3}Ti_{32.4\text{-}34.0}Si_{57.5\text{-}60.9}$ and $Al_{10.0\text{-}11.6}Ti_{34.2\text{-}34.5}Si_{53.9\text{-}55.6}$, respectively. It is also found that the maximum solubility of Si in Al_3Ti at 700 °C is 13.6 at.% [111].

In summary, $Ti_7Al_5Si_{12}$ phase, τ_1 and τ_2 phases are the ternary phases observed in the Al-Ti-Si system.

$(Al,Si)_3Ti$ phase (Solid solution of Si in Al_3Ti):

Pang et al [114] found that 6 at.% of Si dissolved in Al_3Ti phase in Ti-(SiC_P/Al) composite after annealing at 650 °C for 3 h. Si resulted in the lattice distortion of Al_3Ti, thus the elastic modulus and nanohardness increased from 220 GPa and 9.2 GPa to 280 GPa and 10.7 GPa respectively due to the solid solution strengthening of Si.

Zhu et al. [115] investigated the substitution behavior of Si in Al_3Ti ($D0_{22}$) by first principles calculation and indicated that Si has a strong preference for occupying Al sites. Zhu et al. also found that the maximum Si solubility in Al_3Ti lies in the range from 12.5% to 18.75% [116].

The enrichment of Si in Al_3Ti was clearly observed only by a few investigations [103, 117, 118]. For example, Nonaka et al. [117] observed that Si was concentrated in Al_3Ti layer formed on the interface between commercially pure Al which contains 0.27 wt.% Si and 98.7% purity titanium in the temperature range from 773 to 903 K, as shown in Figure 2.38. The Si concentration in the Al_3Ti layer varied from 4 at.% to 11 at.% depending on the annealing condition. It is considered that the Si in the Al_3Ti layer was enriched from the impurity Si in Al base metal.

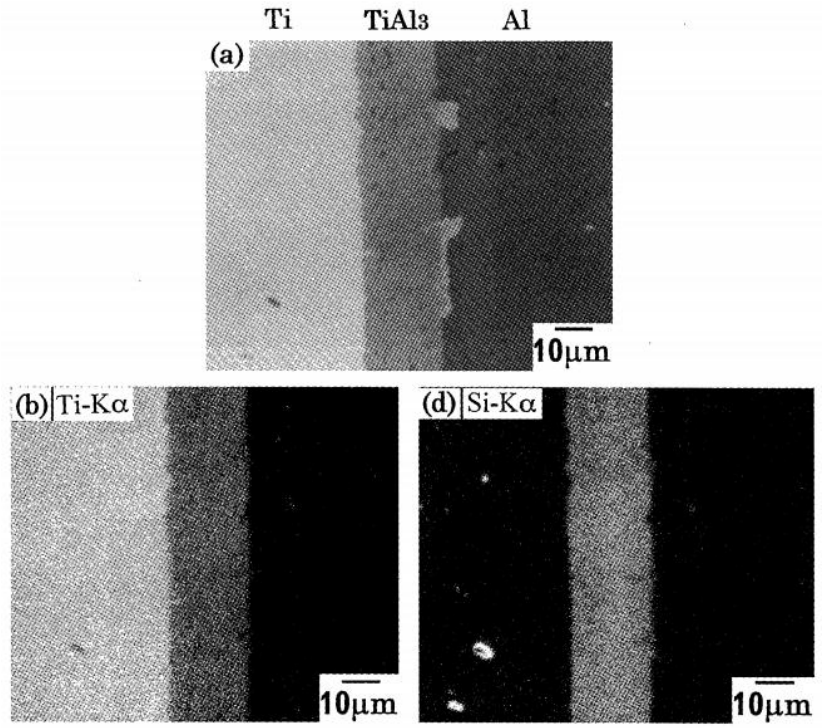

Figure 2.38 Enrichment of Si in the Al_3Ti layer (a) SEM image, (b) Ti distribution, (d) Si distribution (annealing condition: 903K, 28.8 ks) [117]

2.5.4 Summary of the possible reaction products in Al-Ti and Al-Ti-X systems during solid-state reaction

As the present study focused on solid-state reaction between Al and Ti, the possible solid-state reaction products in Al-Ti and Al-Ti-X systems in literature are summarised in Table 2.5.

Table 2.5 Summary of the possible solid-state reaction products in Al-Ti and Al-Ti-X systems

System		Observed phases in solid-state reaction	Comments and Ref
Al-Ti		Al_3Ti ($D0_{22}$)	The typical reaction product in solid state [76-84].
		Al_3Ti ($L1_2$)	Not stable, observed at 350 °C, started to transform to $D0_{22}$ structure when the temperature rose to 400 °C [86].
		$Al_{24}Ti_8$	Not stable, observed at 350 °C [85].
Al-Ti-X	Al-Ti-V	N/A	no data available in solid-state reaction.
	Al-Ti-Cu	Al_3Ti ($D0_{22}$)	[119]
	Al-Ti-Mg	$Al_{18}Ti_2Mg_3$ Al_3Ti ($D0_{22}$)	Mg results in the formation of the second phase $Al_{18}Ti_2Mg_3$ [105] [107].
	Al-Ti-Mn	N/A	no data available in solid-state reaction.
	Al-Ti-Si	$(Al,Si)_3Ti$ ($D0_{22}$)	[114]
	Al-Ti-Ag	N/A	no data available in solid-state reaction.

2.6 Growth kinetics of Al_3Ti reaction layer in Al-Ti couples

As mentioned before, dissimilar metal welding is a great challenge due to the formation of brittle intermetallic compounds on the weld interface [120-122]. Normally, a thick intermetallic compound (IMC) layer on the interface leads to

poor tensile strength and low fracture energy of a dissimilar joint [29, 123]. Therefore, understanding the growth kinetics of the IMC layer has become a common concern and is an important premise of determining how to control the IMC layer growth.

In this section, the deviation of Al_3Ti reaction layer growth from the parabolic law, the role of grain boundary diffusion, the reported activation energy for Al_3Ti layer growth, the atomistic understanding of diffusion in intermetallics, the diffusion anisotropy in intermetallics, the influence of oxidation layer on Al_3Ti layer growth and the anisotropic growth of Al_3Ti are reviewed.

2.6.1 Deviation from the parabolic law

As mentioned before, Al_3Ti phase is typically the only binary Al-Ti reaction product during the Al-Ti solid state welding processing. It is also a potential high strength low density structural material for aerospace applications. Hence, its growth kinetics have been widely investigated [76, 124].

Normally, for solid-state reaction layer growth controlled by diffusion, at a given temperature, the dependence of reaction layer thickness on annealing time can be described by the following equation:

$$x = \eta \cdot \sqrt{D} \cdot t^n \qquad \text{(Equation 2.1)}$$

Where x is the thickness of reaction layer, n=0.5 (according to the solution to Fick's second law), D is the diffusion coefficient, t is the annealing time and η is a constant factor.

However, a few previous investigations [76, 125, 126] found that the Al_3Ti reaction layer thickness and annealing time relationship does not always strictly obey the parabolic law, especially when the annealing temperature is relatively high. Sometimes the real reaction layer thickness is smaller than that calculated from the Equation 2.1. In other words, the exponent of t (n) is smaller than 0.5.

For example, Mirjalili et al. [76] investigated the growth of the Al_3Ti layer at 550, 575, 600, 625, and 650 °C and found that with an increase of annealing temperature, the calculated exponent of t (n) decreased from 0.55 to 0.25. The authors claimed that the Al_3Ti layer growth is controlled by both bulk diffusion and grain boundary diffusion, and Al_3Ti grains coarsened with increasing annealing time. The higher the annealing temperature the faster the grains coarsened. The coarsening of Al_3Ti grains resulted in the reduce of the fraction of grain boundaries, which are fast diffusion paths compared with bulk diffusion, thus the Al_3Ti layer growth was slowed down and the growth exponent n was also decreased.

Loo and Rieck [125] also observed the non-parabolic growth of Al-Ti intermetallic layer and the reason is indicated to be the influence of grain boundary diffusion. It is suggested that grain boundary diffusion decreased steadily with increasing annealing time as a result of grain coarsening in the reaction layer.

The slower growth of the Al_3Ti layer than that predicted by the parabolic law at relatively high temperature (650 °C) was also reported by Cui et al [126], as shown in Figure 2.39. It is claimed that the slower growth is due to the numerous small Kirkendall voids formed during the annealing process.

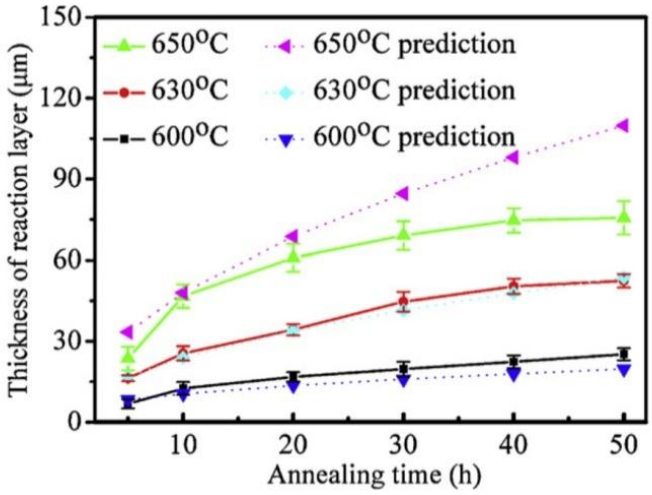

Figure 2.39 Comparion of Al_3Ti layer thickness between the experimental values and the predicted values by parabolic law [126].

Recently, Al_3Ti grain coarsening during annealing was experimentally observed by Mirjalili et al [127] from back-scattered electron images of cross sections of Al-Ti diffusion couples, as shown in Figure 2.40.

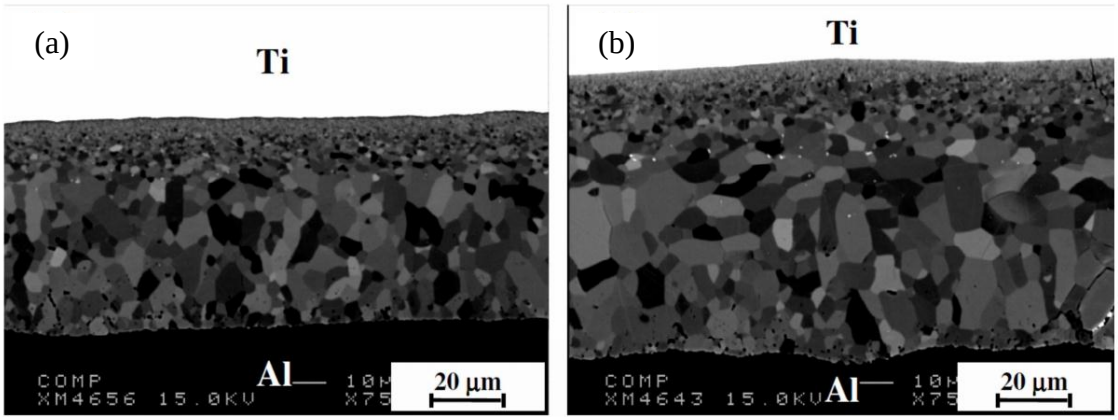

Figure 2.40 Backscattered electrons (BSE) images of Al_3Ti layer annealed at 650°C for 1.75 h (a) and 5 h (b) [127].

In summary, in most real Al-Ti diffusion systems, the diffusion conditions (including the grain size, surface oxidation layer decomposition and the Kirkendall voids) change during the annealing process and thus are not as ideal as that

assumed for the deduction of the parabolic growth law. Thus, the real Al_3Ti layer growth often deviates from the expected parabolic law.

2.6.2 Grain boundary diffusion

There are two types of diffusion in a polycrystalline solid, lattice diffusion (also called bulk or volume diffusion) and diffusion in lattice defects (including diffusion along dislocations, grain boundaries, interfaces and free surfaces) [128]. Among all kinds of diffusion in lattice defects, grain boundary diffusion (GB) is usually believed to be the dominant one. Grain boundaries are considered to be high-diffusivity paths compared with lattice diffusion [129]. As early as 1950, the fast grain boundary diffusion was detected by autoradiographic images [130], from which the ratio between GB diffusion and lattice diffusion was estimated to be several orders of magnitude [131]. Therefore, the fraction of grain boundaries, which is determined by grain size, can markedly influence the whole effective diffusion in a solid. Usually, the more grain boundaries in a solid, the higher effective diffusivity.

The effective diffusion coefficient in a polycrystalline solid, considering both bulk diffusion and grain boundary diffusion, was firstly described by Hart's equation based on a 2D model [129] has been widely accepted and frequently used.

$$D_{eff} = g \cdot D_{gb} + (1-g) \cdot D_L \qquad \text{(Equation 2.2)}$$

Where g is the fraction volume of grain boundaries (GBs), and equals to $\frac{q\delta}{d}$, δ is the width of grain boundary, d is the grain size, q is a factor depending on the grain morphology, q=1 for parallel grain boundaries and q=3 for cubic grains, D_{gb} and

D_L are grain boundary diffusion coefficient and lattice diffusion coefficient respectively .

From Equation 2.2, it can be seen that the grain size and grain morphology can strongly affect the effective diffusion coefficient. Thus, as mentioned in section 2.6.1, this mechanism was frequently used to explain the non-parabolic growth of Al-Ti intermetallic layer due to the Al_3Ti grain size changing during annealing.

2.6.3 Activation energy for Al_3Ti layer growth

The purpose of the section is to give a general idea on the studies so far on the activation energy of Al_3Ti layer growth.

The following equation simplified from Equation 2.1 was often used for describing the reaction layer growth:

$$\ln x = n \cdot \ln t + \ln K \qquad \text{(Equation 2.3)}$$

Where K is the rate constant and t is the annealing time and n is the kinetic exponent.

The rate constant can be express by the following Arrhenius type equation:

$$K = A \cdot \exp(\frac{-Q}{RT}) \qquad \text{(Equation 2.4)}$$

Where A is the pre-exponential factor, Q is the activation energy for the reaction layer growth and T is the absolute temperature.

The activation energy, which is a vital parameter for the diffusion system, has been calculated by many researchers, however the results (calculated activation energy

by different researchers) vary widely. The reported values of the activation energy so far are summarized in Table 2.6. The fluctuation of the calculated activation energy value is understandable, since it can be affected by many factors, including the purity of materials, the protective atmosphere (air furnace, argon gas furnace and vacuum furnace), the initial surface conditions (roughness, degree of surface oxidation), the alloying elements in the base metals, the Al_3Ti grain size coarsening, the formation of Kirkendall voids in the diffusion couples and the pressure applied on the diffusion couples.

Table 2.6 Reported values of activation energy in Al-Ti system.

Temperature range (°C)	Purity of titanium	Purity of aluminium	Activation energy (kJ mol^{-1})	Ref.
516-640	99.7	99.99	95.0	[81]
540–650	99.99	99.999	33.8	[83]
570–650	99.5	99.999	61.4	[83]
375–475	99.6	-	166	[84]
530–600	97	–	105.1	[132]
500–630	98.7	99.2	237	[117]
550–625	99.9	99.99	33.1	[76]
625–650	99.9	99.99	296.2	[76]
600-650	Commercially pure	-	254.9	[126]
500–600	99.5	99.7	207	[133]
500–630	95	99.2	263	[117]

2.6.4 Atomistic understanding of diffusion in binary intermetallics

Whereas diffusion in pure metals and dilute alloys has been systematically and thoroughly studied and is relatively simple and easy to understand, diffusion

studies in intermetallics are limited and the diffusion mechanism has not been well understood. Due to the ordered A-B structure, the atom jump in intermetallic is not as random as that in pure metals and dilute alloys [134]. As a result, the atomistic understanding of diffusion in intermetallics, such as vacancy jump mechanism, is more complex than that for random solid solutions.

Though so far there is no published work on the atomistic diffusion mechanism (vacancy jump mechanism) in Al_3Ti, the vacancy jump mechanism in other Al-Ti intermetallics, Ti_3Al and TiAl has been reported. Y. Mishin and Chr. Herzig [134] have reported two types of diffusion mechanism in Ti_3Al and TiAl, respectively three-jump cycle and six-jump cycle, as shown in Figure 2.41 and Figure 2.42. Three-jump cycle is the simplest vacancy jump mechanism. Six-jump cycle has been also applied for simulating the diffusion in other structures, such as $L1_2$ and B2 structures. More details on vacancy jump mechanism in Al-Ti intermetallics can be found in Ref [134].

The Cu_3Au rule:

The Cu_3Au rule is a simple empirical rule that often provides a good estimate for self-diffusion in non-equiatomic intermetallics suggested by d'Heurle and coworkers [135, 136]. It states that in an A_mB_n type compound, where the m/n ratio is greater than 2, the majority element A diffuses faster than the minority element B:

$$D_A^* > D_B^* \text{ or } D_A^* \gg D_B^*$$

Where D_A^* and D_B^* respectively denote the tracer diffusion coefficient of elements A and B.

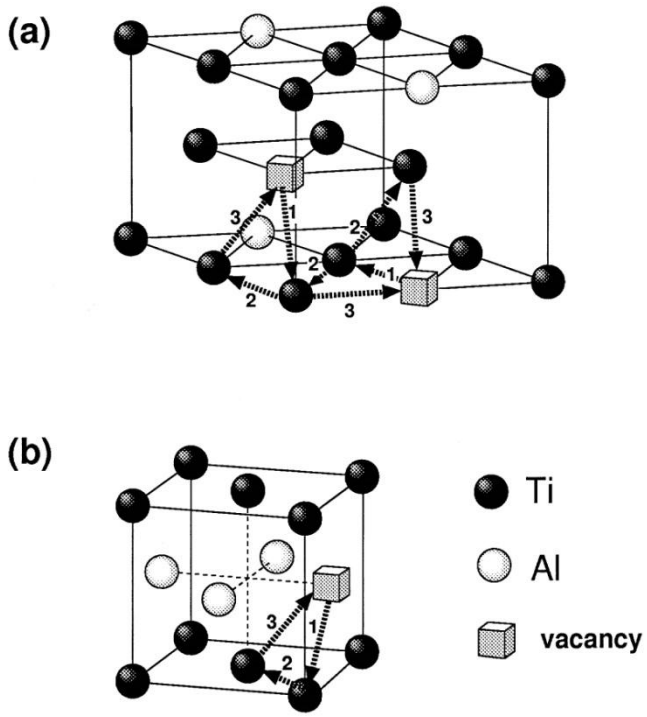

Figure 2.41 Schematic three-jump cycles of Al vacancies in Ti_3Al ($D0_{19}$) (a) and TiAl ($L1_0$) (b) [134].

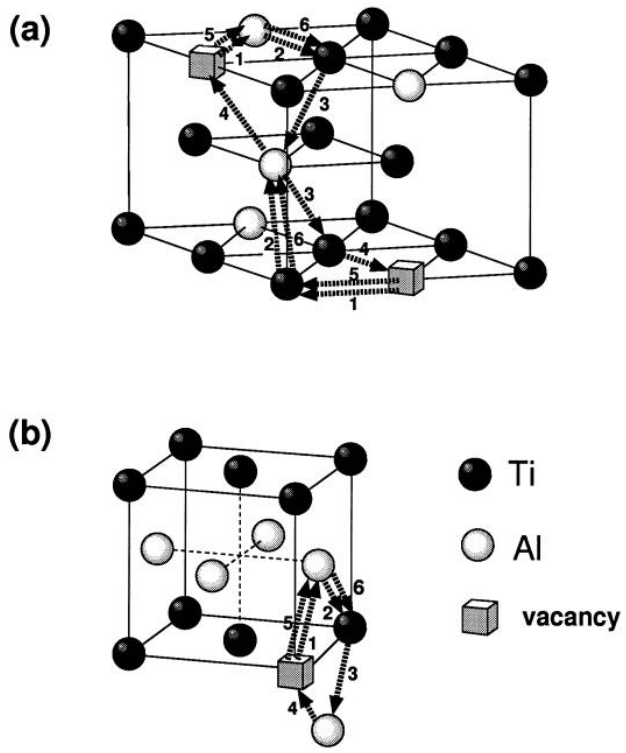

Figure 2.42 Schematic six-jump cycles of Al vacancies in Ti_3Al (a) and TiAl (b) [134].

Many non-equiatomic intermetallics, including Fe_3Si, Cu_3Sn, Ni_3Ge, Co_2Nb and Ni_3Ga, have been found indeed fulfil this rule [137, 138].

The Cu_3Au rule is explained by the fact that majority-component atoms can diffuse via energetically favourable jumps in their own sublattice, minority-component atoms diffuse either by energetically unfavourable jumps to more distant sites in their own sublattice or as antisite atoms on the wrong sublattice [129].

It is worth noting that, due to the origin of the Cu_3Au rule, it only can be applied to intermetallics in which diffusion occurs via vacancies. Compounds such as metal hydrides, carbides and nitrides, where one of the two elements is small enough to occupy interstitial sites do not follow this rule.

2.6.5 Diffusion anisotropy in uniaxial intermetallics

Diffusion anisotropy is a typical phenomenon in non-cubic materials. Non-cubic intermetallics, such as tetragonal, hexagonal or trigonal intermetallic phases, are no exception. Diffusion in non-cubic materials can be described by two diffusion tensors, i.e. the diffusivity parallel to a particular crystallographic axis, $D_{\parallel}$, and the diffusivity perpendicular to the axis, $D_{\perp}$. Normally, they are different from each other.

There is no published work on the diffusion anisotropy in Al_3Ti. However, there are a few studies on the diffusion anisotropy in another Al-Ti binary intermetallic, TiAl, due to its industrial importance as a high-temperature aerospace structure material. It was found that both diffusivity of Ti and impurity Indium (In) in TiAl phase showed obvious anisotropy. The diffusion in the direction perpendicular to the tetragonal axis ($D_{\perp}$) is faster than that in the parallel direction ($D_{\parallel}$) [139, 140],

as shown in Figure 2.43. For Ti self diffusion, $D_{\perp}$ is even almost 10 times faster than $D_{\parallel}$. The crystal structure of TiAl phase is shown in Figure 2.44.

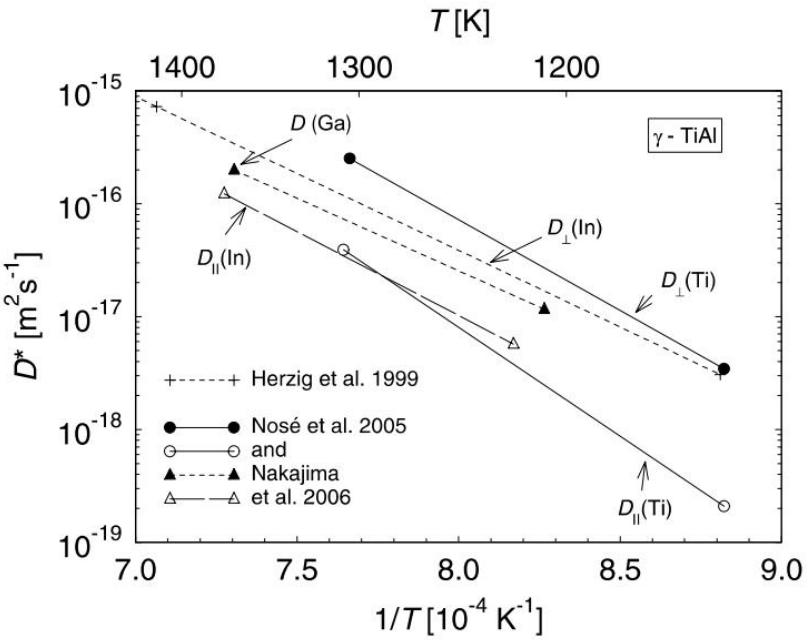

Figure 2.43 The diffusion of Ti and In along the two principle directions of TiAl phase [139, 140].

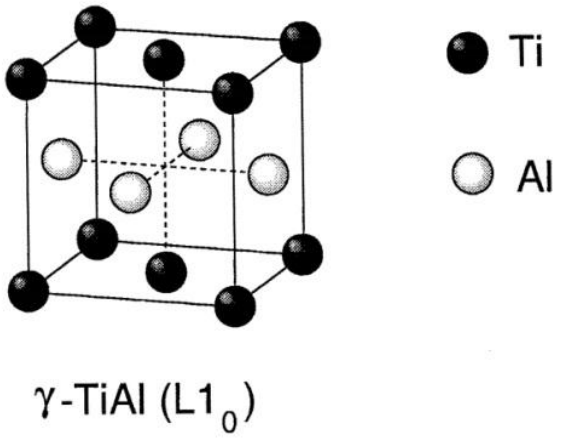

Figure 2.44 Crystal structure of TiAl ($L1_0$) [134].

2.6.6 Anisotropic growth of Al_3Ti

Anisotropic growth of intermetallics is quite common, due to the anisotropic surface free energy of intermetallics [141]. Al_3Ti is no exception [142], as shown in Figure 2.45. Usually, crystal growth rate along the direction, which is normal to the crystal plane with the highest packing density (highest atomic density), is slowest, since the plane with the highest packing density has the lowest surface free energy. The planar density of different planes in Al_3Ti was calculated [142], as listed in Table 2.7. It can be seen that the (001) plane has a much higher density than all other planes, thus the growth normal to (001) plane should be slowest. John and Hogan's study [142] confirmed that, under the given conditions, all the dendrite arms of Al_3Ti grow in the [110] direction, which is parallel to the (001) plane, and the growth of Al_3Ti plates is almost two-dimensional, indicating that the [001] growth rate, i.e. the growth rate normal to the (001) plane, was negligible.

It should be pointed out that, though the anisotropic surface energy is a vital factor that leads to the anisotropic growth of Al_3Ti, other factors such as freezing conditions (supercooling) and third alloying elements also could affect the growth morphology of Al_3Ti and may retard the anisotropic growth [142].

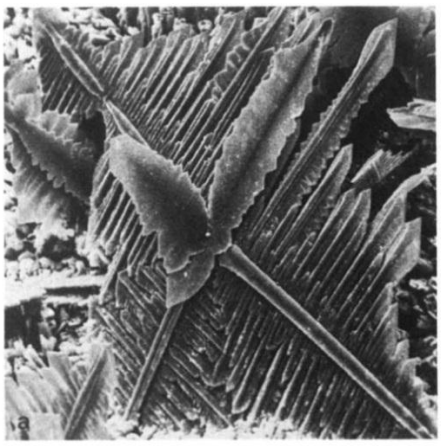

Figure 2.45 The anisotropic growth of Al_3Ti in an Al-Ti alloy [142].

Table 2.7 The planar densities of different planes in Al_3Ti [142].

Plane	Density (atoms Å^{-2})
001	0.202
100,010	0.150
111	0.146
102	0.135
120	0.134
130	0.129
250	0.126
140	0.117
150	0.112
110	0.107

Considering the growth of Al_3Ti into Al in a dissimilar couple, Oishi et al. [143] found a preferred orientation relationship between Al {111} and Al_3Ti {112} due

to the very small mismatch between these two planes. The mismatches in both directions between these two planes were calculated to be ~1% (Figure 2.46).

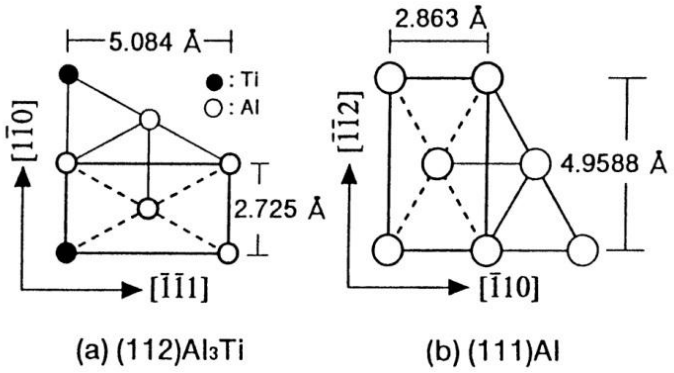

Figure 2.46 The unit cell of Al_3Ti (112) and that of Al (111) [143].

Tardy and Tu [144] also indicated the same epitaxial relationship between Al_3Ti and Al, as shown below. This relationship was experimentally supported by the strong (111) reflection of aluminium and strong (112) reflection of Al_3Ti by XRD analysis, as shown in Figure 2.47.

$$(111)Al//(112)Al_3Ti$$

$$[110]Al//[110]Al_3Ti \text{ or } [110]Al//[012]Al_3Ti.$$

Tardy and Tu [144] also indicated the following epitaxial orientation relationship between Ti and Al_3Ti, since the misfit between (112) Al_3Ti plane and (001) Ti plane is just over 1%.

$$(112)Al_3Ti//(001)Ti,$$
$$[110]Al_3Ti//[110]Ti$$

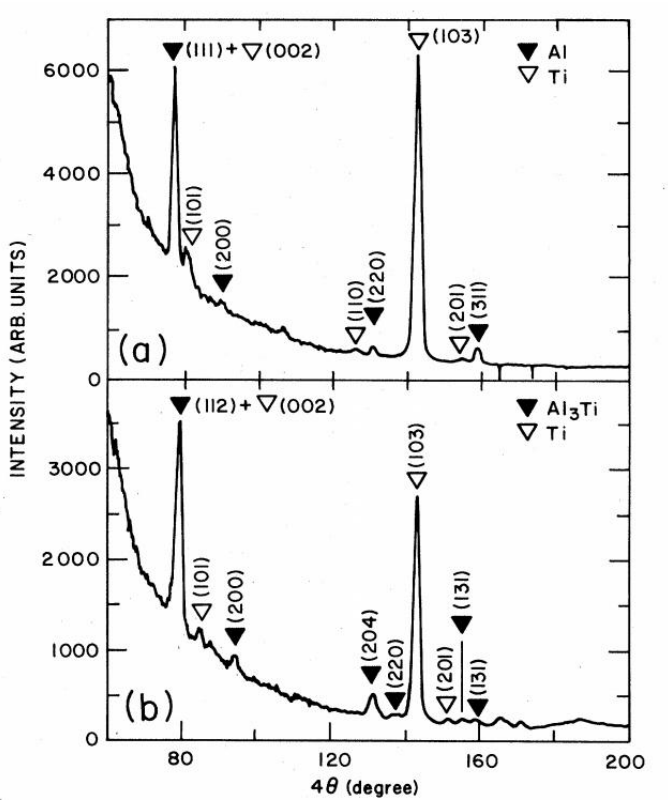

Figure 2.47 X-ray diffraction diagram for the as-deposited Al and Ti filmed without annealing (a) and (b) after annealing for 90 min at 400 °C [144].

Effect of additional elements on anisotropic growth

(1) Effect of Cu on the anisotropic growth of Al-X compound

LeGoues et al. [145] found that Cu addition (9 wt. %) to Al resulted in a much smoother Al_3Hf/Al interface than that without Cu, as shown in Figure 2.48. Without Cu addition, the Al_3Hf growth on the interface showed spike morphology at 450 °C annealing temperature. It is proposed that Cu segregation along the Al grain boundaries prevents the Hf atoms from diffusion along the grain boundaries, thus resulted in a more uniform growth.

It is also found that 1.5 wt.% addition of Cu to Al supressed the spiked growth of $Al_{12}W$ on the interface between Al and Ti-W at 450 °C [119]. Only 0.5 % Cu

addition did not have such effect. This effect of Cu was explained by the same mechanism mentioned above. Increased Cu addition promoted the Cu segregation along Al grain boundaries.

(2) Effect of V and Mo

Abdel-Hamid and Ahmed [146] investigated the influence of V and Mo on the growth morphology of Al_3Ti. Without these alloying elements, Al_3Ti grows as thin and large plates with clearly visible steps at the plate edges. The large plate surface is the (001) plane, which agrees with the fact that (001) plane has the highest packing density. The addition of V encouraged the growth of flat dendritic crystals with many branches growing in the [110] directions. Mo addition enhanced the [001] direction growth rate so that completely facetted block like crystals were formed.

2.7 Effect of alloying elements on reaction layer growth

In the practical industrial production, especially in industrial welding applications, aluminium alloys and titanium alloys are far more often used than pure Al and pure Ti. Therefore, understanding the role of alloying elements on Al_3Ti growth kinetics is important.

Most investigations on Al-Ti reaction belongs to either solid (Al) - solid (Ti) reaction type or liquid (Al) - solid (Ti) reaction type. These two types of reaction have very different mechanisms. The main focus of this section is the solid (Al) - solid (Ti) reaction type, which is the same situation as the present study. Liquid (Al) - solid (Ti) reaction type was reviewed as well. As a large number of Al-Ti reactions are reviewed in this section, to avoid confusion, all the reviews on the

minority liquid (Al) - solid (Ti) reaction are specially marked using a line of boldface letters.

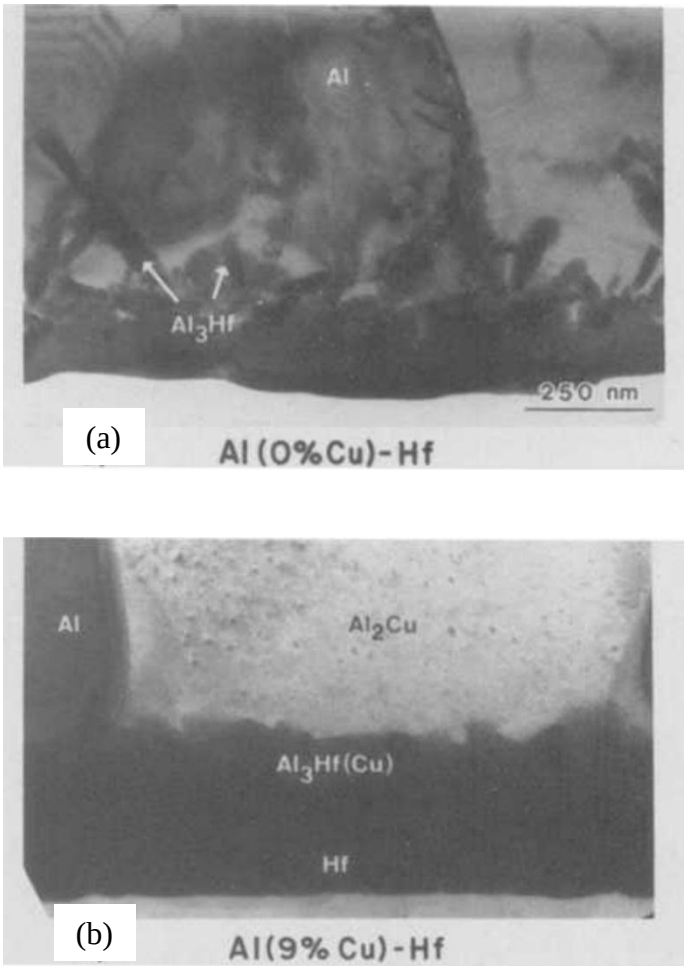

Figure 2.48 The Al_3Hf/Al interfaces (a) 0% Cu (b) 9% Cu [119].

2.7.1 Effect of Cu on Al_3Ti growth

Copper is an important alloying element in Al alloys. Its influence on the Al_3Ti reaction layer growth has been investigated by [119, 144, 147] (mainly in studies with electronic industry background).

Krafcsik et al. [119] studied the Al_3Ti layer growth between Al-Cu (3 at.%)/Ti. The adding of 3 at.% Cu resulted in the decrease of Al_3Ti layer growth rate by an order

of magnitude (Figure 2.49) at 400 °C and increased the activation energy from 1.8 eV to 2.4 eV.

Two possible explanations were proposed [119]: (1) Cu might segregate on the grain boundaries of Al_3Ti and then retarded the diffusion along the grain boundaries; (2) Formation of Al-Cu alloy on the Al-Ti interface impede the release of Al atoms leading to an increase of activation energy.

It was suggested that the activation energy has contribution from both bulk diffusion and grain boundary diffusion, and for the higher 2.4 eV activation energy, bulk diffusion accounts for a larger portion. The above explanations were not proved by experimental evidences [119].

Wittmer et al. [147] investigated the influence of Cu on Al_3Ti layer growth kinetics and microstructure by using different Al alloys respectively containing 0% Cu, 1 % Cu and 4.5% Cu (weight percent). The activation energy increased from 1.60 to 2.05 eV with the increase of Cu content from 0% to 1% and the D_0 increased by three orders of magnitude. The activation energy increases no further when the Cu concentration increases from 1% to 4.5%.

It was also found that the Al/Ti interface was smoother with the presence of Cu [147]. Two mechanisms were proposed to explain this. (1) Al grain boundaries are preferential nucleation sites for Al_3Ti, but with the presence of Cu in Al, Al_2Cu phase could also probably nucleate on the grain boundaries and Cu could segregate on the grain boundaries as well. Both can prevent the Ti diffusion along the Al grain boundaries. Consequently, Al_3Ti grew more uniformly on the Al/Ti interface. (2) Cu can promote the Al grain growth, as a result, the Al containing Cu near the

Al/Ti interface has larger grain size. With much larger Al grains, hence fewer grain boundaries (nucleation sites), the Al-Ti interface became smoother.

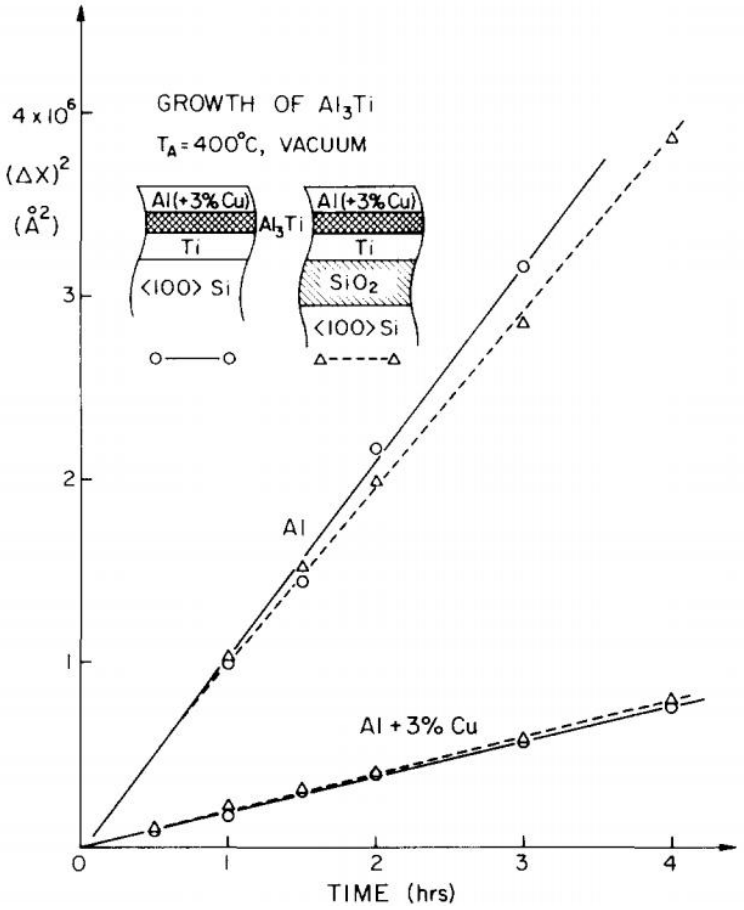

Figure 2.49 Comparison of the Al_3Ti layer growth rate in pure Al/Ti couples and in Al(+3%Cu)/Ti couples [119].

For the mechanism of Cu retarding Al_3Ti layer growth, Wittmer et al. [147] did not fully agree with the explanation of Krafcsik et al. [119]. Wittmer et al. argued that the theory of Cu segregation on Al_3Ti grain boundaries cannot be corroborated by the solid solution data of Cu in Al_3Ti, which was not available. Wittmer et al. proposed that the Al_3Ti grain size increased 3-4 times with the presence of Cu, which means the fraction of grain boundary region decreased about 10 times. This accounts for the the drop of Al_3Ti growth rate with the presence of Cu. Wittmer et al. also proposed another possible explanation for the reduced growth rate with the

presence of Cu. It was the formation of other Al-Ti and Al-Ti-Cu phases in the reaction layer, such as $Al_{23}Ti_9$, $Al_{11}Ti_5$ andAl_4CuTi_2. The presence of a second phase could affect the diffusion process.

Tardy and Tu [144] also reported that Cu addition (0.25 at. %) greatly slowed down the growth kinetics of Al_3Ti and demonstrated that the presence of Cu increased the activation energy of Ti diffusion in Al_3Ti from 1.68 eV to 2.17 eV but the activation energy of Al is much less affected (1.81 versus 1.88 eV).

The pronounced effect of Cu on Ti diffusion was explained by examining the crytal structure of Al_3Ti and assuming that Cu atoms occupied the Al sites in Al_3Ti (because Cu-Ti bonding energy is higher than that of Cu-Al) [144]. Consequently, the jump of Ti atoms will be more difficult when Cu atoms occupy the Al sites because of the stronger attraction between Cu atom and Ti atom, which leads to a higher activation energy for diffusion [144]. Tardy and Tu also found that there was no Cu accumulation at any interface in the Al(Cu)-Ti diffusion system indicating that interfacial barrier effect of Cu can be neglected.

By using a diffusion marker, Tardy and Tu [144], Colgan and Mayer [148] and Nonaka et al. [117] found that Al is the dominant moving species for Al_3Ti layer growth.

2.7.2 Effect of Oxygen

Oxygen is an inevitable impurity or import alloying element in both Al and Ti alloys. Also, the surfaces of aluminium and titanium are easy to be oxidized since they both are very active metals. Its influence on Al_3Ti layer growth could be important.

Effect of oxide film:

Though the oxidation layer is thin, it could act as a diffusion barrier in the initial stage of diffusion [124]. As a result, especially when the annealing temperature is low, the initial stage (incubation period) growth behaviour of Al_3Ti layer is different from the follow-up stage, in which the oxide film has already been dissolved by the interfacial reaction.

When the annealing temperature is low, the decomposition process of the oxide films takes a long time, as a result the difference between initial stage growth and the follow-up stage growth is more evident in the low annealing temperature cases. This different growth behaviour between the initial stage and the follow-up stage results in the whole annealing time - Al_3Ti layer thickness relation no longer obeying the parabolic law.

However, if the follow-up stage of Al_3Ti layer growth is separated from the whole growth process, or the samples were pre-annealed to dissolve the oxide film on the Al and Ti surfaces in advance, the annealing time-Al_3Ti layer thickness relationship still obeys the parabolic law [124]. Shimozaki et al. [124] reported this phenomenon caused by the oxide film is easy to be observed when the annealing temperature is less than or equal to 843 K (570 °C), as shown in Figure 2.50.

Kráľ, J., et al. also has reported the incubation period of Al_3Ti layer growth and also indicated that this is due to the oxide layer on the titanium [132]. Besides, F.J.J van Loo and G.D Rieck [81] also reported an initial linear growth period and they suggested two possible reasons for the linear growth. The first explanation is that the reaction between titanium, aluminium, and the obstructing oxide layer is rate-determining. Their second explanation is that the penetration of Al atoms across the

oxide layer is rate-determining. Furthermore, F.J.J van Loo and G.D Rieck suggested that the incubation period is very likely caused by the oxide layer on the surface of titanium, rather than the oxide layer on the surface of Al, since this effect has not been found in Ni-Al diffusion experiments.

Thuillard et al. [149] investigated the Al/Ti reaction with a purposely pre-produced thin Al-oxide layer on the Al/Ti interface. The annealing was performed at 460 °C. Both the Al layer and the Ti layer are very thin, only several hundred nanometres, since the background of this investigation is integrated circuit industry. TEM observation found that Al_3Ti nucleation occurred on the Al/Al-oxide interface not on the Ti/Al-oxide. It is suggested that Al_3Ti poorly wets the Al-oxide layer, based on the observation that the contact angle between Al_3Ti and Al-oxider layer is larger than 90° (see Figure 2.51). Also, usually the wettability of a metal (Al) is better than its stable oxide (Al_2O_3).

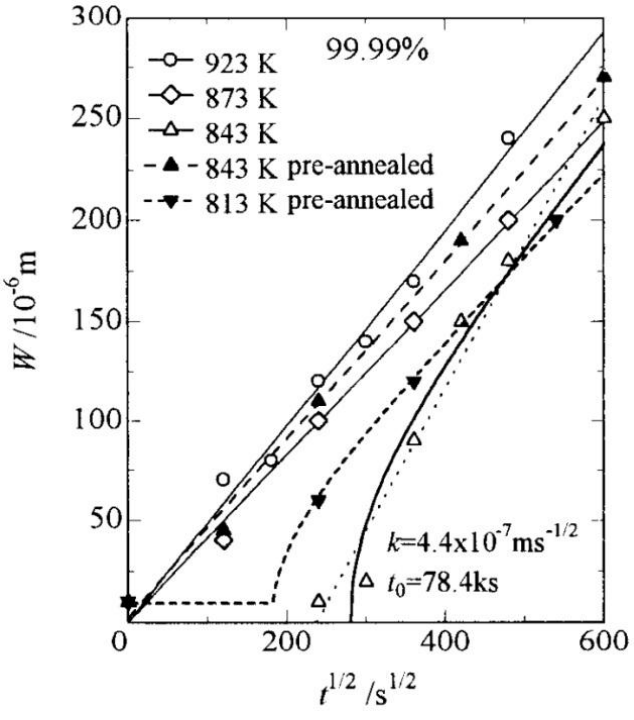

Figure 2.50 Growth kinetics of Al_3Ti layer in Al/Ti diffusion couple [124].

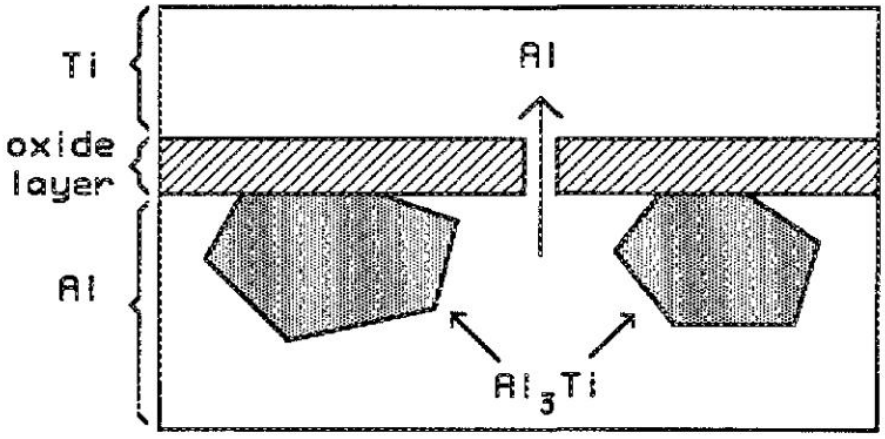

Figure 2.51 The nucleation of Al_3Ti on the Al/Al-oxide interface [149].

Effect of oxygen in titanium alloy matrix:

Wittmer and Goues [147] suggested that the reason for the difference in the calculated activation energies in Al-Ti diffusion systems from different groups could be probably due to the different degree of oxygen contamination of titanium, due to its strong oxygen gettering capability.

Nonaka et al. [117] investigated the effect of oxygen in titanium on the reaction layer growth between Al and Ti. With the presence of 5 at.% oxygen in titanium, no intermetallic compounds other than Al_3Ti were observed in the reaction layer between Al and Ti after annealing at temperatures ranging from 773 to 903 K (500 °C to 630 °C). The addition of oxygen increased the diffusion activation energy from 237 to 263 kJ mol^{-1}. Nonaka et al. [117] proposed that due to that an Al-oxide layer formed on the reaction layer/Al interface (see Figure 2.52) as a result of the reaction between Al and oxygen from titanium, the reaction layer (Al_3Ti) growth was retarded by the Al-oxide layer.

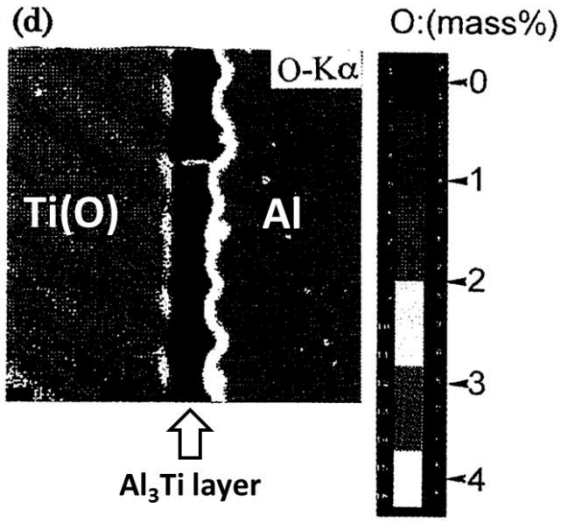

Figure 2.52 EPMA analysis result of oxygen distribution in the Al-Ti(5% O) diffusion couple [117].

Zhao et al. [79] investigated the effect of oxygen from both titanium base metal and the annealing atmosphere on the Al_3Ti formation in the temperature range from 450 °C to 515 °C. It was found that the oxygen in Al/Ti samples can slow down the growth of Al_3Ti layer by decreasing the pre-exponential factor but does not change the activation energy. With an increase of oxygen concentration in Al_3Ti, Al atom transport through the intermetallic was decreased. Oxygen already dissolved in the titanium and oxygen from the annealing atmosphere was incorporated in the growing Al_3Ti phase during annealing. The concentration of oxygen in Al_3Ti layer can reach ~15 at. %. Moreover, unlike Cu, the oxygen content did not affect the smoothness of the interfaces between Al_3Ti and the base metals [79].

2.7.3 Effect of Vanadium

In liquid (Al) - solid (Ti) reaction system

Vanadium is an important alloying element for commercial titanium alloys. Very recently, Nie et al. [150] investigated the effect of vanadium on the Al_3Ti layer

growth by comparing the interfacial reaction between Al/Ti and Al/Ti6Al4V at temperatures above aluminium melting point (720 °C, 740 °C and 760 °C). Low concentration of vanadium was found in the reaction layer between Al and Ti6Al4V. The interfacial reaction in Al/Ti6Al4V was slower than that in Al/Ti though both reaction layers are quite thick (in the range of 100~700 um, see Figure 2.53 and Figure 2.54) due to the high temperatures applied. Besides, it is reported that the maximum strength of Al/Ti6Al4V joint (64 MPa) is lower than that of Al/Ti joint (78 MPa).

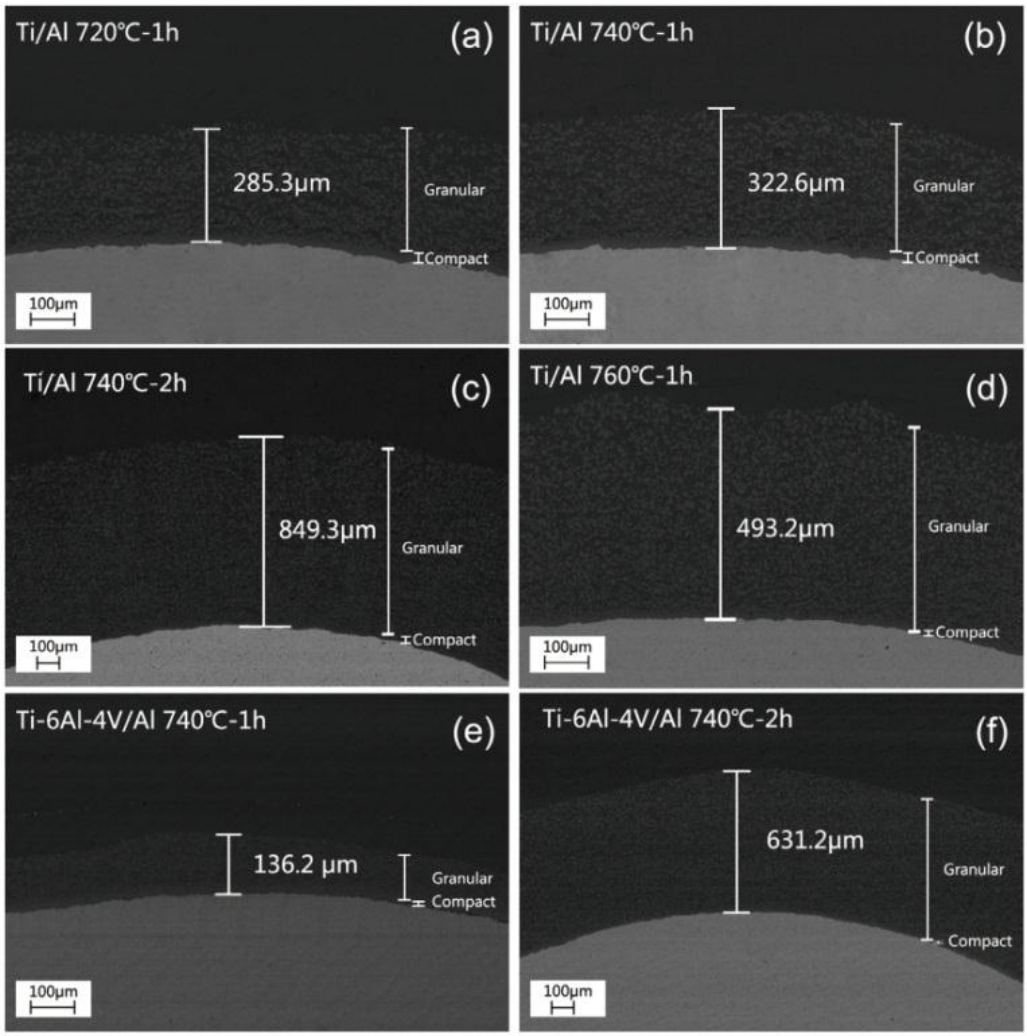

Figure 2.53 Reaction layers in Al/Ti (a-d) and Al/Ti6Al4V (e,f) joints grown at different temperatures [150].

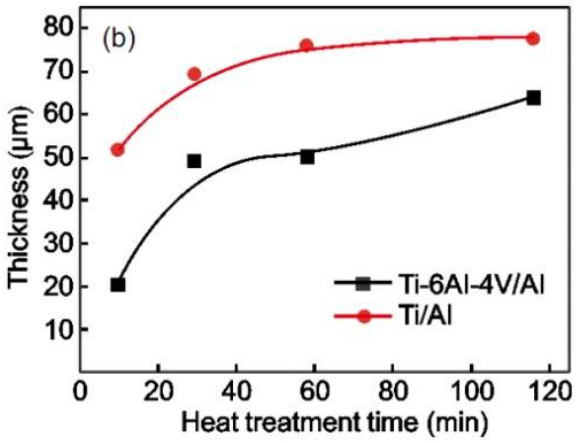

Figure 2.54 Reaction layer growth kinetics in Al/Ti and Al/Ti6Al4V joints [150].

2.7.4 Effect of Zirconium

In liquid (Al) - solid (Ti) reaction system

Lv et al. [151] investigated the influence of Zr addition on the interfacial reaction between an Al-Cu filler metal and Ti6Al4V titanium alloy. Zr addition increased the wettability of melted Al-based filler metal on the surface of Ti6Al4V. With Zr addition, a three-layer reaction product formed on the Al/Ti interface, as shown in Figure 2.55, layer I: Al_3Ti phase, layer II: $Al_3(Ti,Zr)$ phase with low concentration of Zr and layer III: $Al_3(Ti,Zr)$ phase with high concentration of Zr. It is also found that the welds produced using Al-Cu-Zr filler wire have higher tensile strength than those of welds produced using pure Al filler wire.

2.7.5 Effect of Silicon

As an important alloying element in Al alloys, the influence of Si on the Al_3Ti layer growth has been widely investigated.

2.7.5.1 In liquid (Al) - solid (Ti) reaction system

Takemoto and Okamoto [103] investigated Ti-Ti brazing using Al-based filler metal with different Si contents (0.1%, 0.3%, 0.8%, 3%, 10%). A small amount addition of Si (up to 0.8%) to the Al filler metal pronouncedly reduced the Al_3Ti layer growth rate by more than 10 times, as shown in Table 2.8. It can be seen that with the increase of Si concentration from 0.1% to 0.8%, the reaction layer thickness decreased. Si was detected in the Al_3Ti layer and its content (1% to 3%) is higher than that in the filler metal (0.1% to 0.8%), as shown in Table 2.9, which is a common phenomenon as mentioned in Section 2.5.3.

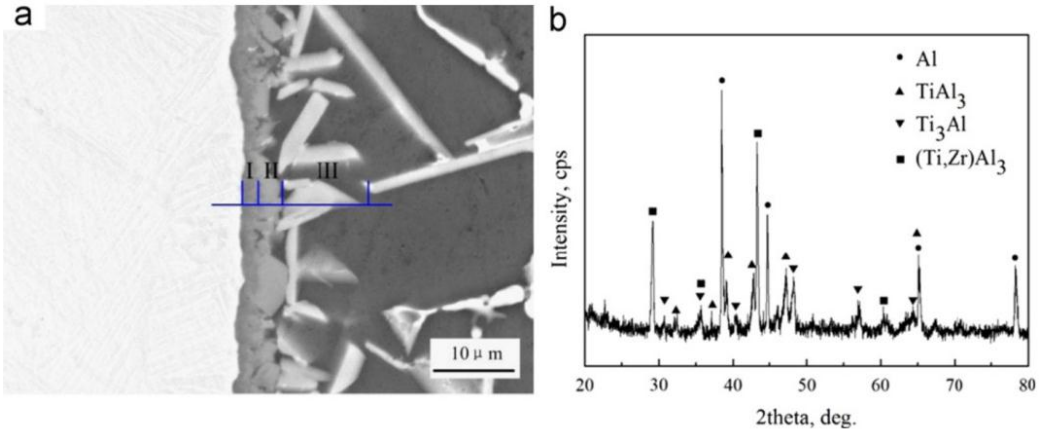

Figure 2.55 Three-layer reaction products on the Al-Cu-Zr/Ti6Al4V interface (a) SEM image and (b) XRD analysis result of the weld interface [151].

However, keeping on increasing the Si concentration in the Al to 3.0%, and further to 10%, resulted in an increase of the reaction layer thickness compared with that when Si concentration was 0.8%. Meanwhile other compounds (Ti_9Al_{23}, $Ti_7Al_5Si_{12}$) formed on the Al/Ti interface. Ti_9Al_{23} also contained dissolved Si.

It is suggested that dissolved Si in Al_3Ti might strongly attract Ti atoms due to their high affinity, consequently Si in the Al_3Ti layer suppressed the growth of Al_3Ti.

It was also found that the Ti dissolution rate into molten Al is suppressed by Si addition in Al. The dissolution rate of Ti into pure molten Al was 14%-20% faster than that into molten Al-0.8Si. Takemoto and Okamoto [103] suggested that this can not be the dominant reason for the reduced Al_3Ti layer growth, as the growth rate difference is more than 10 times. It is also suggested that the saturated concentration of Ti in molten Al at the brazing temperature is almost not affected by the Si addition, though the saturated concentration of Ti could be a factor that affects the Al_3Ti growth.

Table 2.8 Effect of Si content on the reaction layer thickness of Ti/Ti joint brazed at 600 °C for 3 min [103].

Filler metal	Silicon content (wt %)	Intermetallic compound layer	
		Thickness (μm)	Type of compound
Pure Al	0.002	13.3	Al_3Ti
Al–0.1Si	0.14	3.7	Al_3Ti
Al–0.3Si	0.32	3.3	Al_3Ti
Al–0.8Si	0.84	2.6	Al_3Ti
Al–3Si	3.0	6.2	Ti_9Al_{23}, Al_3Ti, $Ti_7Al_5Si_{12}$
Al–10Si	10.1	7.6	Ti_9Al_{23}, $Ti_7Al_5Si_{12}$, Al_3Ti

Table 2.9 The enrichment of Si in the reaction layers formed using different Al-Si filler metals [103].

Filler metal	Composition (at %)			Measured type of intermetallic compound
	Si	Al	Ti	
Al–0.1Si	1.5	74.5	24	Al_3Ti (25 at % Ti)
Al–0.3Si	3	72	25	Al_3Ti (25 at % Ti)
Al–0.8Si	1	74.5	24.5	Al_3Ti (25 at % Ti)
Al–3Si	6.5	68.5	25	Al_3Ti (25 at % Ti)
Al–10Si	10	63	27	Ti_9Al_{23} (28 at % Ti)

It is found that when $Ti_7Al_5Si_{12}$ was the main reaction product on the Al-Ti interface, the joint strength is about 2 times higher than that when Al_3Ti was the main reaction product [103].

Takemoto and Okamoto [103] demonstrated that the reaction layer grows fastest when pure Al is used, adding any other alloying elements (including Ag, Si, Mg, Sn and Cu) into Al resulted in a decrease of growth rate.

2.7.5.2 In solid (Al) - solid (Ti) reaction system

Nahar and Devashrayee [152] also investigated the influence of Si on the growth of reaction layer between Al and Ti. It is found that the Al_3Ti layer growth rate was reduced by a factor of 3 for Al (2% Si)/Ti diffusion couple compared with Al/Ti diffusion couple in the temperature range of 400-500 °C. The activation energy for reaction layer growth was increased to 2.2 eV from 1.7 eV due to the addition of Si to aluminium base metal. It is suggested that Si minimized the Al/Ti interdiffusion and reaction.

Fuji et al. [23] investigated the friction welding of two different aluminium with different Si content (6×10^{-4} wt.% and 0.12 wt.% respectively) to the same titanium. The Al_3Ti intermetallic layer growth in the Al (6×10^{-4} wt.% Si)/Ti weld (HP joint) was much faster than than in the Al (0.12 wt.% Si)/Ti weld (CP joint). As shown in Figure 2.30 and Figure 2.56, more than 20 at.% Si was observed segregated on the interface between the Al_3Ti layer and Ti base metal in the CP joint but no Si segregation was detected in the HP joint, which contains much less Si in Al base metal. It is suggested that the Si segregation layer retarded the Al_3Ti layer growth by acting as a diffusion barrier for Al atoms and Ti atoms diffusion.

Besides in the CP joint, 5 at.% Si enrichment was detected in the Al_3Ti layer, which is much higher than that in the Al base metal (0.12 wt.% Si). No Si enrichment was detected in the Al_3Ti layer in the HP joint.

As a result of the much faster Al_3Ti layer growth in the HP joint, the tensile strength of HP joint decreased much more rapidly than CP joint, as the Al_3Ti layer was much thicker for a given heat treatment time.

2.7.6 Summary of the effects of alloying elements on Al/Ti reaction layer growth

The effects of various alloying elements and oxygen on the Al/Ti reaction layer growth reported in literature and the proposed mechanism for these effects are summarized in Table 2.10.

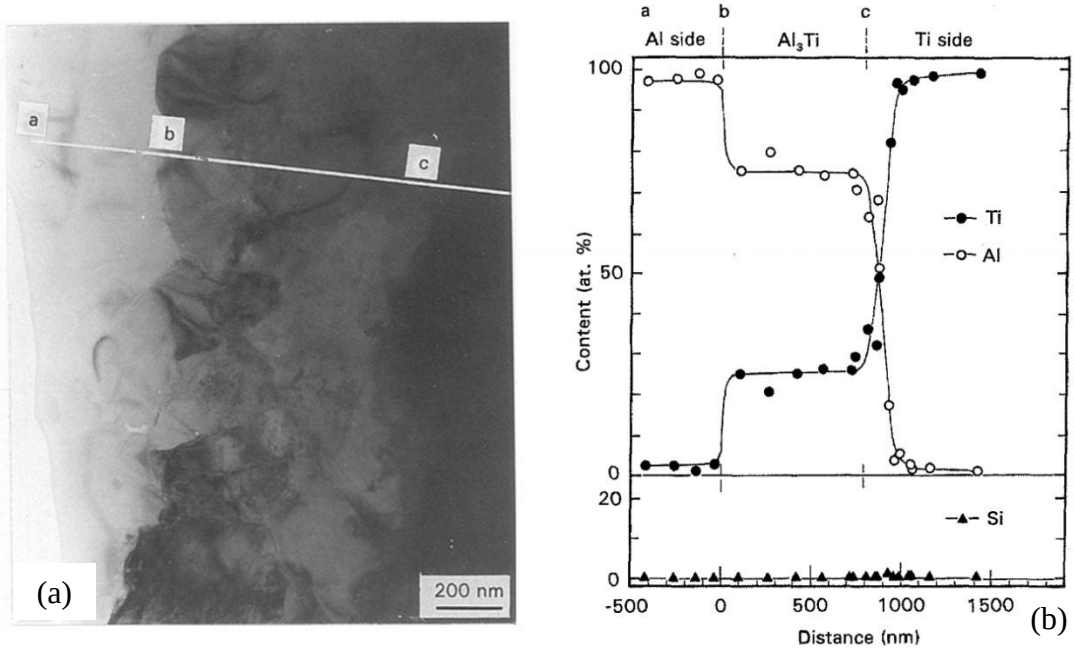

Figure 2.56 TEM bright field image of the (6×10^{-4} wt.% Si)/Ti weld interface (a), Al, Ti and Si concentration profile across the Al-Al3Ti-Ti interfaces (b) [23].

2.8 Summary and main focuses of the thesis

The big challenge of Al/Ti welding is the brittle Al_3Ti layer formation during the welding processes. Thus, one of the important tasks of this study is to address whether the low energy input welding process, USW, can control the reaction layer growth and the reasons for why the reaction layer growth is controlled or not. Also, the detailed Al/Ti interfacial structure is investigated carefully using TEM to understand the bonding nature between Al/Ti. This requires understanding how the layer forms and grows.

The gaps of knowledge:

1. The detailed Al/Ti USW weld interface structure is unknow; this is important for weld properties.

2. The behaviour of alloying elements and oxide film on the as-welded Al/Ti interface is unknow; this is also important for weld properties.

3. The quantitative grain size effect on Al_3Ti layer growth kinetics is unknow; this is important for understanding the Al_3Ti layer growth kinetics.

4. The segregation of Cu on Al_3Ti grain boundaries has not been observed; this is important for understanding the strong inhibition effect of Cu on Al_3Ti layer growth kinetics.

5. The combined effect of alloying elements from AA2139 alumimium on Al_3Ti layer growth kinetics is unknow.

6. The effect of V from Ti6Al4V on Al_3Ti layer growth kinetics is unknow.

Therefore, static annealing experiments are performed on different Al/Ti diffusion couples containing different alloying elements to understand the Al_3Ti layer growth kinetics and the influence of alloying elements such as Cu, V and Si.

High resolution TEM and SEM analysis are applied to carefully study the distribution of these alloying elements in the interface region, such as in grain boundaries, on the interfaces and in grain interior to understand how exactly these alloying element atoms affect the diffusion of dominant diffusion atoms.

The Al_3Ti grain size evolution during annealing and its effect on Al_3Ti layer growth kinetics are investigated as well, since grain boundary diffusion is an important part of the whole effective diffusion.

Table 2.10 Summary of the effects of alloying elements on Al/Ti reaction layer growth.

	Element	**Effect on reaction layer growth rate**	**Effect on activation energy (E_a) for diffusion (Change of E_a)**	**Proposed mechanism and comments**
In solid (Al) - solid (Ti) reaction	Cu	Slow down	1. From 1.8 to 2.4 eV [119]; 2. From 1.6 to 2.05 eV [147]; 3. From 1.68 to 2.17 eV [144].	1. Cu segregates to Al_3Ti grain boundary [119]; (no experimental evidence) 2. Formation of Al-Cu alloy on the Al-Ti interface impede the release of Al atoms; [119] (no experimental evidence) 3. The grain size of Al_3Ti was increased with the presence of Cu, leading to less grain boundary area [147]; 4. Cu-Ti strong inter attraction leading to difficult Ti atom jump [144].
	Si	Slow down	1. From 1.7 to 2.2 eV [152]	1. Si minimized the Al/Ti interdiffusion and reaction [152].
	O (in the surface)	Slow down	N/A	1. Acts as a diffusion barrier in the initial stage of diffusion [124]; 2. Slow growth was caused by the oxide layer on the surface of titanium (no experimental evidence) [81].
	O (in the matrix of Ti)	Slow down	1. From 2.46 to 2.73 eV. [117] 2. Decreases the pre-exponential factor but does not change the activation energy [79].	1. Due to that an Al-oxide layer formed on the reaction layer/Al interface, the Al_3Ti growth was retarded by the Al-oxide layer [117]; 2. With an increase of oxygen concentration in Al3Ti, Al atom transport through the intermetallic was decreased [79].
In liquid (Al) - solid (Ti) reaction	V	Slow down	N/A	Data only available in liquid-solid reaction [150].
	Si	Slow down	N/A	1. Si in Al_3Ti might strongly attract Ti atoms due to their high affinity, consequently Si in Al_3Ti layer suppressed the growth of Al_3Ti [103].

Chapter 3

Experimental methods

3. Experimental methods

To assess the suitability of HP-USW for joining aluminium to titanium, two types of aluminium alloys, AA6111 and AA2139, were selected and welded to the most commonly used titanium alloy Ti6Al4V. The peak load and the fracture energy of the welds were measured by lap shear test. The hardness profile of aluminium side across the weld was measured. The microstructure evolution of base metals caused by the thermal and mechanical process of ultrasonic welding was characterized by scanning electron microscope (SEM). The interfacial structure was analysed by both SEM and transmission electron microscope (TEM). The welding thermal cycle was measured by inserting a thermal couple to the weld centre. To understand the role of the parent materials' alloying elements on the microstructure and growth rate of the intermetallic reaction layer, AA2139/commercially pure (CP)-Ti couples, CP-Al/Ti6Al4V couples and CP-Al/CP-Ti couples were made using ultrasonic welding and then annealed in a furnace. The footprints of different welding tips with different geometry were analysed using high resolution laser scanning. All these methods are explained in this chapter.

3.1 Materials

The materials used in this work are aluminium alloy AA6111 (supplied in T4 temper), AA2139 (supplied in T8 temper), CP-Al, CP-Ti and titanium alloy Ti6Al4V. Background about these materials has been covered in the literature review section. Commercially pure aluminium is used in the present study as a reference to clarify the influence of alloying elements. Commercially pure titanium is used as a reference too. The nominal compositions of these five materials are given in Table 3.1. Coupons measuring 25×75×0.93 mm of 6111-T4 aluminum

alloy, 25×75×1 mm of AA2139-T8 aluminum alloy, 20×70×1 mm of CP-Al, 25×75×1mm Ti6Al4V titanium and 20×70×1 mm of CP-Ti sheets were used for the present study.

Table 3.1 Nominal compositions of materials used in this study in wt%.

	Composition (wt.%)													
	Al	Ti	Mg	Si	Cu	Fe	Mn	Ag	Li	V	C	N	O	H
AA6111	Bal.	-	0.75	0.85	0.70	0.25	0.30	-	-	-	-	-	-	-
AA2139	Bal.	-	0.45	0.03	4.8	0.05	0.3	0.3	0.008	-	-	-	-	-
CP-Al	99.99	-	-	-	-	-	-	-	-	-	-	-	-	-
CP-Ti	-	99.67	-	-	-	0.03	-	-	-	-	0.08	0.03	0.18	0.015
Ti6Al4V	6.15	Bal.	-	-	-	0.30	-	-	-	4.00	0.10	0.05	0.20	0.015

3.2 Ultrasonic spot welding

In this study, the welds were produced using a 2.5 kW Sonobond single-reed ultrasonic welding machine, which converts electrical energy into high frequency vibration. A schematic diagram of the ultrasonic spot welding process is shown in Figure 3.1. The high frequency vibration (20.5 kHz) is transmitted to the welding tip and the welding tip is in touch with the weldment on the upper side under a constant clamping pressure. The clamping pressure is supplied by the compression system, as shown in Figure 3.2. The pressure applied was kept constant at 0.55 MPa. The weldment on the lower side is put on a stationary anvil with a rough surface, as shown in Figure 3.3. The aluminium sheet is always put on the upper side, because titanium sheet is too hard, which could damage the welding tip. The welding tip is made from steel. Once the ultrasonic welder is turned on, high frequency friction occurs between the upper sheet and the lower sheet, which creates a solid-state weld. The welding time is the only variable parameter in this

study, which varies from 0 s to 4 s. The welding time is set through the control panel, as shown in Figure 3.4. Since the weld power is kept constant, the welding energy is simply proportional to the welding time and has a maximum of approximately 4 kJ in this study. The weldment sheet surfaces were ground using #300 grinding paper and cleaned with acetone prior to welding. A nickel and graphite based anti-seize compound (Never-Seez® Pure Nickel Special) was painted on the surface of the welding tip before welding to prevent weldments sticking on it. Never-Seez® Pure Nickel Special is a high temperature anti-seize and extreme pressure lubricant. It includes flake particles of pure nickel, graphite and other additives in a special grease carrier found to give optimum anti-seize performance.

The welding parameters used for producing the samples in Chapter 4:

Combinations: AA6111/Ti6Al4V, AA2139/Ti6Al4V; Welding time: 0 s to 4 s.

The welding parameters used for producing the samples in Chapter 5:

Combination: CP-Al/CP-Ti; Welding time: 1.2 s;

The samples were annealed at 500 – 630 °C after welding to study the IMC layer growth kinetics. (Details on annealing are described in Section 3.8.)

The welding parameters used for producing the samples in Chapter 6:

Combinations: AA2139/CP-Ti, CP-Al/Ti6Al4V;

Welding time: 2.4 s (AA2139/CP-Ti), 1.2 s (CP-Al/Ti6Al4V).

The samples were annealed at 500 – 630 °C after welding to study the IMC layer growth kinetics. (Details on annealing are described in Section 3.8.)

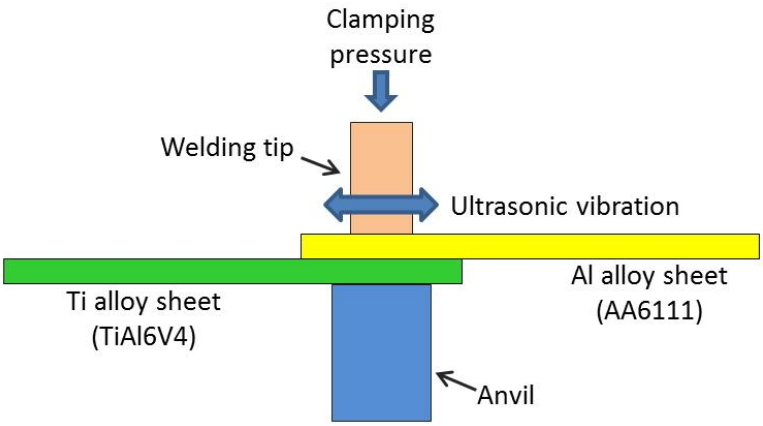

Figure 3.1 Schematic diagram of the ultrasonic spot welding process.

Figure 3.2 Compression system

Figure 3.3 The anvil

Figure 3.4 Control panel of the ultrasonic welder.

3.3 Welding tips

Two different welding tips were utilized in this study, as shown in Figure 3.5. To investigate the effect of welding tip geometry, the welding mechanical properties of two different welding tips with different geometry was compared. The round tip has a diameter of 10mm and the size of the rectangular one is 8×6 mm. The area of the round tip is around 1.6 times the area of the rectangular tip.

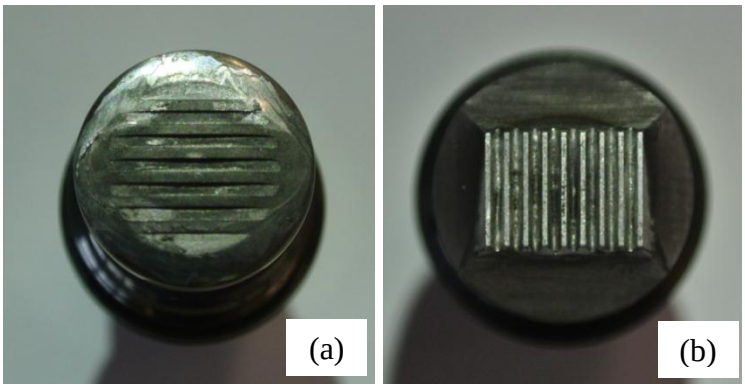

Figure 3.5 The round welding tip (a) and the rectangular welding tip (b).

3.4 Temperature measurement

To measure the thermal cycle during the welding process, 0.5 mm diameter k-type thermocouples were inserted into a groove between aluminium sheet and titanium sheet, as shown in Figure 3.6. The end of the thermocouple is located at the centre

of the clamped region, and is expected to correspond to the maximum temperature position. The thermocouple was connected to a computer and Labview 2014 software was used to collect temperature data (a temperature/time graph).

3.5 Sample preparation

3.5.1 General preparation

Samples for general microstructural investigations were cross-sectioned perpendicular to the welding direction using standard methods. Afterwards the samples were fixed in brass block by screws. Then samples are ground and polished using a Struers TegraPol-31 machine. Grinding was conducted using standard silicon carbide papers from P180 to P1200 with water as a coolant. Polishing was carried out using 6 μm, 3 μm and 1 μm diamond paste in sequence to get a mirror finish. Afterwards an active oxide polishing suspension (OPS) supplied by Struers Ltd. was used for high-quality final polishing, which takes around 10~20 min. Samples were washed by water after each grinding and polishing step to prevent leaving SiC or diamond particles on sample surfaces.

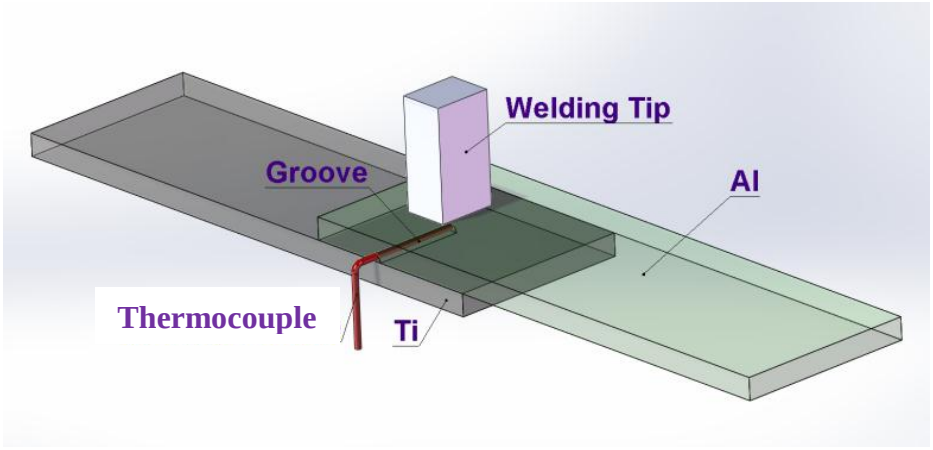

Figure 3.6 Schematic diagram showing the thermocouple positioning used for temperature measurement.

3.5.2 TEM sample preparation

Due to the huge hardness difference between Al, Ti and the Al-Ti intermetallic compound, and the brittleness of the Al-Ti compound, it is of great difficulty to prepare a TEM sample of Al-Ti interface or Al-IMC-Ti interface using traditional "manual thinning+ precision ion polishing" technique. Thanks to the development of Focused ion beam technology (FIB), commercial FIB systems are able to precisely extract a TEM sample from any site of interest on a sample by using a beam of focused ions.

Therefore, in the study thin foils for transmission electron microscopy (TEM) were prepared by FIB using a FEI QUANTA 3D FIB system (as shown in Figure 3.7) operating at 30 kV for rough cutting and milling, and both 5 kV and 2 kV for final cleaning. Figure 3.8 shows the position where the TEM sample was extracted from an as-welded AA6111-Ti6Al4V weld by the FIB technique.

Figure 3.7 The FIB system used for TEM sample preparation in this study.

3.5.3 EBSD sample preparation

The EBSD sample of annealed Al-Ti weld is also very difficult to prepare due to similar reasons for the difficulty in preparing TEM samples mentioned in the last

section. It is especially difficult to achieve a high quality surface for EBSD indexing on the Al-IMC interface and Ti-IMC interface region due to the large hardness difference. By using Gatan Precision Cross Section system (β version, Figure 3.9), this challenge is overcome. This system also uses a controlled ion beam to polished the surface prepared by the "general preparation" mentioned in section 3.5.1. The sample size used for Gatan Precision Cross Section system needs to be smaller than 8 mm (length) × 2 mm (thickness) × 5 mm (height) to fit it into the chamber of the machine. The following ion polishing parametres were used: Step 1: 5 kV, ~30 min; Step 2: 3 kV, ~15 min; Step 3: 1 kV ~60 min.

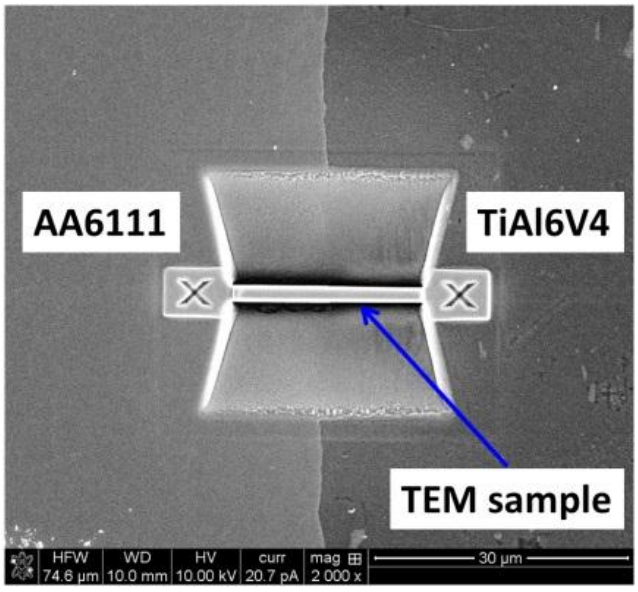

Figure 3.8 The location where the TEM sample was extracted (AA6111-Ti6Al4V weld, Welding time: 1.4 s, welding energy: 1967J).

3.6 Microscopy

3.6.1 SEM&EDS

In the present investigation, the microstructure of samples was observed using a Philips XL30 field emission scanning electron microscope (FE-SEM) or an FEI

Magellan field emission scanning electron microscope or an FEI Quanta 650 field emission scanning electron microscope equipped with energy-dispersive X-ray spectroscopy (EDS) detector.

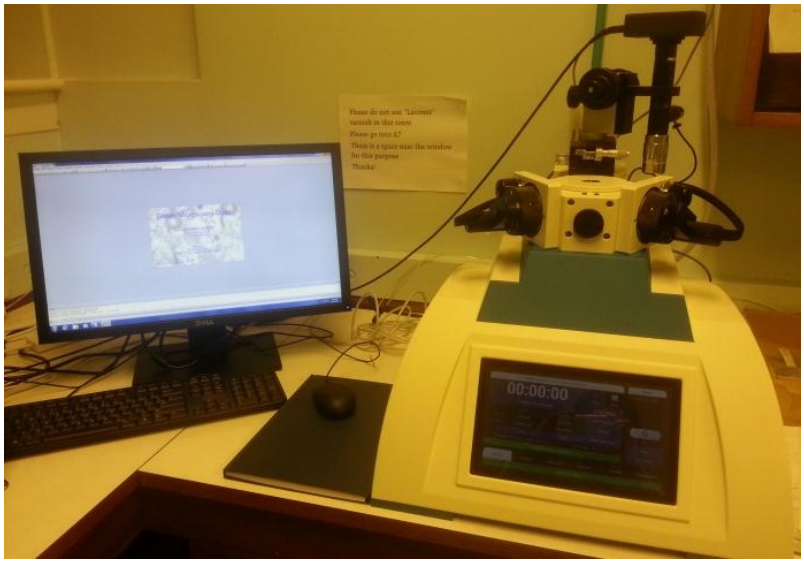

Figure 3.9 The Gatan Precision Cross Section system used for preparing high-quality EBSD sample.

SEM imaging mode used in this study:

In this study, back-scattered electron imaging (BSE) mode is the primary imaging mode used, as BSE mode can provide more chemical composition contrast and the present study focuses on dissimilar material's interfaces.

SEM accelerating voltage used in this study:

In theory, a higher accelerating voltage leads to a stronger signal and a lower signal to noise ratio in the final image. But a higher accelerating voltage is not good for resolution, due to the following reasons:

(1) The electron beam penetration is greater and the interaction volume is larger;

(2) Greater susceptibility to charging on the sample surface;

(3) Easier to damage specimen and over heat sample surface due to higher energy of the incident electron beam.

Thus, in this study, to capture the tiny features in the samples, relatively low accelerating voltages were used to get better resolution. The voltages used were usually equal to or below 10 kV. Usually, when using the more advanced SEMs (FEI Magellan SEM and FEI Quanta 650 SEM), which are more capable of working at low voltages, relative lower voltages, such as 8 kV and 5 kV were used.

Beam spot size used in this study:

An electron beam with smaller diameter is beneficial for a higher resolution. The spot size of the electron beam was set as small as possible to get high resolution images when examining small scale features. For the Philips XL30 microscope, a spot size of 3 was used. For FEI Magellan SEM and FEI Quanta 650 SEM, a spot size of 3.5 was used. It should be noted that that a spot size value in different SEMs corresponds to different actual beam diameters, i.e. the value of spot size in different SEMs cannot be compared directly.

SEM working distance (WD) used in this study:

The WD means the distance between the final condenser lens and the surface of specimen. WD can affect the spherical aberration of the electron imaging system and thus can influence the resolution of the aquired image [153]. When the WD is smaller, the influence of spherical aberration becomes less and therefore the resolution is improved [153]. Thus, in this study, the WD was set as small as possible when the purpose is to get high resolution images. The disadvantage of using small WD is that the focal depth is greatly reduced. WDs varying from 2 mm

to 10 mm were used depending on different purposes of imaging and the SEM machine used.

Energy-dispersive X-ray spectroscopy (EDS) is used for chemical composition analysis, which is used together with a SEM. Incident electrons interact with the atoms in the area of interest in a sample. A unique set of X-rays are then generated, because of unique atom structures of different elements, as shown in Figure 3.10.

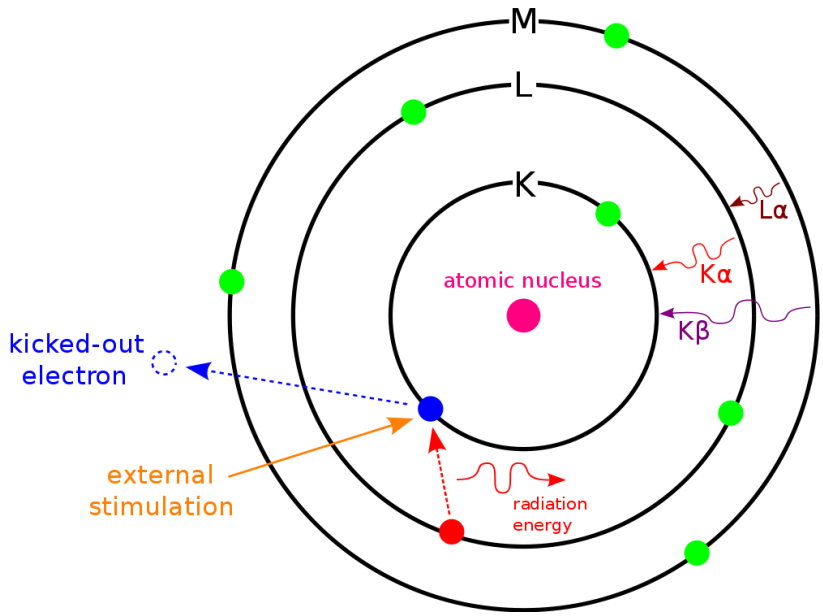

Figure 3.10 Interaction of an external stimulation and an atom [154].

The resolution of SEM-EDS is usually limited by the size of the interaction volume to about 2~5 μm, as shown in Figure 3.11.

3.6.2 Electron backscatter diffraction (EBSD)

In EBSD analysis, an electron beam interacts with a tilted crystalline sample (usually 70^{o}) and the diffracted electrons hit a screen, on which a pattern is formed, as shown in Figure 3.12. This pattern precisely reflects characteristic of the crystal structure and orientation of the electron beam-sample interaction region. It can be applied for many purposes, such as texture analysis, crystal orientation, grain size,

misorientation, grain boundary characterisation, phase identification, phase distribution and so on [155].

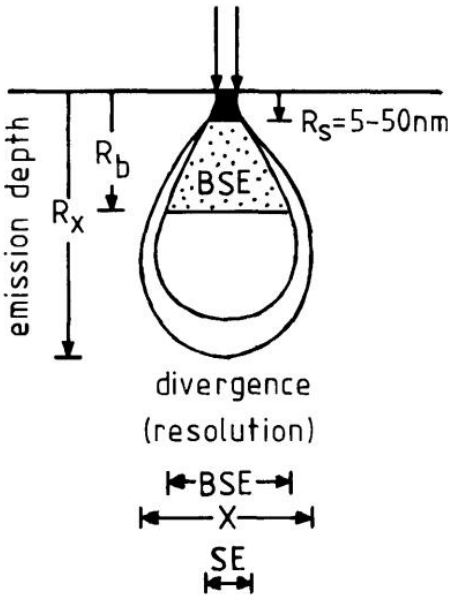

Figure 3.11 The resolution of EDS limited by the size of the interaction volume, X denotes the spatial resolutions for X-ray emission signal. [156]

In this study, an FEI Magellan field emission scanning electron microscope or an FEI Quanta 650 field emission scanning electron microscope integrated with an HKL electron backscatter diffraction (EBSD) system was used.

When performing EBSD analysis, the sample was tilted 70 degree relative to the horizontal plane, an accelerating voltage of 20 kV was used usually, as a high accelerating voltage can enhance electron backscatter diffraction pattern. AZtecHKL EBSD software was used for collecting the raw data. HKL Channel 5 software was used for EBSD data post-processing.

3.6.3 TEM

In this study, a Philips CM200 transmission electron microscope (TEM) operating at 200 kV or an FEI Tecnai F30 operating at 300 kV or an FEI Tecnai F20

operating at 200 kV or an FEI Titan G2 80-200 scanning transmission electron microscope (S/TEM) with ChemiSTEM™ technology was applied to identify phases, measure the distribution of alloying elements and capture images around the interface of titanium and aluminium.

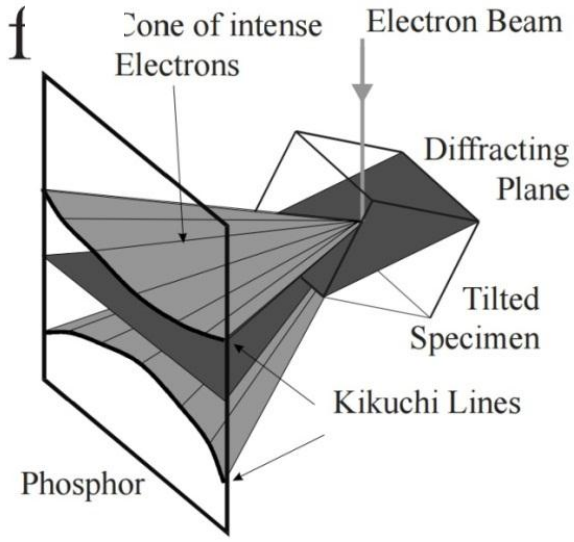

Figure 3.12 Schematic diagram showing how EBSD works [157].

Imaging modes used:

(1) Bright field mode:

Bright field mode is the most basic operational mode of TEM. In this mode, an aperture is put in the back focal plane of the objective lens of a transmission electron microscope as a result only the direct electron beam can pass [158], as illustrated in Figure 3.13. In this situation, the image contrast is from the different weakening level of the direct beam at different sites of the specimen during its interaction with the specimen [158]. Thus, the image formation in this mode is due to mass-thickness and diffraction contrast. For example, thick regions, regions containing heavy element atoms and regions with crystal structures that increase electron scatter show dark contrast.

(2) STEM:

A scanning transmission electron microscope (STEM) is distinguished from traditional TEMs by focusing the electron beam into a very small spot which is scanned over the TEM sample in a raster [159].

With STEM, an intensely-focused electron beam is raster-scanned across the thin TEM sample, and various types of scattering information can be aquired as a function of position.

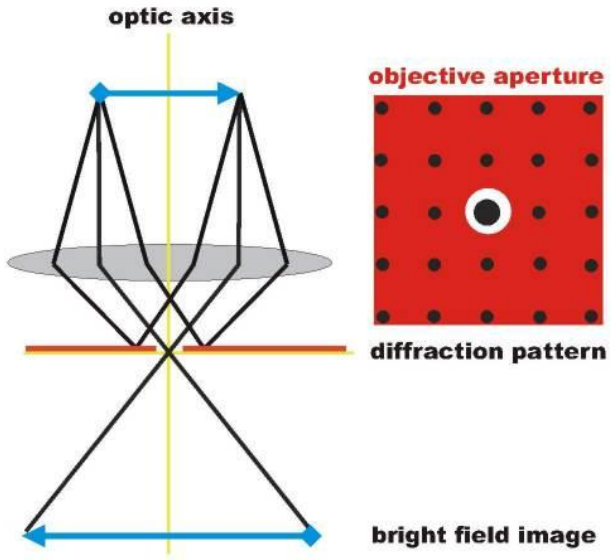

Figure 3.13 The bright field (BF) imaging mode [160].

STEM-HAADF: By using a high-angle annular dark field detector (HAADF) detector (Figure 3.14), the high-scattering-angle transmitted electrons are collected to generate high-resolution atomic number (Z) contrast images [161].

The high-angle annular dark field detector has a disk shape with a hole in its centre. The hole size and disk diameter is large. Thus, it can detect electrons that are scattered to high angles and almost only incoherent Rutherford-scattered electrons contribute to the image [158].

By collecting only Rutherford-scattered electrons, the image produced by the HAADF detector has an intensity (ideally):

$$I \propto t \cdot Z^2$$

Where, t is sample thickness, Z is atomic number.

Thereby, an atomic number (Z-) contrast image is acquired.

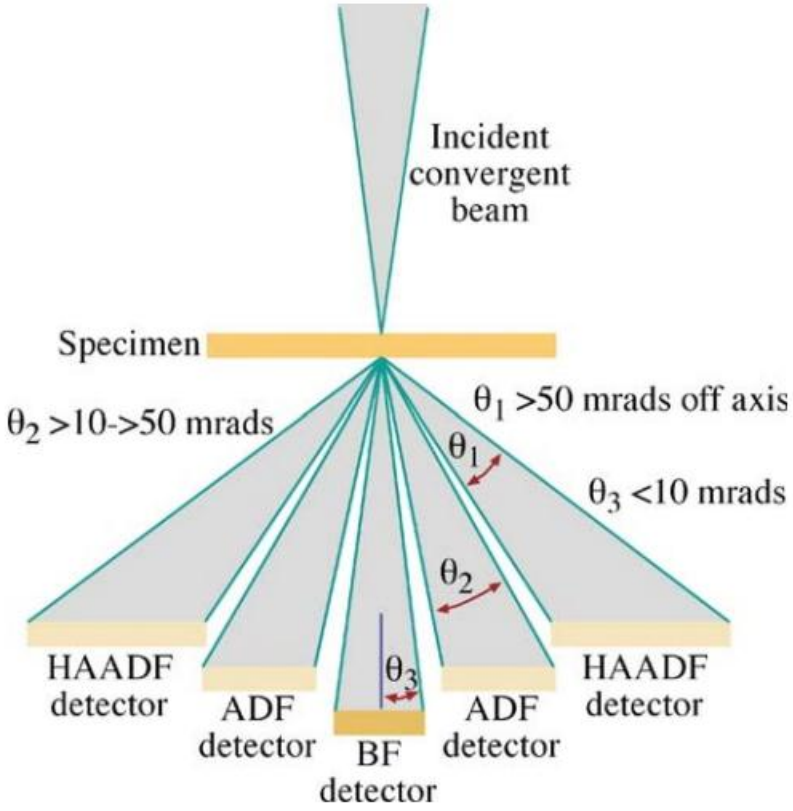

Figure 3.14 Position of HAADF detector in TEM [158].

STEM-EDS: By using an energy-dispersive X-ray spectroscopy (EDS) detector, the X-rays generated by the interaction between electron beam and the TEM sample are collected and used to produce high-spatial-resolution compositional maps. The spatial resolution of EDS analysis in STEM is much higher than that in SEM due to the interaction volume being much smaller in the TEM [162].

It is worth noting that the FEI Titan S/TEM used in this study is equipped with a high sensitivity Super-X EDX (EDS) detector system (ChemiSTEM™ technology, Figure 3.15). It has four windowless silicon drift detectors (SDD) integrated deeply into the objective lens. The windowless EDS detector design considerably enhances the detection of the characteristic X-rays of light elements, such as oxygen. For example, the ChemiSTEM™ technology even can realize atomic oxygen mapping in a Sr and Ti oxide crystal [163].

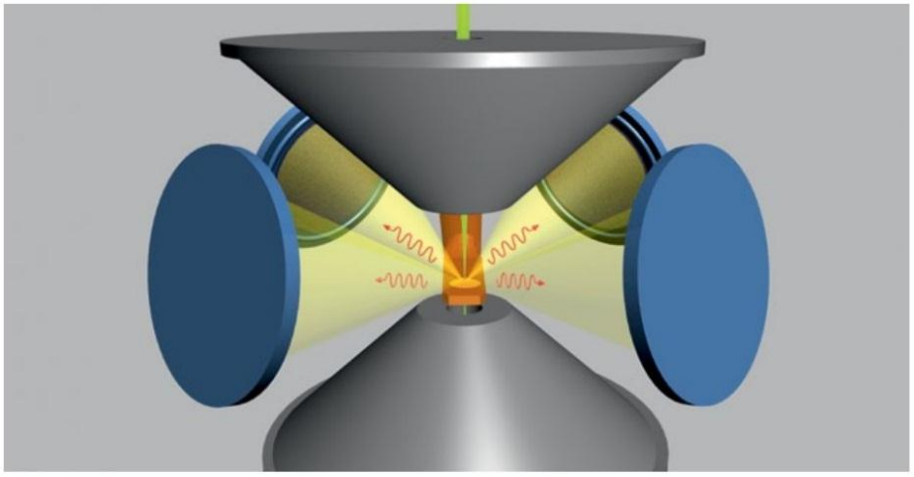

Figure 3.15 A schematic diagram of the high sensitivity Super-X EDX (EDS) detector system in Titan S/TEM, with 4 windowless silicon drift detectors [163].

In this study, STEM-HAADF and STEM-EDS are frequently used together to measure the alloying elements distribution in various Al/Ti joints. Aztec software (The Ultimate EDS System for Transmission Electron Microscopes TEM by Oxford Instruments) and Bruker Esprit 1.9 software were used to collect and process STEM-EDS data.

STEM-EDS in FEI Tecnai F30 TEM:

The FEI Tecnai F30 TEM is equipped with an X-Max^{N} 80 T EDS detector, an 80

mm^2 Silicon Drift Detector (SDD) with a polymer window produced by Oxford Instruments, which allows the pass-through of low energy X-rays, i.e. it is capable of detecting low energy characteristic X-rays of light elements, such as Oxygen.

The TEM sample was tilted to 20° prior to performing STEM-EDS analysis. The tilt of sample is beneficial for collecting a higher intensity X-rays of light elements X-rays signal. Ensuring sufficient signal was detected, the electron beam size was set as small as possible to achieve high spatial resolution, the beam spot size usually used is from 7 to 9 (the greater the number, the smaller the beam).

STEM-EDS in FEI Titan G2 80-200:

The parameters used for STEM-EDS in the FEI Titan G2 80-200 were: Beam current: 1.5 nA; Camera length: 135 mm; Electron beam convergence angle: 21 mrad; EDS dwell time: 50 ms. Different from the Tecnai F30 TEM, the TEM sample does not need to be tilted in the ChemiSTEM Titan, because there are four X-ray detectors distributed in four directions as shown in Figure 3.15.

Selected Area Diffraction (SAD):

SAD was used in this study to identify phases in various Al/Ti joints. Interesting regions were selected and tilted to an angle which can produce symmetrical electron diffraction patterns. The SAD patterns were recorded using DigitalMicrograph software. After capturing the patterns, the distances between the central spot and other spots (R_1, R_2 and R_3, Figure 3.16, each spot corresponds to a crystal plane) and the angles between R_1, R_2 and R_3 were measured. Then, the corresponding interplanar spacings and the angles between different crystal planes were calculated. By comparing these experimentally measured and calculated

spacings and angles with the standard crystallographic parametres, the phases can be identified.

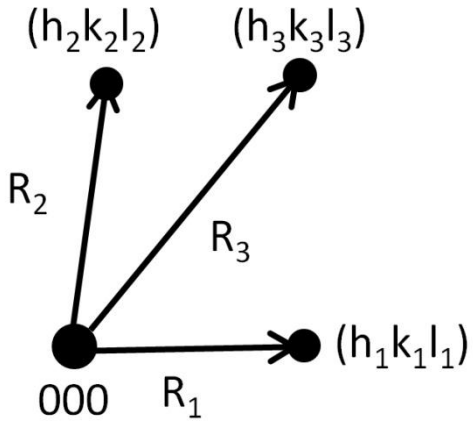

Figure 3.16 An schematic diagram of indexing selected area diffraction patterns.

3.7 Mechanical testing

3.7.1 Lap shear tensile test

Lap shear tensile tests were conducted to measure the peak load and the fracture energy of welds. Testing was carried out on the Instron 5569 system using a 10 kN load cell. The loading velocity in this study was 1 mm/min and the data was collected at 50 Hz. The configuration of the lap shear tensile test coupon is shown in Figure 3.17. Two spacers with the same thickness as the base metal sheets were used when gripping the lap joint to ensure the load was applied in the same plane as the centre line of the joint. The displacement of the grips and the load applied at each moment was recorded using Bluehill®2 Software. Then a displacement (elongation)/load graph was created. From this graph, the peak load and fracture energy for each sample can be determined. The fracture energy was calculated by the area under the displacement (elongation)/load curve.

3.7.2 Microhardness test

Microhardness values provide information about the microstructural state in the samples. To investigate the effect of the welding process on the microstructure evolution, hardness measurements were performed on metallographically polished surfaces across the welds at a depth of 0.5 mm below the top aluminum sheet surface using a Vickers microhardness testing machine with a load of 500 g.

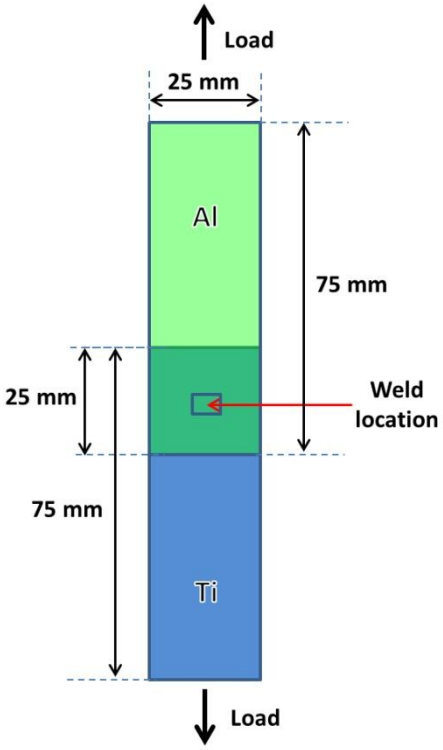

Figure 3.17 Schematic diagram of lap shear tensile test coupon configuration.

A schematic diagram of Vickers hardness test is shown in Figure 3.18. The two diagonal dimensions of the indentation are measured, d1 and d2. Then the Vickers Hardness is calculated by the following equation.

$$HV = \frac{F}{A} \approx \frac{1.8544F}{d^2}$$

where F is the load applied (in kgf) and d is average of d_1 and d_2 in millimeters.

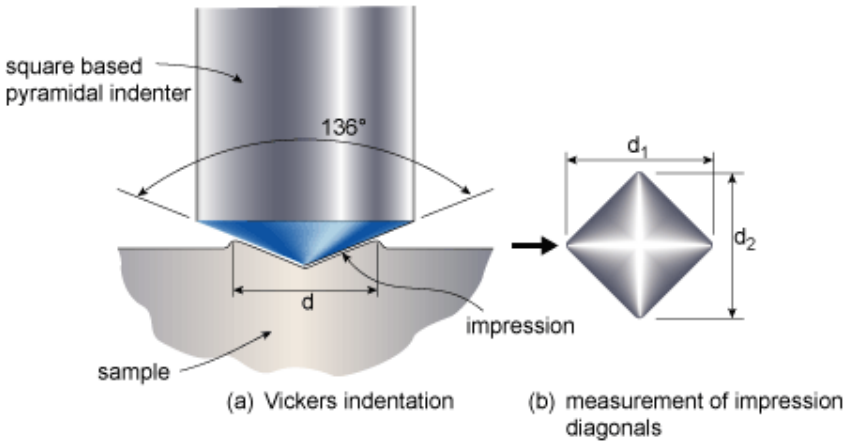

Figure 3.18 Schematic diagram of Vickers hardness test [164].

3.8 Heat treatment

To understand the growth kinetics of the IMC layer, heat treatments at different temperature and different holding time period was carried out. Temperature varies from 500 ℃ to 630 ℃, and heat treatment holding time period varies from 5 h to 480 h. Annealing was performed in a furnace produced by Carbolite equipped with a type 3216 controller and a heavy duty convection fan for good uniformity, as shown in Figure 3.18. After annealing, the samples were cooled in air. Welds used for heat treatments were produced using a welding time (welding energy) just enough to join the Al and Ti sheets with no visible reaction layer on the Al/Ti interface. The couples used for heat treatments includes: CP-Al/CP-Ti, CP-Al/Ti6Al4V, AA2139/CP-Ti.

After heat treatments, the IMC growth rate and IMC microstructure features were compared between CP-Al/CP-Ti and CP-Al/Ti6Al4V (to study the role of alloying elements from Ti6Al4V) and between CP-Al/CP-Ti and AA2139/CP-Ti (to study the role of alloying elements from AA2139).

Figure 3.19 The furnace used for heat treatment.

3.9 Surface Profiling

Welds produced by different welding times and different welding tips have different indent depth and indent area, which affects the weld mechanical properties. It is useful to precisely measure the weld surface profile to understand how it affects the weld properties. Also, an accurate weld profile is useful for finite element modeling of the weld properties. A 3D NanoFoucus µscan SC200 profilometer based on laser scanning was applied to measure the weld geometry precisely in this study, as shown in Figure 3.19. This profilometer and its accompanying software comprise a non-contact autofocus-laser measurement system for measuring fine surface structures, which has a depth resolution of 0.5 µm. µsurf version 6.1 was the accompanying software used to collect and analyse the raw data. A 3D surface profile can be reconstructed from the raw data using this software. The parameters used in this study are: (1) Laser beam movement step size (i.e. horizontal direction resolution): 5 µm; (2) Measurement speed: 10 mm/s; (3) Laser sensor scan frequency: 10 kHz. (4) Wave length of the laser: 780 nm. Weld samples were horizontally put on the flat work table with the surface of weld zone facing the laser sensor prior to do the scanning.

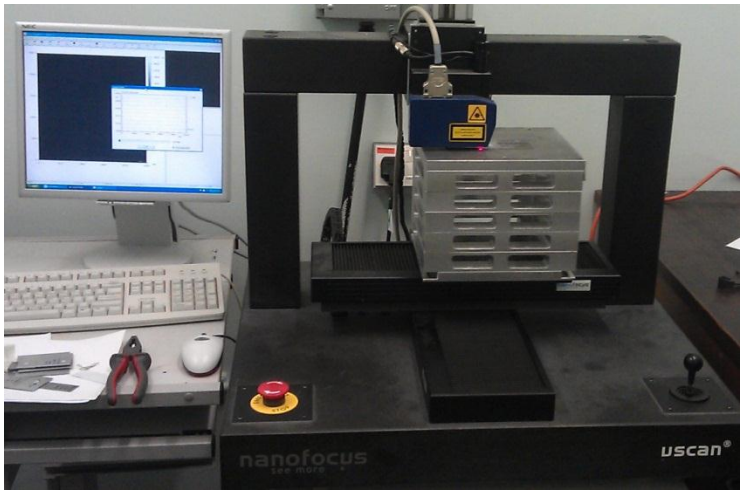

Figure 3.20 The 3D NanoFoucus μscan SC200 profilometer.

Chapter 4

Microstructural characterization and mechanical properties of HP-USWed AA6111-Ti6Al4V and AA2139-Ti6Al4V dissimilar joints

4. Microstructural characterization and mechanical properties of HP-USWed AA6111-Ti6Al4V and AA2139-Ti6Al4V dissimilar joints

In this chapter, the commonly used titanium alloy Ti6Al4V was firstly joined to AA6111, an age hardenable aluminum-magnesium-silicon-copper alloy developed primarily for automotive applications, with the purpose of assessing the suitability of HP-USW for joining this combination of materials. After this, Ti6Al4V was joined to AA2139, an aerospace aluminium alloy with much higher strength than AA6111. The effect of welding time, which is the only variable parameter in this study, on the weld peak load and fracture energy was studied. The weld interface structure was investigated using SEM and TEM, to check if there is brittle intermetallic compound formed on the interface. Because the mechanical properties of welded aluminium alloy changes significantly with aging time, the influence of post-weld natural ageing (of the aluminum alloy) on the joint performance is also examined. The welding mechanical properties of two different welding tips with different geometry were compared.

4.1 USW of AA6111 to Ti6Al4V

4.1.1 Joint appearance

Figure 4.1 (a) shows the appearance of a typical Al-Ti (AA6111-Ti6Al4V) dissimilar weld (welding time 0.6 s, welding energy 956J) produced by USW. The macrostructure of cross-section of a USW joint is shown in Figure 4.1 (b). It can be seen that AA6111 aluminum alloy sheet was severely deformed by the welding tip and there was almost no macro deformation on the titanium side.

Figure 4.2 shows surface appearances of AA6111/Ti6Al4V joints for various welding times. It can be seen that the indent depth increases with increasing welding time.

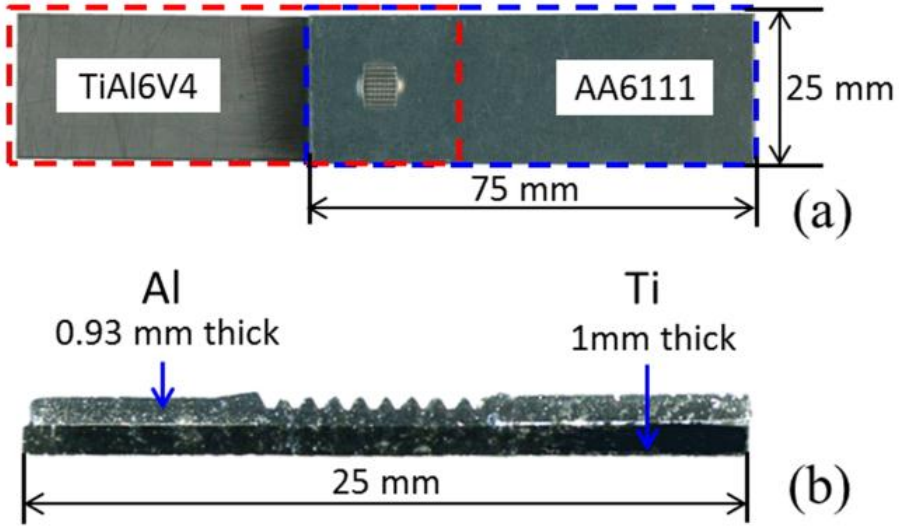

Figure 4.1 (a) Weld appearance of a typical rectangular-tip weld, welding time 0.6 s, welding energy 956J, (b) Macrostructure of cross-section of a typical rectangular-tip weld, welding time 1.2 s, welding energy 1735J.

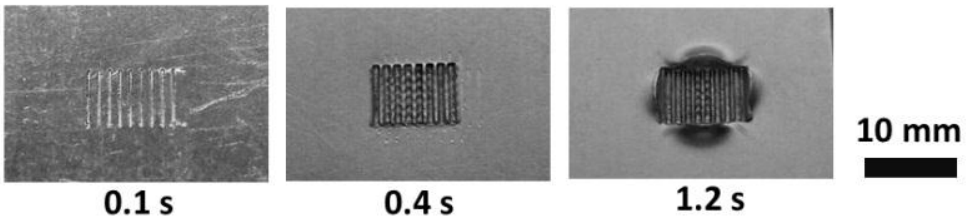

Figure 4.2 Influence of welding time on indent geometry and depth, sample photos (aluminum side).

4.1.2 Weld microstructure

Figure 4.3 (a) and (b) show a typical AA6111-Ti6Al4V weld microstructure (cross section), for a 1.4 s welding time and 1967 J welding energy. No IMC layer was visible in these AA6111/Ti6Al4V weld backscattered electron images even at high magnifications, which is encouraging since the formation of a brittle IMC layer is typically associated with poor mechanical properties.

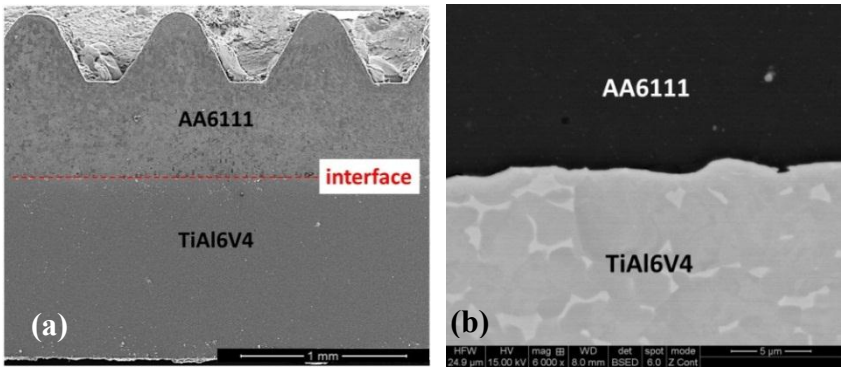

Figure 4.3 SEM images of typical AA6111-Ti6Al4V ultrasonic spot weld interface, (Welding time: 1.4 s, welding energy: 1967 J), (a) low magnification image, (b) high magnification BSE image.

To study the weld interface at higher resolution, TEM was used. A series of bright field images of the same interface region were taken at increasing tilt angle to examine the Al-Ti interface carefully, with examples of these images showed in Figure 4.4. Even using the higher resolution of the TEM, no IMC layer was detected, suggesting if any layer is present it must be extremely (<1 nm) thin. To support the lack of observation of an IMC layer at the interface, selected area diffraction patterns were taken. These diffraction patterns revealed only spots associated with the parent materials, but not with the crystal structure of the expected Al_3Ti IMC phase. Moreover, with the purpose of attempting to reveal how the lattice of Al and Ti was connected, the Al/Ti interface was examined in more detail and a high resolution (HR) STEM-HAADF image was acquired on the interface region, as shown in Figure 4.5. The Al lattice image was acquired near the interface (Figure 4.5), however due to the much higher atomic number of Ti (Ti: 22; Al: 13) and the larger foil thickness on the Ti side, Ti base metal cannot be imaged clearly. Although unusual, similar "clean" (no-reaction-layer) interface structures have been previously observed for other material combinations joined by ultrasonic welding and other techniques; for example, in the metal-metal case [66], metal-

ceramic case [165], and metal-glass combination [166]. These no-reaction-layer interfaces are typically associated with a very low welding energy, a very high energy barrier for nucleating the IMC or a case where the two materials being joined have complete solid solubility.

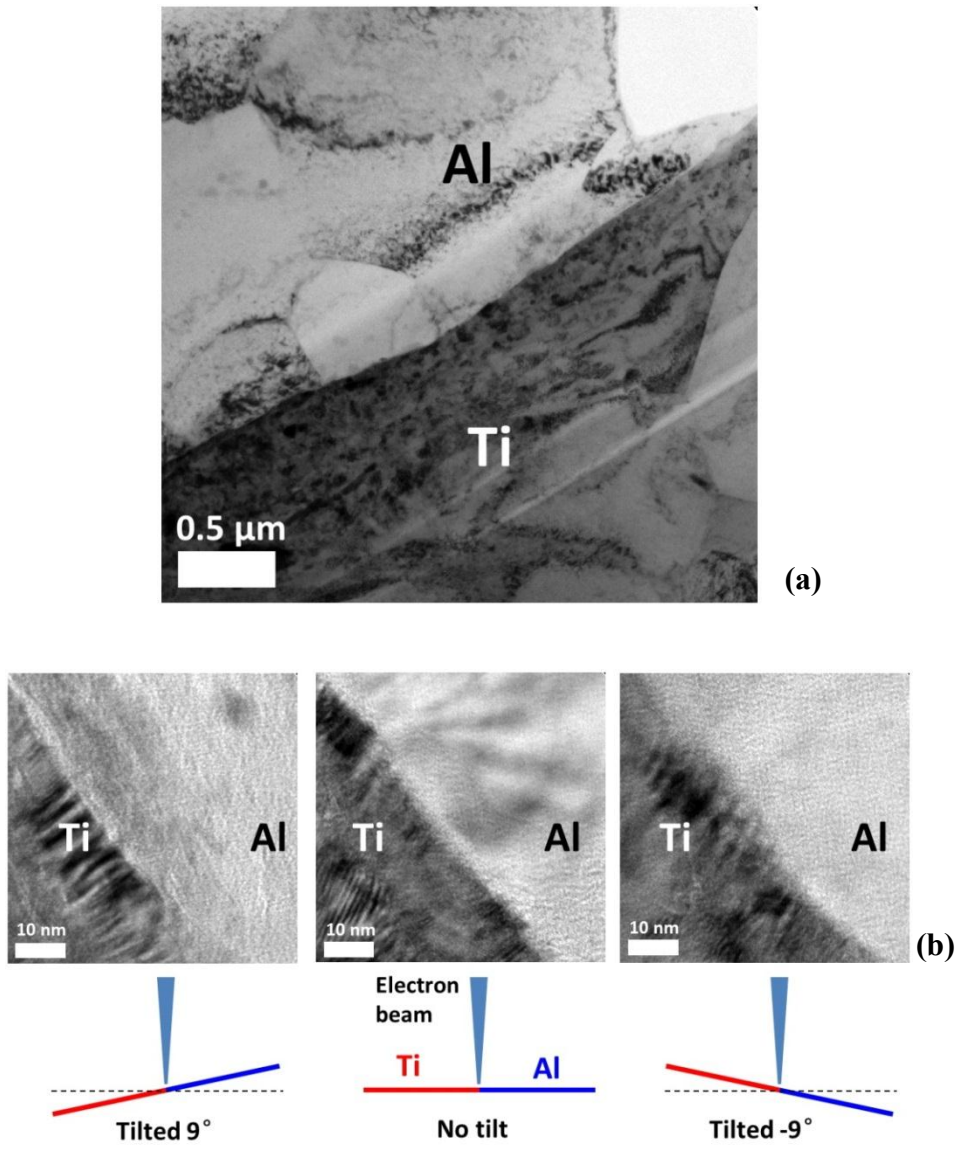

Figure 4.4 TEM bright field images of a naturally aged Al-Ti USW weld interface, (a) A low magnification image showing a large region of the interface, (b) High magnification images acquired at different tilt angles, (Welding time: 1.4 s, welding energy: 1967J).

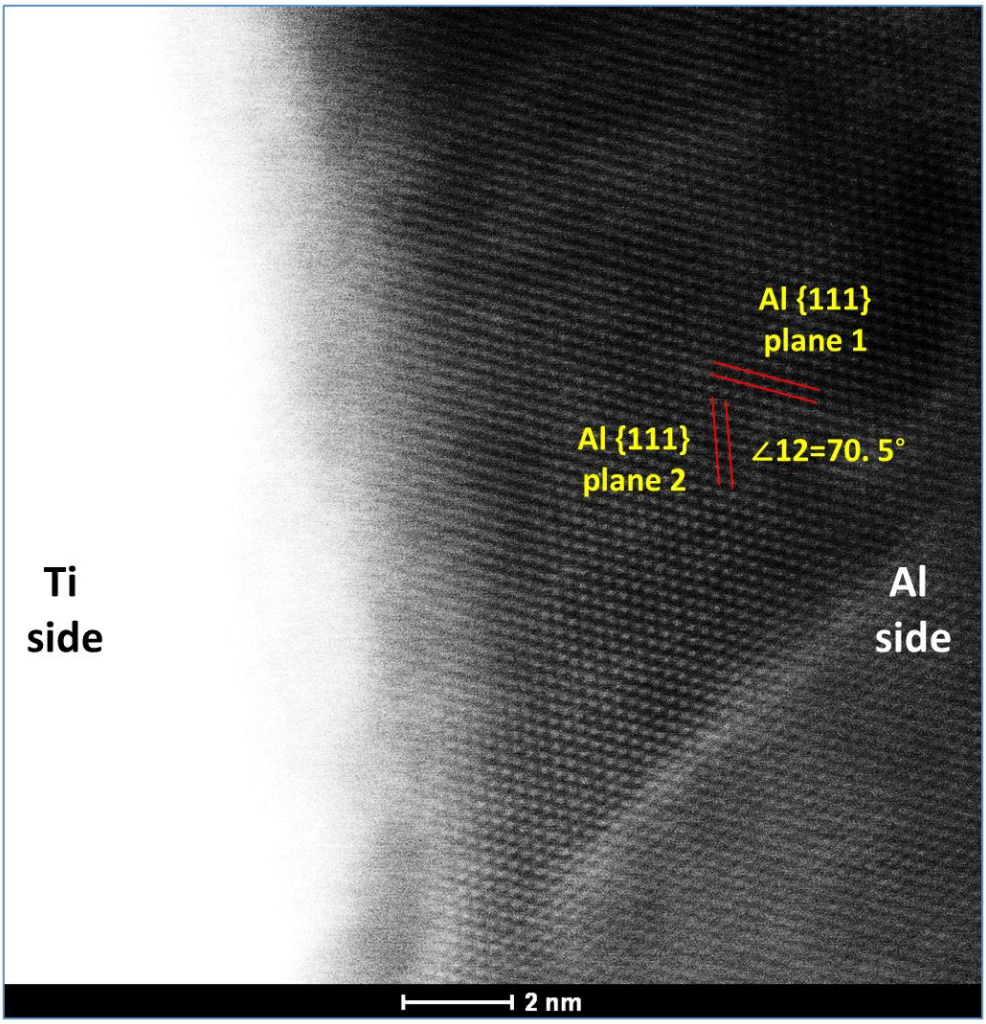

Figure 4.5 High resolution (HR) STEM-HAADF image of the AA6111/Ti6Al4V interface.

Figure 4.6 shows the microstructure of AA6111 near the weld interface and the microstructure of unwelded AA6111 base metal in the near surface region at the same magnification. It can be seen that the Al grains near the weld interface have been markedly refined by the ultrasonic spot welding process, which has also been found in research on Al-Al USW and Al-Fe USW by Bakavos et al and Prangnell et al [29, 167].

Figure 4.7 shows the microstructure of Ti6Al4V near the weld interface and the microstructure of unwelded Ti6Al4V base metal in the near-surface region at the same magnification. It can be seen that there is no apparent difference between

them. This suggests that little deformation occurred on the titanium side near the weld interface, which might be expected due to the much higher strength of titanium at the peak temperature reached during welding (approximately 520 ^{o}C, as discussed in detail later). At this temperature, the estimated yield strength of the titanium alloy is over 2.5 times that of the aluminum alloy. A similar phenomenon was also reported in an Al-Fe USW research for the same reason by Prangnell et al. [29].

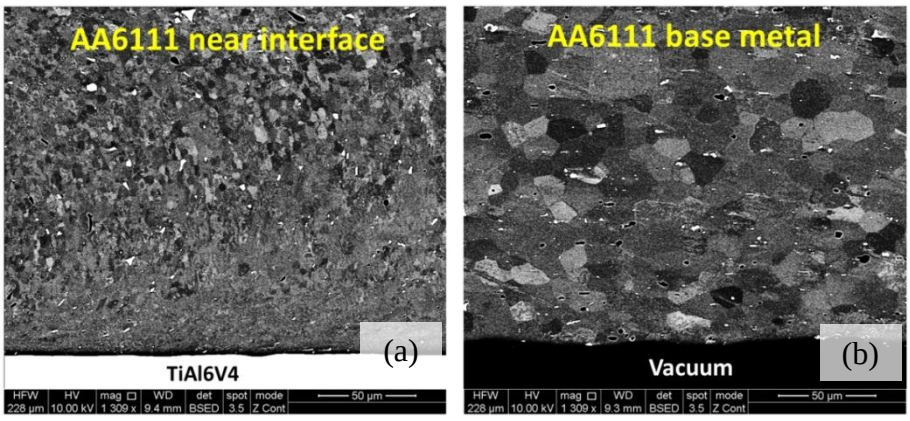

Figure 4.6 Comparison of microstructure between aluminum alloy AA6111 near the weld interface (a, welding time 1.4 s) and AA6111 base metal near surface region (b, not welded).

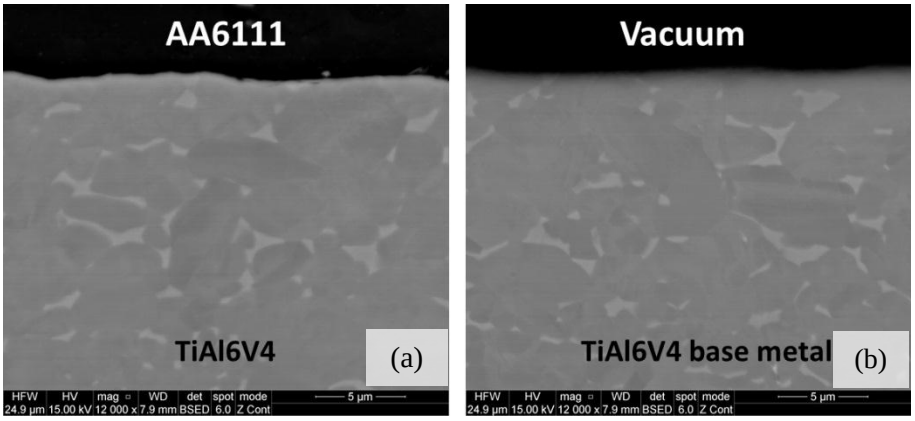

Figure 4.7 Comparison of microstructure between Ti6Al4V near the weld interface (a, welding time 1.4s) and not-welded Ti6Al4V base metal near surface region (b, not welded).

4.1.4 Mechanical properties

4.1.4.1 Fracture modes

Figure 4.8 shows examples of the 2 different fracture modes observed in the ultrasonic spot welds produced in the present investigation. They are respectively the 'interfacial failure' mode and the 'pull-out' mode. For the 'interfacial failure' mode, fracture occurred across the interface, and no aluminum remained stuck on the titanium sheet after testing. For the 'pull-out' mode, the weld nugget stuck on the titanium sheet and fracture path went along the edges of weld nugget through the aluminum alloy sheet.

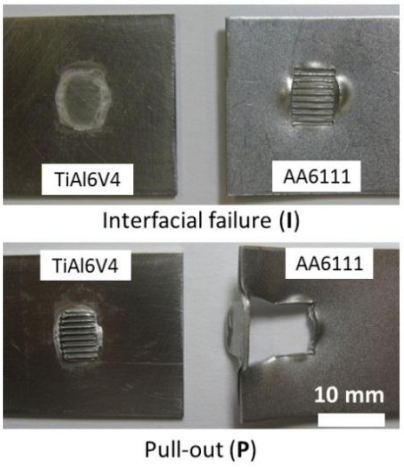

Figure 4.8 Fracture modes of AA6111/Ti6Al4V welds, the 'interfacial failure' mode (I) and the 'pull-out' mode (P).

4.1.4.2 Effect of welding time

In this study, the only variable welding parameter is the welding time. Since the weld power remained fixed, an increase in weld time also corresponds to an increase in total energy input into the weld.

As shown in Figure 4.9, in as-welded AA6111/Ti6Al4V joints, which are lap shear tested immediately after welding, the peak load increased with an increase of

welding time from 0 s to 0.8 s. For times longer than this, peak load plateaus, with an upper limit around 3.1 kN. This peak load is higher than that of optimized Al-Mg USW welds (~2.0 kN) and Al-Fe USW welds (~2.8 kN) of similar dimensions and is close to that of similar Al-Al USW welds (~3.5 kN) reported by Panteli et al, Bakavos et al and Prangnell et al. respectively [29, 30, 167]. The transition in fracture mode from "interfacial failure" to "pull-out" mode occurred when the welding time reached 0.8 s. Hence the plateau in weld strength coincides with the welding conditions that lead to nugget pull-out. For welding times below 0.6 s, the aluminum sheet and the titanium sheet cannot be successfully welded together. Sufficient welding time is necessary to break the surface oxides to allow metallurgical bonding to take place and also to allow some diffusion across the weld interface to form a bond. For welding times below 0.6 s there is insufficient time for either or both of these processes. An increase of welding time (welding energy) is accompanied by an increase of interfacial strength and the softening of aluminum sheet by the welding heat, as a result, in the as-welded condition, with an increase of welding time (welding energy) the fracture mode transferred from interfacial failure to nugget pull-out, with failure occurring in the softened aluminum. Typical displacement-load curves of an "interfacial failure" weld (produced by a short welding time of 0.6 s) and a "pull-out" failure weld (produced by a longer welding time of 0.8 s) are shown in Figure 4.10. The fracture energy of weld was calculated from the area below the displacement-load curve. As expected, failure by nugget pull-out is associated with a much higher fracture energy than interfacial failure.

As shown in Figure 4.11, the maximum fracture energy recorded for the Al-Ti combination was around 7.5 kN·mm, which is much higher than that previously

obtained for Al-Mg USW joints (~1.2 kN mm) [30] and Al-Fe USW joints (~3.8 kN) and is comparable to that of Al-Al USW welds (~7.8 kN mm) [29, 167]. The reduction in fracture energy for weld times greater than 1.2 s is associated with a decrease in the thickness of the aluminium sheet due to the welding tool sinking into the softened aluminium sheet during welding and causing excessive thinning of the aluminium sheet, thereby reducing the cross sectional area of the aluminium able to support the applied load.

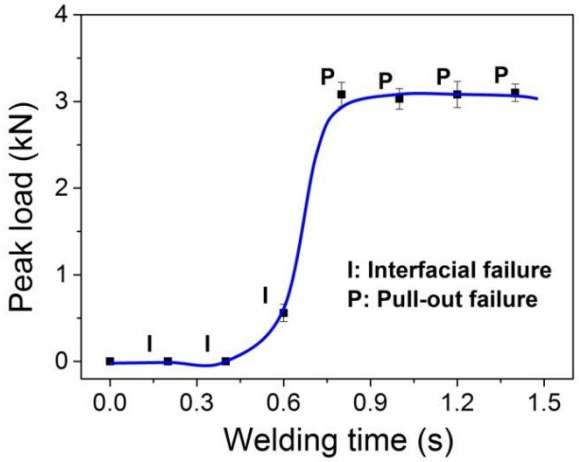

Figure 4.9 Effect of welding time on the peak load of as-welded AA6111/Ti6Al4V USW welds.

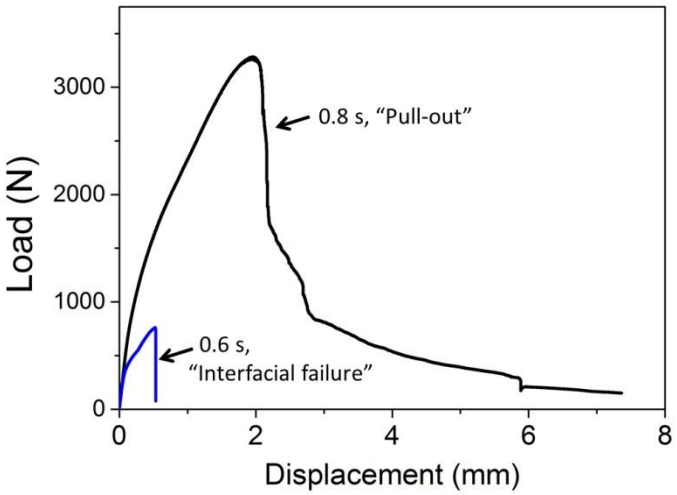

Figure 4.10 The lap shear test load–displacement curves recorded for a "pull-out" failure weld (welding time, 0.8 s) and an 'interfacial failure' weld (welding time, 0.6 s), both are lap shear tested immediately after welding.

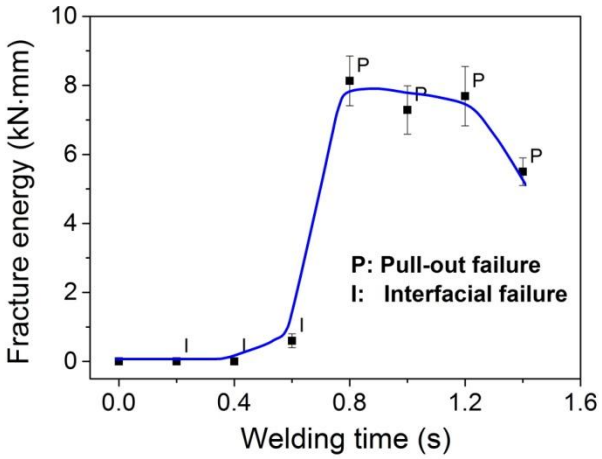

Figure 4.11 Effect of welding time on fracture energy of rectangular-tip welds AA6111/Ti6Al4V (as-welded).

4.1.4.3 Effect of natural aging

Figure 4.12 shows the hardness profile measured in the AA6111 aluminum alloy across the weld parallel to the welding direction within both 30 minutes of welding and after 4 days natural ageing. It can be seen that natural ageing has led to a significant (approximately 30%) increase in the hardness of the aluminum alloy in the weld zone. Indeed, the maximum hardness in the weld zone after natural ageing exceeds the hardness in the original T4 temper which is ~80 HV. Furthermore, the hardness minima that are observed in the heat affected zone of the aluminum alloy after welding (on either side of the footprint created by the welding tip) are eliminated by natural ageing. This hardness recovery is due to natural ageing as a result of the alloying elements taken into solution as precipitates are partially dissolved during the welding process. It is commonly seen in the post-weld hardness profiles of age hardenable aluminium alloys and is well explained elsewhere [168]. Lap shear strength testing of joints immediately after welding leads to failure of the aluminum alloy by ductile fracture that initiates in these softened regions. However, as shown in Figure 4.12, once the strength of the

aluminum alloy has recovered by natural ageing, failure transfers to the weld interface, leading to lower fracture energy (Figure 4.13). The transfer of fracture mode occurs because the increase in strength of the aluminum due to natural ageing enables a greater stress to be imposed on the interface before failure by plastic deformation of the aluminum. For the conditions studied here, the applied load that is sufficient to cause interfacial fracture is greater than the critical applied load required to cause fracture in the softened (as-welded) and thinned aluminum sheet, but less than that required to cause fracture in the aluminum sheet after natural ageing. Since failure occurs by the mode that reaches the relevant critical stress for failure first, a transition in modes is observed as the aluminum hardens.

As shown in Figure 4.13, the fracture energy of naturally aged joints, though lower than that of as-welded joints, stayed at the same level when welding time exceeded 1.2 s, compared with the fracture energy drop of as-welded joints when the welding time was longer than 1.2 s. This is because for naturally aged welds, fracture occurred on the interface not across aluminum, so the thinning of aluminum by welding tip penetration did not affect the energy absorbed during fracture.

As shown in Figure 4.14, the naturally aged Al-Ti USW welds always have higher peak load than as-welded joints. This is because that peak load is determined by the strength of the weakest part of a weld, and the weakest part of naturally aged welds is the interface (due to hardness increase in the heat affected zone of the aluminum alloy).

After natural ageing, the optimized peak load of Al-Ti USWs weld reached ~3.5 kN (Figure 16), which is still markedly higher than that of Al-Mg USW joints (~2.0 kN) [30] and Al-Fe USW joints (~2.8 kN) [29] and is comparable to that of

similar metal Al-Al USW joints (~3.5 kN) [167]. The optimized fracture energy of USW Al-Ti weld reached ~5.0 kN•mm (Figure 15, after natural ageing), which is also markedly higher than that of Al-Mg USW joints (~1.2 kN•mm) [30] and Al-Fe USW joints (~3.8 kN•mm) [29]. The comparison to Al-Mg and Al-Fe USW joints again suggests that a reaction layer that quickly forms for these combinations is very harmful to weld properties. The good performance of Al-Ti joints is attributable to the very limited reaction between the two metals. The mechanical property results indicate that USW is a potential technique for Al-Ti dissimilar welding, which can give weld performance similar to that of similar Al-Al joints.

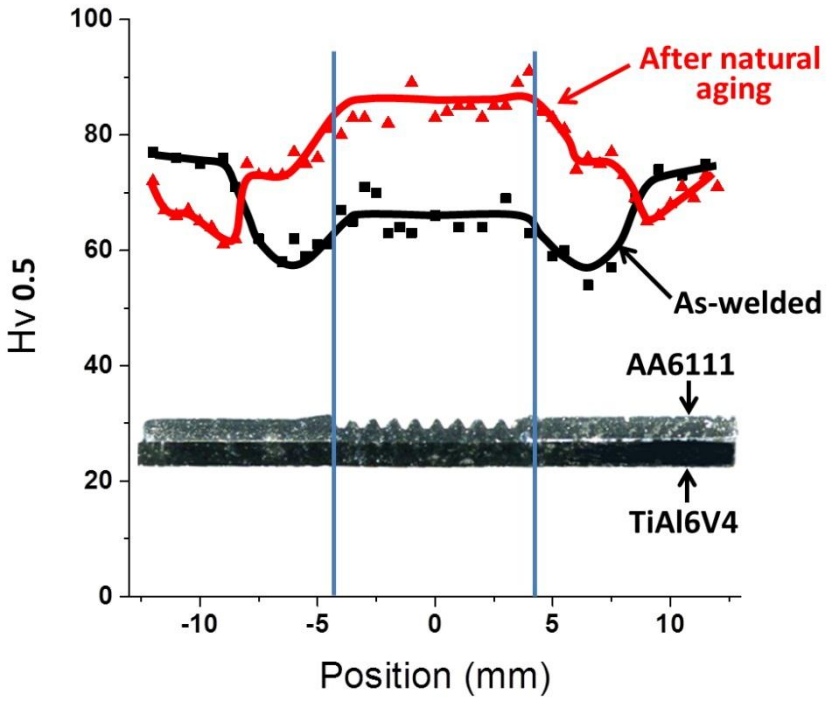

Figure 4.12 Hardness profile across the aluminum alloy in AA6111/Ti6Al4V weld (1.2 s, 1769J) measured 30 minutes (square markers) and 4 days (triangle markers) after welding. (Hardness test load: 500 g, dwell time: 10 s, the hardness was measured along a line ~0.5 mm above the Al-Ti interface.)

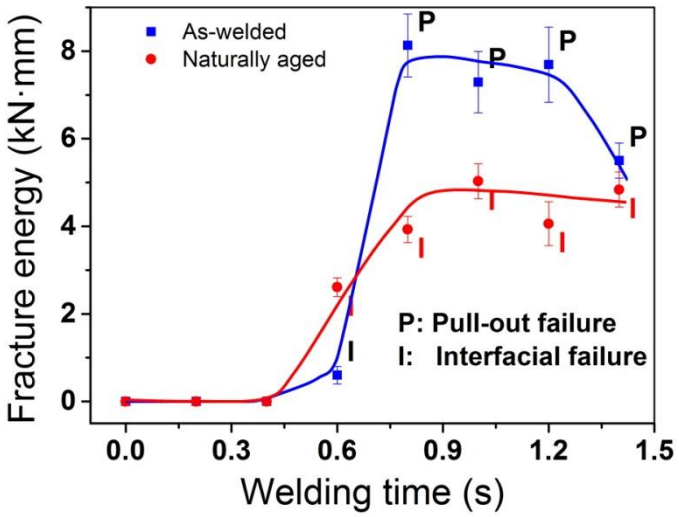

Figure 4.13 Comparison of fracture energy between as-welded and naturally aged Al-Ti USW joints.

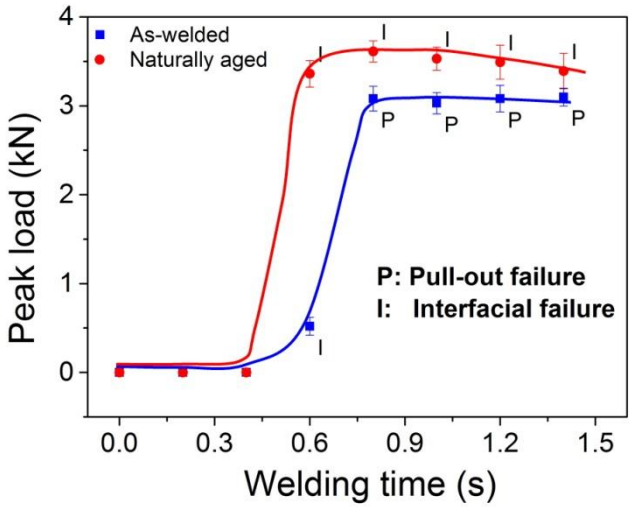

Figure 4.14 Comparison of lap shear strength between as-welded and naturally aged Al-Ti USW joints.

4.1.5 Temperature Analysis

Figure 4.15 shows the relationship between welding time and peak welding temperature, determined at the centre of the weld as described in the method section. With an increase of welding time from 0 s to 0.6 s, the peak temperature increased markedly. However, with an increase of welding time from 0.6 s to 1.2 s, the peak temperature increased slightly and reached a plateau. This is a common

phenomenon in welding processes where heat is generated by deformation of the material; as the aluminium gets hotter, it softens, and a near steady state is reached between heat generation and heat loss (by heat conduction through welding tool and heat radiation). The sharp increase of peak temperature when welding times are short (from 0 s to 0.6 s) and the slight increase (near plateau) when welding times are longer (from 0.6 s to 1.2 s) agree with the feature of a thermal cycle profile of a 1.2 s weld, in which temperature increased extremely rapidly when time is shorter than 0.4 s and temperature remains almost at a plateau when time is longer, as shown in Figure 4.16.

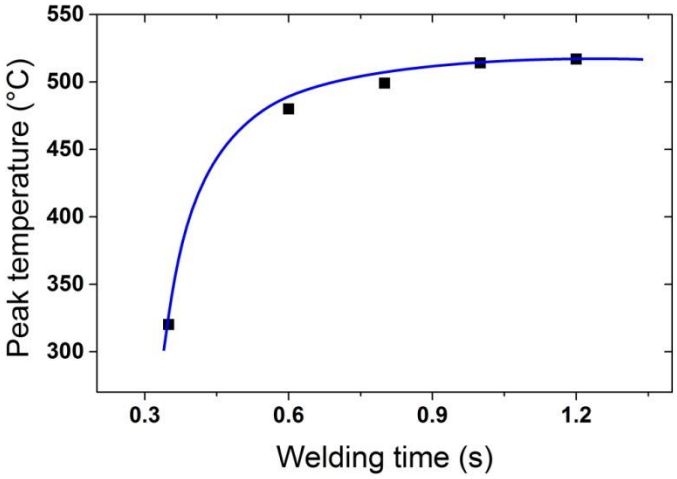

Figure 4.15 The relationship between welding time and peak temperature.

Figure 4.16 (a) shows two typical thermal profiles for a 0.6 s weld and a 1.2 s weld. To show more detail, the thermal cycle profiles indicated in the blue rectangular region in Figure 4.16 (a) was enlarged and is shown in Figure 4.16 (a) shows two typical thermal profiles for a 0.6 s weld and a 1.2 s weld. To show more detail, the thermal cycle profiles indicated in the blue rectangular region in Figure 4.16 (b). The thermal cycle can be divided into three periods, as shown in Figure 4.16 (b), period A is the temperature-rise period, in which temperature increases in an extremely high rate of 1135 K/s. This heating rate is much higher that of Fe/Al

USW couple and Mg/Al USW couple (300–600 K/s), because the thermal conductivity of Ti6Al4V alloy (6.6 $W \cdot m^{-1} \cdot K^{-1}$) is low compared with that of steel (Carbon steel: 54 $W \cdot m^{-1} \cdot K^{-1}$) and magnesium alloy (AZ91 Mg: 72 $W \cdot m^{-1} \cdot K^{-1}$). Period B is the high temperature holding period, in which temperature stays almost constant close to the peak value. In this period, the temperature neither increases nor decreases as a steady state becomes established. As discussed, the steady state occurs in USW (as with other friction welding processes such as FSW) because the heat generation due to plastic deformation varies inversely with temperature leading to a self compensating effect. The length of this period is quite important for forming a strong weld since most diffusion across the interface will occur during this time. Period C occurs once welding power input has been stopped, and the temperature reduces rapidly back to room temperature as the sheets are thin with a relatively high surface area to volume ratio.

4.1.6 Discussion

4.1.6.1 The interface reaction

Microstructural analysis shows that there is no visible reaction layer in the USWed Al-Ti welds. However, in previous investigations, in USWed Al-Mg and Al-Fe welds [29, 169], in FSWed Al-Ti welds [18] and in laser welded Al-Ti welds [3], reaction layers have been observed. For Al-Mg dissimilar ultrasonic spot welding and even shorter welding times, a reaction layer of several micrometres was observed in a previous study [30].

In general, for dissimilar metals welding, reaction layer formation and growth depends on mutual solid solubility, interdiffusion rate (which depends on activation energy for diffusion), temperature and energy barrier for nucleating IMC and so on.

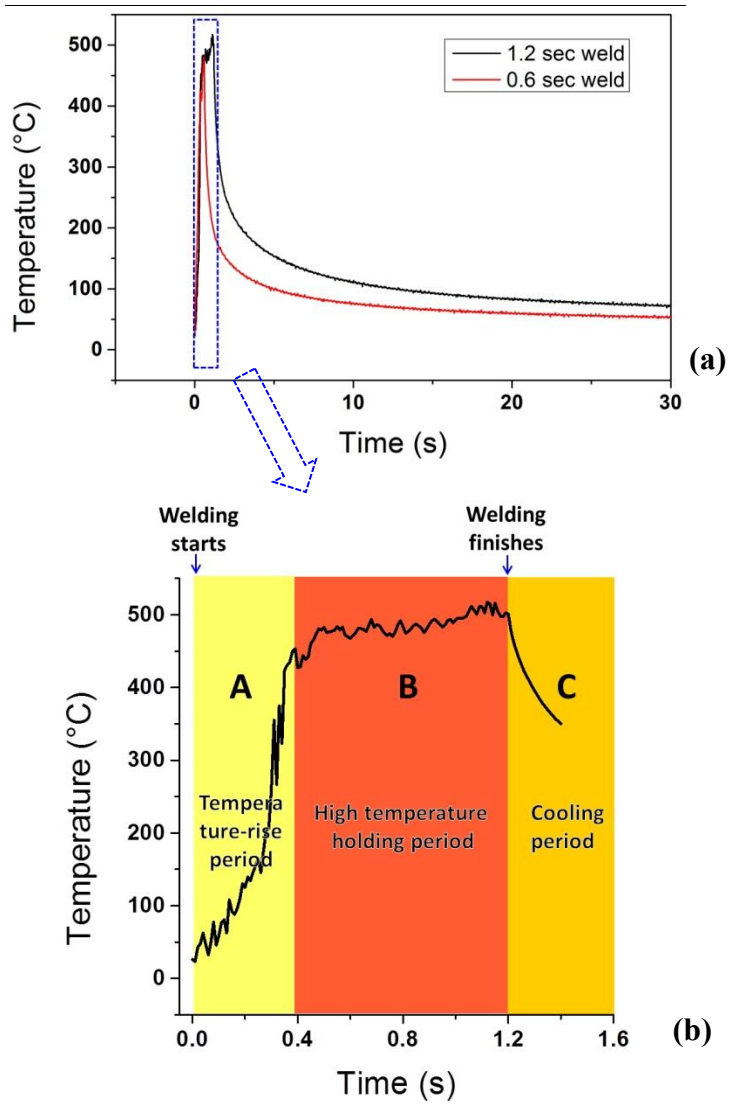

Figure 4.16 Weld thermal cycles of different welding times (0.6 s, redline and 1.2 s, black line) measured in the middle of welds, (a) the total cycle, (b) the partial thermal cycle of 1.2 s weld near the peak temperature region which is indicated by the blue rectangular in (a).

The calculated mutual solubilities for the Al-Mg, Al-Fe, and Al-Ti binary combinations in solid state are shown in Figure 4.17. These calculations were performed using thermodynamic software package Pandat with PanAl2012 database. To form a successful weld, some mutual solubility is expected to be necessary so that atoms will diffuse across the join line. The Al-Ti case is similar to the Al-Fe case in that both Fe and Ti have very low solubilities in Al, but Al does have some solubility in Ti (and Fe). Once the solubility limit is exceeded, there will

be a driving force for IMC formation. The observation that IMC forms rapidly in the Al-Fe case but not the Al-Ti case suggests that the lack of IMC in the latter combination is due to the kinetics of the process rather than solubility limit effects alone, as discussed below.

The inter-diffusion rate is also critical in determining the time required before sufficient enrichment occurs across the interface to nucleate IMC. Inter-diffusion in the Al-Ti system has a relatively high activation energy of 250~300 $kJ\ mol^{-1}$ [126], compared with 60~70 $kJ\ mol^{-1}$ reported for the Al-Mg system and 190 $kJ\ mol^{-1}$ for the Al-Fe system [29, 169]. If interdiffusion is slow, then a long welding time will be needed before sufficient enrichment occurs to nucleate IMC. Indeed, by prolonged isothermal heat treatment at high temperature, it is shown that IMC can be made to form in Al-Ti USWs, but this process is very slow compared to that observed in Al-Mg [170] and Al-Fe [29] couples (See Chapter 6, Section 6.1).

The energy barrier to nucleation of the IMC phase is also an important parameter in determining how quickly intermetallic will nucleate. Even when there is a driving force for IMC formation due to the solubility limit being exceeded, there will remain an energy barrier due to the interfacial and strain energy associated with IMC nucleation. If this is high, then nucleation will occur more slowly. It is difficult to compare the energy barriers expected for IMC nucleation in the Al-Fe, Al-Mg and Al-Ti systems since values for parameters such as interfacial energy are not available for all the relevant IMC phases.

Regarding temperature, for all fusion welding methods (which have a much higher temperature than solid state welding methods), at least one of the metals (Al and Ti) is melted. Liquid to liquid and liquid to solid reactions are much faster than solid to

solid reactions. As a result, in all fusion welded Al-Ti welds a thick reaction layer grows very fast even if the heat source (e.g. laser beam) is directed to one side of the weld interface [3]. However, in the case of USW, the welding energy input is much lower, which is only around 2% of resistance spot welding (a fusion welding process), and is ~30% of friction stir spot welding (a solid state welding process) [167], as a result the welding temperature is lower (only ~520 ℃, peak welding temperature, Figure 4.15). Besides, the welding time, usually less than 1.4 s, is shorter than friction stir welding, friction stir spot welding [167] and diffusion bonding [26], which also can limit the growth of IMC layer.

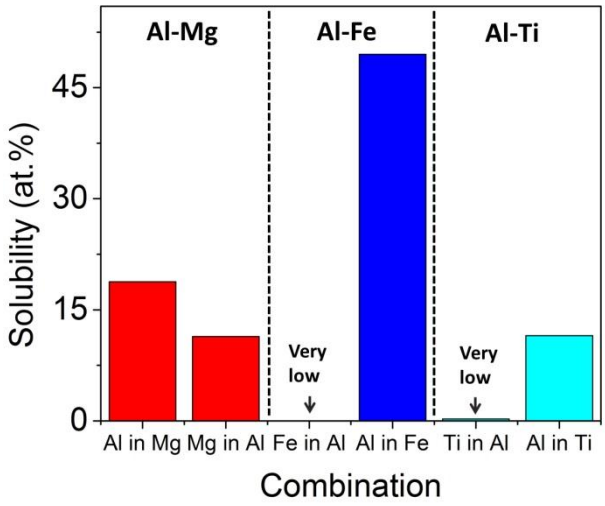

Figure 4.17 Mutual solid solubility of Al-Mg (in solid state below eutectic temperature ~450 ℃), Al-Fe and Al-Ti (both at 530 ℃, which is roughly the maximum peak welding temperature measured in USW).

4.1.6.2 The influence of welding time

In general, for USW, welding time can affect the welded area, the thickness of reaction layer, the microstructure and geometry of welded sheets [167, 171]. With an increase of welding time, the oxide film on the surfaces being joined is broken down [167, 169], the pure metal contact increases and microwelds develop and spread on the interface, i.e. the welded area or metallurgical bond area increases.

The welding time must be sufficient to ensure this process is complete, i.e. the oxide is fully broken up and the maximum area of metallurgical bonding is achieved.

Meanwhile, an increase in welding time also leads to an increase of temperature and gives more time for reaction layer growth in dissimilar metal joining. For combinations such as Al-Mg where the reaction layer formation is very rapid, a sharp drop in weld strength and toughness is therefore often observed with increased welding time [31]. However, in the present case, since no reaction layer was observed even after the longest welding time used, no sharp drop in weld performance occurs as welding time increases. This means that the process window to produce a good weld for Al-Ti dissimilar USW will be wider than that for Al-Mg or Al-Fe combinations.

In addition to the effect of welding time on reaction layer formation, the holding time at high temperature during welding also controls the dissolution of precipitates or solute clusters (depending on the temper condition of the material) [168] and the degree of sheet thinning in the welded region (Figure 4), because softened aluminum is displaced by the welding tip. Thinning of the welded region leads to a lower fracture energy because there is less metal to bear load.

As shown in the results section, for as-welded joints, the minimum welding time required to produce the highest failure load and fracture energy is coincident with the minimum time to cause a transition in the fracture mode from “interfacial failure” to “pull-out”. Longer welding times than this critical condition are detrimental since the additional heat and deformation input further softens and thins the aluminum alloy sheet. However, as demonstrated, this drop off in

properties is gradual, so that the weld properties are far less sensitive to welding time than has been observed in other dissimilar metal USW combinations (e.g. Al-Mg, Al-Fe) [29, 169] .

4.1.6.3 Natural aging

The effect of natural ageing in other dissimilar USW combinations (e.g. Al-Mg and Al-Fe) is usually unimportant to weld properties, since for all conditions failure occurs by fracture of the brittle reaction layer and has little relationship with the strength of base metals [30, 172]. However, in USWed Al-Ti welds, the lack of an embrittling IMC phase leads to a different situation.

As shown in section 4.1.4, in the Al-Ti case, the failure mode changed markedly from 'pull-out' mode (ductile fracture) when tested after welding to 'interfacial failure' after several days of natural aging due to the strength recovery of the aluminum alloy (Figure 15, 16). The transition in failure mode with natural ageing is accompanied by a reduction in fracture energy. These results suggest that if the objective is to maximize the fracture energy, then the softening that occurs in the heat affected zone of the as-welding condition is desirable, since it leads to ductile failure in this zone and not brittle interfacial failure. There may be situations where it is beneficial to encourage local softening of the aluminum alloy (which could be achieved by local over-aging with another heat source) to get the desired weld properties.

4.2 The influence of welding tip geometry

As mentioned in Chapter 3, there are two different welding tips (Fig. 3.5) used for ultrasonic welding of AA6111 and Ti6Al4V. As shown in Fig. 3.5, the round tip has a larger surface area than the rectangular one. In terms of welding tip tooth, the

rectangular one has more teeth and its tooth is sharper and is shaped like a triangle. The tooth of the round tip is wider and blunter and has a square shape. As a result of the tooth design, the rectangular tip grips aluminium plate more easily and plunges deeper into it. The cross-sections of two different type welds are shown in Figure 4.18.

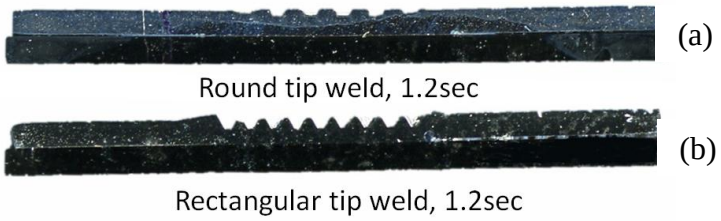

Figure 4.18 Macrograph of cross-sections of two different type welds, (a) a round tip weld, (b) a rectangular tip weld.

In general, tip geometry can influence: 1. the depth of welding tip footprint; 2. the extent of stress concentration; 3. the fracture path. Then, the mechanical properties of USWed joints were affected.

The footprint depth:

Figure 4.19 a) shows the high resolution profiles of a rectangular tip weld and a round tip weld in the positions labelled by the red lines in Figure 4.19 b). The profiles were collected using a laser profilometer with a resolution of 10 μm. These two welds were joined using the same welding time 1.2 s and other same parameters, except the welding tip. However, the depth of their footprints has a large difference, as shown in Figure 4.19. In Figure 4.19 b), d1 and d2 stands for the distance between the surface of aluminium plate with the first valley bottom at the edge of the round tip weld (d1) and the rectangular tip weld (d2). Here, d1 is 120 μm and d2 is 455 μm. Since first valley bottom at the edge of welds is the first

weak region exposed to stress when load is applied (other valley bottoms are protected by the wave crest regions and the interface bonding), its depth has a strong influence on the load bearing capacity of welds. Due to the large difference between d1 and d2, when other things are equal and fracture occurs at the weak region of aluminium and goes through aluminium, the strength and fracture energy of rectangular tip welds are lower than that of round tip welds, as shown in Figure 4.20 and Figure 4.21.

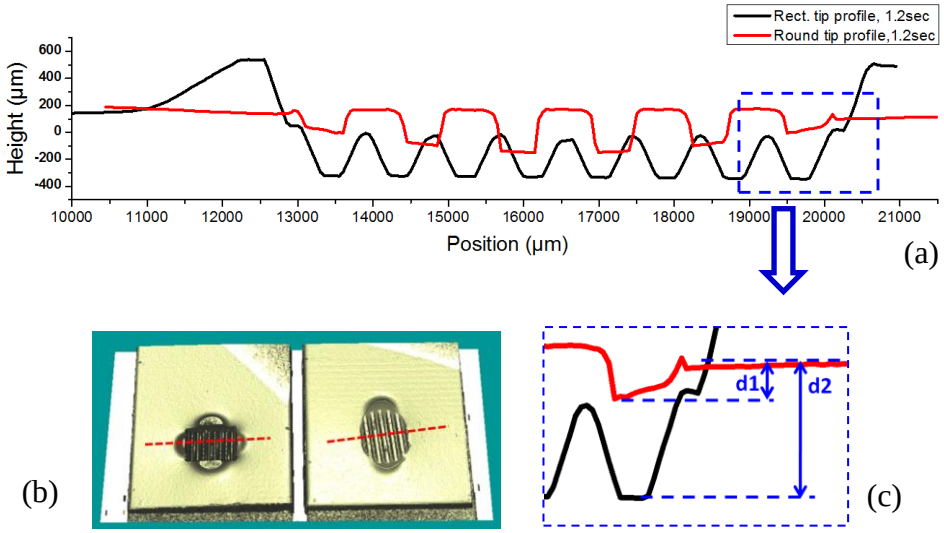

Figure 4.19 (a) High precision profiles of two types of welds joined by the same welding time, (b) the positions (labelled by the red lines) of profile curves and (c) the partial enlarged view of the edge region.

The extent of stress concentration:

As shown in Figure 4.18, the significant difference of height between the wave crest at the edge of weld and the first adjacent valley bottom in the rectangular tip weld caused much higher stress concentration than round-tip welds, which has a much smooth transition from welded region to the unwelded base metal. When load was applied, the higher stress concentration led to low shear strength.

Previous research by Watanabe et al also demonstrated that the joint produced by a tip with a geometry similar to the round tip has a higher strength than the joint produced by a tip with a geometry similar to the rectangular tip [39].

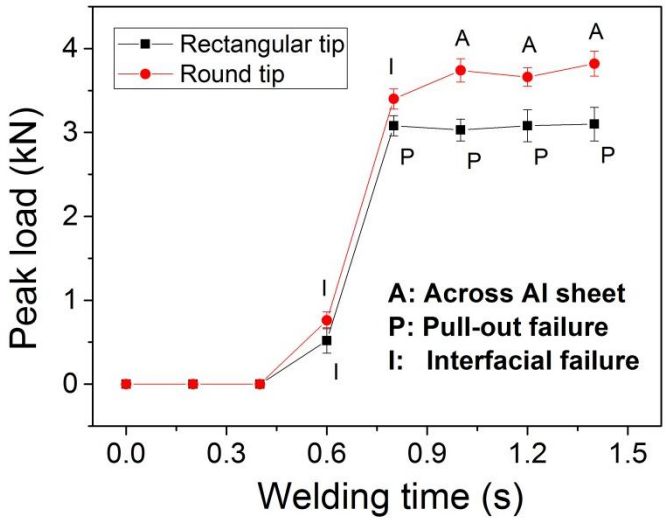

Figure 4.20 Comparison of peak leads between as-welded rectangular-tip welds and round-tip welds.

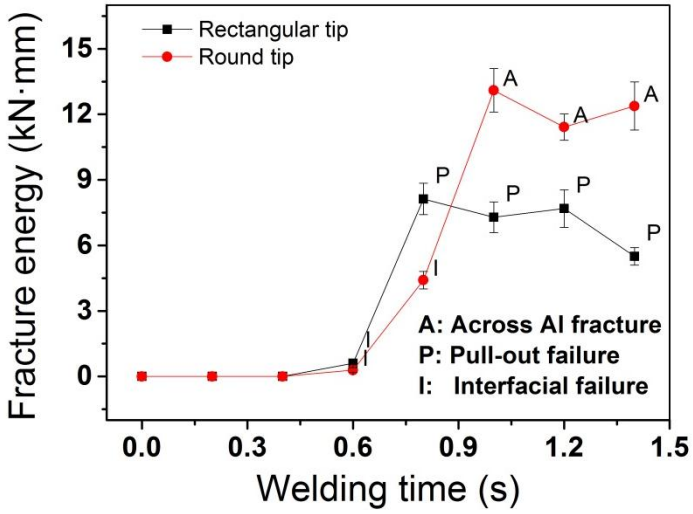

Figure 4.21 Comparison of fracture energy between as-welded rectangular-tip welds and round-tip welds.

The fracture path:

As shown in Figure 4.22, in as-welded condition, for both rectangular-tip welds

and round-tip welds, the fracture type is ductile fracture, but the fracture path is different because of the influence of footprints of two different tips. For rectangular-tip welds, the fracture mode is the 'Pull-out' mode, in which fracture path goes through the edges of welded region, which are thin and weak. For round-tip welds the fracture mode is 'Across aluminium fracture' mode, in which fracture path mainly goes through aluminium base metal which is much thicker and stronger than the edges of welded region of rectangular-tip weld. As a result, the fracture of round-tip welds required more energy than that of rectangular-tip weld.

Also, generally the round tip weld has a larger welded area, which is beneficial for the weld properties. John et al. [38] also found tip geometry has important effects on the properties of welds. They found that the welded area increased with the increase of tip size and a trend of increasing peak load with the increase of welding tip size.

In all, the results suggest that a welding tip with smooth edges and a larger area is beneficial for joint mechanical properties.

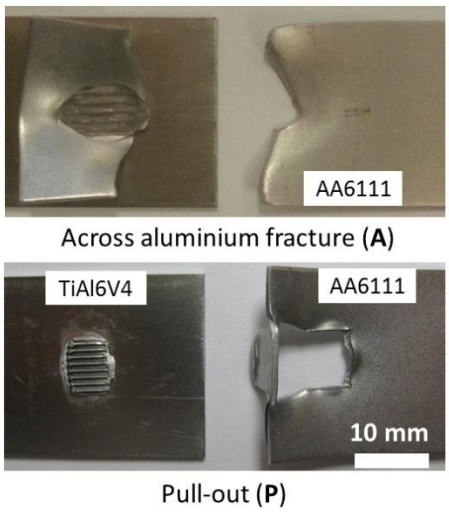

Figure 4.22 Fracture path of round tip weld (upper) and rectangular tip weld (lower), both in as-welded condition.

4.3 USW of AA2139 to Ti6Al4V

Since it has already been proved that round welding tip can produce welds with better mechanical properties in the last section (section 4.2), the round welding tip is selected as the only welding tip used for welding AA2139 to Ti6Al4V.

4.3.1 Joint appearance

Figure 4.23 (a) shows the appearance of a typical AA2139-Ti6Al4V dissimilar weld (welding time 4.0 s, welding energy 4120 J) produced by USW. The macrostructure of cross-section of a USW joint is shown in Figure 4.23 (b). It can be seen that AA2139 aluminum alloy sheet was severely deformed by the welding tip and there was almost no macro deformation on the titanium side. The reason for this is discussed later in the weld microstructure section.

Figure 4.23 (c) shows surface appearances of AA2139/Ti6Al4V joints for different welding times. It can be seen that the indent area increased with increasing welding time, due to the softening of AA2139 aluminium alloy and the downward movement of the welding tip with increasing welding time.

4.3.2 Weld microstructure

Figure 4.24 (a) and (b) show a typical AA2139-Ti6Al4V weld microstructure (cross section), for a 4 s welding time joint. No IMC layer was visible in these AA2139/Ti6Al4V weld backscattered electron images even at the highest magnifications, which is encouraging since the formation of a brittle IMC layer is typically associated with poor mechanical properties.

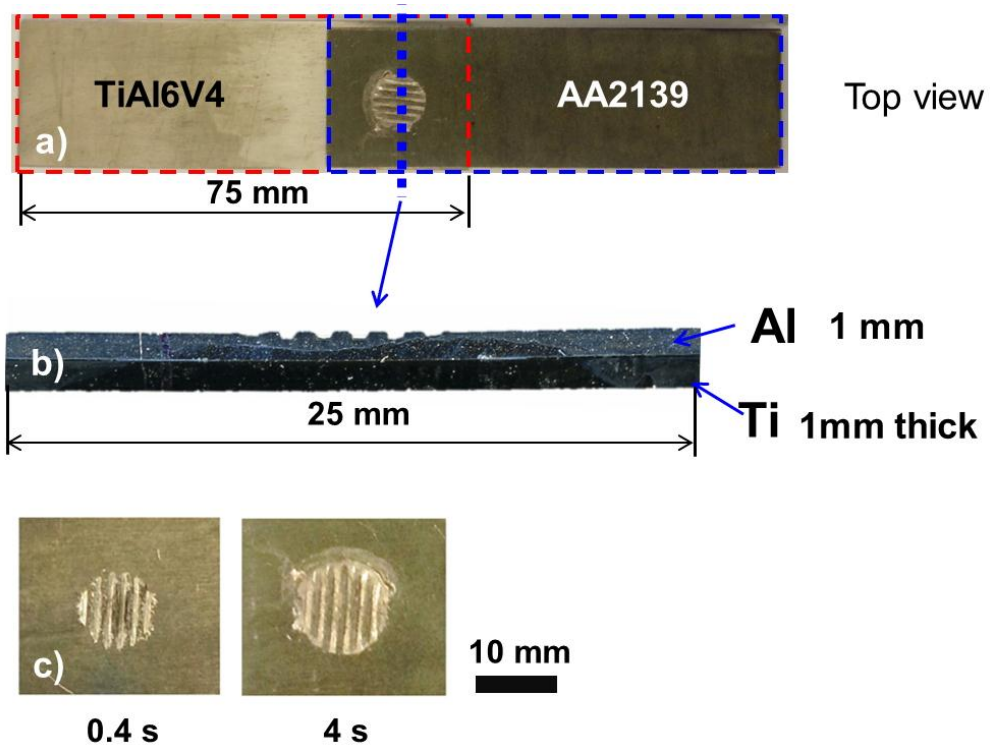

Figure 4.23 (a) Weld appearance of a typical USW weld, welding time 4 s, welding energy 4120 J, (b) Macrostructure of cross-section of a typical USW weld, welding time 4.0 s, welding energy 4120 J, (c) Influence of welding time on welding time indent area, sample photos (aluminum side).

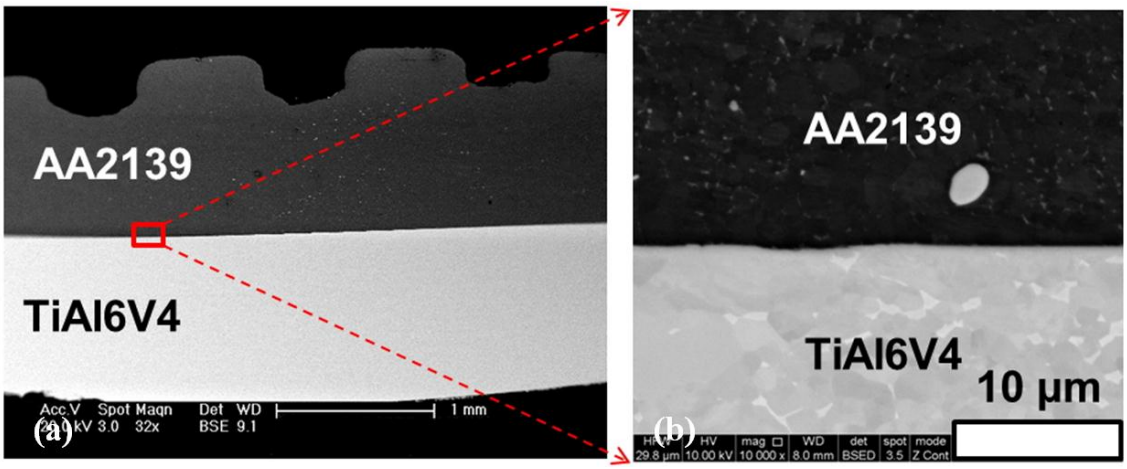

Figure 4.24 SEM images of typical AA2139-Ti6Al4V ultrasonic spot weld interface (Welding time: 4 s, welding energy: 4120 J) (a) low magnification image, (b) high magnification BSE image.

To investigate the weld interface at higher resolution, TEM was used. To make a careful study of the Al-Ti interface, both bright field images and high-angle annular dark field images (HAADF) were taken of the interface region with examples of these images shown in Figure 4.25. Even using the higher resolution of the TEM, no obvious IMC layer was detected, suggesting if any layer is present it must be very thin. Although atypical, similar with the observation in Section 4.1.2, "clean" (no-IMC-layer) interface structures have been noticed for both AA6111/Ti6Al4V USW joints and other material combinations joined by ultrasonic welding and other approaches [66, 71, 165]. In this case, a prolonged post-weld heat treatment (e.g. 5 h at 500 ℃) is required to form detectable IMC layer.

The microstructure of AA2139 near the weld interface and the microstructure of unwelded AA2139 base metal in the near surface region at the same magnification are shown in Figure 4.26 (a) and Figure 4.26 (b). It can be seen that similar to the observation in USWed AA6111/ Ti6Al4V joint (Section 4.1.2), the AA2139 grains near the weld interface have been refined by the USW process, which has also been found in other investigations on Al-Al and Al-Fe USW by Bakavos et al and Prangnell et al [29, 167].

The microstructure of Ti6Al4V near the weld interface and the microstructure of unwelded Ti6Al4V base metal in the near-surface region at the same magnification are shown in Figure 4.26 (c) and Figure 4.26 (d). No apparent difference between them can be noticed. This again suggests that little deformation occurred on the Ti6Al4V side near the weld interface. The possible explanation for this has been discussed in Section 4.1.2 in the case of USWed AA6111/ Ti6Al4V joint.

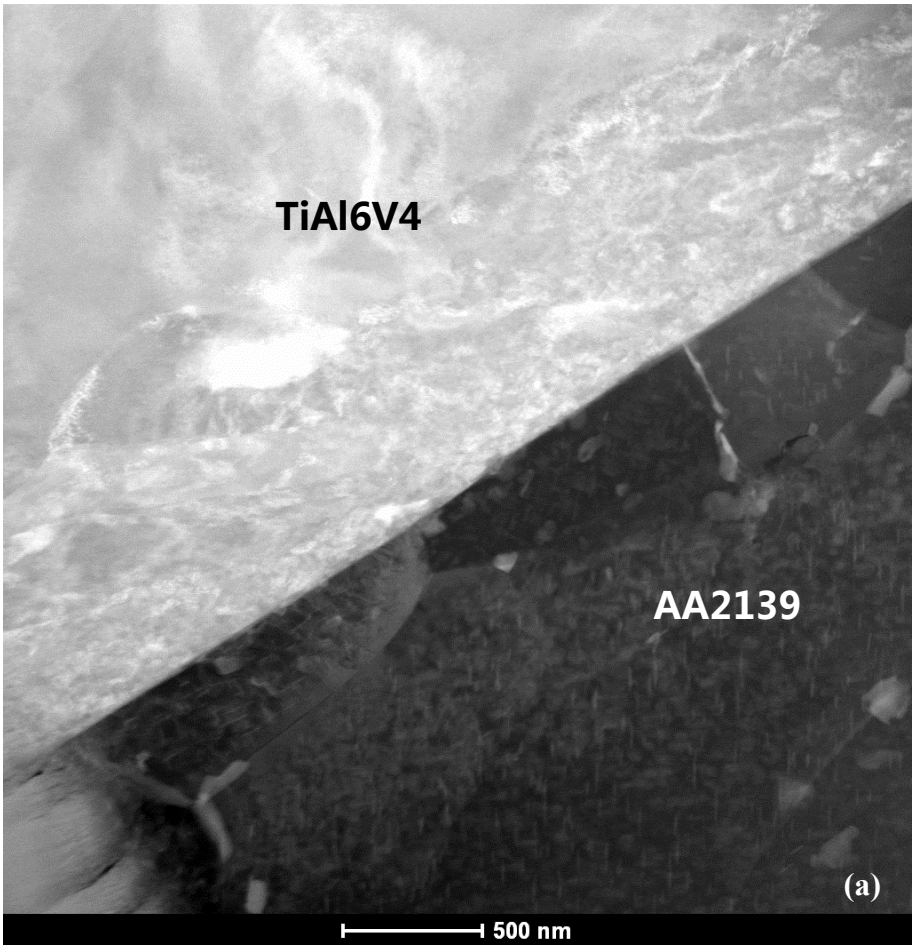

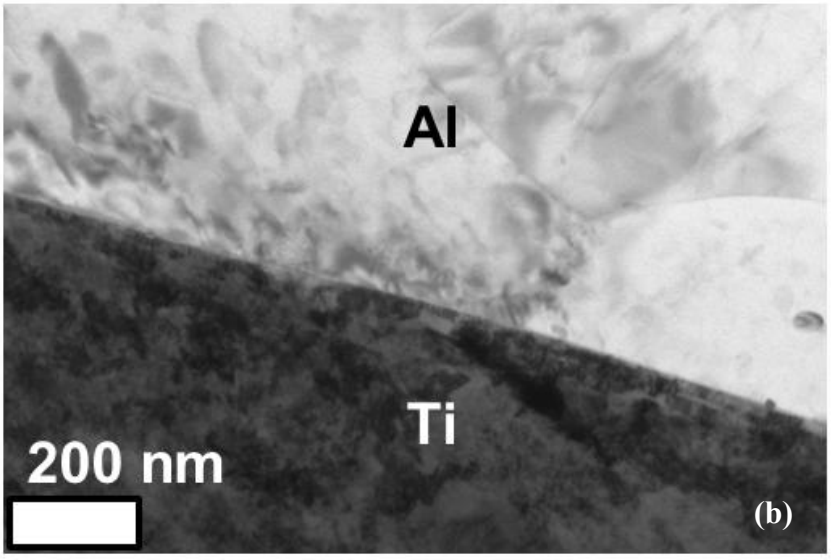

Figure 4.25 TEM images of an AA2139-Ti6Al4V USW weld interface, (a) A low magnification HAADF image showing a large region of the interface, (b) Higher magnification bright field image, (Welding time: 4.0 s, welding energy: 4120 J).

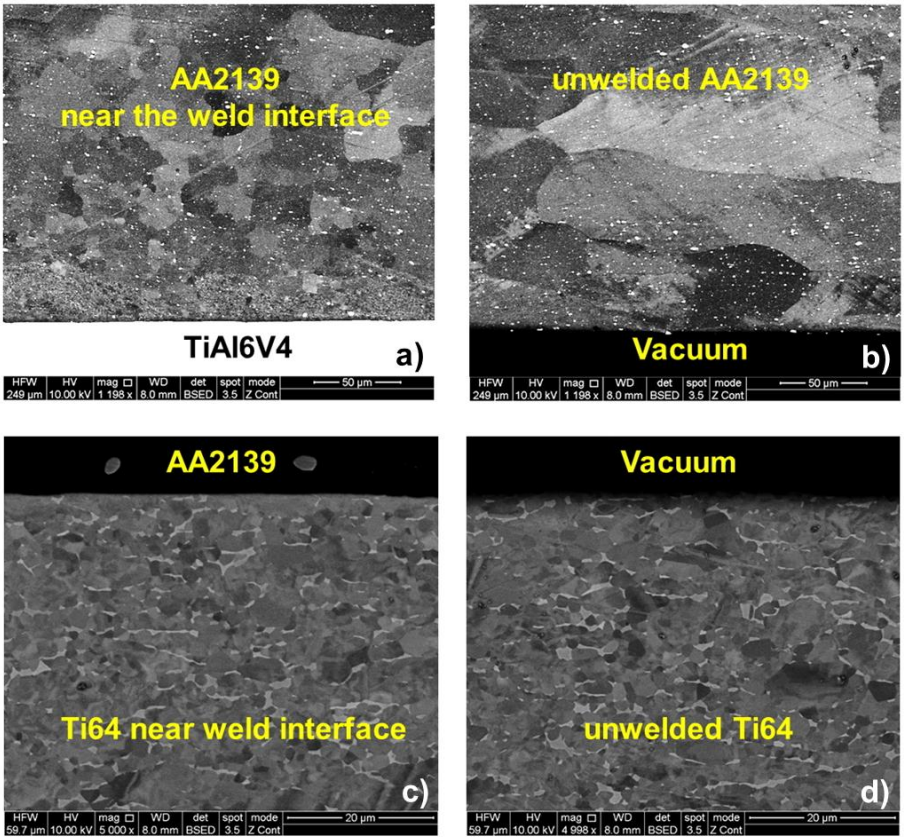

Figure 4.26 Comparison of microstructure between aluminum alloy AA2139 near the weld interface (a, welding time 3.0 s) and AA2139 base metal near surface region (b, not welded); Comparison of microstructure between Ti6Al4V near the weld interface (c, welding time 3.0 s) and not-welded Ti6Al4V base metal near surface region (d, not welded)

4.3.3 Mechanical properties

4.3.3.1 Effect of welding time

As shown in Figure 4.27 (a), the peak load that can be sustained before failure of the Al-Ti weld increased with an increase of welding time from 0 s to 2.0 s. For times longer than this, peak load plateaus, with an upper limit around 5.3 kN. This peak load is much higher than that measure during testing of optimized Al-Mg [169] USW welds (~2.0 kN) and Al-Fe [29] USW welds (~2.8 kN) of similar dimensions. This is mainly due to the very limited interfacial reaction between Al and Ti

compared with the rapid interfacial reaction in Al-Mg welds and Al-Fe welds, which has been discussed in more detail in Section 4.1.

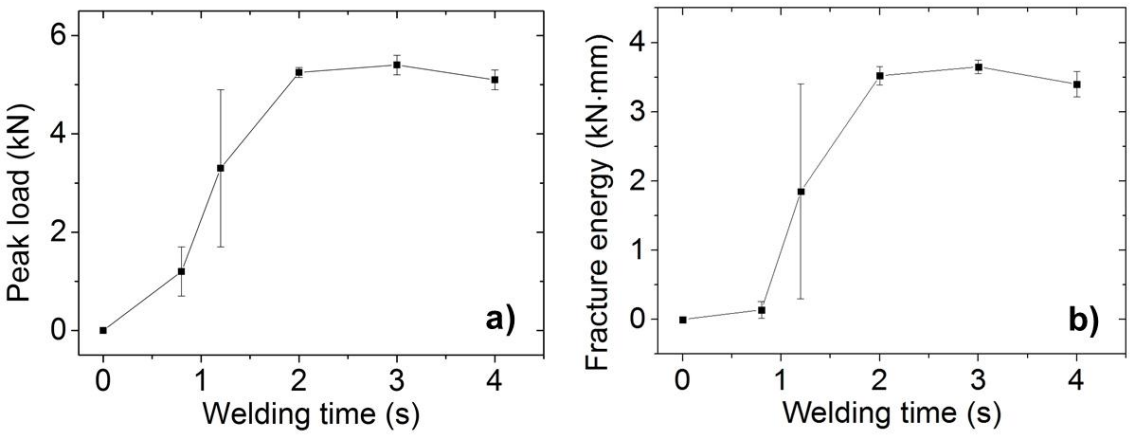

Figure 4.27 (a) Effect of welding time on the peak load of AA2139/Ti6Al4V USW welds; (b) Effect of welding time on fracture energy of AA2139/Ti6Al4V welds.

The highest peak load reached is also higher than (~51%) that of optimized AA6111-Ti6Al4V USW welds (~3.5 kN) [173], which shared a similar interfacial failure mode. This can be largely attributable to the increased area of the welding tool used in the present study (tool cross-section area: 79 mm^2 , ~46% larger) compared with that used for welding AA6111/Ti6Al4V [173]. A larger welding tool leads to a larger welded area and thus increased failure load.

The high degree of scatter in the peak loads for the joints made using welding time 1.2 s is because this time corresponds to the transition between the partially bonded (short welding time) and fully bonded conditions (long welding time, ＞2.0 s). As shown in Figure 4.27, for welding times shorter than 0.8 s, almost no weld can form; for welds longer than 2 s, a fully bonded weld always forms. Comparing with the AA6111-Ti6Al4V welds, it takes longer time to produce a fully bonded AA2139-Ti6Al4V weld. This is probably due to that: 1. The welding tool used for joining AA2139 to Ti6Al4V is larger, and thus leads to a larger heat transfer area

(quicker heat loss); 2. The welding energy density is lower due to the larger welding tool, as the welding power is identical. In general, the welding time – peak load relationship of AA2139-Ti6Al4V welds is quite similar to that of AA6111-Ti6Al4V welds [173], with peak load initially increasing with increasing welding time before reaching a plateau.

As shown in Figure 4.27 (b), the variation of fracture energy with increasing welding time is similar with the variation of peak load (Figure 4.27 a). The fracture energy reached an upper limit around 3.7 kN ·mm when the welding time is longer than 2 s.

As Figure 4.28 shows, weld failure at all weld times was observed to occur by fracture across the interface, and no aluminum remained stuck on the titanium sheet after testing. This is in contrast to USW AA6111-Ti6Al4V joints, where a nugget pull out condition could be achieved which was accompanied by extensive deformation of aluminium leading to a high fracture energy [173]. This difference is due to the higher strength of AA2139 alloy compared with the AA6111 alloy, which means that interfacial failure occurs before significant plastic deformation of the aluminium alloy.

Though the optimized AA2139-Ti6Al4V USW weld peak load (~5.3 kN) is 51% higher than that of AA6111-Ti6Al4V USW weld (~3.5 kN) [173], the optimized AA2139-Ti6Al4V USW weld fracture energy (~3.7 kN · mm) is 26% lower than that of AA6111-Ti6Al4V USW weld (~5 kN · mm, naturally aged) [173]. This is consistent with the interfacial failure mode always observed for the AA2139-Ti6Al4V welds as already noted.

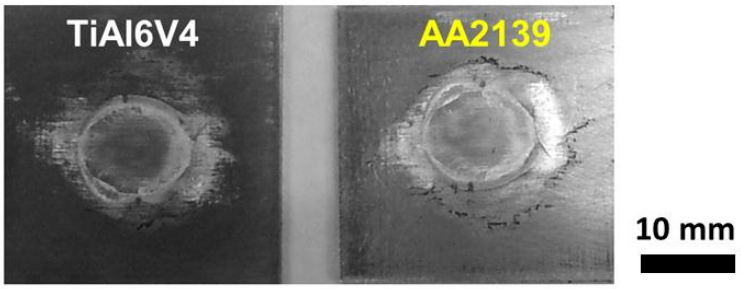

Figure 4.28 The 'interfacial failure' mode of AA2139/Ti6Al4V.

4.3.3.2 Hardness profile

Figure 4.29 shows the hardness profile in the AA2139 aluminum alloy close to the interface along the weld, measured within 30 minutes of welding and after 8 days natural ageing. It can be seen that similar to other solid state welding processes, such as friction stir welding[174], the USW process has led to a significant (approximately 37%) softening of the aluminium alloy in the weld zone and the heat affected zone, due to the dissolution and coarsening of the strengthening precipitates [174]. After 8 days natural ageing, the hardness recovered partly, because of the re-precipitation of the alloying elements dissolved during the welding process. In contrast to the AA6111-Ti6Al4V USW joints [173], the strength recovery of AA2139 did not lead to the change of failure mode of the AA2139-Ti6Al4V USW welds since even in the “as welded” (soft) condition, the AA2139 alloy is strong enough to produce an interfacial failure mode in the weld.

4.3.4 Temperature Analysis

Figure 4.30 (a) shows a typical thermal profile for a 4.0 s weld measured at the centre of the weld as described in the experimental section. To show more detail, the thermal cycle profile indicated in the blue rectangular region in Figure 4.30 (a) was enlarged and is shown in Figure 4.30 (b).

Similar to the ultrasonic welding thermal cycle of AA6111/Ti6Al4V joints (Section 4.1.5), the welding thermal cycle of AA2139/Ti6Al4V can be divided into three phases: 1. Temperature-rise phase; 2. High temperature holding phase; 3. Cooling phase.

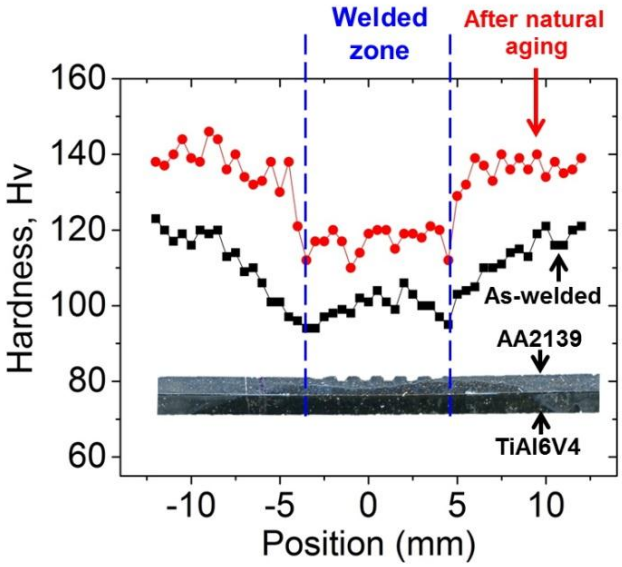

Figure 4.29 Hardness profile across the aluminum alloy in AA2139/Ti6Al4V weld (4 s, 4250J) measured 30 minutes (square markers) and 8 days (circular markers) after welding. (Hardness test load: 500g, dwell time: 10 s, measured along a line 0.5 mm above the weld interface.)

The long "temperature-rise phase" (~2.0 s) of AA2139/Ti6Al4V weld led to poor bonding in welds produced using welding times shorter than 2 s. The temperature at times < 2 s is not high enough for sufficient inter-diffusion between AA2139 and Ti6Al4V to form a fully bonded weld. This is consistent with the poor mechanical properties measured for such short time welds.

4.4 Segregation of alloying elements on Al/Ti interface

During the ultrasonic welding process, the Al/Ti interface has experienced a high welding temperature thermal cycle and severe deformation. As stated in previous sections, no IMC layer has been detected on the Al/Ti interface. Meanwhile, the

Al/Ti interface, like grain boundaries, is a high energy region compared with the bulk metal interior. Therefore, the alloying elements in both the aluminium alloy and the titanium alloy could possibly segregate to the Al/Ti interface.

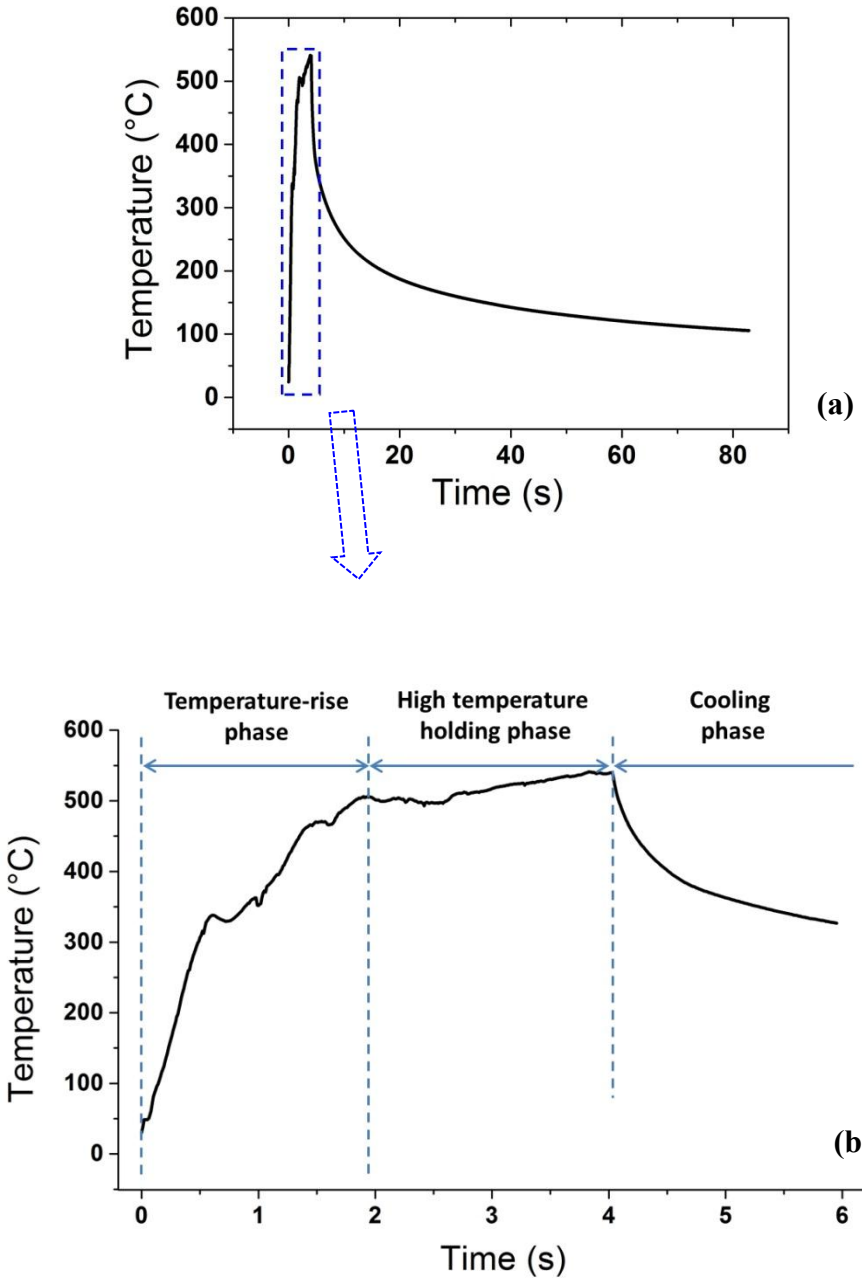

Figure 4.30 Welding thermal cycle, (a) the total cycle of a 4.0 s welding time measured in the middle of the AA2139-Ti6Al4V weld, (b) the partial thermal cycles of the 4.0 s weld near the peak temperature region which is indicated by the blue rectangular in (a).

More importantly and usefully, the segregation of these alloying elements on the

Al/Ti interface could affect the weld mechanical properties and the reaction layer growth. Thus, in this chapter, high resolution TEM-EDS was used to investigate the alloying elements segregation on the Al/Ti interface.

4.4.1 Mg, O and Si on the Al/Ti interface

The Al/Ti (AA6111/Ti6Al4V) interface analysed in this section was produced using a welding time: 1.4 s and a welding energy: 1967 J. As presented in Section 4.1.2, no Al-Ti IMC layer was detected on this interface. A typical Al/Ti interface region (~1000 nm × 1500 nm) on a FIB-thinned TEM sample was selected for STEM-EDS analysis using the state-of-the-art FEI Titan G2 80-200 scanning transmission electron microscope (S/TEM) with ChemiSTEM™ technology.

As shown in Figure 4.31 and Figure 4.32, Mg, O and Si enrichment was detected on the the AA6111/Ti6Al4V interface using STEM-EDS technique.

4.4.1.1 Mg and O

According to previous investigations [175-178], for aluminium alloys containing Mg, Mg strongly segregated to the surface of Al alloys and the segregation concentration can reach 10 at. %. Bloch et al. also found that Mg segregation on the surface of Al alloy greatly enhanced the oxygen adsorption rate at room temperature [177]. Hence, most of the observed Mg and O "enrichment" on the Al/Ti interface probably had existed on the surface of AA6111 before ultrasonic welding. The segregated Mg could be oxidized due to its high activity. Besides, the oxidation of segregated Mg on the surface layer can be further increased in the initially unstable stage of USW due to the welding heat and the breaking of the original surface oxide layer by the severe friction of USW. The severe friction

allows more contact between the fresh metals with air before the aluminium surface was totally protected from air, i.e. before an intact Al/Ti weld was formed. Field et al. [179] found that thick layers of Mg oxide formed rapidly on the surface of an Al-Mg alloy at temperatures higher than 377 °C. As stated in Section 4.1.5 and 4.3.4, the ultrasonic welding temperature is higher than this temperature, which allows the rapid formation of Mg oxide in the surface layer.

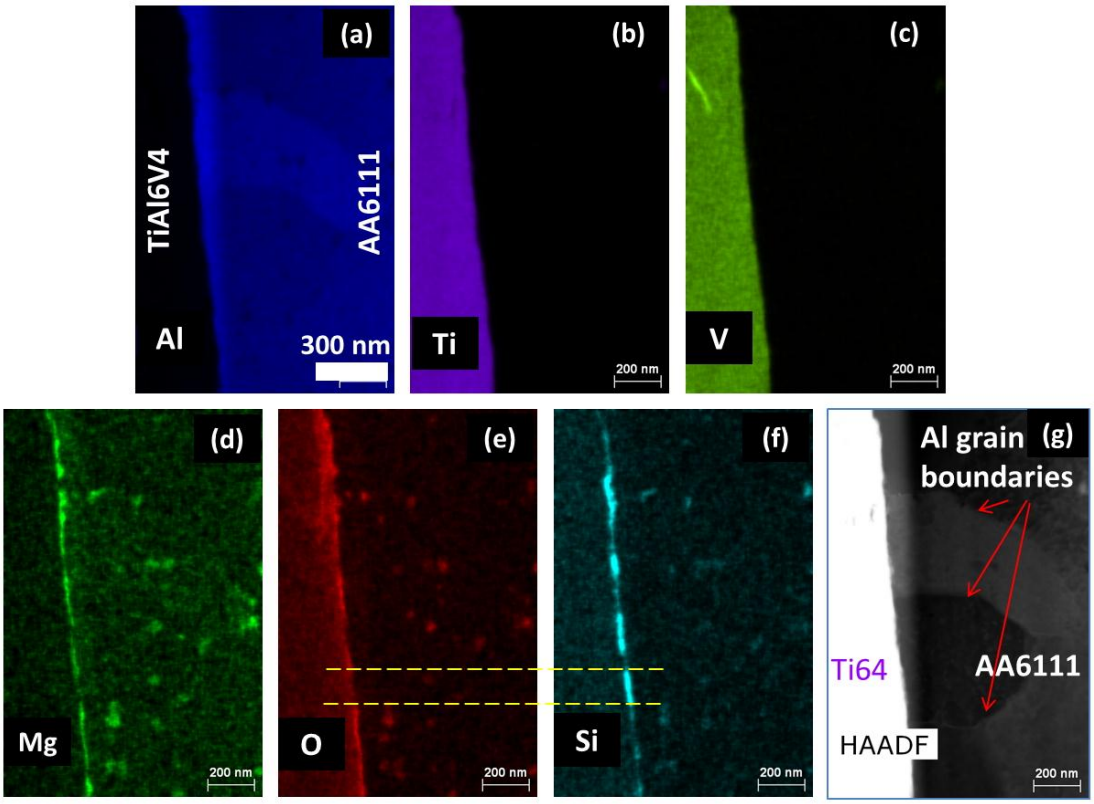

Figure 4.31 STEM-EDS element maps in the AA6111/Ti6Al4V interface region, (a) Al map, (b) Ti map, (c) V map, (d) Mg map, (e) O map, (f) Si map, (g) STEM-HAADF image. (Low magnification view compared with Figure 4.32).

From Figure 4.31 and Figure 4.32, it can be seen that the distribution of Mg on the Al/Ti interface is coincident with that of Oxygen. This again indicates that the concentrated Mg and O on the interface are probably from the magnesium oxide (or O-rich Mg) in the surface layer of AA6111 alloy. Besides, the discontinuous distribution of magnesium oxide suggests that the original surface oxide layer has

not been totally removed by the ultrasonic welding process, but only was broken into pieces, as illustrated in Figure 4.33. The reason for the surface oxide layer not being totally removed could be that the amplitude of ultrasonic vibration is very small (only ~6 μm) compared with the 10 mm wide welded region.

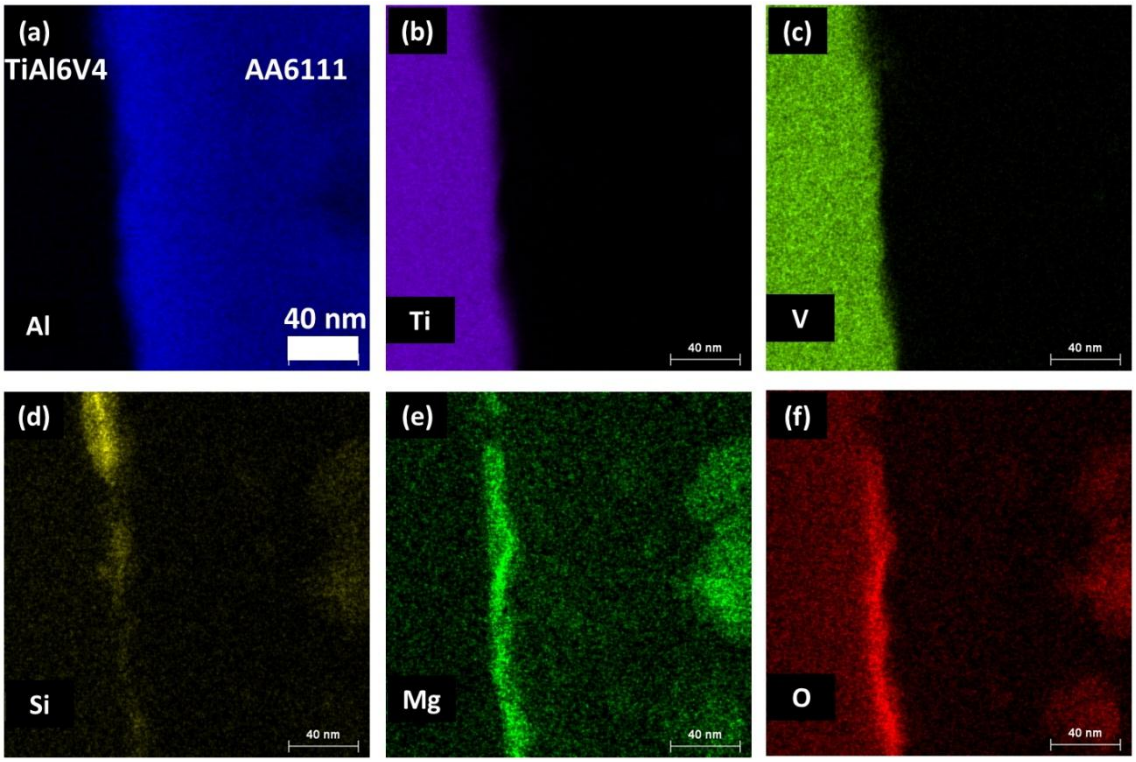

Figure 4.32 STEM-EDS element maps in the AA6111/Ti6Al4V interface region, (a) Al map, (b) Ti map, (c) V map, (d) Si map, (e) Mg map, (f) O map. (Higher magnification view compared with Figure 4.31)

Effect of the residual oxides on IMC layer growth:

These discontinuous residual oxides (including Mg oxides) on the Al/Ti interface could retard the formation and growth of the Al-Ti reaction intermetallic layer, and consequently could be a reason for the formation of the no-IMC-layer Al-Ti interface as observed in previous sections. The effect of the residual oxide layer on the IMC layer growth after prolonged heat treatment will be discussed in Chapter 5.

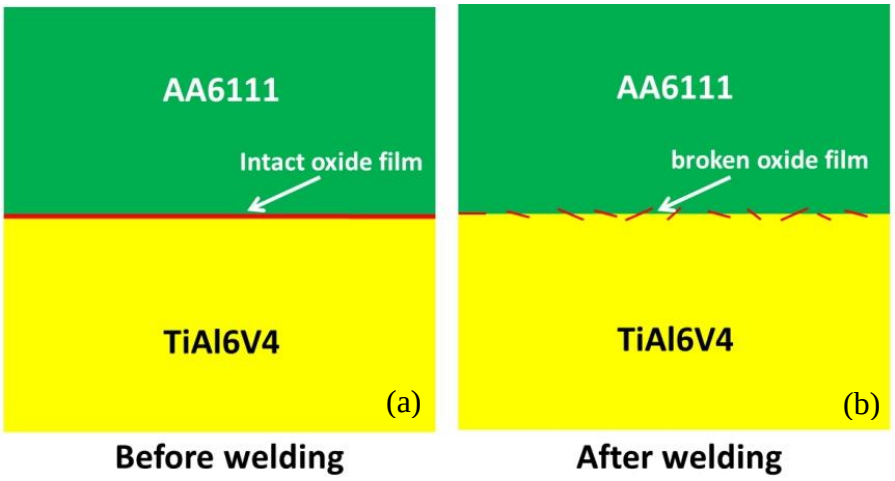

Figure 4.33 The schematic diagram of intact oxide films (long red line) on AA6111 and Ti6Al4V surface before USW (a) and broken oxide film (short red lines) on interface after USW (b).

The residual oxide layer on ultrasonic welded Al-Ti interface has also been experimentally observed by Magin and Balle using TEM-Electron energy loss spectroscopy (EELS), which is a technique capable of measuring light elements [180] and the presence of oxide layer on the interface of various Al-Ti diffusion couples also has been suggested by many previous investigations [81, 124] .

4.4.1.2 Si

Si enrichment on surface of as-received Al alloys is not expected [181]. This suggests that the Si enrichment on the Al/Ti interface (Figure 4.31 and Figure 4.32) was formed during the ultrasonic welding process, with the Si originally from the AA6111 alloy base metal. The reason for Si segregation on the Al/Ti interface is likely to be that the affinity between Si atoms and Ti atoms is very strong, stronger than the affinity between Si atoms and Al atoms [103, 182].

From Figure 4.31 and Figure 4.32, it can be seen that the distribution of silicon on the Al/Ti interface was discontinuous (like Mg and O), but notably its distribution is inverse to that of oxygen and magnesium. This could be because the broken

oxide pieces (containing both magnesium oxide and aluminium oxide) on the Al/Ti interface acts as a barrier which prevents direct contact between AA6111 alloy and Ti6Al4V, so that the attraction of Ti to Si atoms in AA6111 was blocked. It should be pointed out that the observed Si distribution is not absolutely inverse to that of oxygen and magnesium because the TEM specimen is not a 2 dimensional thin foil, in the thickness direction of the TEM specimen there could be Si enriched below or above the residual oxide pieces.

Also, as shown in Figure 4.31, no Si segregation was detected on the grain boundaries of AA6111 near the Al/Ti interface. This suggests that the driving force for Si segregation to the Al/Ti interface is much higher than that for Si segregation to AA6111 grain boundaries.

Similar to the present study, more than 20 at.% Si segregation was observed by Fuji et al [23] using TEM-EDS on the Al_3Ti/Ti interface in a post-weld heat-treated Al (containing Si)/Ti friction weld.

Similar to the residual oxide on the interface, the segregated Si on the Al/Ti interface also could act as a barrier between Al and Ti, which can slow down the inter diffusion of Al and Ti. Inter diffusion is the prerequisite for Al-Ti intermetallic nucleation. If the inter diffusion is slow, Al-Ti intermetallic nucleation would be expected to be retarded. Thus, this could be another reason for the observation of the no-IMC-layer Al-Ti interface. The much slower IMC layer growth due to the presence of Si was also observed by by Fuji et al [23].

In common with the AA6111/Ti6Al4V joint, Si segregation and residual oxides including Mg oxides were also detected on the as-welded AA2139/Ti6Al4V joint

interface. The effect of Si on the IMC layer growth in prolonged heat treatment will be discussed in Chapter 6.

4.4.2 Discussion of the driving force for segregation

The driving force for segregation of solute atom A in matrix B to matrix B/ matrix C interface:

According to thermodynamic theory, the greater the absolute value of negative chemical mixing enthalpy (ΔH_{X-Y}^{mix}) between element X and element Y, the more chemical attraction between them. Thus, in the case of present study, for solute atom A in matrix B, if the negative value of chemical mixing enthalpy between A and the other matrix C (ΔH_{A-C}^{mix}) (which shares an interface with matrix B) is smaller than ΔH_{A-B}^{mix}, solute atom A will segregate to the matrix B/ matrix C interface, which leads to lower system free energy, as illustrated in Figure 4.34.

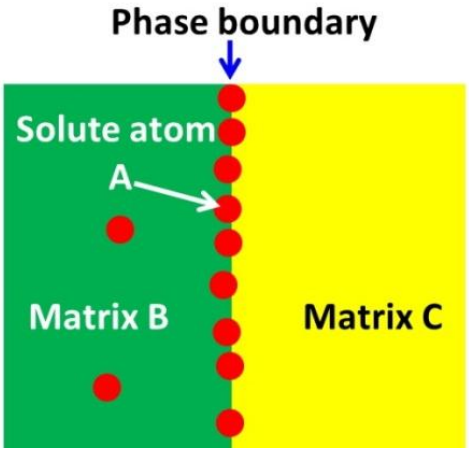

Figure 4.34 Schematic diagram of segregation of solute atom A in matrix B to matrix B/ matrix C interface.

The chemical mixing enthalpies ΔH_{X-Y}^{mix} between the alloying elements (Si, V, Cu, Mg, Fe, Ag) and the matrices (Al,Ti) reported in the literature are listed in Table 4.1.

(1) Si:

It can be seen that in all combinations, ΔH_{Ti-Si}^{mix} has the lowest value (-66 kJ mol^{-1}), much lower than ΔH_{Al-Si}^{mix} (-19 kJ mol^{-1}). Thus, there is a strong driving force for Si to segregate to the Al/Ti interface from AA6111 base metal.

Table 4.1 The chemical mixing enthalpies ΔH_{X-Y}^{mix} between the alloying elements (Si, V, Cu) and the matrices (Al,Ti) [182-184].

System	ΔH_{X-Y}^{mix} $(kJ \cdot mol^{-1})$	System	ΔH_{X-Y}^{mix} $(kJ \cdot mol^{-1})$
Al-Ti	-30	Ti-Al	-30
Al-Mg	-2	Ti-Mg	16
Al-Si	-19	Ti-Si	-66
Al-V	-16	Ti-V	-48
Al-Cu	-1	Ti-Cu	-9
Al-Fe	-11	Ti-Fe	-17
Al-Mn	-19	Ti-Mn	-27
Al-Ag	-4	Ti-Ag	-2 [184]

(2) V, Mg and Ag:

ΔH_{Ti-V}^{mix} is much lower than ΔH_{Al-V}^{mix}, so vanadium in Ti6Al4V is not expected to segregate to the Al/Ti interface, which is in agreement with the experimental observation, as shown in Figure 4.31 and Figure 4.32.

Similarly, there is also no driving force for Mg segregating to Al/Ti interface ($\Delta H_{Ti-Mg}^{mix} > 0 > \Delta H_{Al-Mg}^{mix}$), this further supports the conclusion that the observed Mg on Al/Ti interface was not due to the attraction of Ti but was due to the

spontaneous segregation of Mg to the surface of aluminium [175-178]. A Monte Carlo simulation by Deng et al. [176] showed that surface segregation of Mg in Al-Mg alloys leads to the system free energy drop, as mentioned in Section 4.4.1.1.

Ag is an important alloying element (0.3 wt. %) in AA2139 alloy, but no Ag segregation was observed on the AA2139/Ti6Al4V interface. This is consistent with the reported enthalpies, which show that ΔH_{Al-Ag}^{mix} is lower than ΔH_{Ti-Ag}^{mix}, thus there is no driving force for Ag segregation.

(3) Cu, Fe and Mn:

Judging from the chemical mixing enthalpies ΔH_{X-Y}^{mix}, Cu, Fe and Mn might also be expected to segregate to the Al/Ti interface from thermodynamic consideration alone. However, none of them were observed segregated to the interface, as shown in Figure 4.35. This is probably because the diffusion rates of Cu, Fe and Mn in Al (see Figure 4.36) are relatively slow compared with Si, which has a much smaller atomic size (Table 4.2). Since the welding time is very short, only 1.2 s, during which the temperature is high (~500 °C), only rapidly-diffusing elements can segregate to the Al/Ti interface in such a short time.

4.4.3 Semi-quantitive analysis of Si, Mg and O on the Al/Ti interface

(1) Si:

As shown in Figure 4.37, ~11 at. % of Si was observed segregated on the Al/Ti interface. This concentration is much higher than its content in the AA6111 base metal, 0.85 %. Such high concentration of Si segregation was formed in only 1.4 s (the welding time), this suggested that the Si diffusion in the Al alloy during ultrasonic welding process was very fast. The estimated Si diffusion distance in Al

at 500 °C for 1.4 s is ~4.4 μm ($D_{Si} = 1.5 \times 10^{-9} cm^2 / s$). It was possible that the severe plastic deformation occurring during USW also accelerated the Si diffusion. This measured concentration of Si segregation (~11 at. %) in the present study was lower than the previously reported more than 20 at. % Si segregation [23] in an Al/Ti joint post-weld heat treated at 600 °C for 1 h. This indicates that the Si segregation on the Al/Ti interface may not have reached saturation equilibrium during the welding process.

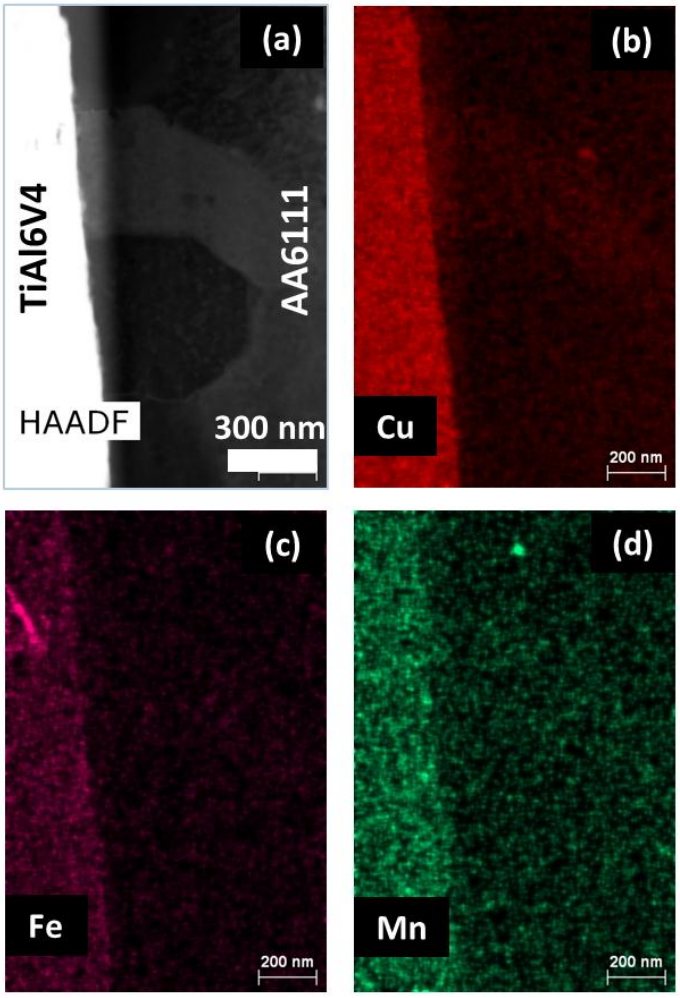

Figure 4.35 STEM-EDS element maps in the AA6111/Ti6Al4V interface region, (a) STEM-HAADF image, (b) Cu map, (c) Fe map, (d) Mn map. (in the same region with Figure 4.31)

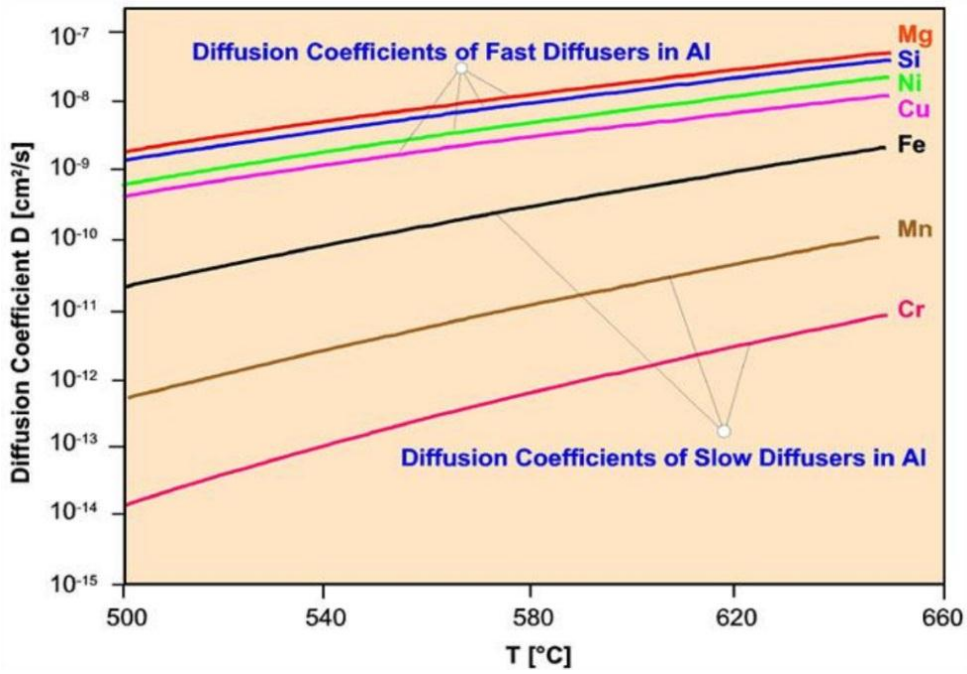

Figure 4.36 Diffusion coefficients of various alloying elements in Al [185]

Table 4.2 Atom radius [186].

Element	Al	Ti	Mg	Si	Cu	Fe	Mn
Radius (pm)	118	176	145	111	145	156	161

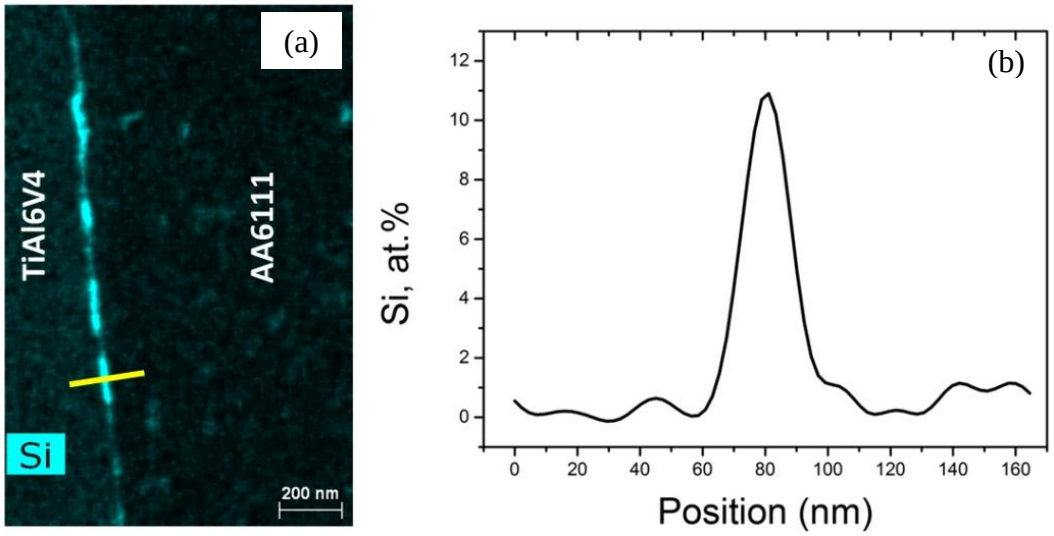

Figure 4.37 STEM-EDS line scan across the Si rich region on the Al/Ti interface, (a) STEM-EDS Si map, (b) the Si concentration profile across the interface. (in the same region with Figure 4.31)

(2) Mg and O:

From the quantified Mg and O profiles (Figure 4.38) across the Al/Ti interface, it can be seen there was ~8.3 at. % Mg on the Al/Ti interface, which is also much more than that in the AA6111 Al base metal (0.75 %). However, there was more than 50 at. % oxygen on the interface, which indicates that in addition to magnesium oxides, there also were aluminium oxides and titanium oxides. It can also be seen that there was more oxygen in the near surface region of titanium than in aluminium side. This is in consistent with the fact that the oxygen solubility in titanium (more than 20 at. % at room temperature) is much higher than that in aluminium (close to 0 %) according to the Ti-O [187] and Al-O [188] binary phase diagrams. Previous studies show that a passive, amorphous, very thin (5-10 nm [189]) oxide film can form on titanium surface, when it is exposed to ambient air at room temperature. From the surface to the inside, the oxide film is composed of three layers [190, 191]: TiO_2 layer in direct contact with the environment, Ti_2O_3 layer in the middle and TiO layer adjacent to metallic titanium. In the present study, the surface of titanium underwent severe friction and relatively high temperature during USW process, and at this time the oxide film could be thickened in the initial unstable stage of USW (before the titanium surface was totally protected from air). Also, an oxidation kinetics study shows that the titanium oxide film grows fastest at the initial stage of heating [192]. This process is accompanied by oxygen absorption into the titanium beneath the oxide film [193].

4.4.4 Discussion of the influence of residual oxide layer and Si segregation on the weld mechanical properties

4.4.4.1 The influence of residual oxide layer

As stated before, the residual discontinuous oxide layer at the Al/Ti weld interface prevented direct contact between Al and Ti and furthermore can deteriorate the final weld mechanical properties. Similarly, residual discontinuous oxides were often also observed in friction stir welds [194-197], which are also solid-state welds, and it was found that fracture occurred along the joint line containing residual oxides after heat treatment [195]. Crack initiation tends to occur along the residual oxides as well [197].

4.4.4.2 The influence of Si segregation

To evaluate the influence of segregated Si on the strength of Al/Ti joints, a simple model was built based on a theory of Seah [72].

In Seah's theory [72], it is assumed that the boundary cohesion is in direct proportion to the "broken-bond" energy of the element at the boundary which is determined by the molar sublimation enthalpy per unit area, H^{sub}/a^2. The change in boundary cohesion energy ΔE_c caused by a segregant A is then approximately given by the difference of its sublimation enthalpy with that of the matrix B, and is proportional to its concentration on the grain boundary X_b, in the ideal solution approximation.

$$\Delta E_c = \frac{Z_g}{N \cdot Z} \cdot \left[\frac{H_A^{sub}}{a_A^2} - \frac{H_B^{sub}}{a_B^2} \right] \cdot X_b \qquad \text{(Equation 4.1)}$$

Where, N is the Avogadro's number, Z_g and Z are the coordination number in the boundary and in the pure element, respectively. a_A and a_B are the atomic diameters of solute A and matrix B.

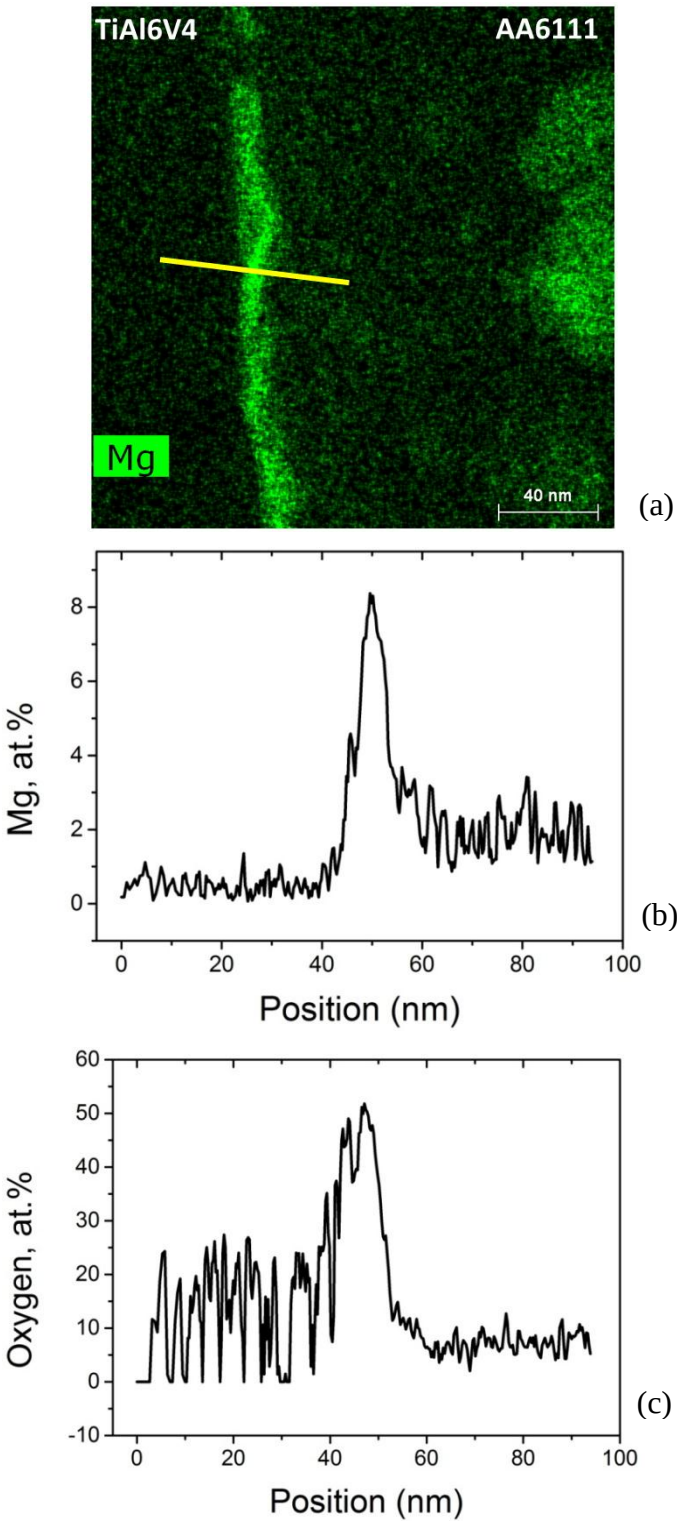

Figure 4.38 STEM-EDS line scan across the Mg rich region on the Al/Ti interface, (a) STEM-EDS Mg map, (b) the Mg concentration profile across the interface, (c) the O concentration profile across the interface. (in the same region with Figure 4.32)

Here, this equation is slightly modified to predict the influence of segregated elements on the cohesion energy of phase boundary where there are two different

matrices, matrix B and matrix C. The schematic diagram showing the matrix B/ matrix C interface with solution atoms is shown in Figure 4.34.

It is assumed that the "broken-bond" energy of matrix B - matrix C bond on the boundary is determined by the average molar sublimation enthalpy per unit area of element B and element C, $\frac{1}{2}\cdot\left(\frac{H_B^{sub}}{a_B^2}+\frac{H_C^{sub}}{a_C^2}\right)$.

Then the change in phase boundary (between matrix B and matrix C) cohesion energy $\Delta E_{c[B-C]}$ by a segregant A is approximately given by:

$$\Delta E_{c[B-C]}=\frac{Z_g}{N\cdot Z}\cdot\left[\frac{H_A^{sub}}{a_A^2}-\frac{1}{2}\cdot\left(\frac{H_B^{sub}}{a_B^2}+\frac{H_C^{sub}}{a_C^2}\right)\right]\cdot X_b \qquad \text{(Equation 4.2)}$$

Where, a_A, a_B and a_C are the atomic diameters of solute A, matrix B and matrix C respectively.

A plot of the sublimation enthalpy per unit area, H_I^{sub} vs. lattice parameter of the corresponding solute, a_I is show in Figure 4.39. According to this graph, the elements having a value of H_I^{sub} higher than the average H_I^{sub} of matrix B and matrix C (for example Al and Ti as suggested by the dashed red horizontal line) increase the cohesion energy of the phase boundary (between matrix B and matrix C). Those with a lower value of H_I^{sub} decrease the cohesion energy of the phase boundary. According to this theory, segregated Si atoms on Al/Ti interface could increase the cohesion energy and adding Mg atoms on the interface could reduce the cohesion energy. Hence, it is possible to predict that Ti/Al-Si alloy dissimilar

joint could have better mechanical properties than Ti/Al-Mg alloy dissimilar joint when other conditions are identical.

It is worth noting that numerous experimental studies showed that Equation 4.1 is valid. For example, carbon can enhance the grain boundary cohesion of iron, molybdenum and tungsten, however the effect of oxygen is opposite [198], segregations of silicon and thorium reduced the iridium grain boundary cohesion [199], lithium reduced the cohesion of aluminium [200] but boron segregation strengthened grain boundaries of Ni_3Al [201] and copper [202].

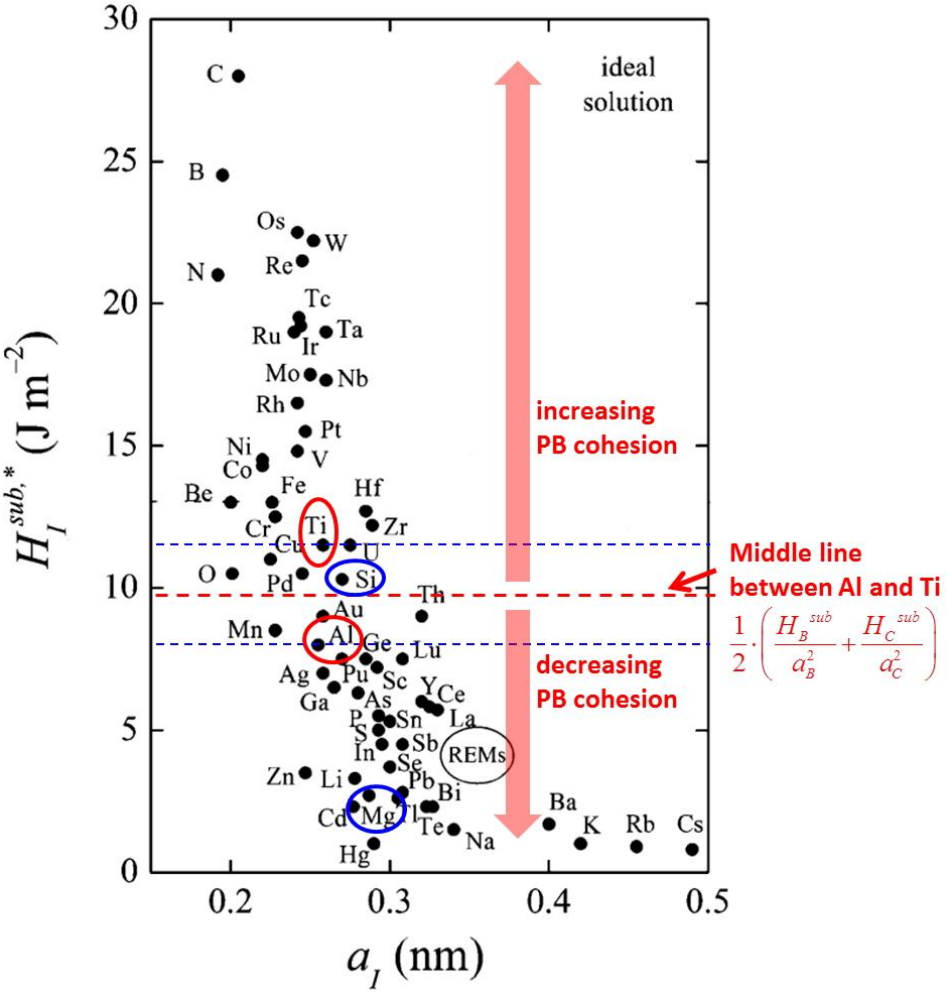

Figure 4.39 The plot of the sublimation enthalpy per unit area, H_I^{sub} vs. lattice parameter of the corresponding solute, a_I. [203] (PB: phase boundary, i.e. Al/Ti boundary.)

Moreover, by this theory, it is predicted that increasing the content of Si on the Al/Ti weld interface can enhance the Al/Ti weld strength. This suggests that for potential industrial applications, adding Si to either the surface of Al or the surface Ti could increase the Al/Ti weld strength.

4.5 Summary

4.5.1 Summary of USW of AA6111-Ti6Al4V

1. 0.93 mm thick AA6111 aluminum alloy sheet and 1 mm thick Ti6Al4V sheet can be successfully welded by high power ultrasonic spot welding.

2. No visible IMC layer was detected in as-welded AA6111/Ti6Al4V USW welds by scanning and transmission electron microscopy.

3. There are two different fracture modes in the ultrasonic spot welds. They are respectively the 'interfacial failure' mode and the 'pull-out' mode.

4. The peak failure load of Al-Ti welds in a lap shear test reached 3.5 kN, the same level as similar Al-Al welds. The excellent strength of Al-Ti joints compared to that of other dissimilar combinations, e.g. Al-Mg and Al-Fe is attributed to the lack of formation of brittle intermetallic in the Al-Ti case.

5. After natural ageing the fracture mode of Al-Ti USW welds transferred from 'pull-out' mode to 'interfacial failure' for all welding times due to the strength recovery of AA6111 aluminum alloy. This change in fracture mode was accompanied by a decrease in failure energy.

4.5.2 Summary of the influence of welding tip geometry

1. Generally, the results suggest that a welding tip with smooth edges and a larger area is beneficial for joint mechanical properties.

2. The footprint of rectangular tip is deeper than that of round tip when welding parameters are the same.

3. The fracture path of as-welded rectangular-tip welds goes through the thinned edge of welded region; the fracture path of as-welded round-tip welds goes through unwelded aluminium base metal which leads to higher fracture energy.

4. When other things are equal, the lap shear strength and fracture energy of round tip welds are higher than those of rectangular tip welds.

4.5.3 Summary of USW of AA2139-Ti6Al4V

1. 1 mm thick AA2139 aluminum alloy sheet and 1 mm thick Ti6Al4V sheet can be successfully welded by high power ultrasonic spot welding.

2. No obvious IMC layer was detected in AA2139/Ti6Al4V USW joints by scanning and transmission electron microscopy.

3. The peak failure load of AA2139-Ti6Al4V welds in a lap shear test reached 5.6 kN.

4. All the AA2139-Ti6Al4V welds show an ‘interfacial failure’ mode and have a low fracture energy. The 2139 aluminium alloy is sufficiently strong that it does not extensively plastically deform before the critical stress for interfacial failure is reached. This is in contrast to dissimilar welding of AA6111-Ti6Al4V welds, where it has been previously demonstrated that (for certain welding conditions) the

softer 6111 aluminium alloy produces extensive plastic deformation in the aluminium side and a ductile nugget pull out failure mode.

5. The peak welding temperature reached was 540 ℃ (for the 4.0 s weld), but the time taken to reach this peak temperature was around 2 s, which is longer than that observed for the AA6111-Ti6Al4V material combination.

4.5.4 Summary of segregation of alloying elements

1. Enrichment of Mg, O and Si were found on USWed AA6111/Ti6Al4V and AA2139/Ti6Al4V interfaces.

2. The observed Mg and O "enrichment" on the Al/Ti interface probably had existed on the surface of AA6111 before ultrasonic welding.

3. The segregated Si distribution varied inversely with that of oxygen and magnesium.

4. The residual oxides and the segregated Si on the Al/Ti interface could act as a barrier for Al_3Ti nucleation and growth.

5. The strong chemical attraction (chemical bond) between Ti-Si, i.e. the very great negative chemical mixing enthalpy between Si and Ti ΔH_{Ti-Si}^{mix} (-66 kJ mol^{-1}) may be the driving force for Si segregation to Al/Ti interface.

6. The residual discontinuous oxides on the Al/Ti weld interface can deteriorate the weld mechanical properties, however the segregated Si atoms on Al/Ti interface are predicted to increase weld strength.

Chapter 5

Static Growth Kinetics of IMC layer in CP-Al/CP-Ti joints

5. Static Growth Kinetics of IMC layer in CP-Al/CP-Ti joints

In Chapter 4 it was shown that there is no visible IMC layer in as-welded USW Al-Ti joints, which is quite different from the fast IMC layer growth in Al-Mg and Al-Fe welds. To understand the very slow IMC layer growth in the Al-Ti weld, it is necessary to investigate the static growth kinetics of IMC layer by prolonged post-weld heat treatment.

In this chapter, the growth rate of IMC in CP-Al/CP-Ti weld was studied at different annealing temperatures to understand the influence of grain size evolution during annealing and the influence of oxide film (on the base metals surface) on IMC layer growth. It should be pointed out that there is no visible IMC layer in the CP-Al/CP-Ti joints before static annealing. Also, understanding the IMC layer growth kinetics in the pure Al and pure Ti diffusion couple is the basis for further understanding the IMC layer growth kinetics in Al/Ti diffusion couples containing various alloying elements, which will be addressed in Chapter 6.

5.1 Phase identification in the IMC layer in annealed CP-Al/CP-Ti joint

As discussed in Section 2.5.1, though Al_3Ti phase ($D0_{22}$ structure) is the typical reaction product between Al and Ti at low annealing temperatures (in solid-state condition), the presence of other phases are possible. The presence of other phases could affect the interdiffusion through the IMC layer. Thus, prior to study the growth kinetics, the phase in the IMC layer needs to be identified.

The example shown in Figure 5.1 demonstrates that the IMC phase in annealed CP-Al/CP-Ti joints was identified as Al_3Ti ($D0_{22}$ structure), and no other phase was observed in the IMC layer, which is consistent with most previous investigations [76-84].

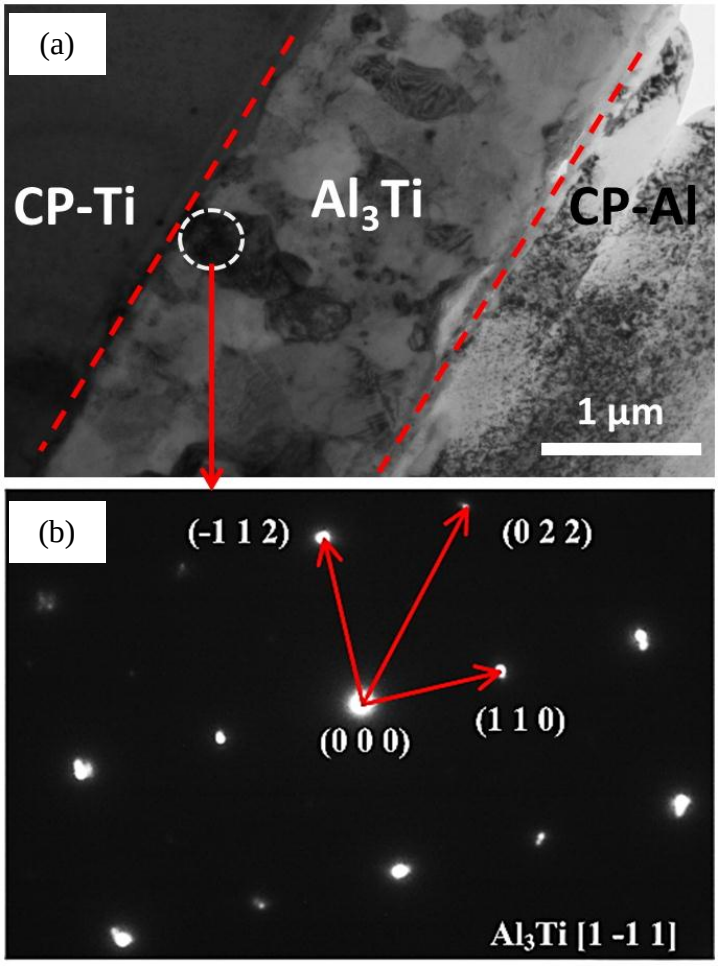

Figure 5.1 (a) Bright field TEM image of the IMC layer in CP-Al/CP-Ti joint annealed at 500 ℃ for 72 h, (b) Selected area diffraction pattern of the white circle region in the IMC layer.

5.2 Comparison of IMC layer growth at 600 °C and 630 °C

5.2.1 The growth kinetics

The average thickness of the Al_3Ti layer between CP-Al and CP-Ti at 600 °C and 630 °C is shown as a function of annealing time in Figure 5.2. Interestingly, this

shows that after ~12 h annealing the thickness of Al_3Ti layer grown at 600 °C exceeded that grown at 630 °C. The faster Al_3Ti layer growth at lower annealing temperature is surprising, and the likely explanation for this observation is discussed in detail later. The same phenomenon was also found in the growth kinetic data reported by Mirjalili et al. [76], although they did not discuss the possible origins of this effect.

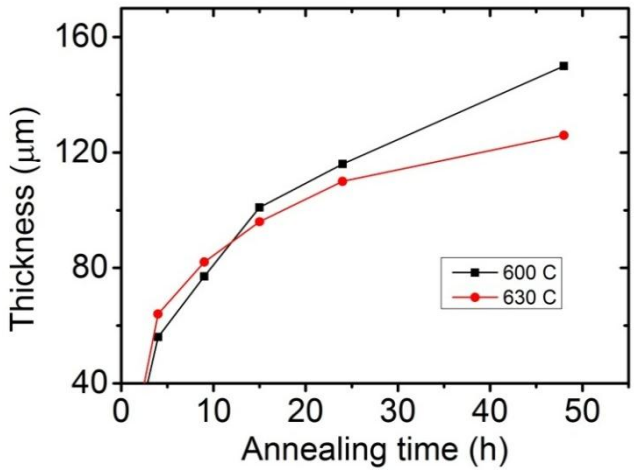

Figure 5.2 Growth kinetics of Al3Ti layer in CP-Al/CP-Ti joint at 600 °C (black line) and 630 °C (red line).

5.2.2 Al_3Ti grain size evolution

The microstructures of Al_3Ti layer produced after different annealing conditions were analysed to understand the observed kinetic behaviour. The microstructures of Al_3Ti layer annealed at 600 °C and 630 °C for 4 h at the same magnification are shown in Figure 5.3.

The average Al_3Ti grain size in the reaction layer annealed at 630 °C (~3.6 μm, in the coarsest grain zone) is markedly larger than that annealed at 600 °C (~1.5 μm, in the most-coarse-grain zone) due to the higher annealing temperature, which promotes grain growth.

This difference becomes extremely large when annealing time is increased to 48 h, i.e. ~12.9 μm in the most-coarse-grain zone annealed at 630 °C compared with ~1.5 μm at 600 °C and as shown in Figure 5.4.

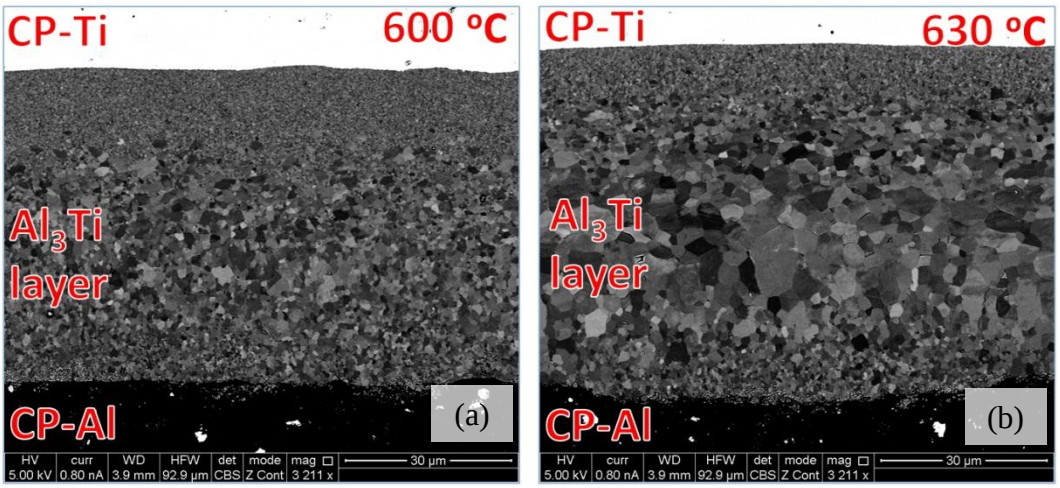

Figure 5.3 Comparison of Al_3Ti grain size in IMC layers annealed at 600 °C (a) and 630 °C (b) for 4 h. (at the same magnification)

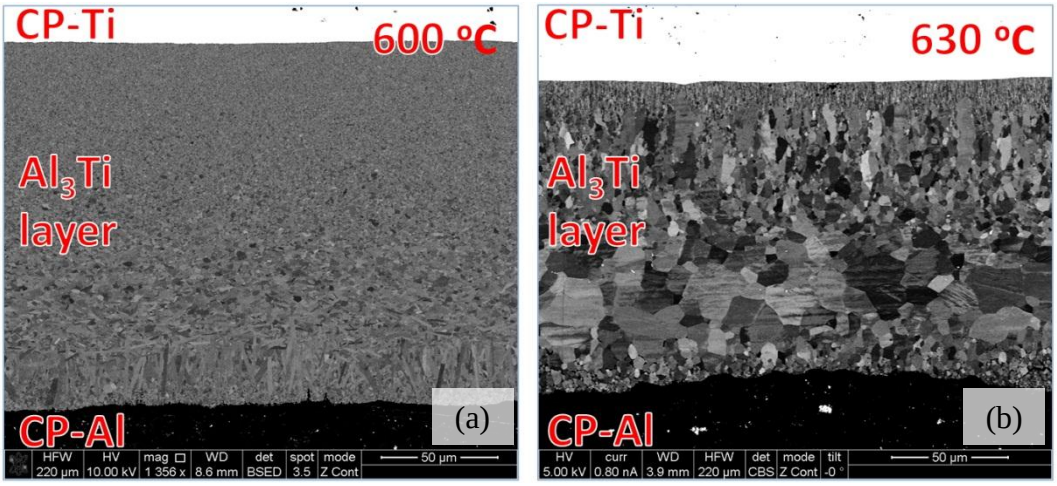

Figure 5.4 Comparison of Al_3Ti grain size in IMC layers annealed at 600 °C (a) and 630 °C (b) for 48 h. (at the same magnification)

It is worth noting that the Al_3Ti grain size annealed at 600 °C almost remains unchanged, however the Al_3Ti grains annealed at 630 °C grew rapidly with increasing annealing time.

5.2.3 Discussion of microstructural effect on diffusion

It is generally believed that Al_3Ti layer growth is controlled by diffusion [76, 119, 147]. The diffusion of Al and Ti atoms in the Al_3Ti layer is jointly determined by lattice diffusion and grain boundary diffusion. Diffusion in grain boundaries is much faster than that in grain lattice. The higher the grain boundary fraction, the faster the effective diffusion. The grain boundary fraction is determined by the grain size. Thus, the slower Al_3Ti layer growth at higher temperature mentioned above is probably due to the reduction of grain boundary fraction. A quantitative understanding of the microstructural effect on the diffusion in Al_3Ti layer and then on the growth of Al_3Ti is discussed in detail below.

The role of grain boundary diffusion:

As mentioned in section 2.6.2, the effective diffusion coefficient in a polycrystalline solid can be described by the following equations:

$$D_{eff} = g \cdot D_{gb} + (1-g) \cdot D_L \qquad \text{(Equation 5.1)}$$

$$D_{gb} = D_{gb0} \cdot \exp(-\frac{\Delta Q_{gb}}{RT})$$

$$D_L = D_{L0} \cdot \exp(-\frac{\Delta Q_L}{RT})$$

Where g is the fraction volume of grain boundaries (GBs), and roughly equals $\frac{3\delta}{d}$ for cubic grains, δ is the width of grain boundary, d is the grain size, D_{gb} and D_L are grain boundary diffusion coefficient and lattice diffusion coefficient respectively. δ is estimated to be 0.5 nm in this paper, which is of the same order

with experimentally measured grain boundary width in metals [128]. R is the gas constant and T is absolute temperature.

It is reasonable to consider that the effective diffusion coefficient D_{eff} in the whole Al_3Ti layer (which has strongly varying grain size along the thickness direction) is limited by diffusion through the coarse grain zone (CGZ) due to bottleneck effect; the effective diffusivity through this zone will be lowest since the contribution from fast grain boundary diffusion will be least. Therefore, the D_{eff} of the CGZ was considered as the effective diffusion coefficient of the whole layer. D_{L0} ($3.4\times10^{-7}\ m^2/s$) and ΔQ_L (296.2 kJ/mol) used in the present study are from [147] and [76] respectively. It should be pointed out that the value of D_{L0} and ΔQ_L used in this study were estimated from literature data, where the Al_3Ti grain is very large and thus D_{L0} and ΔQ_L can be roughly treated the same as the D_0 and ΔQ reported in literature (when Al_3Ti grain is very large, diffusion is mainly dominated by lattice diffusion). For grain boundary diffusion, due to the lack of direct experimental measurement, D_{gb0} and ΔQ_{gb} are estimated through a commonly accepted and reasonable approximate treatment, i.e. D_{gb0} is roughly given a value which equals to D_{L0} and ΔQ_{gb} is considered as half of ΔQ_L [204].

Effect of grain size on diffusion:

The plots of D_{eff} as a function of Al_3Ti grain size at 600 °C and 630 °C respectively are shown in Figure 5.5. These calculated effective diffusion coefficients are of the same order of magnitude as previous studies [147]. Since the average Al_3Ti grain size in the CGZ of the reaction layer annealed at 600 °C is

approximately constant at ~1.5 μm with increasing annealing time (Figure 5.3 and Figure 5.4), to simplify the calculation, the effective diffusion coefficient of the reaction layer annealed at 600 °C was treated as a constant as labelled by the left red circle and the horizontal dotted line shown in Figure 5.5. Then, using Equation (6.1), it is predicted that when the Al_3Ti grain size in the IMC layer annealed at 630 °C grows and exceeds 2.65 um, the D_{eff} of the whole reaction layer at 630 °C becomes lower than that of the reaction layer at 600 °C (where Al_3Ti grain size is constant at ~1.5 μm with increasing annealing time), which means that once the Al_3Ti grain size exceeds 2.65 um, the reaction layer at 630 °C would be expected to grow more slowly than in the layer annealed at 600 °C.

This analysis is consistent with the experimental observations and explains why for longer annealing times the layer grown at 600 °C, which has a fine grain size, becomes thicker than the layer grown at 630 °C, contrary to what would usually be the expected effect of temperature.

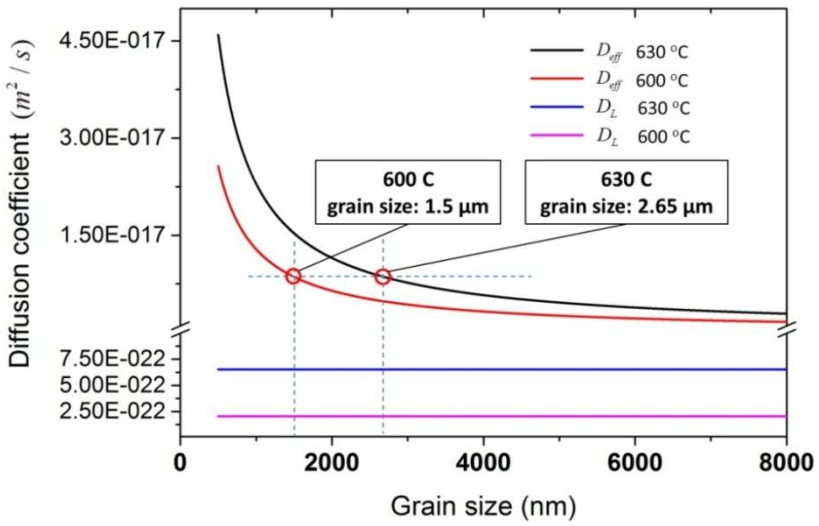

Figure 5.5 Plots of D_{eff} as a function of grain size at 600 °C (red line) and 630 °C (black line), and plots of D_L at 600 °C (purple line) and 630 °C (blue line).

Though in most cases the intermetallic compound layer (IMC) growth between

dissimilar metals is faster at higher annealing temperatures [77, 126], as demonstrated above, if the grain size difference is big enough, the IMC layer growth at higher temperatures may be slower due to grain size effects.

In addition, Figure 5.5 also shows the plots of the contribution of lattice diffusion (D_L) at 600 °C and 630 °C respectively. It can be seen that compared with the effective diffusion coefficient, the contribution from lattice diffusion is very small at both 600 °C and 630 °C due to its high activation energy. This is further evidence that that grain boundary diffusion plays a crucial role in the Al_3Ti layer growth.

5.3 Comparison of IMC layer growth at 550 °C and 600 °C

5.3.1 The growth kinetics

The growth kinetics of the Al_3Ti layer between CP-Al and CP-Ti at 550 °C and 600 °C are shown in Figure 5.6. It can be seen that the growth behaviour shows the usual relationship with temperature, with a thicker layer formed at higher temperature, and not the abnormal behaviour observed comparing the Al_3Ti layer growth between CP-Al and CP-Ti at 600 and 630 °C (Section 5.2.1).

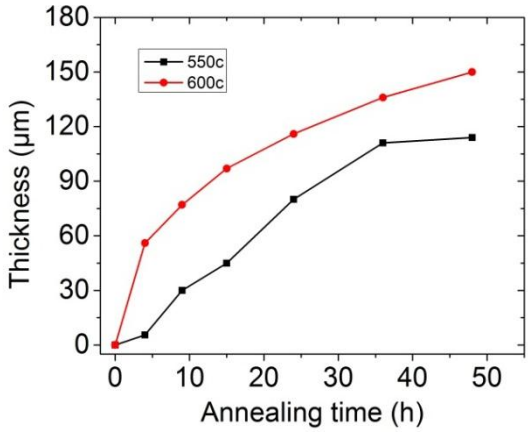

Figure 5.6 Growth kinetics of Al3Ti layer in CP-Al/CP-Ti joint at 550 °C (black line) and 600 °C (red line).

5.3.2 Al_3Ti grain size

The grain sizes in Al_3Ti layers produced at 550 °C and 600 °C were examined by SEM. An example of grain size comparison between the IMC layer grown at 550 °C and 600 °C after 24 h annealing was shown in Figure 5.7. It can be seen that though the Al_3Ti grain size in the CGZ (grown at 600 °C) was larger than that grown at 550 °C, the grain size difference here is much less obvious than that between 600 °C and 630 °C, see Figure 5.3 and Figure 5.4.

The relatively similar Al_3Ti grain size (in CGZ zone) at 550 °C and 600 °C and the very different Al_3Ti grain size at 600 °C and 630 °C indicate that the Al_3Ti grain growth was slow at annealing temperatures lower than 600 °C and was activated for fast growing when the annealing temperature increased to 630 °C. The much faster Al_3Ti grain coarsening at higher temperatures was also observed by Mirjalili et al. [76].

Due to the similar Al_3Ti grain size at 550 °C and 600 °C, the difference in effective diffusion D_{eff} is dominated by the difference in annealing temperature as espected. Hence, the IMC layer grew faster at 600 °C than at 550 °C.

5.4 IMC layer growth at 500 °C

5.4.1 The growth kinetics

The growth kinetics of Al_3Ti layer between CP-Al and CP-Ti at 500 °C is shown in Figure 5.8. It can be seen that compared with the growth rate of Al_3Ti layer at 550 °C, 600 °C and 630 °C, the growth rate at 500 °C is extremely slow, especially in the initial annealing stage.

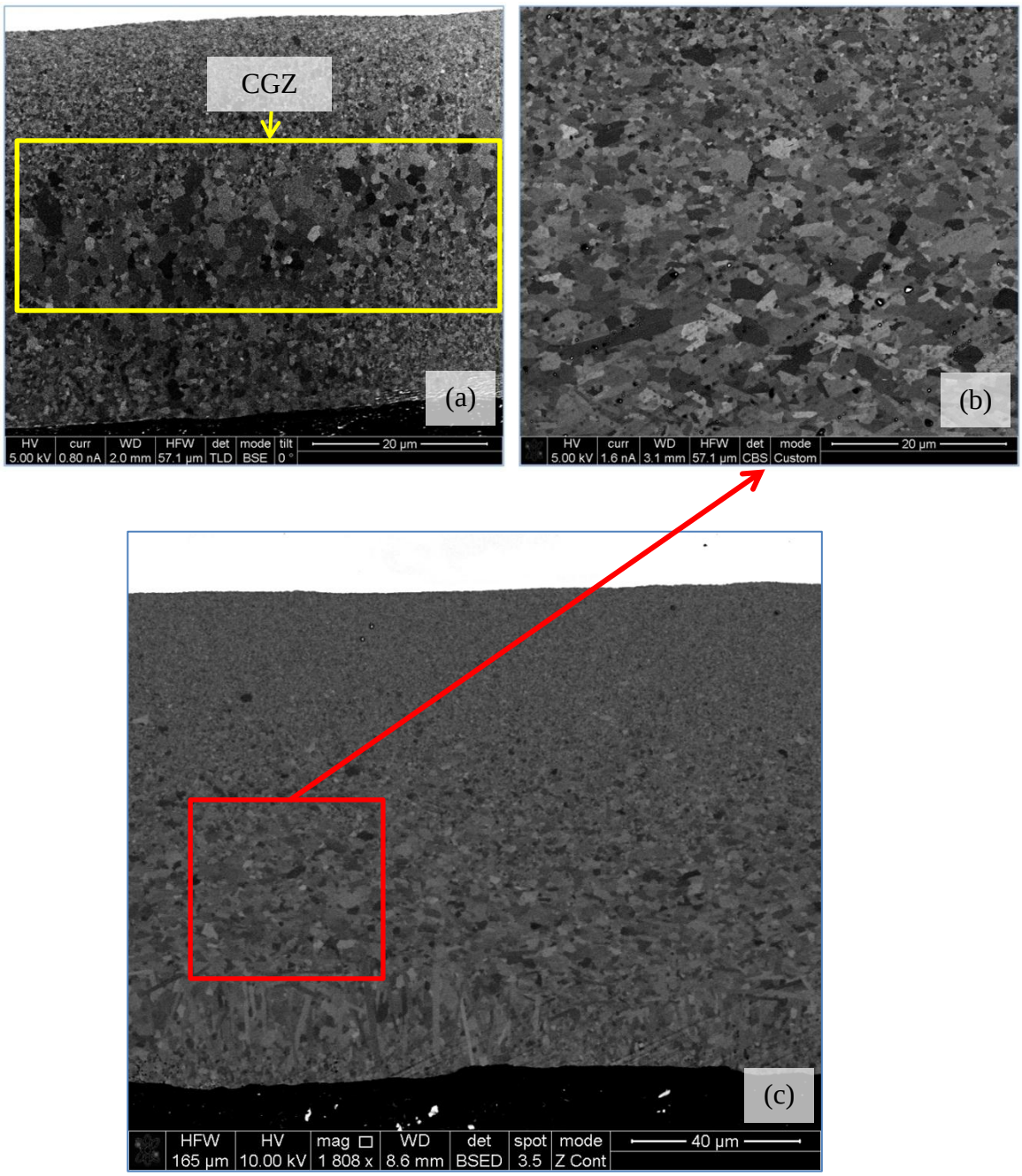

Figure 5.7 Comparison of Al_3Ti grain size in the CGZ zone of different IMC layers annealed at 550 °C (a) and 600 °C (b) for 24 h ((a) and (b) at the same magnification), (c) Al_3Ti layer annealed at 600 °C for 24 h (lower magnification to show the whole layer)
Note: The red rectangular in (c) indicates the rough position of the region where the image (b) was acquired not the exact position.

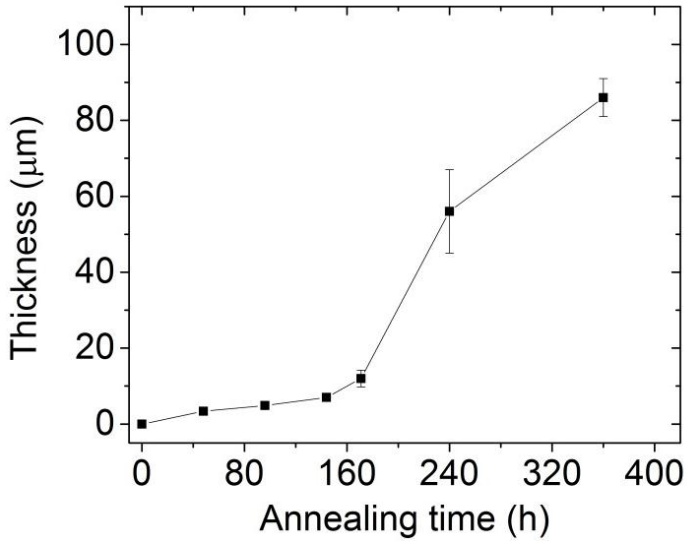

Figure 5.8 Growth kinetics of Al_3Ti layer in CP-Al/CP-Ti joint at 500 °C.

5.4.2 Discussion of the very slow growth in the initial annealing stage

This kind of very slow growth in the initial annealing stage (or the incubation stage) was also observed by some other investigators [81, 83, 132], especially at low annealing temperature. It is generally believed that the very slow growth in the initial annealing stage is caused by the oxide film on base metals, which acts as a diffusion barrier between Al and Ti. F.J.J van Loo and G.D Rieck [81] suggested that it is very likely caused by the oxide film on titanium but not the oxide film on aluminium, since they did not observe the incubation stage in Al-Ni diffusion couples, where the same Al base metal was used. The thin titanium oxide layer on the surface of CP-Ti base metal was experimentally observed by Magin and Balle using high resolution TEM [180]. It is also worth noting that the solubility of oxygen in titanium is much higher (~25 at. % at 500 K) than that in aluminium (virtually 0 % at 500 K). The much higher solubility of oxygen in titanium could promote the formation of oxides in both the surface and the near surface region of titanium. It was suggested that the incubation stage finishes when the titanium

oxide film is broken up by the reaction between aluminium and titanium oxides [132, 205].

The much shorter but observable incubation stage at 550 °C annealing temperature compared with the very long incubation stage at 500 °C (as shown in Figure 5.6 and Figure 5.8 respectively) suggested that the length of the incubation stage becomes shorter with increasing annealing temperature, which is also reported by [132]. This could be because the titanium oxides layer decomposes faster at higher temperature. Moreover, the incubation stage became unobservable when the annealing temperature reaches both 600 °C and 630 °C, probably due to the much faster decomposition of the titanium oxide layer.

5.4.3 The solid-state reaction between Al and titanium oxides

Though there are several different titanium oxides, TiO_2 is the thermodynamically stable one. The following solid-state reaction between Al and TiO_2 has been observed frequently in Al-matrix composite containing TiO_2 particles [206-210]:

$$3TiO_2 + 13Al \rightarrow 2Al_2O_3(\alpha) + 3Al_3Ti$$

The relationship between the standard Gibbs free-energy variation (ΔG_T^0) and temperature (T) of the above reaction is given below:

$$\Delta G_T^0 = -96766.7 + 27.2T$$

According to the above equation, the reaction can occur spontaneously only if the system temperature is below 3557 K [210].

In previous investigations [81, 83, 132], in the Al/Ti diffusion couples the decomposition of titanium oxides was not experimentally observed due to the difficulties in accurately measuring the oxygen (a light element) content change. In the present study, a series of SEM-EDS analysis were performed on the Al_3Ti/CP-Ti interface to examine the oxygen concentration change (i.e. titanium oxide decomposition) with increasing annealing time at 500 °C. It is found that in the samples annealed less than 177 h (i.e. in the incubation stage, in which IMC layer grew very slowly), there was always around 1.5 at. % oxygen detected at the Al_3Ti/CP-Ti interface. In the samples annealed longer than 177 h, no oxygen was detected at the interface, as show in Figure 5.9. Though Al_2O_3 (which contains oxygen) is one of the reaction products; its amount is small and it is distributed in the majority reaction product Al_3Ti. As a result oxygen became undetectable after a long annealing time. It should be pointed out that this analysis is tentative since the EDS analysis of oxygen content is not of high accuracy. The SEM-EDS data here might be used for qualitatively estimating the tendency of oxygen concentration change with increasing annealing time but not for quantitive high-accuracy analysis.

To acquire more reliable evidence to support the argument that titanium oxide layer decomposition is the reason for the break-away growth behaviour, a TEM sample of the Al_3Ti/CP-Ti interface (grown at 500 °C for 96 h, which is in the incubation stage) was prepared by FIB, and further high resolution STEM-EDS analysis was preformed on this interface. The enrichment of oxygen in the titanium side near the interface (in the CP-Al/CP-Ti joint annealed for 96 h) was confirmed, as shown in Figure 5.10. (It is worth noting that as presented in Section 3.6.3, the FEI Titan G2 80-200 S/TEM used for acquiring the present STEM-EDS data is featured by its ability to sensitively detect light elements, eg. oxygen.) However, further

STEM/EDS work on the Al_3Ti/CP-Ti interface grown by longer annealing time (eg. 240 h), i.e. in the fast-growth stage is still needed to be quantitively examined to find out if the oxygen concentration really dropped to support the above mentioned argument.

5.5 Microstructure analysis of Al_3Ti layer

5.5.1 Al_3Ti layer growth direction

As shown in Figure 5.11, the Al_3Ti layer grew into both the Al and Ti side in a CP-Al/CP-Ti joint annealed for 48 h at 600 °C. The thickness of Al_3Ti layer growing into Ti side is one third of that growing into Al side. This is consistent with the stoichiometric ratio of the Al_3Ti compound.

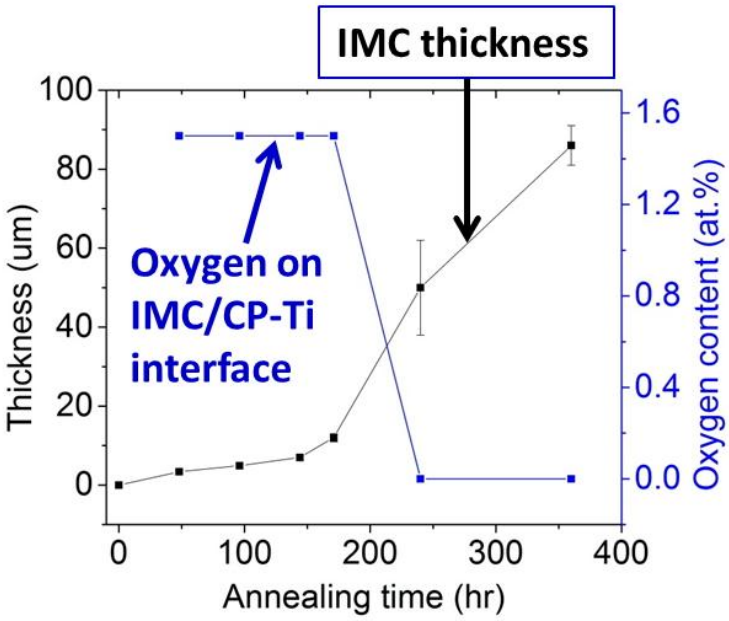

Figure 5.9 Growth kinetics of Al_3Ti layer between at 500 °C and the corresponding oxygen content on the Al_3Ti/CP-Ti interface with increasing annealing time.

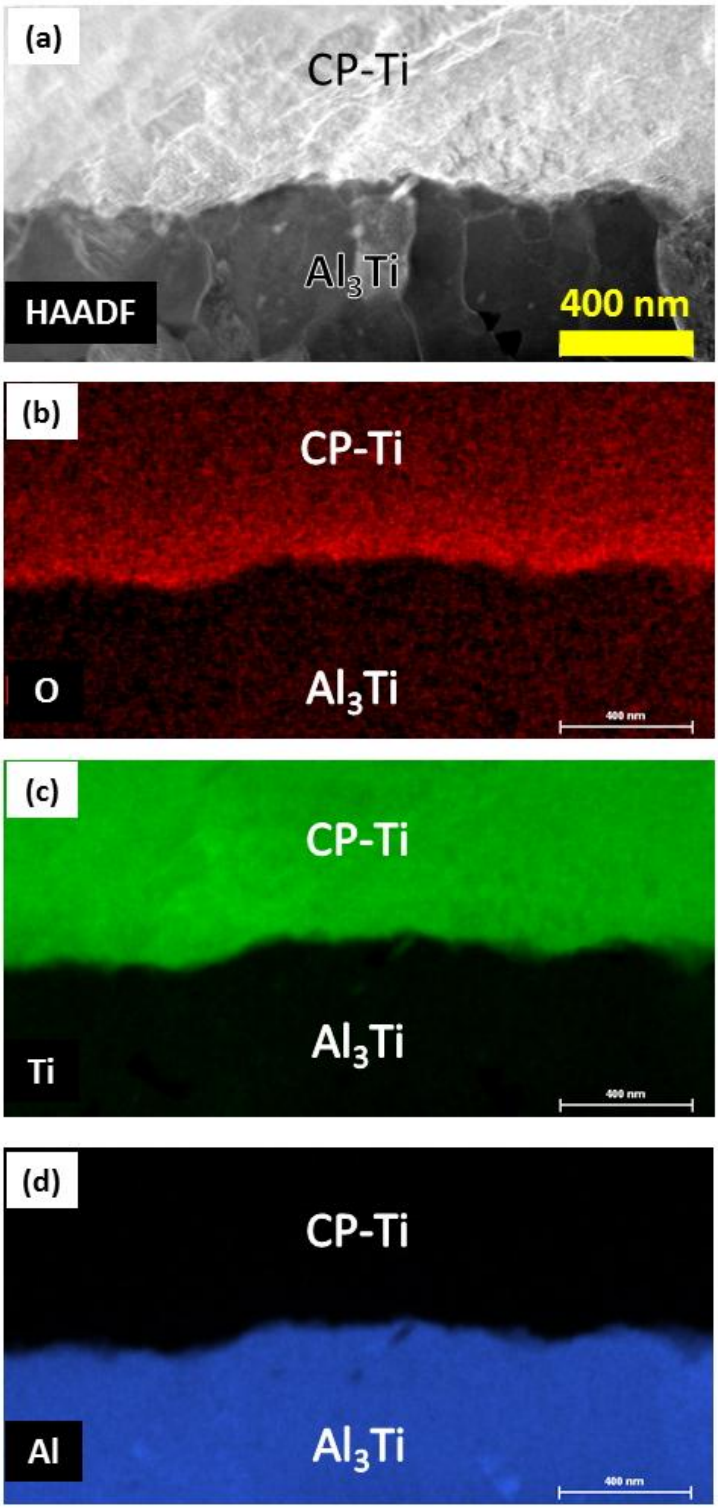

Figure 5.10 The composition maps in the region near the CP-Ti/Al_3Ti interface, measured by STEM-EDS, (a) STEM-HAADF image, (b) O map, (c) Ti map, (d) Al map. (CP-Al/CP-Ti joint, annealed at 500 ℃ for 96 h)

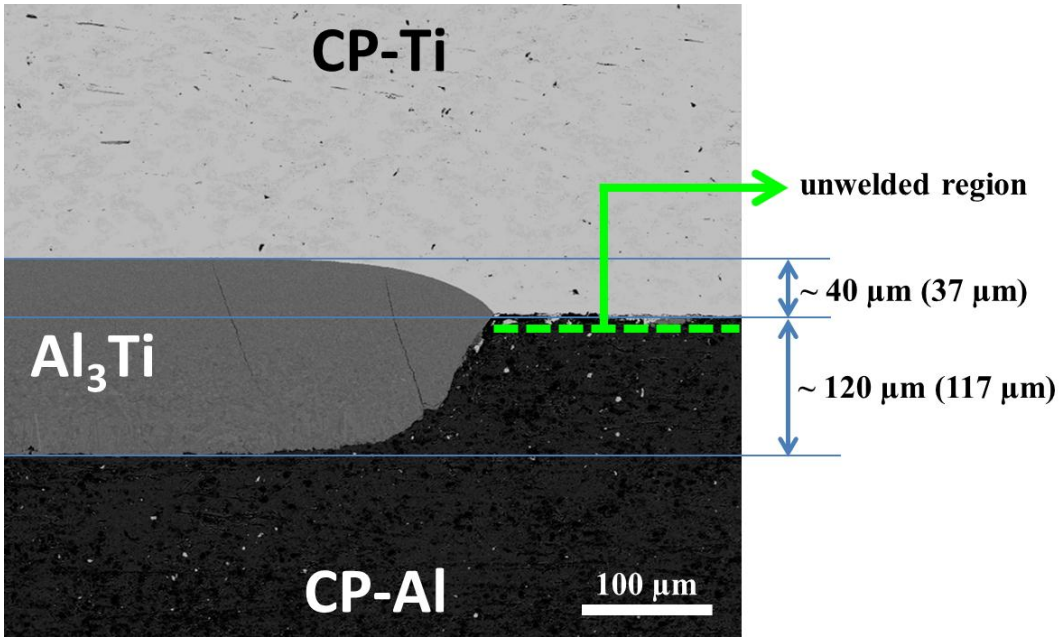

Figure 5.11 Growth of an Al_3Ti layer in a CP-Al/CP-Ti joint annealed for 48 h at 600 °C, the green dotted line indicates the original interface position and corresponds to the unwelded region.

5.5.2 Al_3Ti grain size variation in the thickness direction

As shown in Figure 5.12 and Figure 5.4, the Al_3Ti grain size varied greatly in the thickness direction in the IMC layer grown at relatively high annealing temperatures ($\geqslant$600 °C). The Al_3Ti grain was finest in the region close to the Al_3Ti/CP-Ti interface, and the average grain size in this region (Region A, Figure 5.12 (b)) is around 200-300 nm and the grain morphology is equiaxed. However, in the region close to the Al_3Ti/CP-Al interface, the Al_3Ti grain is around 10 times larger than that in Region A, besides columnar Al_3Ti grains formed in Region B. This suggests that most Al_3Ti grains nucleated on the Al_3Ti/CP-Ti interface and the early-formed Al_3Ti grains grew larger and longer towards the Al side. Similar Al_3Ti grain size variation in the thickness direction of an Al-Ti reaction layer were also observed by Mirjalili et al. [76, 127], Hamajima et al. [211] and Dietrich et al. [212].

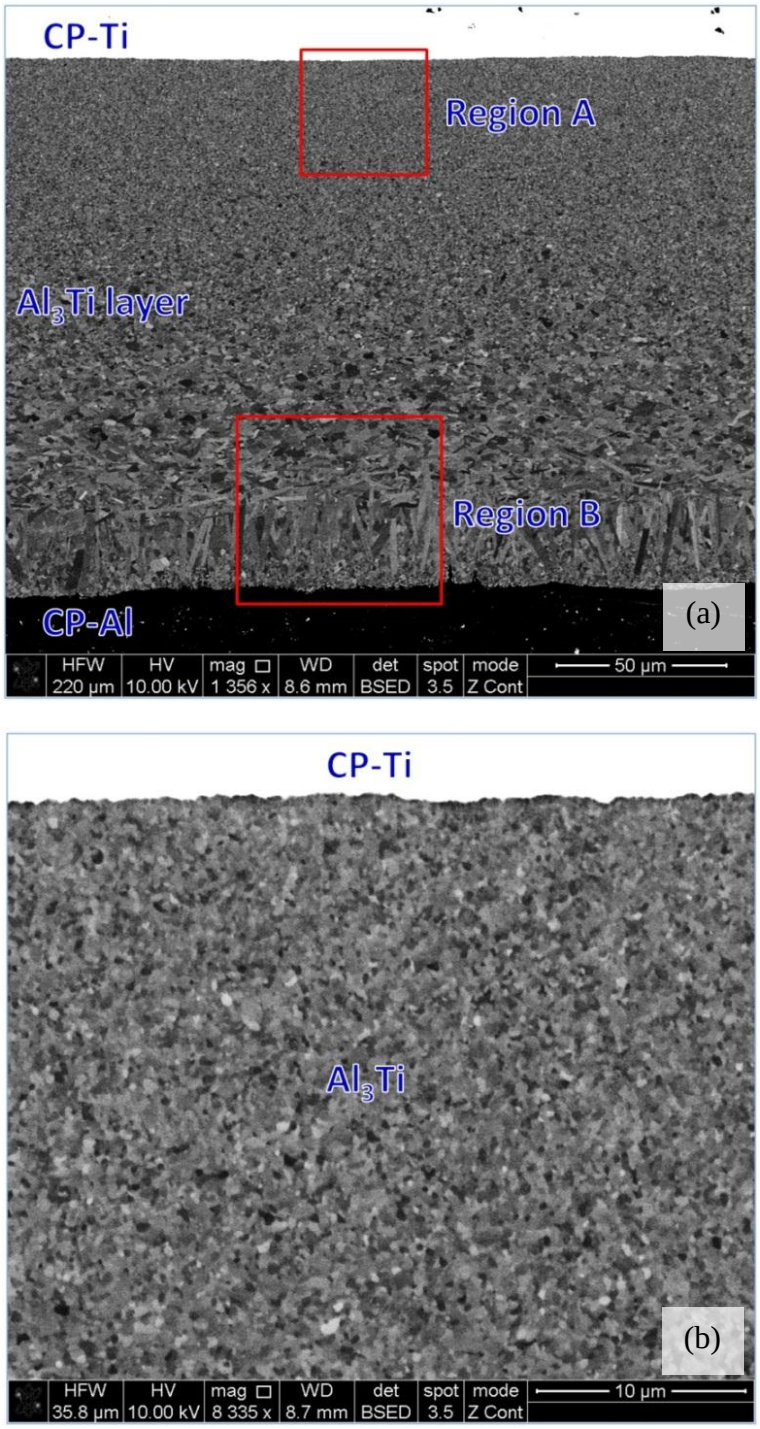

Figure 5.12 (a) and (b), (c) to be continued on next page. (The sub-image size was set large to show the fine microstructural features clearly.)

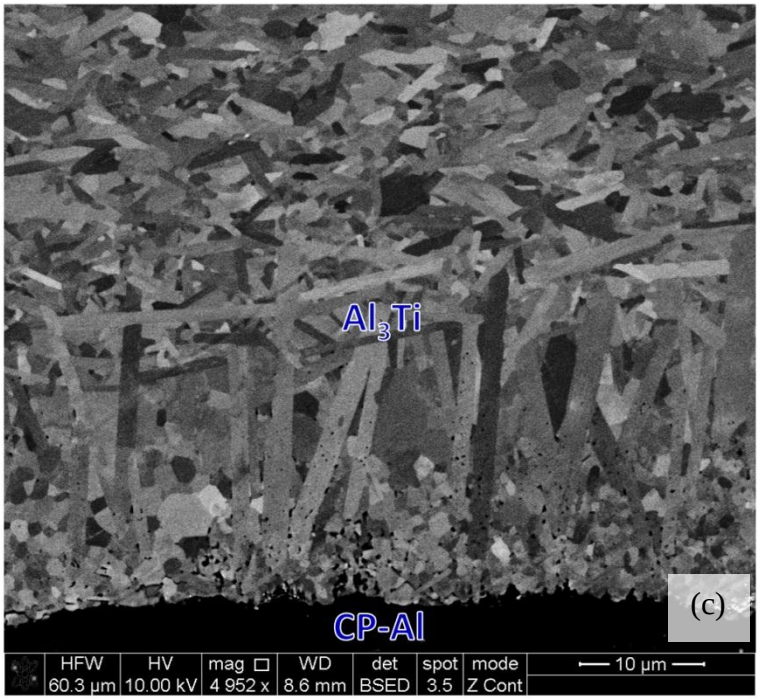

Figure 5.12 Microstructure of the Al_3Ti layer in an CP-Al/CP-Ti joint annealed for 48 h at 600 °C, (a) the whole view, (b) the enlarged image of Region A, (c) the enlarged image of Region B.

5.5.3 The influence of annealing temperature on anisotropic growth of Al_3Ti

As shown in Figure 5.13, the Al_3Ti grain morphology in the near Al_3Ti/CP-Al interface region was changed greatly when the annealing temperature increased from 600 °C to 630 °C. The strong columnar anisotropic growth of Al_3Ti was greatly suppressed due to the rise of temperature. As stated in section 2.6.6, the anisotropic growth of Al_3Ti is driven by the greatly different surface energy of different crystal planes. The greatly different surface energy is caused by the highly ordered structure of Al_3Ti. With the increase of annealing temperature, the atomic thermal vibration is enhanced, consequently the degree of order of intermetallic compounds can be reduced [213]; and thus the greatly different surface energy of different crystal planes may be reduced. Then, the anisotropic growth of Al_3Ti was retarded. This effect of increasing annealing temperature on Al_3Ti grain

morphology was also observed in annealed AA6111/Ti6Al4V joints, as shown in Figure 5.14.

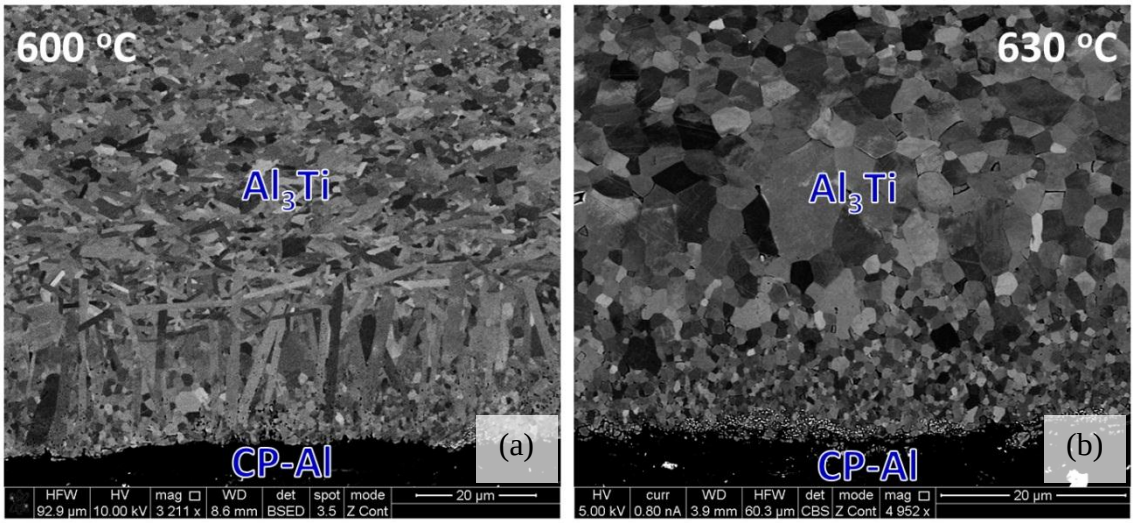

Figure 5.13 Comparison of Al_3Ti grain morphology at different annealing temperature in the near Al_3Ti/CP-Al interface region (in annealed CP-Al/CP-Ti joints), (a) 600 °C, 48 h, (b) 630 °C, 48 h.

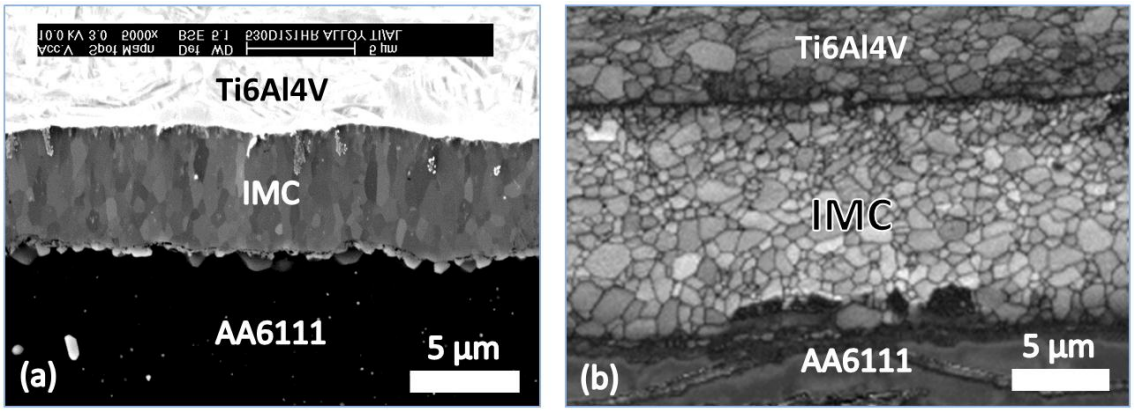

Figure 5.14 Comparison of Al_3Ti grain morphology at different annealing temperature in the annealed AA6111/Ti6Al4V joints, (a) 530 °C, 121 h, BSE image; (b) 600 °C, 103 h, EBSD band contrast image.

5.6 Summary

Al_3Ti phase ($D0_{22}$ structure) was the only intermetallic phase observed in the reaction layer between CP-Al and CP-Ti, which is consistent with most previous

investigations.

By comparing the IMC layer growth and analysing the grain size evolution at 600 °C and 630 °C, it has been shown that an abnormal (reverse) effect of temperature was observed with a thicker layer formed at lower annealing temperature due to the much faster Al_3Ti grain coarsening at 630 °C, the IMC layer growth at 630 °C became slower than that at 600 °C after a certain annealing time. The quantitative influence of grain size on the effective diffusion coefficient was analysed. Calculations showed that the lattice diffusion make little contribution to the effective diffusion coefficient due to the very high activation energy for lattice diffusion. Grain boundary diffusion therefore dominates for all the annealing conditions and grain sizes studied.

The comparison of IMC layer microstructure at 550 °C and 600 °C showed that there is no significant difference between the Al_3Ti grain size in layers grown at 550 °C and 600 °C. As a result, the difference in effective diffusion coefficient D_{eff} is dominated by the difference in annealing temperature, and growth was faster at the higher temperature, which is normal behaviour.

It is also found that Al_3Ti grain growth is very slow at 550 °C and 600 °C, and only became rapid when the annealing temperature increased to 630 °C.

A very long incubation stage of Al_3Ti layer growth was found in the Al/Ti diffusion couple annealed at 500 °C. This very long incubation stage is probably caused by the oxide layer on titanium, which acts as a diffusion barrier. The length of the incubation stage becomes shorter with increasing annealing temperature

probably due to the higher reaction rate between titanium oxides and aluminium at higher temperatures.

The thickness ratio of Al_3Ti layer growing into Ti side and Al side is very close to 1:3, which is in consistence with the stoichiometric ratio of Al_3Ti compound.

Anisotropic growth of Al_3Ti was suppressed when the annealing temperature was increased from 600 °C to 630 °C.

Chapter 6

Static Growth Kinetics of IMC layer in AA2139/CP-Ti joints and CP-Al/Ti6Al4V joints

6. Static Growth Kinetics of IMC layer in AA2139/CP-Ti joints and CP-Al/Ti6Al4V joints

In Chapter 4, it was found that there was no visible IMC layer on the as-welded Al/Ti interface. In Chapter 5, the effect of grain size and oxide layer on the growth of IMC layer was investigated. It was proposed that the oxide layer could be a reason for the very slow IMC layer growth. However, the effect of alloying elements from both aluminium alloy and titanium alloy on IMC layer growth is not clear.

In this chapter, the effect of alloying elements on the grain size and grain morphology, the segregation of alloying elements on the Al_3Ti grain boundaries, and the solubility of alloying elements in Al_3Ti are explored. The reaction between the IMC layer and the particles in aluminium alloy AA2139, the effect of alloy elements on the amount of voids and the trapped Al islands in the reaction layer were studied as well.

6.1 Static Growth Kinetics of IMC layer in AA2139/CP-Ti joints

The IMC layer growth rates in AA2139/CP-Ti joints and in CP-Al/CP-Ti joints were compared in this section. The effect of alloying elements, such as Cu and Si, on IMC layer growth is discussed.

6.1.1 Comparison of IMC layer growth in annealed AA2139/CP-Ti joints and in annealed CP-Al/CP-Ti joints

The IMC layer growth at 500 °C and 550 °C in AA2139/CP-Ti joints was compared with that in CP-Al/CP-Ti joints, as shown in Figure 6.1 and Figure 6.2.

The IMC layer growth at higher temperature has not been studied since AA2139 starts melting at higher annealing temperatures. It can be seen that the IMC layer growth in AA2139/CP-Ti joints is much slower than that in CP-Al/CP-Ti joints. AA2139 is mainly alloyed by Cu and contains 4.8 wt. % Cu. This kind of slower IMC layer growth in Al-Cu/Ti diffusion couples has also been observed by a few previous studies [119, 144, 145, 147]. The slower growth could be due to microstructural reasons, such as Cu segregation in the IMC layer grain boundaries and grain size difference. The purpose of the work reported here was to explain this difference.

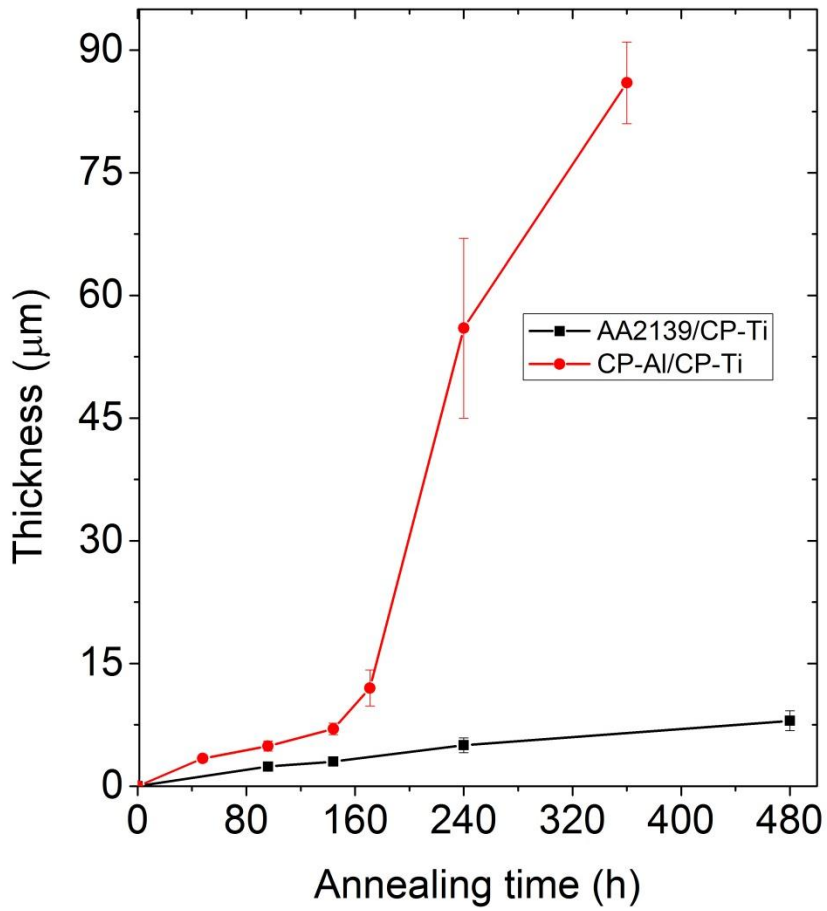

Figure 6.1 Growth kinetics of IMC layer in CP-Al/CP-Ti joint and in AA2139/CP-Ti weld at 500 ℃.

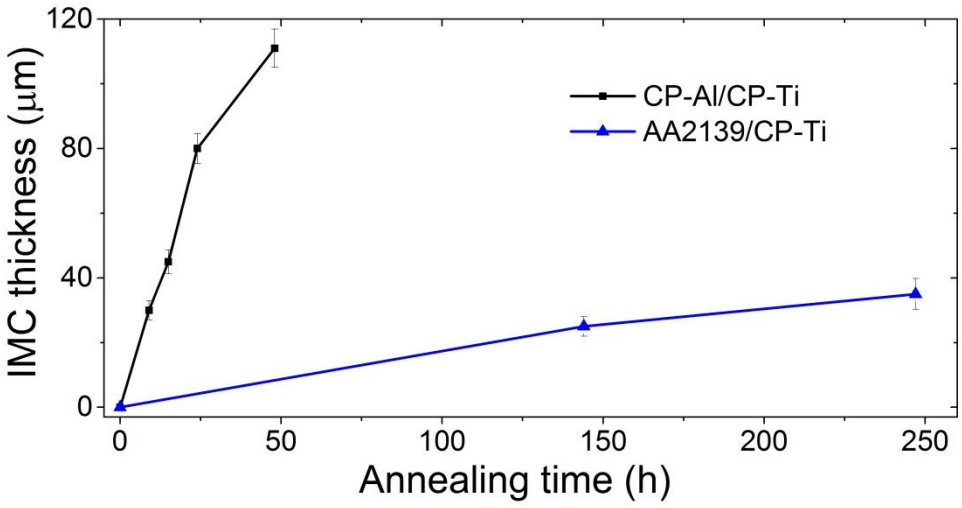

Figure 6.2 Growth kinetics of IMC layer in CP-Al/CP-Ti joint and in AA2139/CP-Ti weld at 550 ℃.

6.1.2 Microstructure of IMC layer

In this section, the microstructure, including phase composition and grain size, of the reaction layers in both CP-Al/CP-Ti joints and AA2139/CP-Ti joints were investigated.

6.1.2.1 Phase identification in the IMC layer

Though in most cases Al_3Ti is the only reaction product on the Al/Ti interface at low annealing temperatures, other phases have also been observed [85, 86] occasionally, especially when other alloying elements are present [25, 102]. Thus, first of all, TEM and EBSD were applied to identify the phases in the IMC layer.

An example of phase identification in the IMC layer in AA2139/CP-Ti joint is shown in Figure 6.3, the phase in the IMC layer was identified as Al_3Ti ($D0_{22}$ structure) and no other intermetallic phase was observed in the IMC layer, which is consistent with most previous investigations [76-84]. This indicates that the

reaction product type in annealed Al/Ti weld in this study has not been affected by the alloying elements from the aluminium alloy.

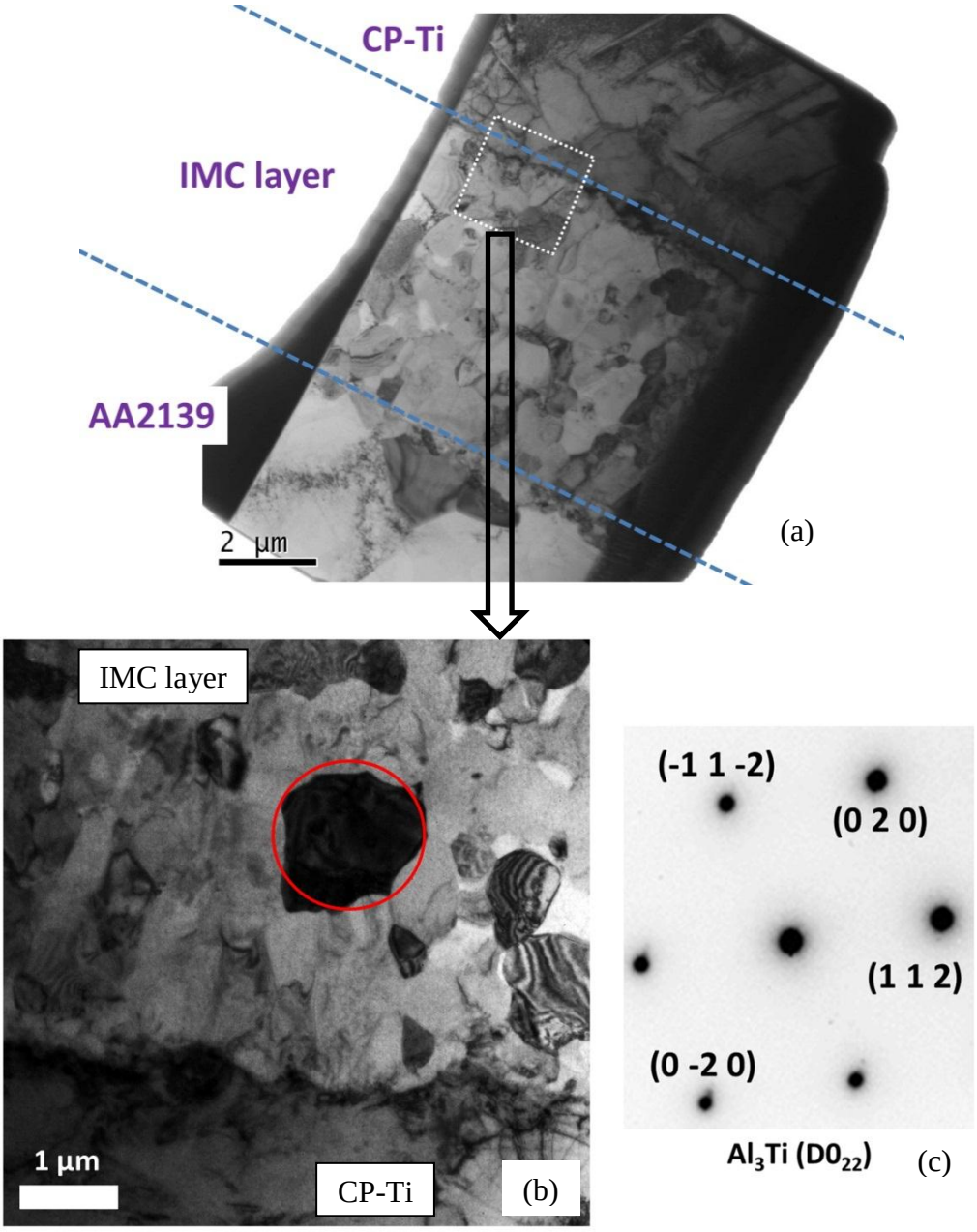

Figure 6.3 Identifying the phase structure in the IMC layer in AA2139/CP-Ti joint by TEM-SAD, (a) TEM bright field image of the IMC layer, (b) lager view of the with square region in (a), (c) the diffraction patter of the selected area as labelled by the red circle in (b). (the IMC layer was grown by annealing at 500 °C for 360 h.)

To examine the phase composition of the IMC layer in a larger view, the cross-section of the AA2139/CP-Ti joint was carefully polished using a Gatan Precision

Cross Section system to get a high quality surface, and then EBSD analysis was performed near the Al/Ti interface region. It is found that the reaction layer was mainly composed of Al_3Ti ($D0_{22}$ structure), but some trapped Al islands were also observed in the layer, as shown in the phase map (Figure 6.4). From the Cu map (Figure 6.5), it can be seen that these Al islands contain Cu, which indicates that they are trapped AA2139 aluminium alloy. The formation mechanism of the trapped Al islands will be discussed in Section 6.3.

Texture analysis in the reaction layer:

Figure 6.6 presents the sample coordinate system during EBSD analysis. The IPF map of the Al_3Ti reaction layer annealed at 500 ℃ for 480 h is shown in Figure 6.7. From the {001}, {110} and {112} pole figures in Figure 6.8, it can be seen that there is pronounced texture in the reaction layer and the [001] Al_3Ti growth direction is inclined to be parallel with the Al/Ti interface plane, i.e. the ID-ND plane. Similar texture in the Al_3Ti reaction layers was also observed in other combinations (CP-Al/CP-Ti joint and CP-Al/Ti6Al4V joint) annealed at different annealing temperatures (550 ℃ and 600 ℃) for different times (24 h and 48 h), as shown in the pole figures in Figure 6.9 and Figure 6.10. However, Dietrich et al. [212] reported fully random Al_3Ti grain orientation in a solid state reaction layer between CP-Al and CP-Ti. The difference could be due to the different chemical composition of Al, but another possibility is that their EBSD data was not carefully analysed. Their conclusion was deduced from an inverse pole figure (IPF) map. No pole figure was presented in their paper, hence it is difficult to accurately analyse the texture.

It can be seen from Figure 6.11 that the majority of grain boundaries in the Al_3Ti layer are high-angle grain boundaries. The majority of the grain boundaries have a

misorientation angle larger than 30°.

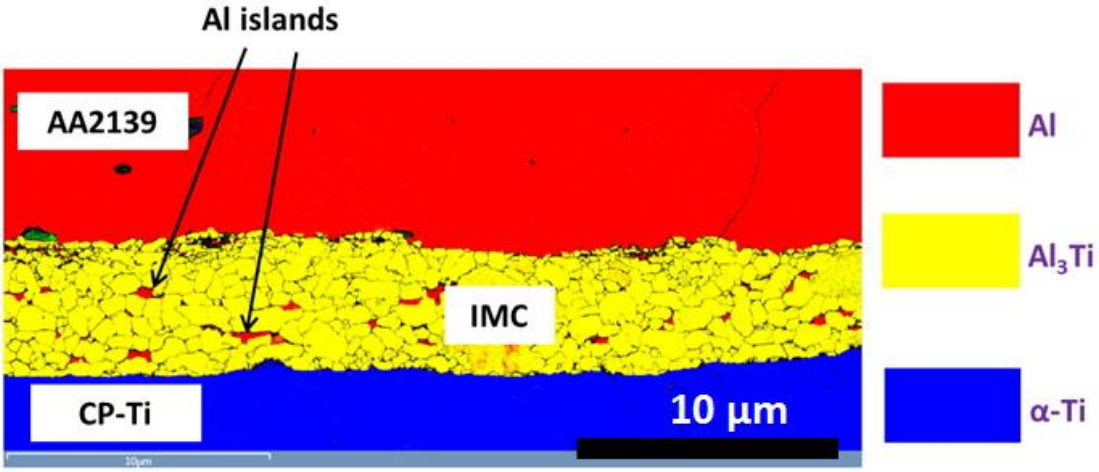

Figure 6.4 EBSD phase map of the IMC layer between AA2139 and CP-Ti (annealed at 500 ℃ for 480 h).

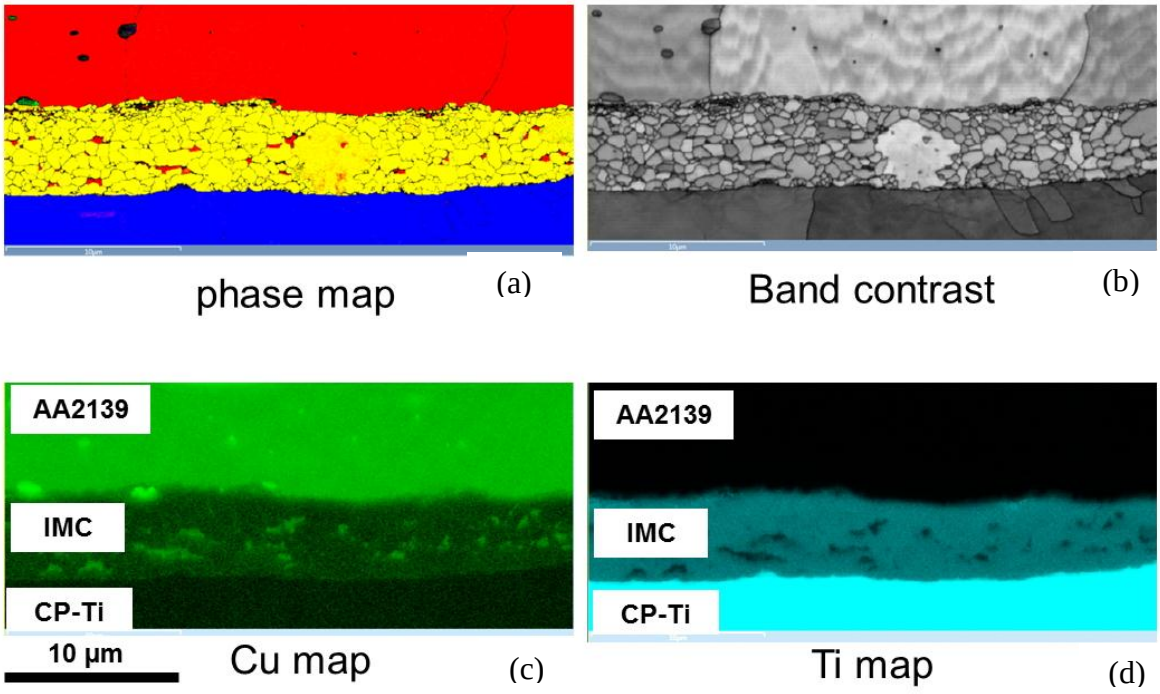

Figure 6.5 (a) EBSD phase map, (b) band contrast image, (c) Cu map, (d) Ti map of the reaction layer region between AA2139 and CP-Ti (annealed at 500 ℃ for 480 h).

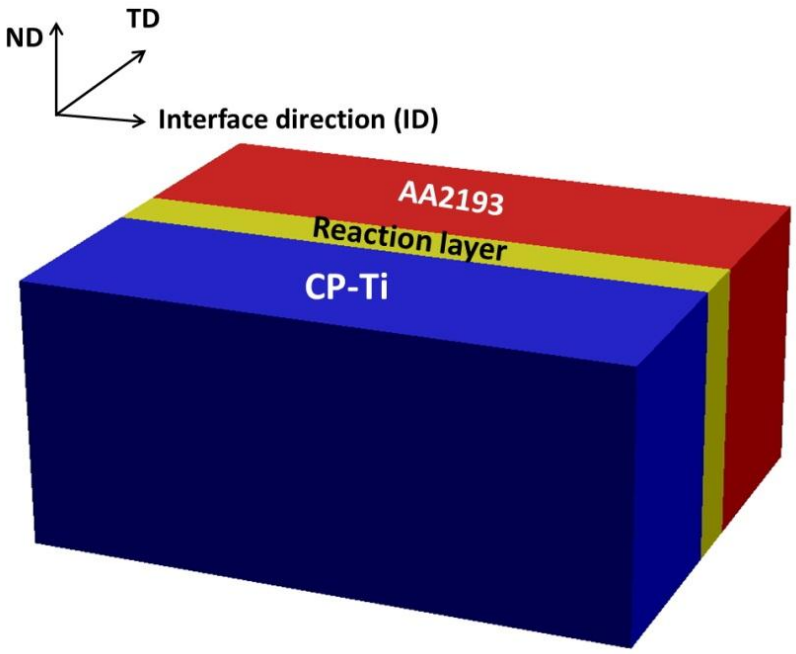

Figure 6.6 The sample coordinate system

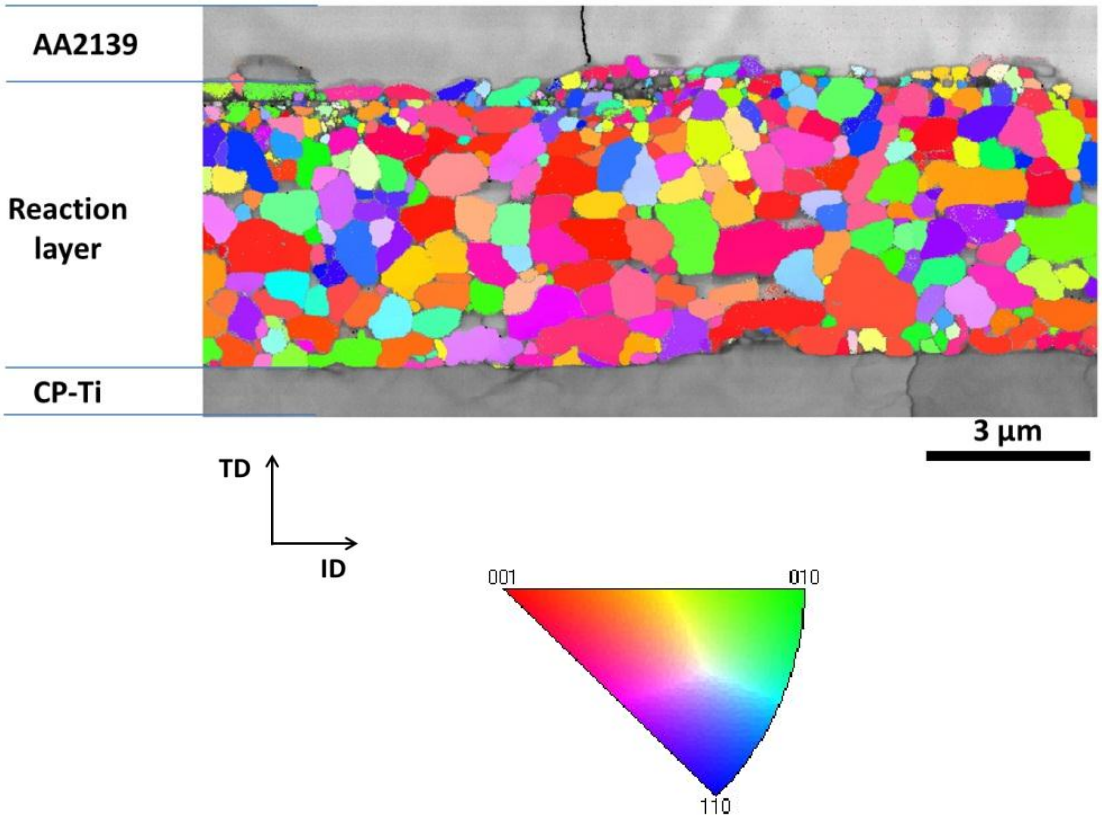

Figure 6.7 The IPF (inverse pole figure) map of the Al_3Ti reaction layer. (annealed at 500 ℃ for 480 h)

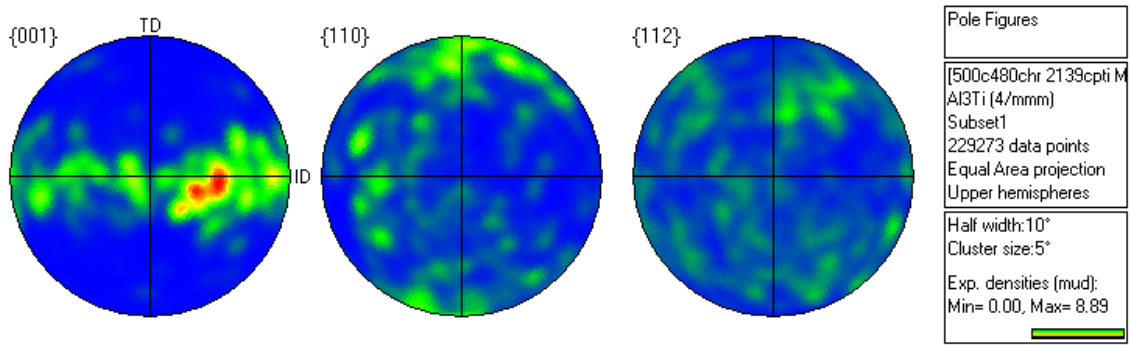

Figure 6.8 The {001}, {110} and {112} pole figures of the Al_3Ti in the reaction layer shown in Figure 6.7 (annealed at 500 ℃ for 480 h).

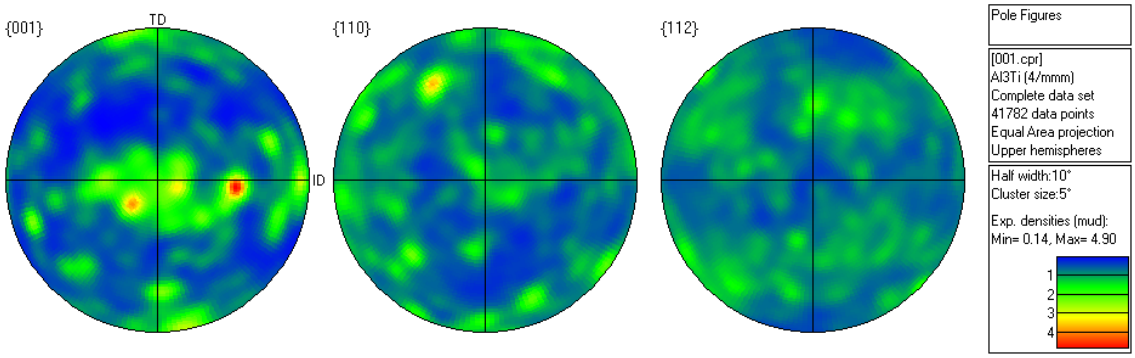

Figure 6.9 The {001}, {110} and {112} pole figures of the Al_3Ti in the reaction layer in a CP-Al/CP-Ti joint (annealed at 550 ℃ for 48 h).

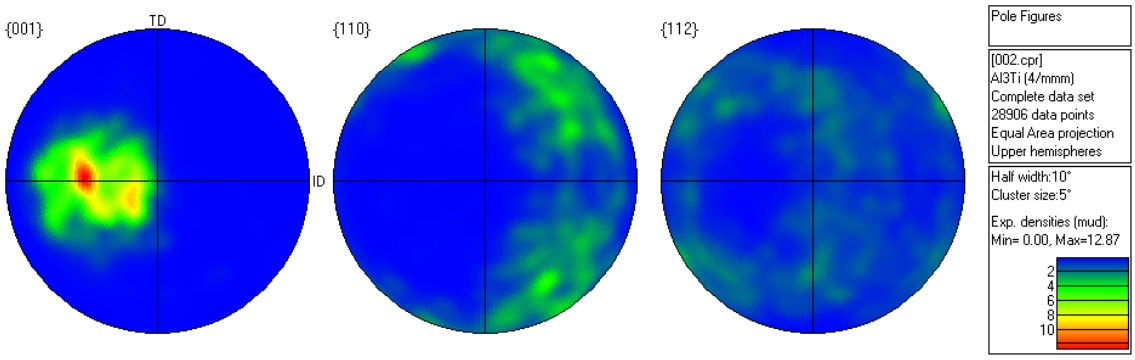

Figure 6.10 The {001}, {110} and {112} pole figures of the Al_3Ti in the reaction layer in a CP-Al/Ti6Al4V joint (annealed at 600 ℃ for 24 h).

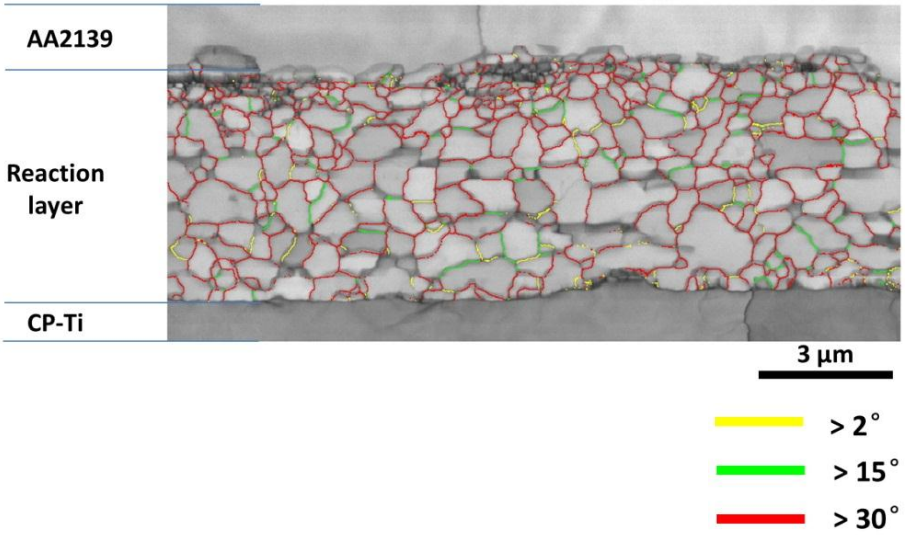

Figure 6.11 Grain boundary map in the reaction layer. (Annealed at 500 ℃ for 480 h)

6.1.2.2 Comparison of IMC grain size in annealed AA2139/CP-Ti joints and in annealed CP-Al/CP-Ti joints

As mentioned in Section 6.1.1, the growth rate of IMC layer is quite different comparing AA2139/CP-Ti joints and CP-Al/CP-Ti joints. Grain size differences are a possible factor, as discussed in Section 5.1. Thus, the Al_3Ti grain size evolution in the two types of annealed joints was studied using SEM and TEM, as shown in Figure 6.12. It can be seen that the Al_3Ti grain size in CP-Al/CP-Ti joint is almost constant with increasing annealing time and is smaller than that in AA2139/CP-Ti joint. The Al_3Ti grain size in AA2139/CP-Ti joint became more than 2 times larger than that CP-Al/CP-Ti joint after a long time annealing. A similar phenomenon was also observed by Wittmer et al [147]; they also found that with the presence of Cu, Al_3Ti grain size increased 3-4 times when Al/Ti samples were annealed at 450 ℃. Both the observation of the present study and that of Wittmer et al [147] suggest that the presence of Cu can lead to larger Al_3Ti grain size.

The larger Al_3Ti grain size in the reaction layer of annealed AA2139/CP-Ti joint resulted in a lower grain boundary fraction, and thus fewer fast diffusion paths. This could be a factor that results in the slower IMC layer growth in AA2139/CP-Ti joint.

It is also worth noting that, in contrast to the near constant Al_3Ti grain size in the CP-Al/CP-Ti joint annealed at 500 ℃, there is noticeable Al_3Ti grain growth with increasing annealing time in the reaction layer of AA2139/CP-Ti joint, which can further reduce the reaction layer growth.

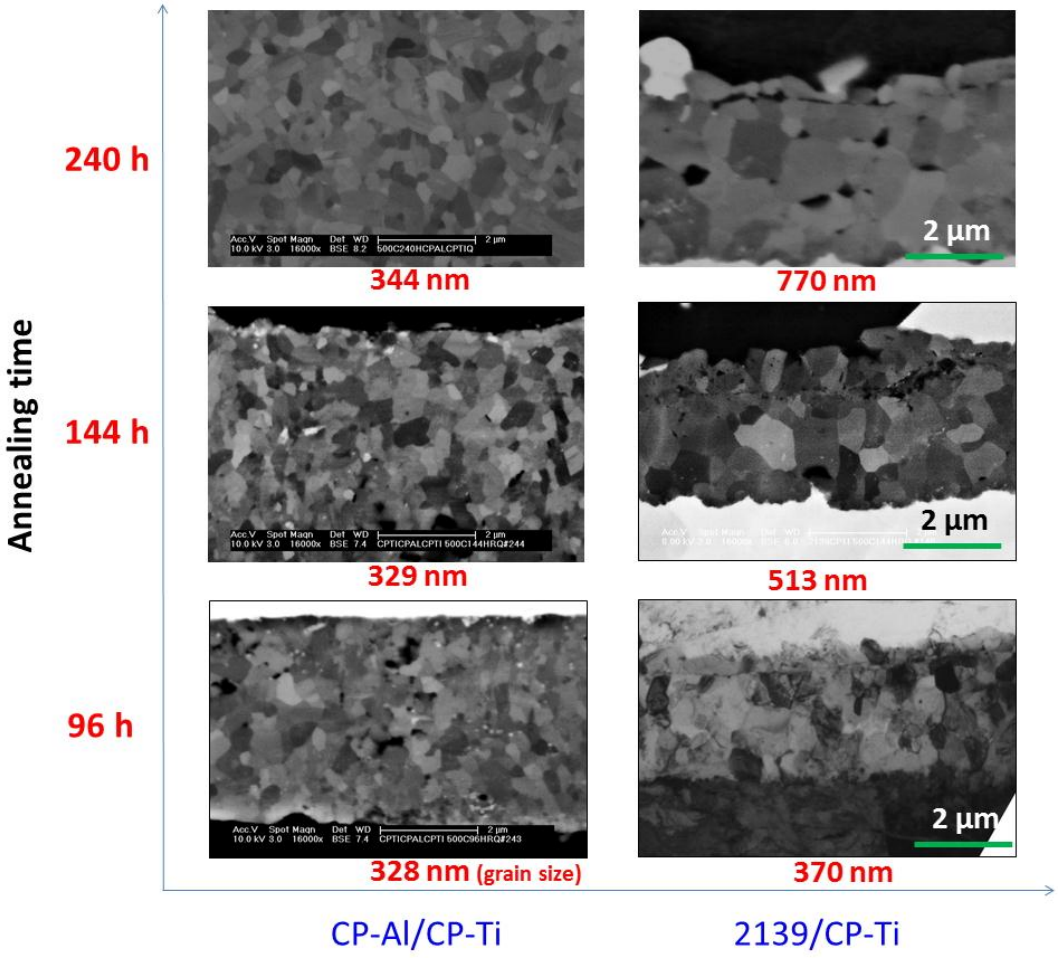

Figure 6.12 Comparison of Al_3Ti grain size in the reaction layers in AA2139/CP-Ti joints and in CP-Al/CP-Ti joints annealed at 500 ℃ for various time. (all images at the same magnification)

6.1.3 Behaviour of alloying elements

6.1.3.1 Cu segregation on Al_3Ti grain boundaries

Though the reduction of grain boundary fraction is probably an important reason for the slower IMC layer growth, there could be other important factors, such as segregation of alloying elements on Al_3Ti grain boundaries, which can block the diffusion paths in grain boundaries, or a difference in the oxide behaviour (eg. there may be more oxides on the AA2139/CP-Ti interface than on the CP-Al/CP-Ti interface). Thus, high resolution STEM-EDS was used to analyse the distribution of alloying elements in the IMC layer.

It should be pointed out that the TEM foil was specially put on a molybdenum (Mo) TEM grid but not on a normal copper TEM grid to prevent the influence of copper from grid biasing results when performing STEM-EDS analysis. As shown in Figure 6.13, Cu segregation was detected on the Al_3Ti grain boundaries. However, no other alloying element segregation, such as Si and Mg, was detected on the grain boundary (Figure 6.14). This demonstrated that Cu was the only alloying element segregated to the grain boundary, which is probably because there is a large amount of Cu in the AA2139 aluminium alloy (4.8 wt. %) and the solubility of Cu in Al_3Ti is expected to be low [99]. Segregation of Cu on Al_3Ti grain boundaries could be another important reason for the slower IMC growth with the presence of Cu. This viewpoint has also been suggested by a previous investigation [119], though they did not experimentally observe the Cu segregation.

Finally, Cu has a stronger affinity for Ti than Al [144, 182], which could influence the diffusion coefficient of Al and Ti within the layer.

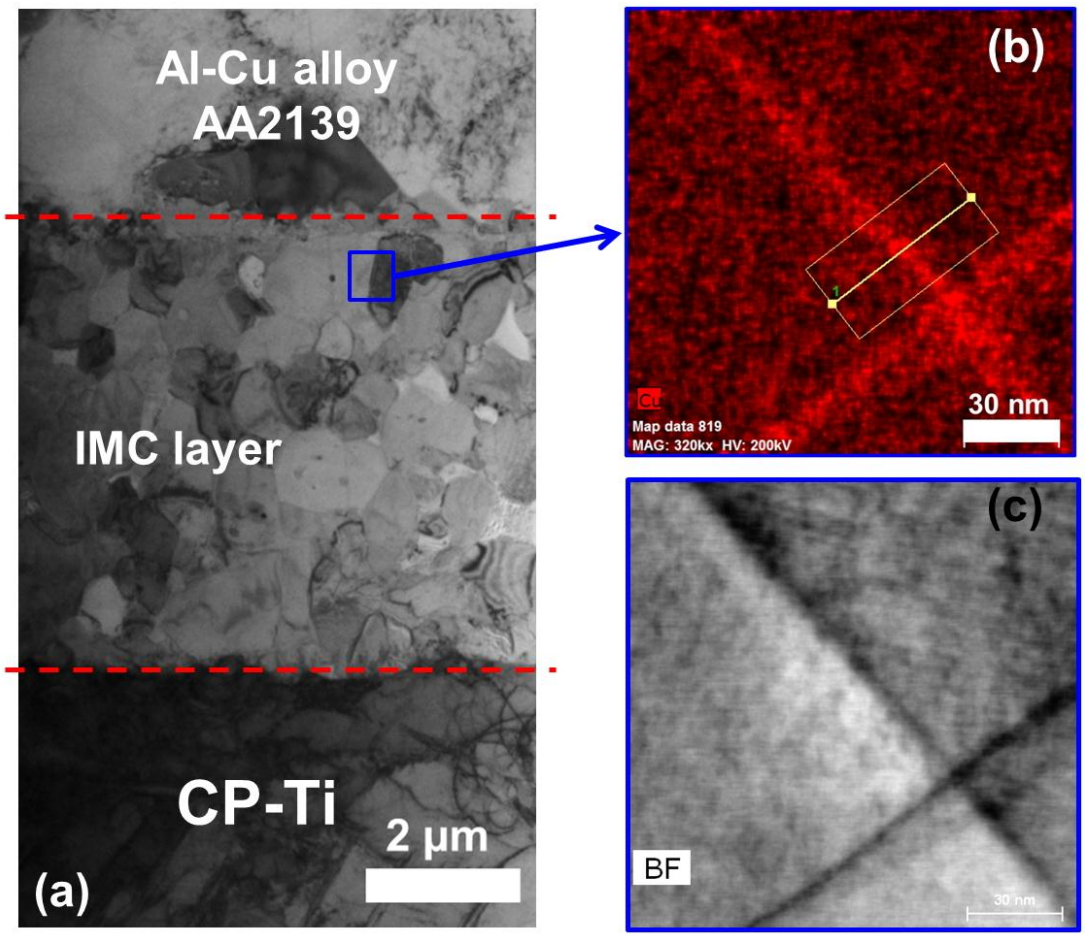

Figure 6.13 Segregation of Cu on Al_3Ti grain boundaries, (a) bright field TEM image of the Al_3Ti reaction layer between AA2139 and CP-Ti, (b) STEM-EDS Cu map, (c) Bright field image of the same region as the Cu map. (annealed at 500 ℃ for 360 h). Note: The blue rectangular in (a) just indicates the rough position of the region where the EDS mapping was performed not the exact position.

Semi-quantified Cu concentration on Al_3Ti grain boundary and in Al_3Ti grain in interior:

STEM-EDS data was semi-quantified and it was estimated that the Cu concentration segregated to grain boundaries reaches ~0.65 at. % and the Cu concentration in the Al_3Ti bulk is ~0.2 at. %. Though of small amount, the solid solution of Cu in Al_3Ti grain interior may also have a direct effect on lattice diffusion.

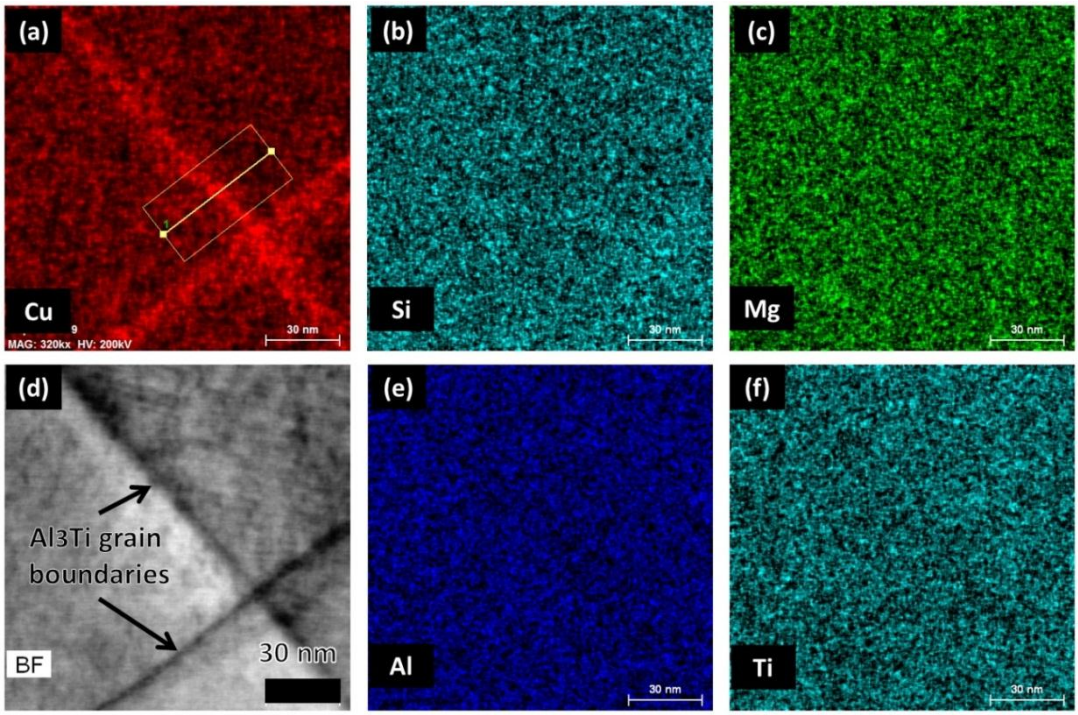

Figure 6.14 The composition maps in the same region as Figure 6.13 measured by STEM-EDS, (a) Cu map, (b) Si map, (c) Mg map, (d) TEM bright field image, (e) Al map, (f) Ti map. (annealed at 500 ℃ for 360 h)

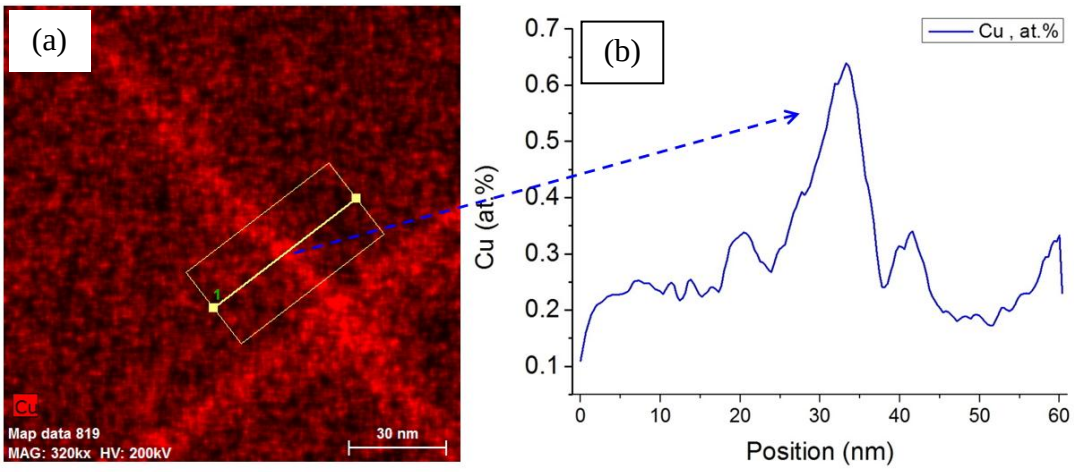

Figure 6.15 Semi-quantified Cu concentration on Al_3Ti grain boundary and Al_3Ti grain interior, (a) Cu map by STEM-EDS, (b) the semi-quantified Cu concentration profile across the grain boundary.

6.1.3.2 Cu segregation on Al_3Ti/CP-Ti interface

As Cu and Ti are two elements that are strongly attractive to each other [144], Cu also could segregate to the Al_3Ti/CP-Ti interface. To fully understand the role of Cu, STEM-EDS analysis was performed on the Al_3Ti/CP-Ti interface to investigate whether Cu segregate on this interface or not. As shown in Figure 6.16, Cu segregation to the Al_3Ti/CP-Ti interface was observed, which could also act as a diffusion barrier and then retard the Al_3Ti layer growth. Semi-quantitative analysis shows that the Cu segregation concentration reached ~2.8 at. % (Figure 6.17), which is much higher than the detected Cu segregation concentration on Al_3Ti grain boundaries (~0.65 at. %). This indicates that Cu atoms diffused through Al_3Ti layer and were deposited and adsorbed on the Al_3Ti/CP-Ti interface.

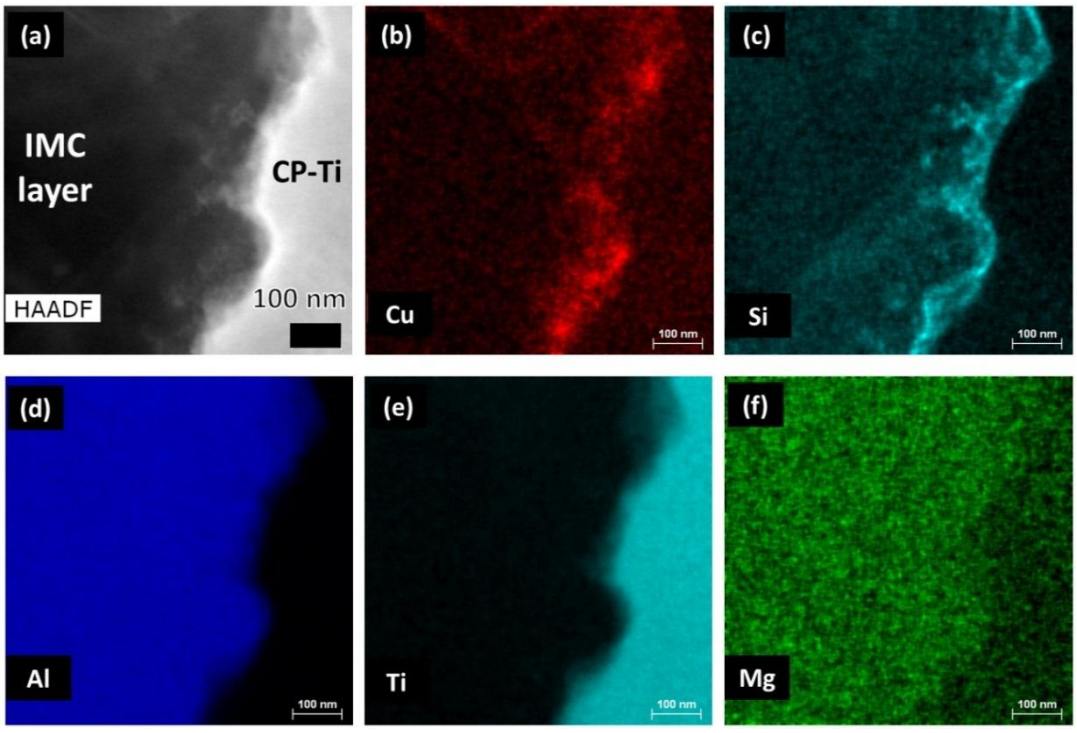

Figure 6.16 The composition maps in the region near the Al_3Ti/CP-Ti interface measured by STEM-EDS, (a) STEM-HAADF image, (b) Cu map, (c) Si map, (d) Al map, (e) Ti map, (f) Mg map. (annealed at 500 ℃ for 360 h)

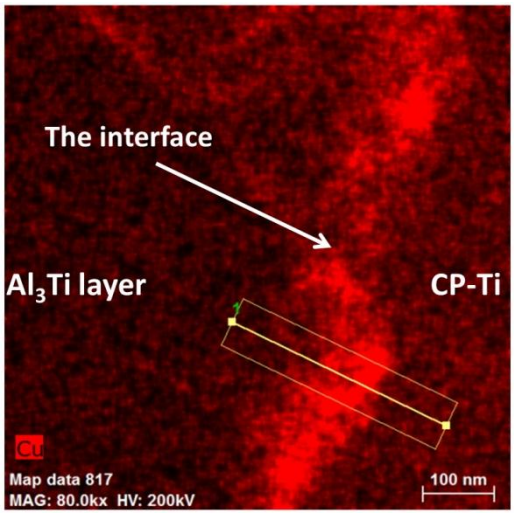

(a)

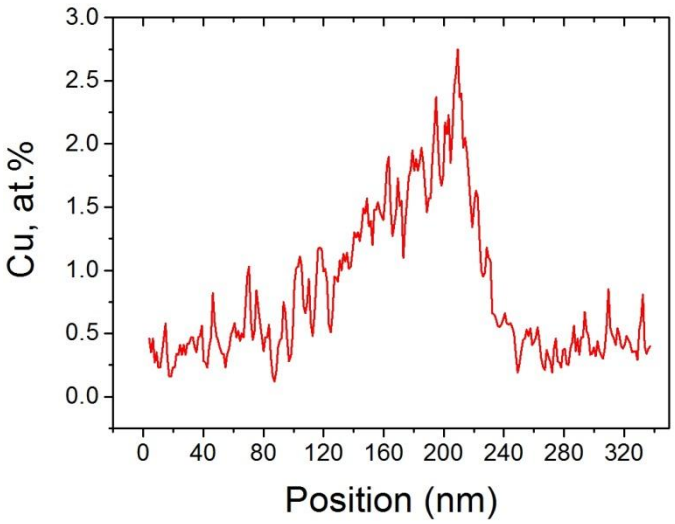

(b)

Figure 6.17 STEM-EDS line scan across the Cu rich region on the Al3Ti/CP-Ti interface, (a) the Cu map in the same region with Figure 6.16, (b) the semi-quantified Cu concentration profile along the yellow line labelled in (a).

6.1.3.3 Si segregation on Al_3Ti/CP-Ti interface

Though Si is an impurity in AA2139 aluminium alloy (its content was controlled at a very low level, 0.03 wt. %), the possibility of Si taking part in the Al/Ti solid-state reaction still exists. Similar to Cu, Si and Ti also strongly attract each other. As shown in Figure 6.16, Si segregation on the Al_3Ti/CP-Ti interface was detected using the STEM-EDS technique. Like the Cu segregation layer, Si segregation on this interface could also act as a diffusion barrier.

Semi-quantitative analysis shows that the Si segregation concentration reached ~7 at. % (Figure 6.18), which is much higher than its content in AA2139 base metal (0.03%). This segregation concentration (~7 at.%) is much lower than that observed by Fuji et al. [23] (more than 20 at.%) on the same interface in an Al (0.12% Si)/Ti jointed annealed at 600 ℃ for 1 h. This indicates that the Si segregation concentration on Al_3Ti/CP-Ti interface could be affected by both the Si concentration in Al base metal and the annealing temperature. A high content of Si in Al base metal and high annealing temperature could increase the Si segregation concentration on Al_3Ti/CP-Ti interface.

6.1.3.4 Si enrichment in the Al_3Ti layer

Apart from segregating on the Al_3Ti/CP-Ti interface, Si was also found to enrich in the Al_3Ti layer observed by both SEM-EDS and STEM-EDS techniques, as shown in Figure 6.18. The Si concentration in Al_3Ti layer reached ~2 at.% after annealing for 360 h at 500 ℃ in an AA2139/CP-Ti joint. The observed Si enrichment in the Al_3Ti layer is in consistent with many investigations [23, 103, 114, 116-118, 152, 212]. For example, Nonaka et al. [117] observed experimentally up to to 11 at. % Si enrichment in Al_3Ti layer with Al base metal containing 0.27% Si. Takemoto and Okamoto [103] found that the Si enrichment concentration up to 6.5 at % in Al_3Ti, which increased with increasing Si content (up to 3%) in Al base metal when the annealing temperature is constant (680 ℃) .

The relatively lower Si concentration (~2 %) in the Al_3Ti layer in the present study compared with those of [117] and [103] could be due to the lower Si content (0.03 %) in AA2139 Al alloy and the lower annealing temperature 500 ℃, compared to the higher annealing temperatures (above 550 ℃) and the higher Si

concentration (above 0.27 %) in Al base metals used in Takemoto et al.'s and Nonaka et al.'s investigations.

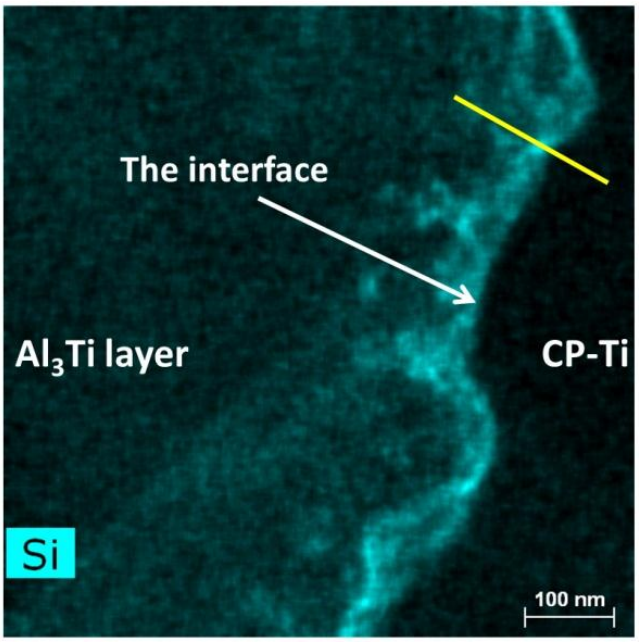

(a)

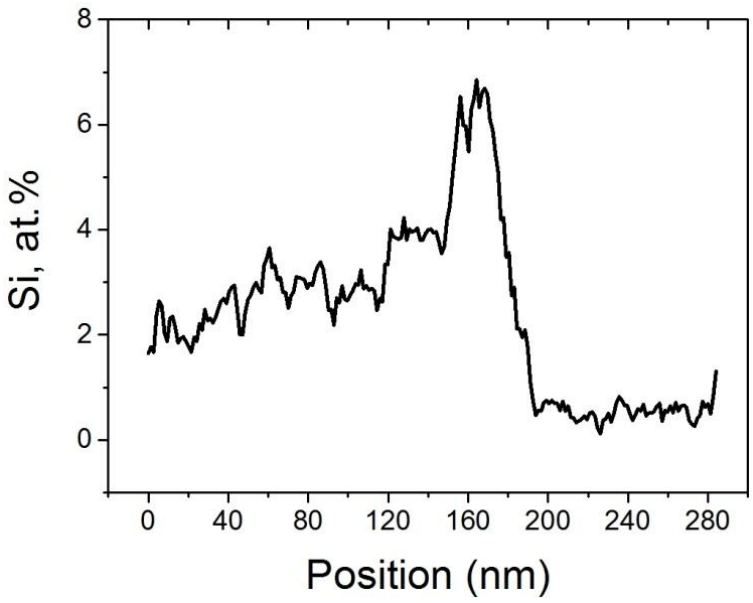

(b)

Figure 6.18 STEM-EDS line scan across the Si rich region on the Al_3Ti/CP-Ti interface, (a) the Si map in the same region with Figure 6.16, (b) the semi-quantified Si concentration profile along the yellow line labelled in (a).

Similar to the Si segregation to Al/Ti interface (as mentioned in section 4.4.2), the driving force for the uphill diffusion of Si from AA2139 alloy to Al_3Ti could also

be the very negative chemical mixing enthalpy between Ti and Si (-66 kJ mol^{-1}), compared with that between Al and Si (-19 kJ mol^{-1}). Many investigations [103, 114, 115, 117, 118] showed that Al_3Ti strongly attracted Si. This has been explained in a past publication, eg. Al_3Ti particles were used for purifying molten aluminium, which contains low concentration of impurity Si [115].

The present study and previous literature suggest that the Si segregation concentration on Al_3Ti/CP-Ti interface is always around 3-4 times of that in Al_3Ti layer (both for the present study and Fuji et al.'s [23]).

Like the function of Cu in Al_3Ti, it was suggested that the strong attraction between Si atoms and Ti atoms can retard Ti diffusion through the Al_3Ti layer [103]. As stated in Section 2.7.5, many investigations found that the effect of Si on Al_3Ti layer growth was very significant [23, 103, 152]. For example, Takemoto and Okamoto reported that up to 0.8 % Si addition to Al base metal can reduce the Al_3Ti layer growth rate by more than 10 times [103].

6.1.4 The double-layer structure of the reaction layer

A double-layer structure was repeatedly observed both in the reaction layer annealed for a relative short time (96 h) and in the reaction layer annealed for a long time (360 h) by TEM images (Figure 6.19 and Figure 6.20). The double-layer structure means that in the growth front of Al_3Ti layer near Al side, there are two layers of Al_3Ti; the layer close to Al is very thin and there is a clear straight interface between the two layers. The double-layer structure was only found in the reaction layer region near the Al side.

As shown in Figure 6.21 and Figure 6.22, there was Mg and O enrichment detected on the interface of the double-layer structure by STEM-EDS. The formation

mechanism of the Mg and O enrichment on the interface was discussed below.

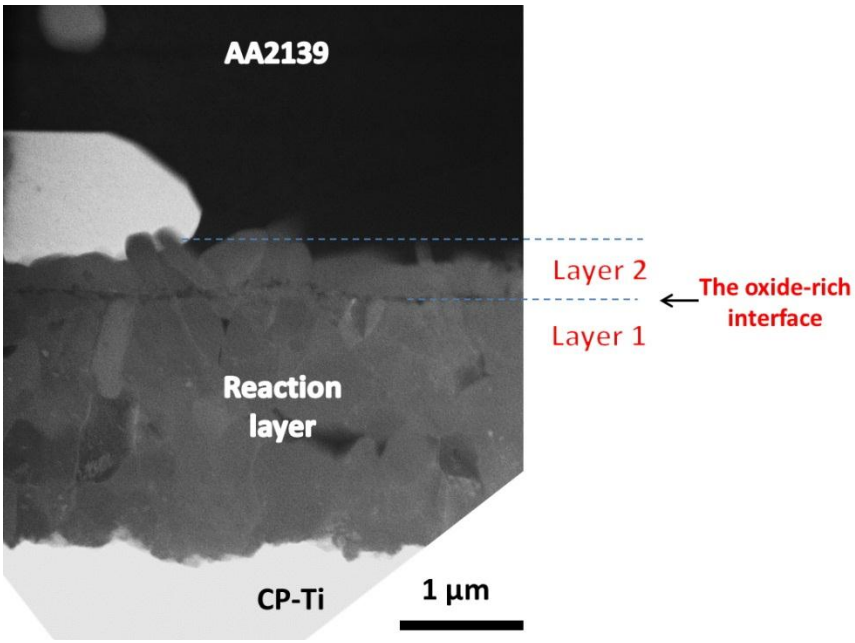

Figure 6.19 The double-layer structure in the near Al side side of a reaction layer, TEM-HAADF image, annealed at 500 ℃ for 96 h.

Mg is second most abundant alloying element in AA2139 aluminium alloy, but the affinity between Mg and Ti is quite weak [214]. However, Mg enrichment was still observed at the interface of the double-layer structure very near the AA2139/Al_3Ti interface. Its enrichment concentration reached 12 at. % (Figure 6.22), which is much higher than that in AA2139 base metal (0.45 %). This concentration is at a similar level with that observed on the as-welded Al/Ti interface (Figure 4.38) and the Mg distribution is also mostly coincident with that of oxygen (Figure 6.21). This suggests that the observed Mg enrichment at the AA2139/Al_3Ti interface in the sample annealed at 500 °C for 360 h is the Mg already existing at the as-welded Al/Ti interface prior to annealing, which was formed probably due to the surface segregation of Mg (as discussed in Section 4.4), which forms Mg oxide, and the probable fast surface oxidation in the initial stage of USW.

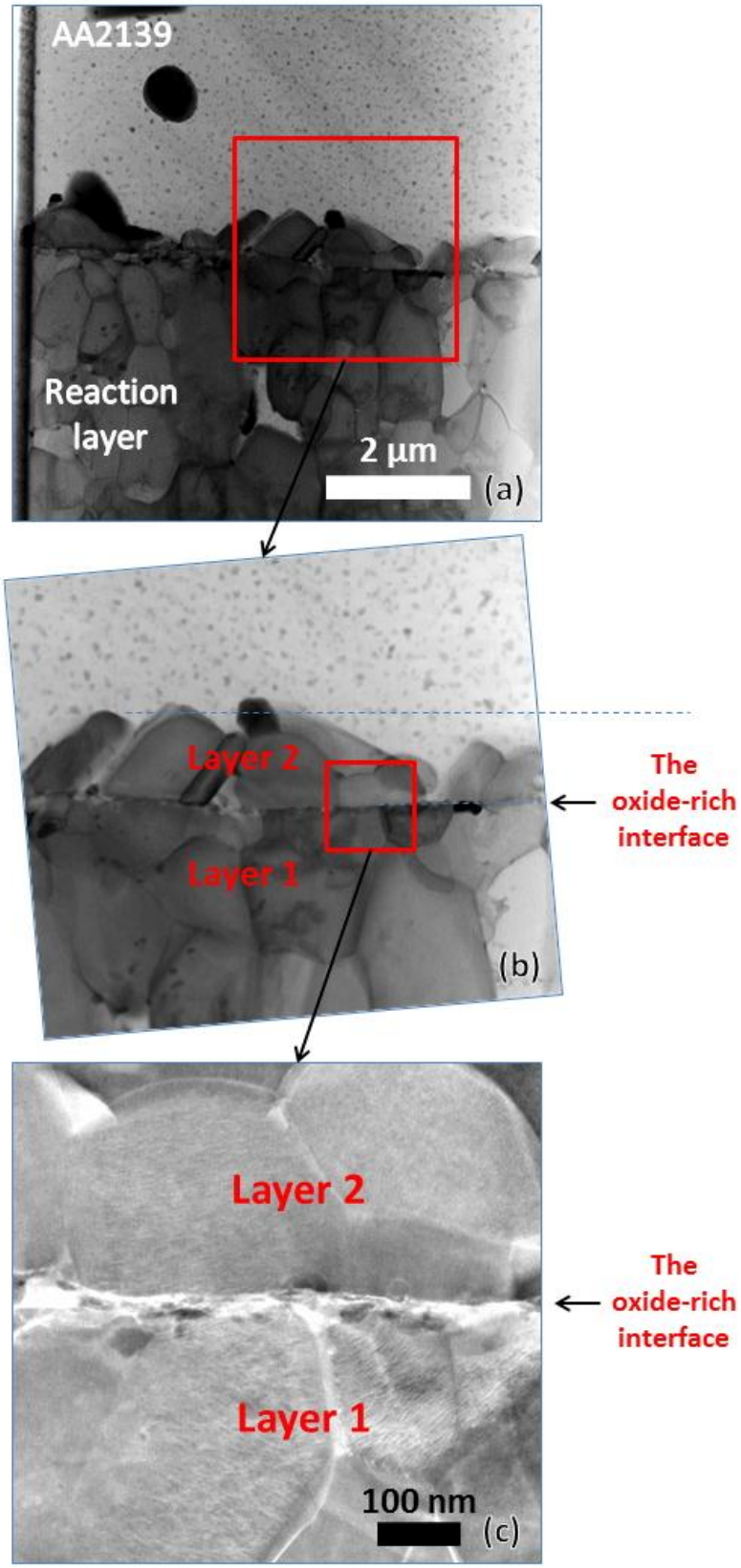

Figure 6.20 TEM image of the double-layer structure in the near Al side side of a reaction layer: (a) Low magnification TEM bright field image, (b) High magnification TEM bright field image, (c) High magnification STEM-HAADF image. (annealed at 500 ℃ for 360 h)

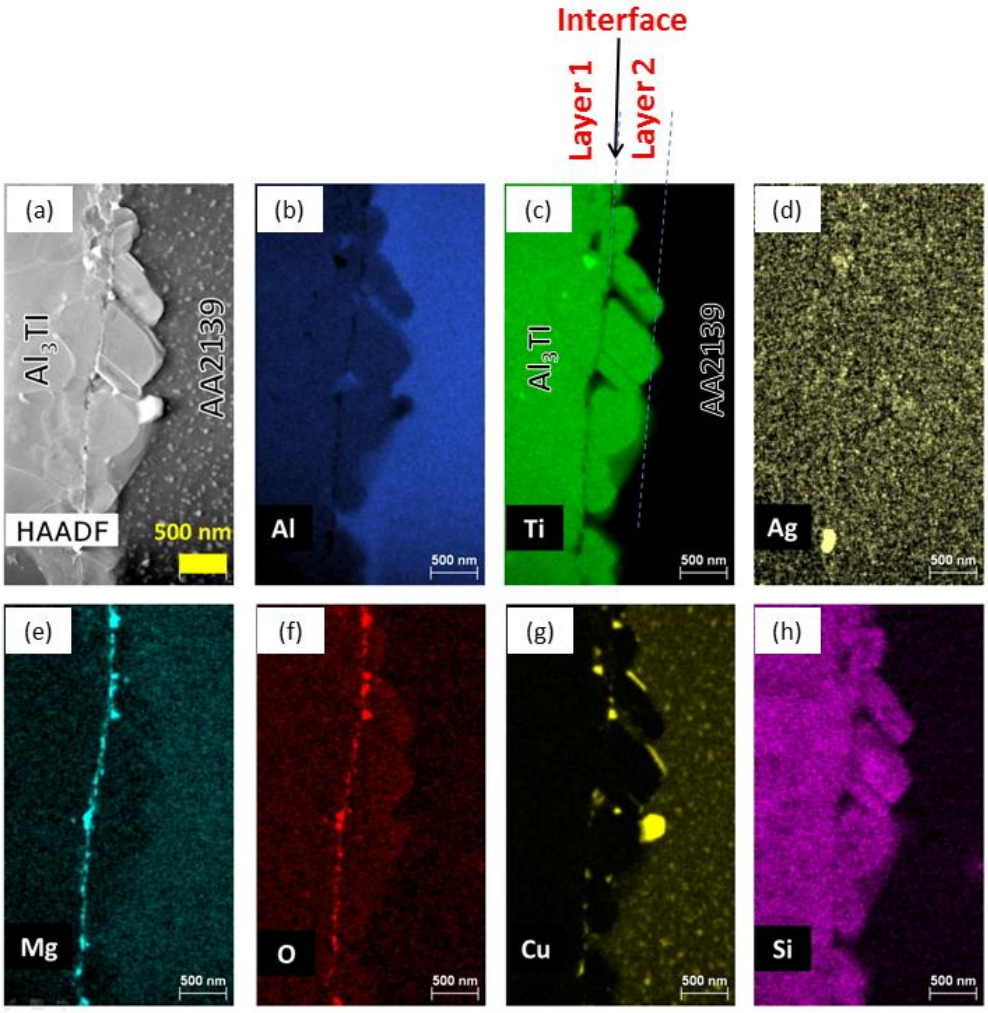

Figure 6.21 The composition maps near the double-layer interface region measured by STEM-EDS, (a) STEM-HAADF image, (b) Al map, (c) Ti map, (d) Ag map, (e) Mg map, (f) O map, (g) Cu map, (h) Si map. (annealed at 500 ℃ for 360 h)

The persistent existence of the double-layer structure (the Mg and O rich interface) in the near Al side with increasing annealing time suggests that the residual oxide from the surface of AA2139 cannot be decomposed during the Al-Ti solid state reaction due to its very high chemical stability. Wang et al. [215] have observed the solid state reaction ($Mg+TiO_2 \rightarrow MgO+Ti$) in the temperature range of 673-923 K (implying MgO is more stable than TiO_2). Park et al. [216] observed the reaction between Oxygen and Al_3Ti and detected the Al_2O_3 as an oxidation product (implying Al_2O_3 is more stable than Al_3Ti). Meanwhile, both MgO and Al_2O_3 are

refractory materials and have very high melting point (MgO, 2852 ℃; Al_2O_3, 2072 ℃). All of these suggest that both MgO and Al_2O_3 are very stable and cannot be decomposed spontaneously or react with the diffused Ti atoms at the annealing temperatures (500-630 ℃) used in the present study. Therefore, they exist like a diffusion marker on the growth front of the reaction layer and moves with the movement of the Al/reaction layer interface.

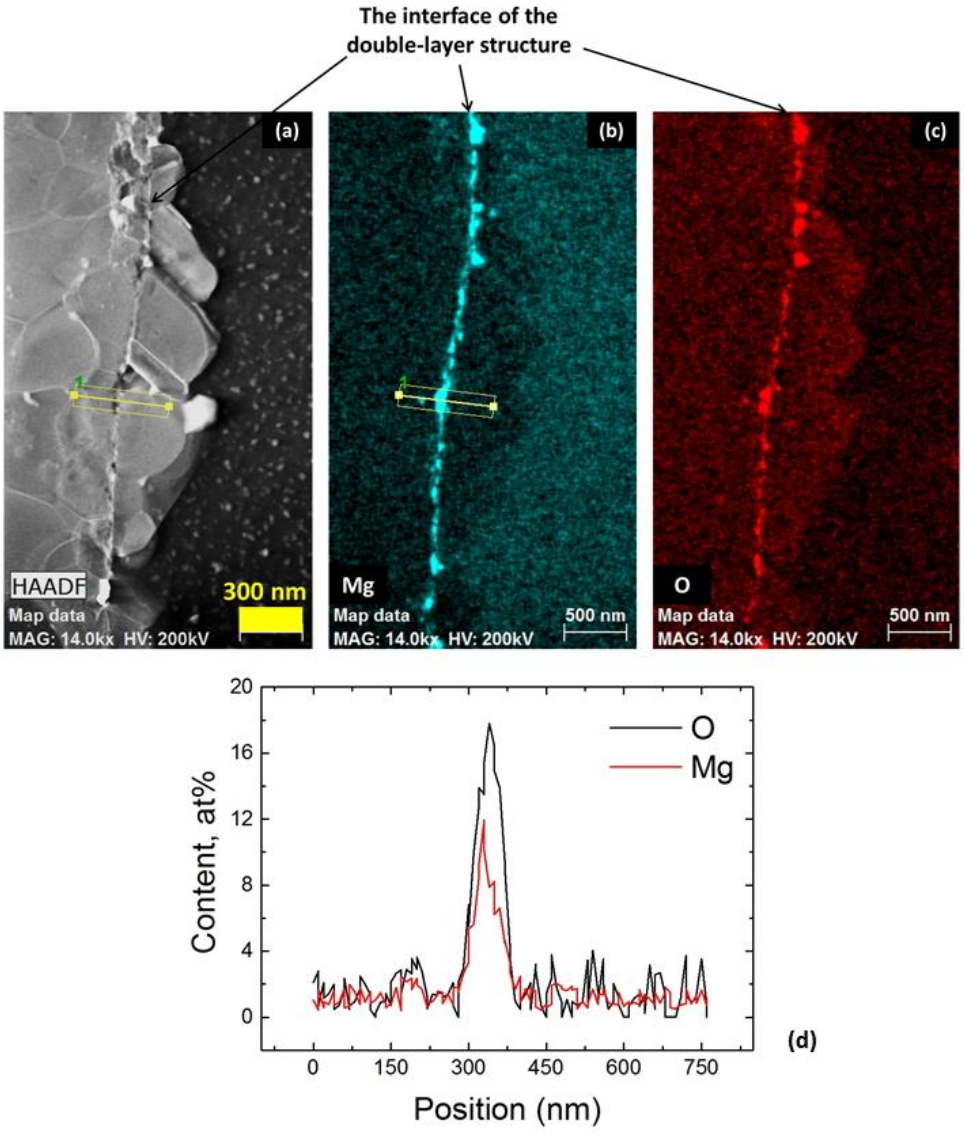

Figure 6.22 Enrichment of Mg and O on the interface of the double-layer structure near the AA2139/Al_3Ti interface, (a) STEM-HAADF image, (b) Mg map measured by STEM-EDS, (c) O map, (d) semi-quantified Mg and O concentration profile across the interface along the yellow line labelled in (a).

However, no double-layer structure was observed on the interface between the reaction layer and CP-Ti (Figure 6.23, Figure 6.24 and Figure 6.19). This indicates that the Ti oxide film on titanium surface can take part in the Al-Ti reaction and be decomposed during annealing. The solid state reaction between Ti oxide and Al has been frequently observed [206-210] as mentioned in Section 5.4.3 since Al_3Ti is more stable than Ti oxide.

The formation mechanism of the double-layer structure is proposed to be as follows: in the initial stage of Al-Ti reaction, a small amount of Ti diffusion occurs through the Al-Ti interface where the oxide film is broken and forms a few Al_3Ti islands on the Al side. At the same time Al_3Ti is also formed on the titanium side, leading to the residual broken oxide film (containing Mg oxide, Al oxide and absorbed oxygen) becoming trapped in between Al_3Ti grains grown on the both sides of it.

Similar to the segregation of Cu and Si on the Al_3Ti/Ti interface, the Mg enrichment (probably existing as oxide, Figure 6.21) on the interface of the double-layer structure near the Al_3Ti growth front also could act as a diffusion barrier and retard the Al_3Ti layer growth.

It is worth noting that there are also a few copper rich particles (Figure 6.21) on the double-layer interface, and it seems that Cu rich particles are inclined to precipitate on the Al_3Ti/AA2139 interface and grow to large particles. Their interaction with the growing Al_3Ti layer will be discussed in the next section (Section 6.1.5). Similarly, the white particles in Figure 6.19 and Figure 6.23 are also Cu rich particles in AA2139, their interaction with the Al_3Ti layer will also be discussed later.

It can also be seen from Figure 6.21 that the Si enrichment in the Al_3Ti layer was again observed in this TEM sample, which is in consistent with the observation in Section 6.1.3.4.

A large Ag rich particle was also observed on the Al_3Ti/AA2139 interface, which may be due to the presence of Ag as an alloying element in AA2139 alloy.

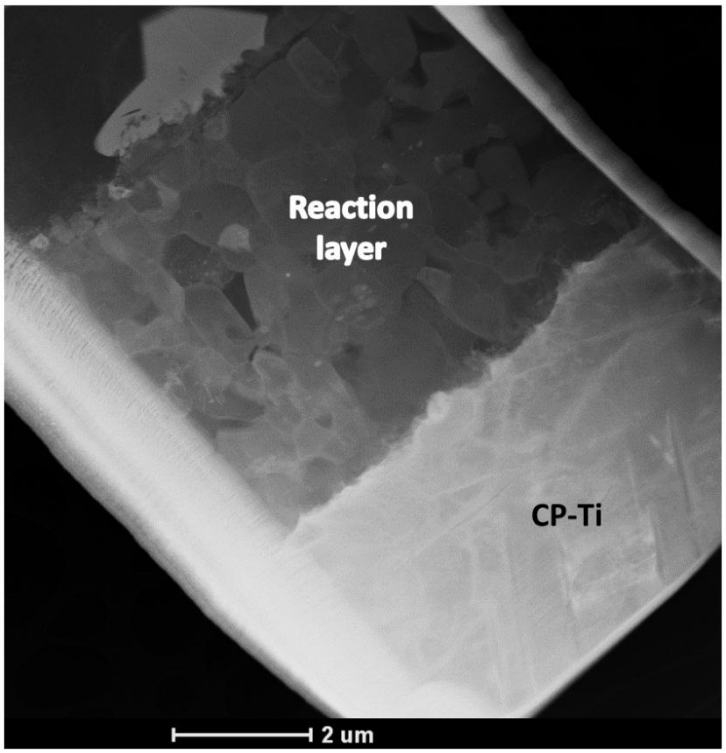

Figure 6.23 The clear reaction layer/CP-Ti interface without double-layer structure, TEM-HAADF image, annealed at 500 ℃ for 360 h.

The double-layer structure in annealed CP-Al/CP-Ti joint:

The double-layer structure of the Al_3Ti layer was also observed in an annealed CP-Al/CP-Ti joint (Figure 6.25), where there is no Mg presence (an easy to be oxidized element) in aluminium. Similarly, a thin discontinuous oxide layer was observed on the interface of the double-layer structure. Besides, some Fe rich particles were observed on the interface and in the Al_3Ti layer, which may be due to the presence of Fe as an alloying element in CP-Ti. (Fe is often used as an

alloying element to form a small amount of β phase in CP-Ti to pin the α-Ti grain boundaries, and thus control the grain size of α-Ti and increase the strength).

6.1.5 Decomposition of particles in AA2139 by IMC layer growth

There are lots of precipitate phases, such as Al_2Cu [55, 59] and $Al_7Cu_2(Fe,Mn)$ in AA2139 aluminium alloy, as show in Figure 6.26 (the white particles in the AA2139 side). During the Al_3Ti reaction layer growth, the growing Al_3Ti will inevitably come into contact with these precipitates or particles. If these particles can react with the growing Al_3Ti, they will be decomposed, if not they can be trapped in the Al_3Ti layer.

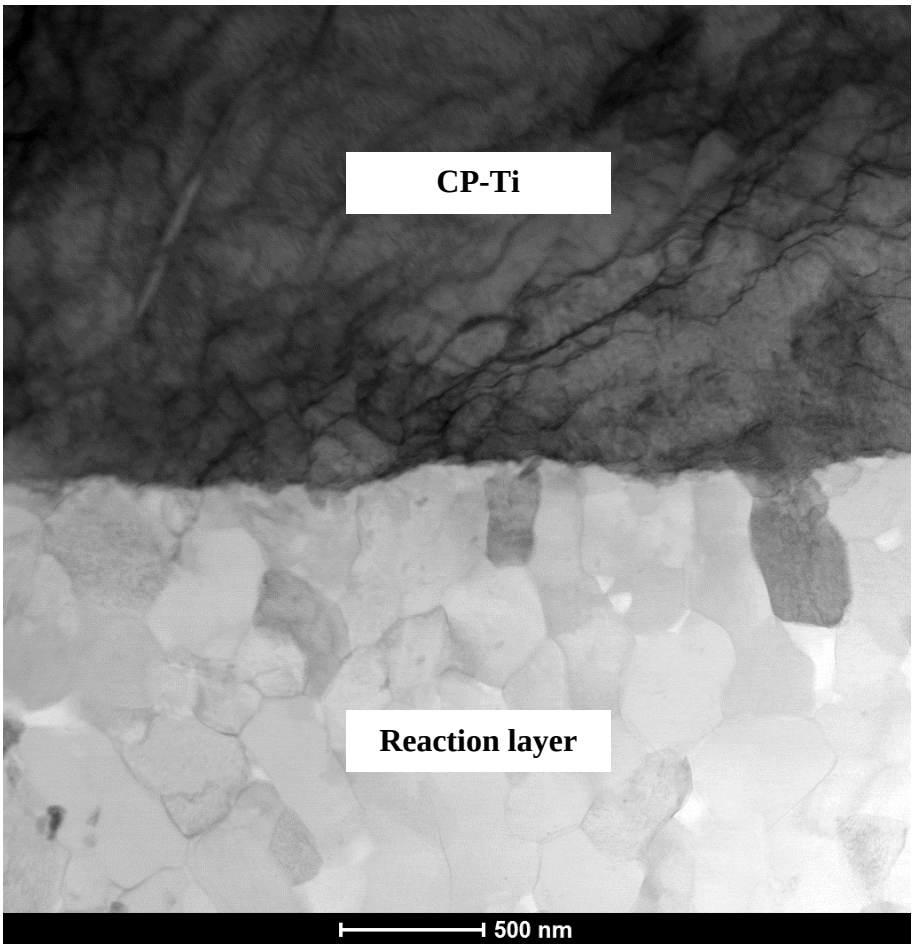

Figure 6.24 TEM bright field image of the IMC layer/CP-Ti interface without double-layer structure, the reaction layer was grown in a CP-Al/CP-Ti joint annealed at 500 ℃ for 96 h.

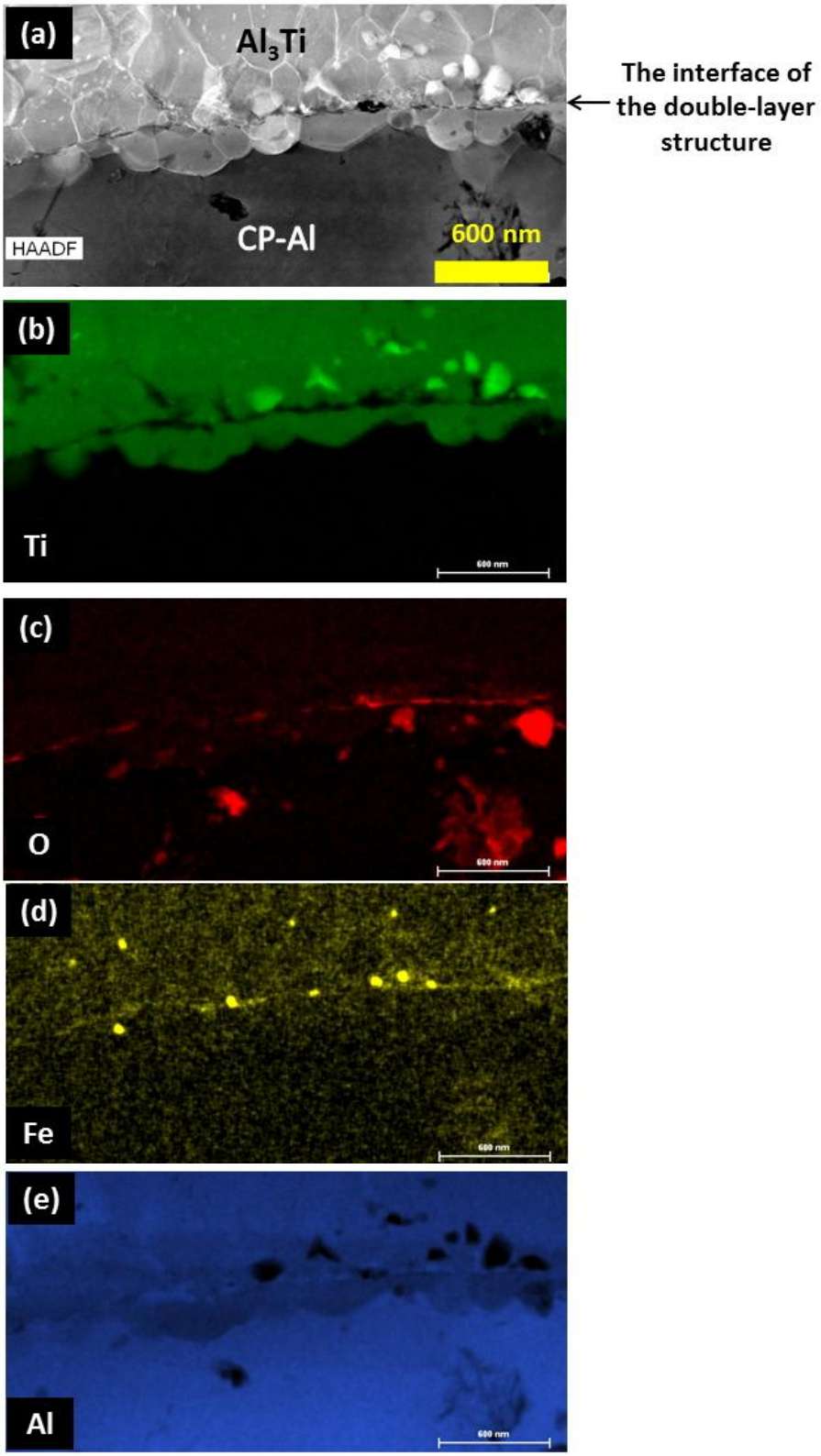

Figure 6.25 The composition maps in the double-layer interface region measured by STEM-EDS, (a) STEM-HAADF image, (b) Ti map, (c) O map, (d) Fe map, (e) Al map. (CP-Al/CP-Ti joint, annealed at 500 ℃ for 96 h)

As shown in Figure 6.26, a few big copper rich particles (as labelled) intersect the IMC layer on the AA2139/Al_3Ti interface but no particles from AA2139, such as Al_2Cu and Al_7Cu_2Fe, were found in the IMC layer. This indicates that these particles were decomposed by the growth of Al_3Ti layer. It is worth pointing out that, according to Al-Cu phase diagram and calculation by JMatPro simulation software, at 500 °C Al_2Cu and Al_7Cu_2(Fe,Mn) phases are stable in AA2139. Besides, calculations by PANDAT software demonstrated that the following reactions has a negative Gibbs change at the temperature of 500 °C, which implies that the decomposition reaction of Al_2Cu and Al_7Cu_2Fe can occur spontaneously at the reaction front driven by a reduction in free energy.

$$Al_2Cu + Ti \rightarrow Al_3Ti + Cu \qquad \Delta G=-336.379 \text{ kJ/mol}<0$$

$$Al_7Cu_2Fe + Ti \rightarrow Al_3Ti + Cu + Fe \qquad \Delta G=-23.56 \text{ kJ/mol}<0$$

Moreover, it also can be seen from Figure 6.27 that Al_3Ti grains were growing into the Cu rich particle. The particle was identified as Al_7Cu_2Fe phase by SAD.

During the decomposition process, the Al atoms from Al_2Cu and Al_7Cu_2(Fe,Mn) phases were consumed by the growth of Al_3Ti layer, however other elements, such as, Cu and Fe, were rejected and diffused to the neighbouring region. (As mentioned in section 6.1.3.1, the Cu concentration in Al_3Ti is very low, much lower than that in AA2139).

6.2 Static Growth Kinetics of IMC layer in CP-Al/Ti6Al4V joints

In this section, to understand the influence of vanadium on the growth kinetics of Al_3Ti layer, CP-Al/Ti6Al4V welds and CP-Al/CP-Ti welds, both without visible reaction layer in as-welded condition, were annealed at identical temperatures. The

growth rate of the IMC layer and the microstructural evolution were analysed and compared in detail.

6.2.1 Phase identification in the IMC layer

Similar to Section 6.1.2.1, first of all, TEM-SAD was applied to identify the phases in the IMC layer to make sure Al_3Ti ($D0_{22}$) is the only phase in the IMC layer.

An example of phase identification in the IMC layer in the CP-Al/Ti6Al4V joint is presented in Figure 6.28, the phase in the IMC layer was identified as Al_3Ti ($D0_{22}$) and no other intermetallic phase was observed in the IMC layer, which is again in consistent with most previous investigations [76-84]. This also indicates that the reaction product type in annealed CP-Al/Ti6Al4V weld in this study has not been affected by the alloying elements from the titanium alloy Ti6Al4V.

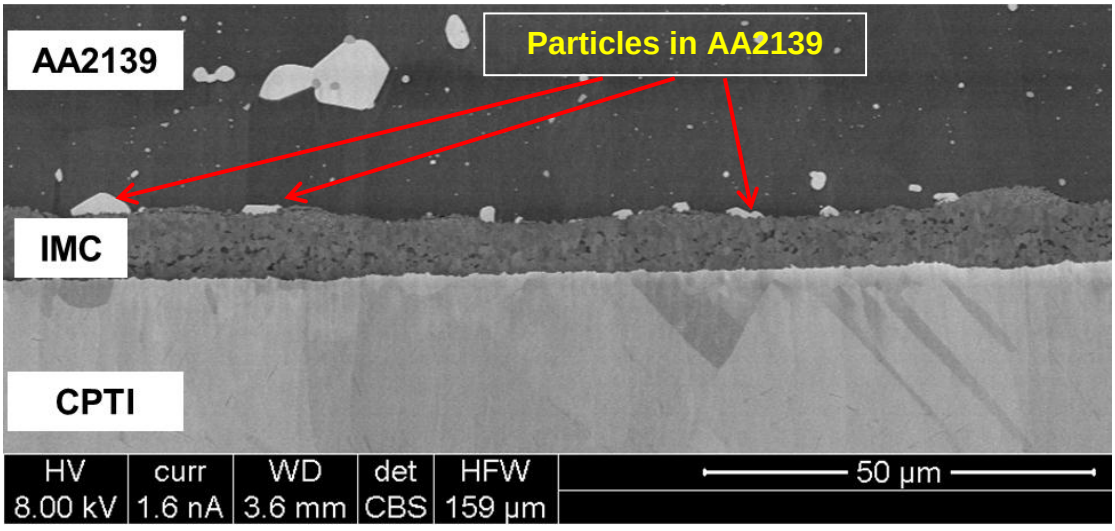

Figure 6.26 SEM-BSE image of the IMC layer (grown at 500 °C for 480 h), which contains no Al_2Cu and Al_7Cu_2Fe

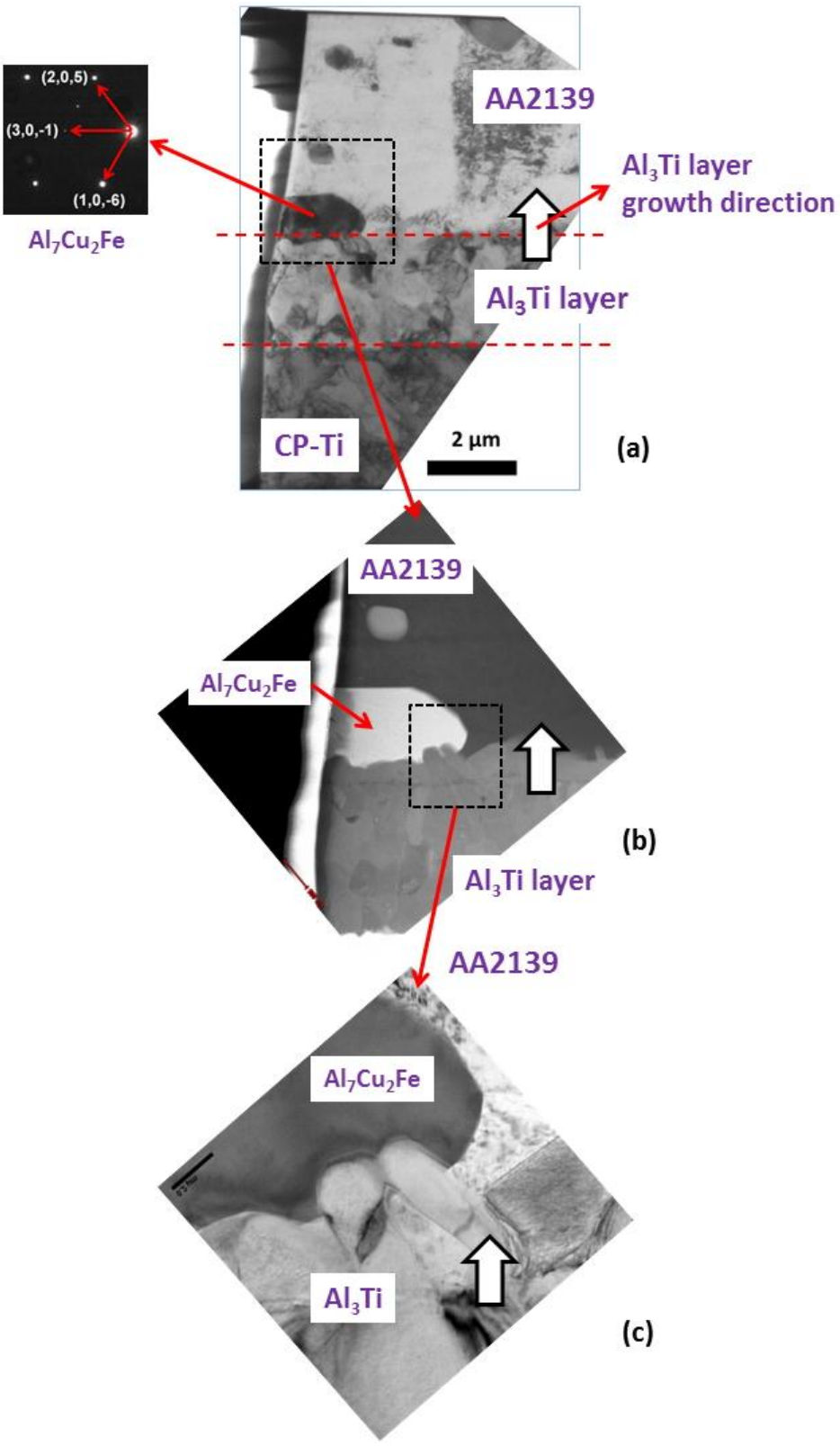

Figure 6.27 (a) TEM bright field image of an Al_7Cu_2Fe particle intersecting the IMC layer, (b) HAADF-STEM image of the Al_7Cu_2Fe particle intersecting the IMC layer (in the region labelled by the box in (a)), (c) Enlarged TEM bright field image of the Al_7Cu_2Fe particle intersecting the IMC layer in the region labelled by the box in (b). (the IMC layer was grown at 500 °C for 96 h in an AA2139 and CP-Ti joint.)

6.2.2 Comparison of IMC layer growth in CP-Al/Ti6Al4V joints and in CP-Al/CP-Ti joints

CP-Al/CP-Ti joints and CP-Al/Ti6Al4V joints (all without visible reaction layer in as-welded condition) were annealed at 600 °C and 630 °C for times ranging from 0 h to 48 h to study the reaction layer growth behaviour. The growth kinetics of Al_3Ti layer in the above mentioned joints are shown in Figure 6.29.

At the lower annealing temperature 600 °C, the growth rate of the Al_3Ti layer in CP-Al/ Ti6Al4V weld was found to be slower than that in CP-Al/CP-Ti weld (Figure 6.29 (a)). This is easy to understand as the presence of Al and V in titanium will reduce the concentration gradient of both Al and Ti compared with the CP-Al/CP-Ti weld.

However, interestingly this trend was reversed when annealing temperature rises to 630 °C (Figure 6.29 (b)). This indicates that there are other influences of the alloying additions in the Ti6Al4V alloy on the reaction layer growth, that are dominant at 630 °C annealing temperature.

6.2.3 Comparison of IMC grain size in annealed CP-Al/Ti6Al4V joints and CP-Al/CP-Ti joints

The vanadium content in the reaction layers in CP-Al/Ti6Al4V joints annealed at 600 °C and 630 °C were both measured by EDS. They were both detected to be around 1% (at.%), which is consistent with the V concentration in Al_3Ti layer reported by Nie et al. [150] in a similar study. The observed 1% vanadium in the IMC layer is also in consistent with the stoichiometric ratio of the balanced chemical reaction Ti6Al4V (Ti85.6-Al10.6-V3.6, at%) + Al $\rightarrow$ Al_3(Ti,V). This

indicates that the reason for the relative growth rate reverse observed at 630 °C is not caused by different vanadium content in Al_3Ti layer.

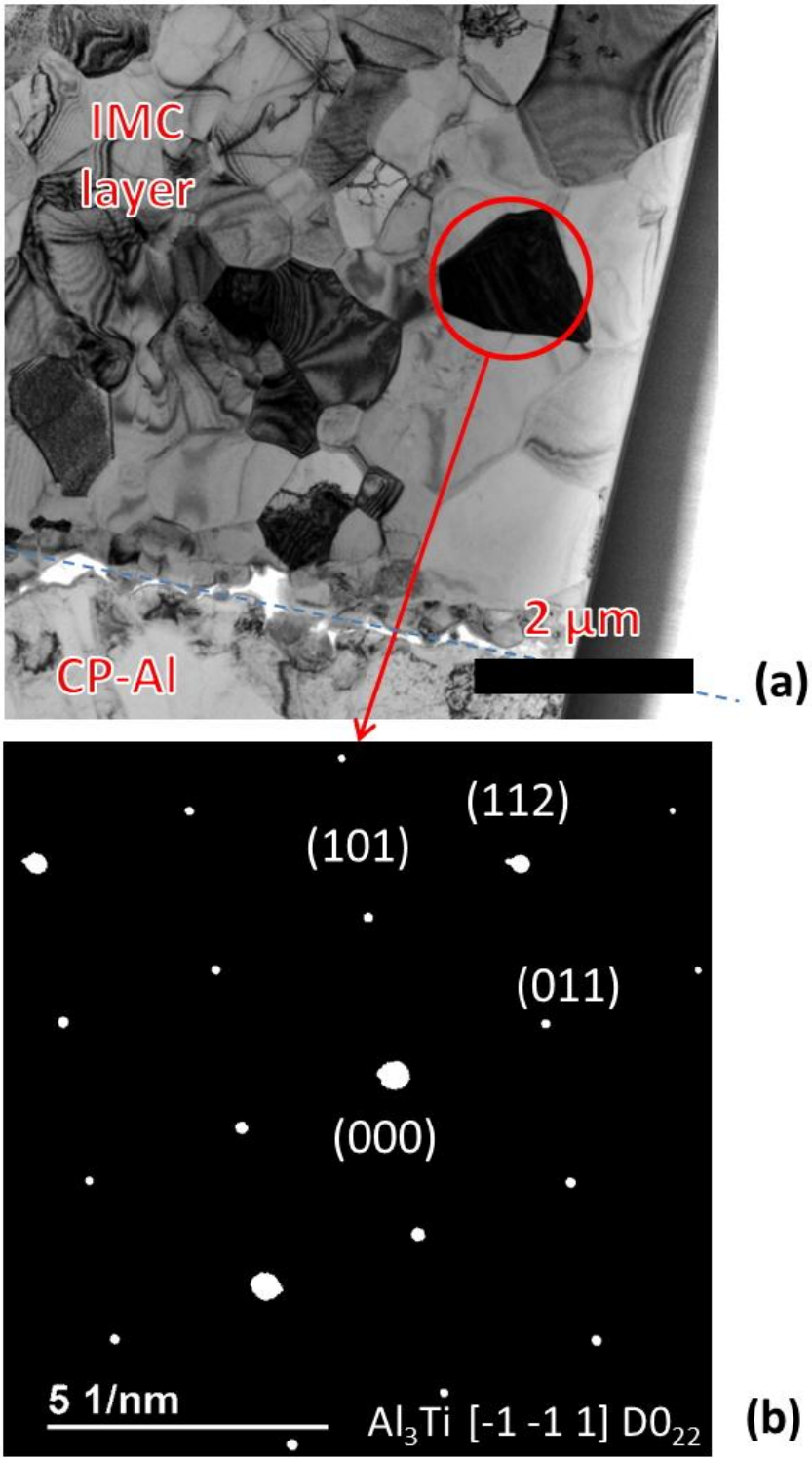

Figure 6.28 (a) TEM bright field image of the IMC layer grown in an CP-Al/Ti6Al4V joint annealed at 550 °C for 24 h, (b) the diffraction pattern of the selected area as labelled in (a).

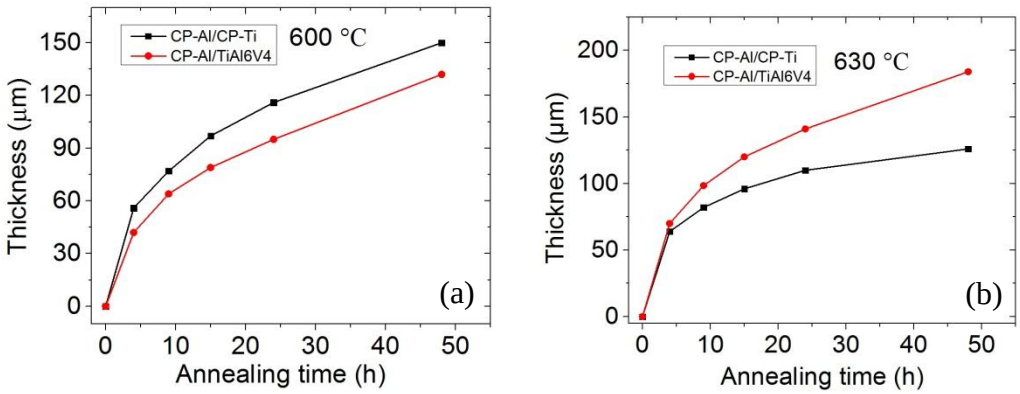

Figure 6.29 Growth kinetics of Al_3Ti layer between CP-Al and CP-Ti (black line) and between CP-Al and Ti6Al4V (red line) at 600 °C (a) and 630 °C (b) respectively.

The microstructure features of typical reaction layers annealed at different temperatures and in different materials combinations are shown in Figure 6.30, Figure 6.31, Figure 6.32 and Figure 6.33.

It can be seen that the grain size in the reaction layers are not uniform, the grain size is larger in the middle of the reaction layer and in the region near the Al side. Also, at 600 °C the grain size of the coarse grain zone (CGZ) in the CP-Al/CP-Ti weld is slightly larger than that in the CP-Al/Ti6Al4V weld, as shown in Figure 6.30 and Figure 6.31.

However, the situation became quite different when annealing temperature was 630 °C. At 630 °C, the grain size of the CGZ in the CP-Al/CP-Ti weld is about 3 times larger than that in the CP-Al/Ti6Al4V joint, as shown in Figure 6.32 and Figure 6.33.

As discussed in Chapter 5, the Al_3Ti grain size can pronouncedly affect the effective diffusion in the reaction layer and then can influence the Al_3Ti layer growth rate. In this case, the comparison of the Al_3Ti grain size in different combinations and at different annealing temperatures suggests that the presence of vanadium greatly retarded the Al_3Ti grain growth at higher annealing temperature

(630 °C) and then retained a greater fraction of grain boundary in the Al_3Ti layer, thus the Al_3Ti layer grew much faster in the CP-Al/Ti6Al4V weld. However, at a lower annealing temperature of 600 °C, both the Al_3Ti grains in CP-Al/CP-Ti weld and in CP-Al/Ti6Al4V weld grew very slowly, and then there was no significant difference in the Al_3Ti grain size in the layer, hence the Al_3Ti layer growth rate was dominated by the concentration gradient of Al and Ti.

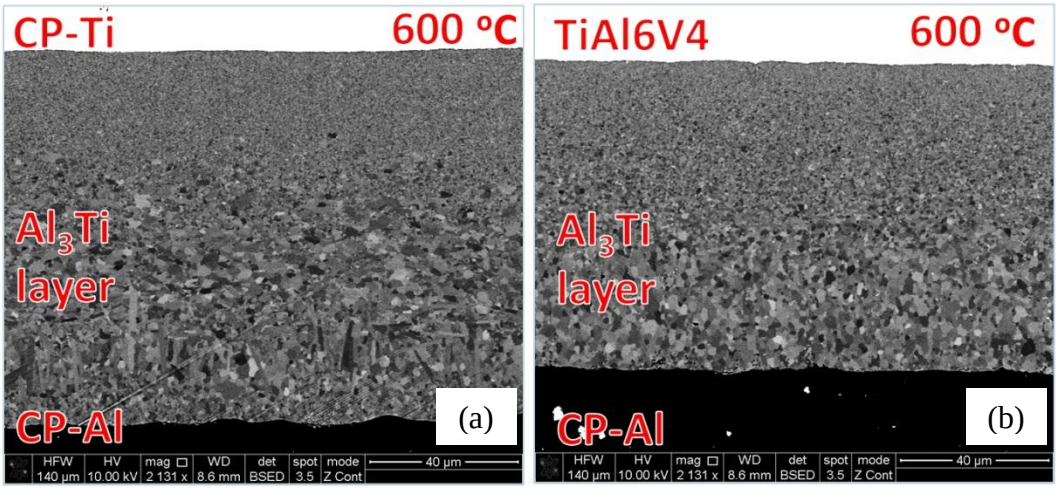

Figure 6.30 Comparison of Al_3Ti grain size and reaction layer thickness annealed at 600 °C for 15 h, (a) IMC layer between CP-Al and CP-Ti, (b) IMC layer between CP-Al and Ti6Al4V. (at the same magnification)

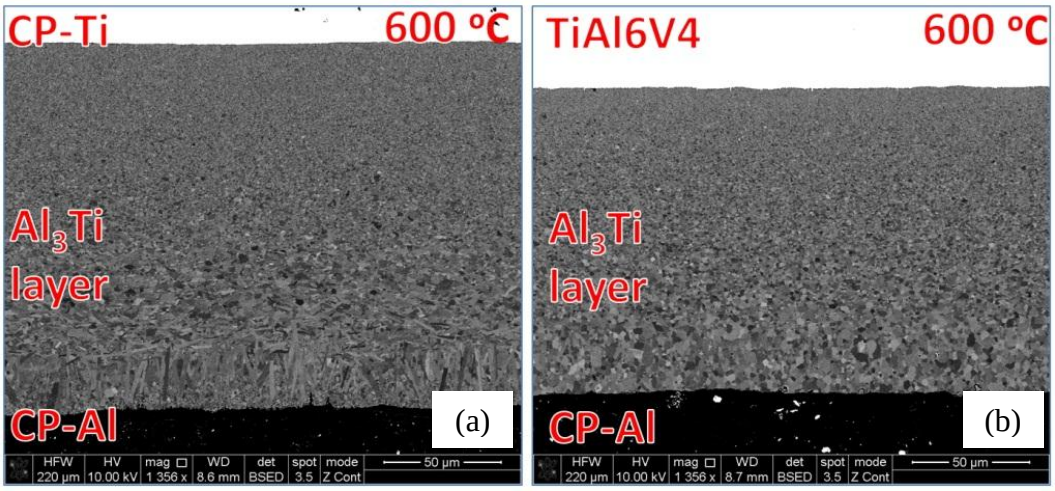

Figure 6.31 Comparison of Al_3Ti grain size and reaction layer thickness annealed at 600 °C for 48 h (a) IMC layer between CP-Al and CP-Ti, (b) IMC layer between CP-Al and Ti6Al4V. (at the same magnification)

6.2.4 Discussion of effect of vanadium on Al_3Ti grain boundary energy

As shown in Figure 6.32 and Figure 6.33, the presence of vanadium greatly retarded the Al_3Ti grain growth. Since the driving force for grain growth is the drop of total grain boundary energy, it can be deduced that the solid solution of vanadium in Al_3Ti reduced the grain boundary energy or grain boundary mobility.

It is possible that vanadium segregation on the Al_3Ti grain boundaries reduced the grain boundary energy or increased the grain boundary mobility, but this possibility seems remote, as the atom size and other properties of vanadium are expected to be similar to titanium atom, which would be expected to result in little driving force for segregation.

6.2.5 Discussion of other possibilities of vanadium segregation

(1) The possibility of Vanadium segregation on Al_3Ti/Ti interface

As the solubility of vanadium in both Ti and in Al_3Ti is quite high [97, 217, 218], the vanadium segregation on Al_3Ti/Ti interface is expected to be of low possibility. Usually low solubility alloying elements are easier to be segregated on interface.

(2) The possibility of Vanadium segregation on Al/Al_3Ti interface

Accoring to the Al-V phase diagram [219], the solubility of V in Al is quite low. So the possibility of vanadium segregation on Al_3Ti/Al interface is higher than on Al_3Ti/Ti interface. However, by STEM-EDS study, no vanadium segregation was observed on the Al_3Ti/Al interface, as shown in Figure 6.34. Besides, some voids were observed on the interface (Figure 6.34). The formation mechanism of the voids will be discussed in Section 6.2.7.

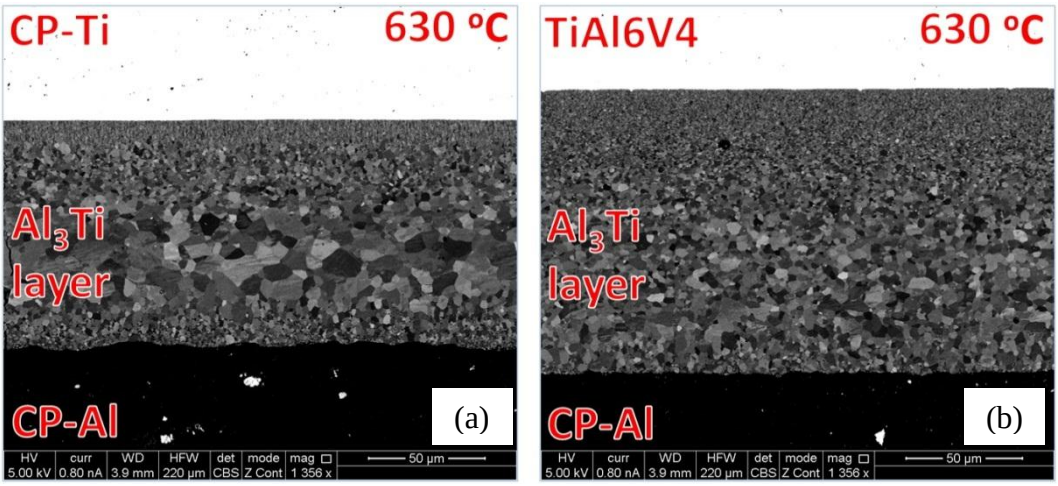

Figure 6.32 Comparison of Al_3Ti grain size and reaction layer thickness annealed at 630 °C for 15 h. (a) IMC layer between CP-Al and CP-Ti, (b) IMC layer between CP-Al and Ti6Al4V. (at the same magnification).

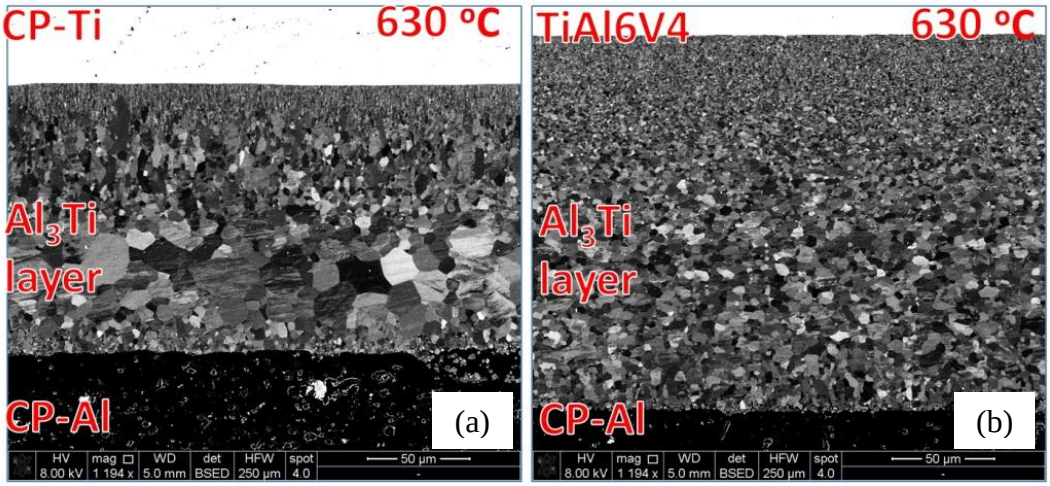

Figure 6.33 Comparison of Al_3Ti grain size and reaction layer thickness annealed at 630 °C for 48 h. (a) IMC layer between CP-Al and CP-Ti, (b) IMC layer between CP-Al and Ti6Al4V. (at the same magnification).

6.2.6 Effect of vanadium on anisotropic growth of Al_3Ti

As shown in Figure 6.35, the anisotropic growth of Al_3Ti growth was significantly retarded by the presence of vanadium. Usually, the anisotropic growth of Al_3Ti ($D0_{22}$ structure) is due to the much lower surface energy of (001) plane compared with that of all other planes [142]. Thus, the influence of vanadium on the anisotropic growth of Al_3Ti indicates that the relative surface energy of (001) plane

might have been increased by the addition of V, so that the surface energy difference between different crystal planes became smaller.

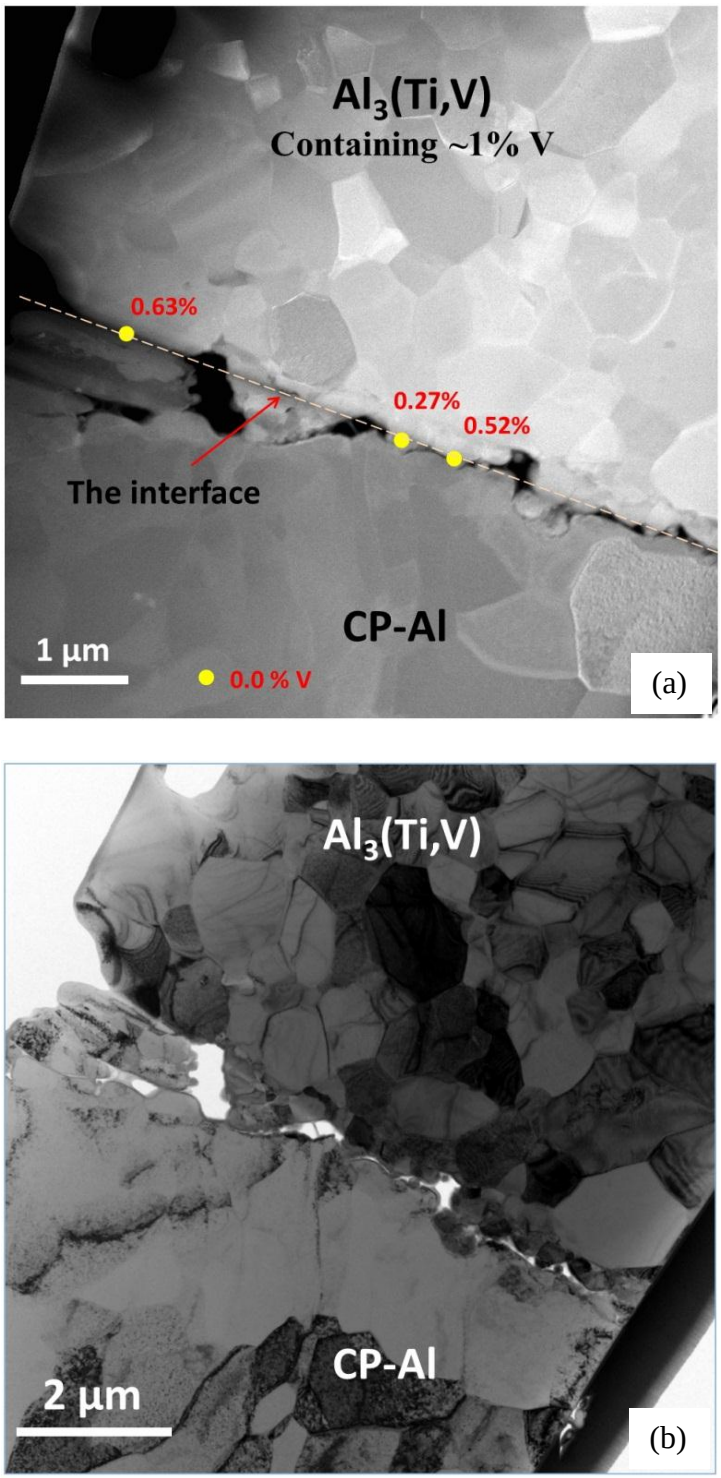

Figure 6.34 The V concentration on the Al_3Ti/Al interface measured by STEM-EDS, (a) the HAADF-STEM image of the Al_3Ti/Al interface, the yellow dots indicate the positions of EDS analysis, the red percentages are the corresponding V concentrations measured at these positions. (b) the bright field image of the same region. (annealed at 550 °C for 24 h)

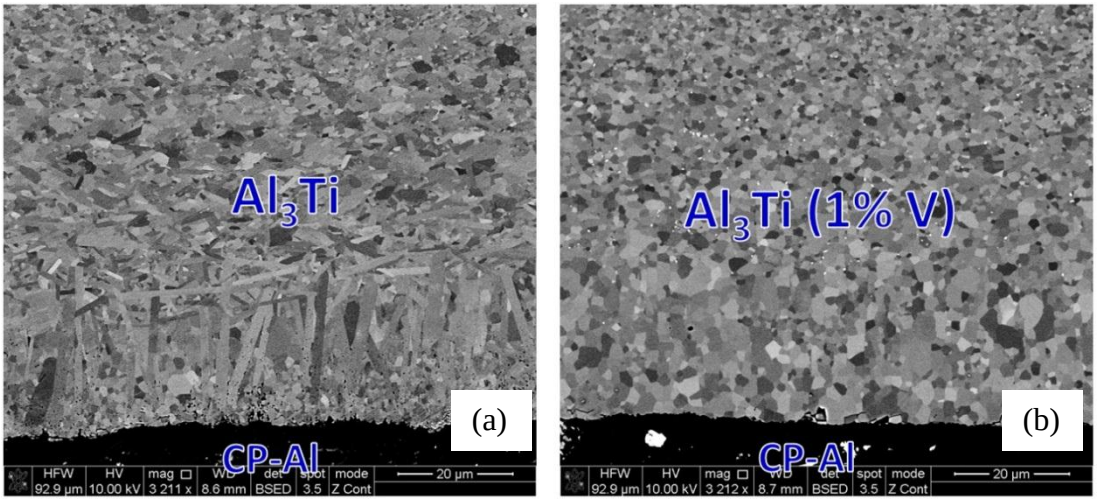

Figure 6.35 Anisotropic growth of Al_3Ti greatly retarded by V, (a) no vanadium present, (b) containing vanadium. (annealed at 600 C for 48 h) .

6.2.7 Discussion of the effect of V on void formation

By comparing Figure 6.36 (a) and (b), it can be seen that there are less voids at the Al_3Ti/CP-Al interface in the annealed CP-Al/Ti6Al4V joint than in the annealed CP-Al/CP-Ti joint. The formation of voids in diffusion couples are usually thought to be caused by the Kirkendall effect, which is the result of the non-reciprocal atom fluxes of the two diffusion species in the case of vacancy diffusion mechanism. The faster Al diffusion compared with Ti diffusion in Al/Ti system has been widely realized [144, 148]. Thus, Kirkendall effect could be one important reason for the formation of the voids. However, in the case that there is a third intermetallic phase formed on the interface of the two different metals, there is usually a volume contraction due to the formation of the intermetallic compound [220, 221]; and this volume contraction also may lead to the formation of voids [220, 222, 223]. Thus, in the case of the present study, it is possible that the observed voids are caused by both the Kirkendall effect and the volume contraction effect. It is reported that there is a volume contraction of ~6% [220, 221] associated with the formation of Al_3Ti (i.e., the mole volume contraction associated with the reaction $3Al + Ti = Al_3Ti$). Tiffin et al. [220] and Besser et al. [222, 223] suggested that the

stress caused by the volume contraction is an important reason for the void formation on the Al/Ti reaction interface. Yu et al. [222, 223] suggested that the stress around the voids is an important driving force for the void growth in Cu/Sn diffusion system, in which intermetallic compounds also forms on the dissimilar metal interface.

Therefore, in the case of the present study, it is proposed that both Kirkendall effect and the volume contraction effect lead to the formation (nucleation) of the voids, and the stress caused by the volume contraction could be a driving force for the void growth.

The effect of V on the unit cell volume of Al_3Ti:

Previous investigations by both Lee et al. [96, 224] and Takahashi et al [97] showed that the addition of vanadium in Al_3Ti was found to be able to increase the unit cell volume of Al_3Ti. Therefore, on the Al_3Ti/CP-Al interface in the annealed CP-Al/Ti6Al4V joint, due to around 1% vanadium solid solution in Al_3Ti layer, the volume contraction is reduced, leading to smaller void volume on the interface. But this effect is a minor one, as the unit cell volume change is small. According to the lattice parameters reported by Lee et al. [96, 224], with the presence of 6.25 at.% V in Al_3Ti, the a and c only increased 0.47% and 0.33%.

The effect of V on the gross vacancies clustering in Al side and the gross Al_3Ti layer volume contraction:

(1) Less vacancy clustering

The presence of vanadium slowed down the Al_3Ti layer growth (in the case of annealing at 600 °C, see Section 6.2.2), i.e. less Al_3Ti gross formation. Less Al_3Ti

formation means less (non-reciprocal) Al and Ti atom fluxes, i.e. less vacancies clustering in the Al side. Thus, a lower volume of voids were formed.

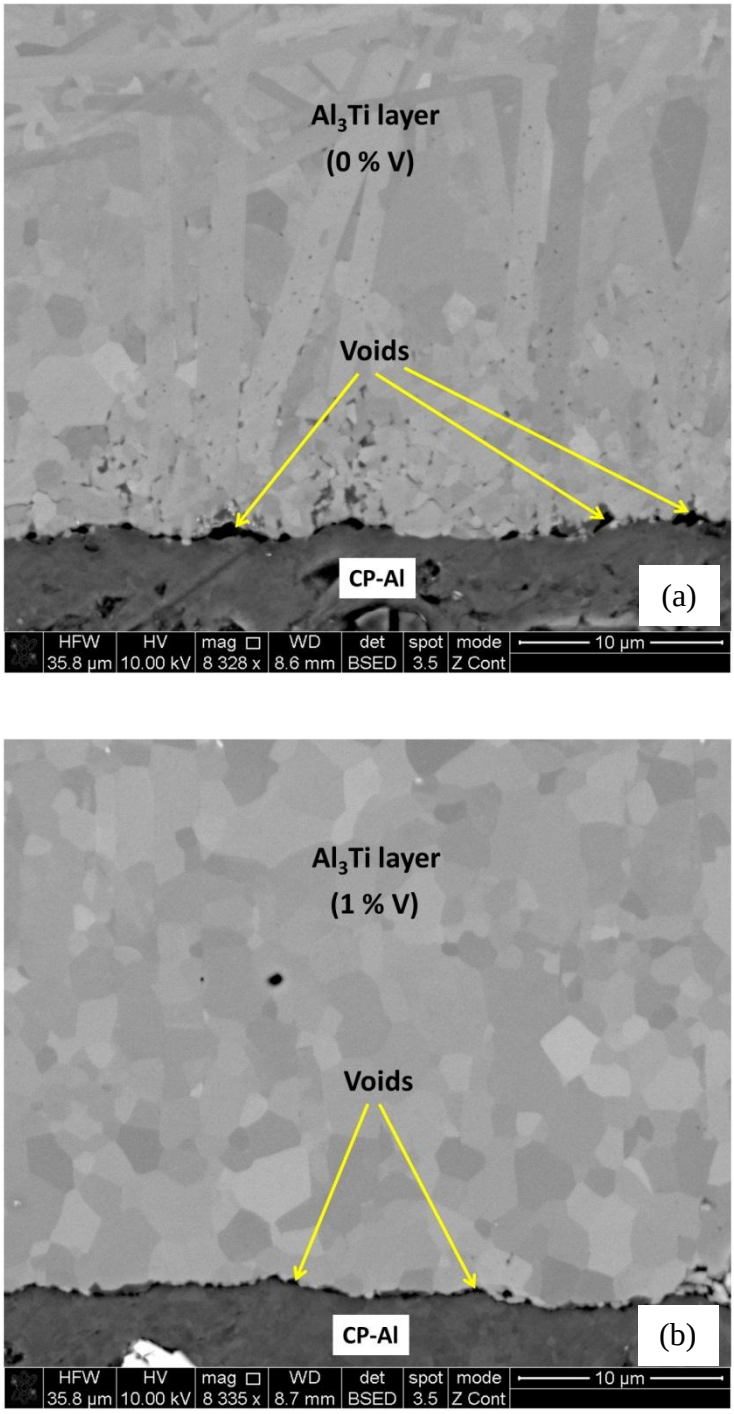

Figure 6.36 Voids on the Al_3Ti/CP-Al interface, (a) in the IMC layer in annealed CP-Al/CP-Ti joint, (b) in the IMC layer in annealed CP-Al/Ti6Al4V joint containing V, both were annealed at 600 °C for 48 h. (at the same magnification)

(2) Less gross Al_3Ti layer volume contraction

Less Al_3Ti gross formation (thinner Al_3Ti layer) also resulted in less absolute volume contraction thus reduced the void volume. In the case of annealing at 600 °C for 48 h, the Al_3Ti layer in the CP-Al/Ti6Al4V joint is 12% thinner than that in the CP-Al/CP-Ti joint.

6.2.8 Other microstructural features of $Al_3(Ti,V)$ layer

As shown in Figure 6.30, Figure 6.31, Figure 6.32 and Figure 6.33, the presence of vanadium in the Al_3Ti the layer did not change the tendency for smaller Al_3Ti grains in the region close to Ti side and larger grains in the region close to Al side. Also it can be seen with the increase of annealing temperature from 600 °C to 630 °C, the thickness of coarse grain zone increases significantly, which is the same as noted in annealed CP-Al/CP-Ti joint.

As stated in section 6.2.2, although the Al_3Ti (containing V) grain size increase with increasing annealing temperature is far less significant than that without alloying elements, the Al_3Ti grain size of the coarse grain zone still increased around 2 times when the annealing temperature increased from 600 °C to 630 °C, as shown in Figure 6.37.

6.3 Trapped Al islands in IMC layer

As mentioned in Section 6.1.2.1, Al islands were found trapped in the IMC layer in the annealed AA2139/CP-Ti joint. Besides, the trapped Al islands were also observed in IMC layers in annealed CP-Al/CP-Ti joint and in annealed CP-Al/Ti6Al4V joint (Figure 6.38), although the Al islands in the IMC layer (CP-Al/Ti6Al4V) are very tiny. Other investigations also reported the observation of Al islands in IMC layer [76, 212] by both STEM-EDS and SEM. Among them, Dietrich et al. [212] suggested that the formation of Al islands in IMC layer is due

to the mechanical impact and the short process time during solid-state bonding (their Al/Ti sample was produced by a co-extrusion technique). This is obviously not the reason for Al island formation in the present study, since there is no mechanical impact during static annealing and the annealing time was very long.

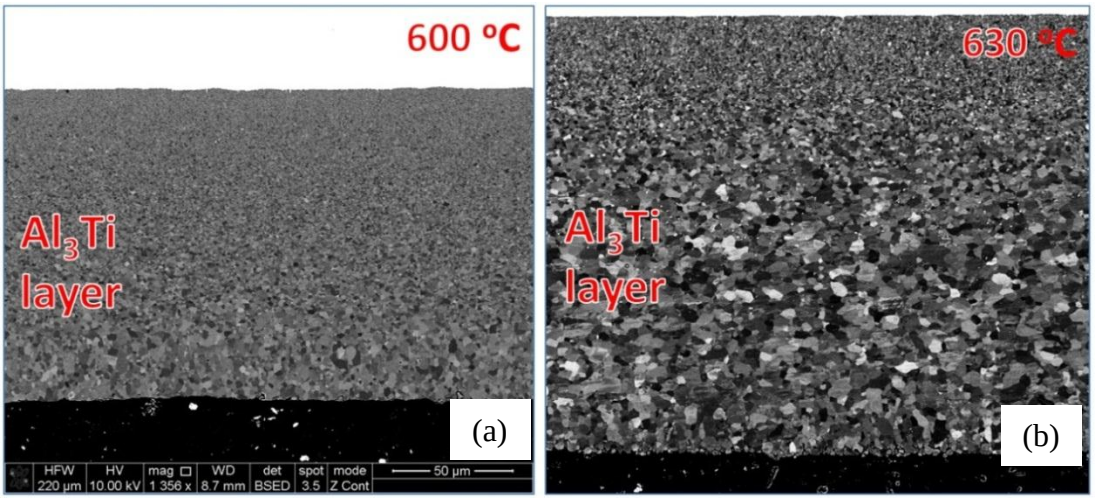

Figure 6.37 Effect of annealing temperature on Al_3Ti (containing V) grain size, (a) annealed at 600 °C, (b) annealed at 630 °C (both annealed for 48 h, at the same magnification).

6.3.1 Formation mechanism of the trapped Al islands

The orientation relationship between Al islands and the Al_3Ti grains

Some typical trapped Al islands and the Al_3Ti grains in contact them were selected for orientation relationship analysis, as shown in Figure 6.39. Table 6.1 lists the the Euler angles (i.e. orientations in the sample coordinate system, Figure 6.6) of the trapped Al islands and the neighbouring Al_3Ti grains acquired by EBSD. Figure 6.40 presents the stereographic projection of the {100} and {111} planes of the Al-1 grain and the stereographic projection of {100} and {112} planes of the Al_3Ti-1 grain. To know the exact projection positions of the above mentioned plans, Table 6.2 presents the measured position data (angles and the distances to the projection plane centre) of the projection points of the {100} planes of Al-1 grain and Al_3Ti-1 grain.

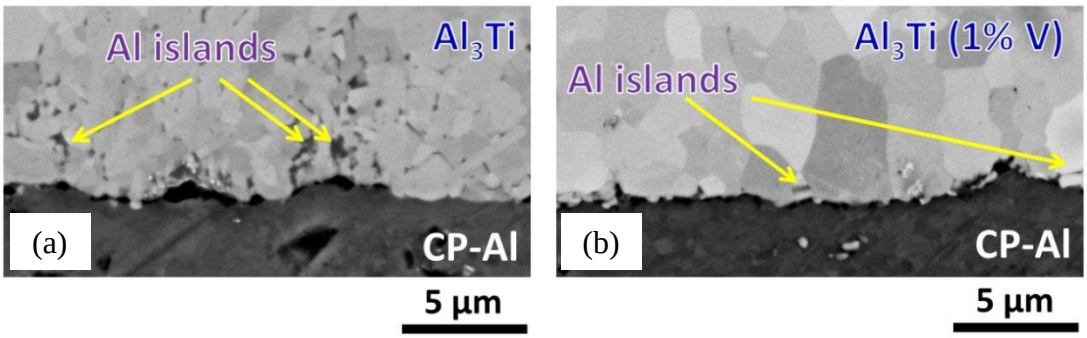

Figure 6.38 Trapped Al islands in IMC layer, (a) in annealed CP-Al/CP-Ti joint, (b) in annealed CP-Al/Ti6Al4V joint, both were annealed at 600 ℃ for 48 h.

From Table 6.2 and Figure 6.40, it can be seen that the {100} planes of Al-1 grain and those of Al_3Ti-1 grain have the same projection position on the projection plane, which means they are parallel with each other. It should be noted that for Al_3Ti, the (100) plane is not in the same family of lattice planes with (010) and (001) planes due to the different Ti atom amount and distribution in these planes.

Likewise, as shown in Figure 6.40, {112} planes of the Al_3Ti-1 grain are also parallel with the {111} planes of the Al-1 grain, as they also have the same stereographic projection.

Similarly, as presented in Figure 6.42 and Figure 6.44, the same parallel orientation relationship also exists between Al-2 grain and Al_3Ti-2 grain and between Al-3 grain and Al_3Ti-3 grain. All these parallel relations are also shown by the virtually recreated unit cells of the Al grains and the Al_3Ti grains as presented in Figure 6.41, Figure 6.43 and Figure 6.45.

In summary, a constant orientation relationship was observed between a trapped Al island and the Al_3Ti grain adjacent to it and just below it. The orientation relationship is :

$(111)Al//(112)Al_3Ti$,
$(001)Al//(001)Al_3Ti$
$[110]Al//[110]Al_3Ti$

This favourable orientation relationship between Al and Al_3Ti has also been experimentally observed by other investigations [143, 144]. As stated in Section 2.6.6, the parallel relationship between Al (111) and Al_3Ti (112) plane is due to the very small mismatch between these two planes. The mismatches in two crystal directions between these two planes were calculated to be ~1% [143]. The very small mismatch means the interfacial energy is quite small. An interface with a single layer of atom matching will grow slowly and will end up becoming the dominant surface.

Therefore, formation mechanism of the trapped Al islands is postulated to be as follows: when the (112) plane of a growing Al_3Ti grain meets the (111) plane of an Al grain on the Al/reaction layer interface, the Al_3Ti grain growth rate normal to the Al (111) plane becomes much slower compared with the growth rate of surrounding other Al_3Ti grains, which do not have this type orientation relationship with Al grains. As a result, the small patch of Al is trapped by other relatively rapidly growing Al_3Ti grains that engulf it. This formation mechanism is also illustrated in Figure 6.46.

It is worth noting that the stereographic projection positions of these parallel planes are not ideally overlapped due to the slight lattice parameter changes (compared the with the lattice of Al) caused by the Ti atoms in Al_3Ti.

Apart from the above mentioned mechanism, there could be another possible mechanism for the formation of the trapped Al islands, the anisotropic growth of Al_3Ti, which will be discussed in Section 6.3.2.4.

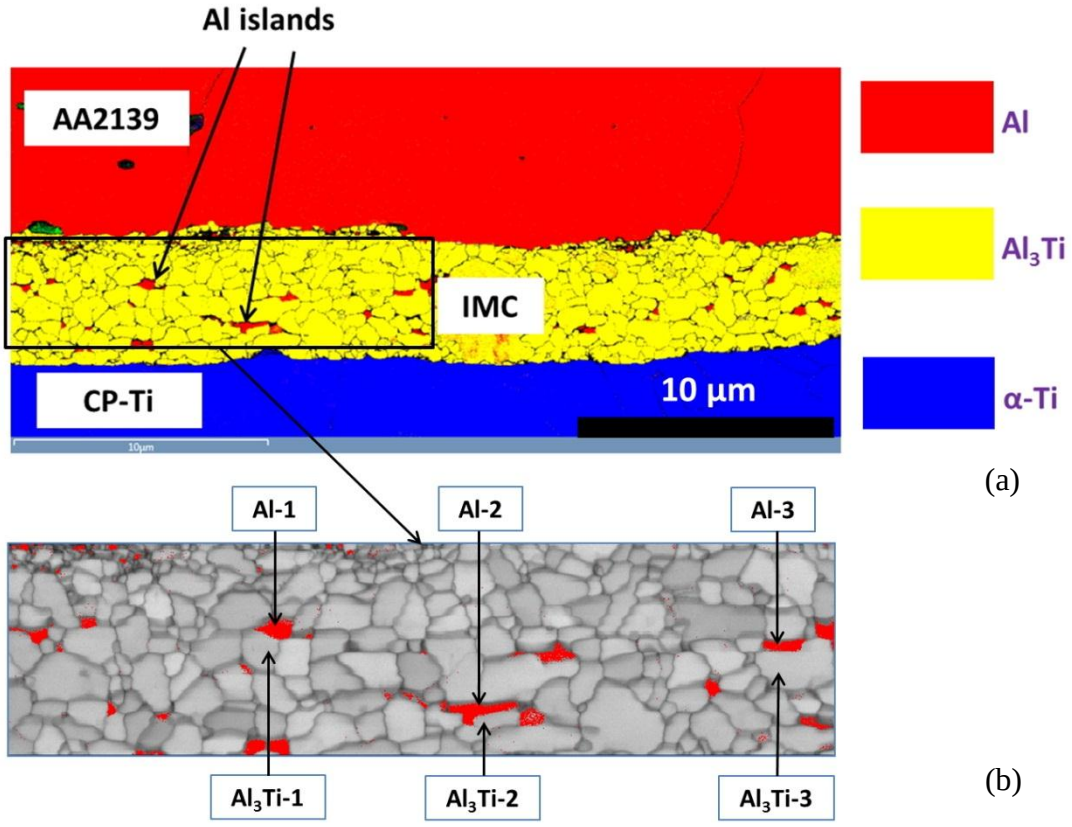

Figure 6.39 The typical trapped Al islands (Al-1, Al-2 and Al-3) and the Al_3Ti grains (Al_3Ti-1, Al_3Ti-2 and Al_3Ti-3) just below them selected for orientation relationship analysis (annealed at 500 ℃ for 480 h), (a) EBSD phase map, (b) EBSD Al phase map and EBSD band contrast image.

Table 6.1 The Euler angles (orientation) of the trapped Al islands and the Al_3Ti grains just below them in the sample coordinate system.

	Euler angles		
Grain	**ϕ 1**	**Φ**	**ϕ 2**
Al-1	93.5	46.9	69.0
Al_3Ti-1	89.7	47.8	71.4
Al-2	276.3	40.4	74.4
Al_3Ti-2	100.3	137.0	17.7
Al-3	101.7	24.2	86.3
Al_3Ti-3	100.8	113.8	88.8

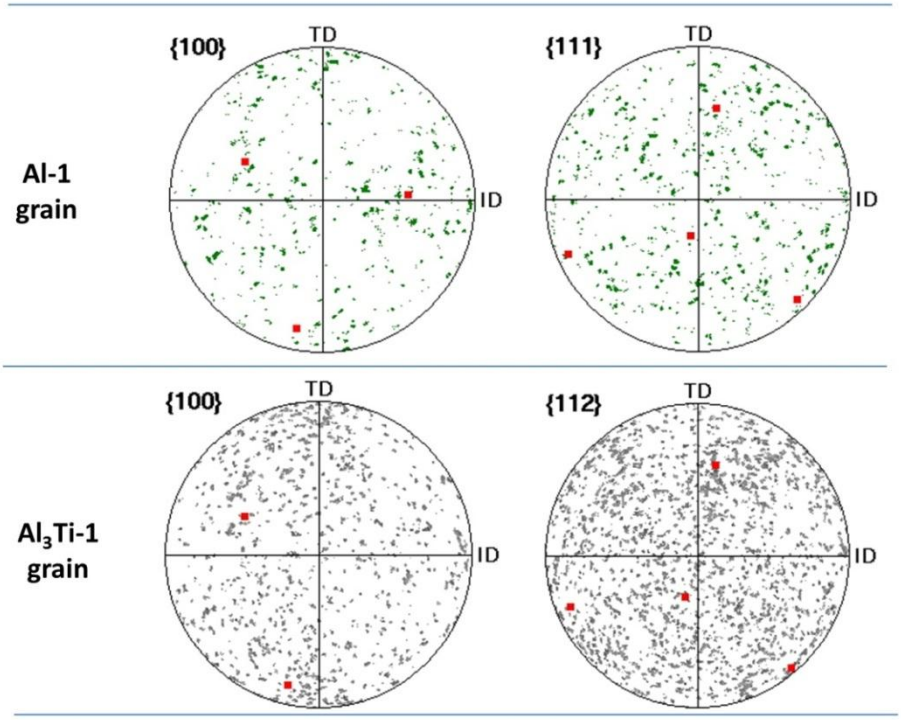

(a)

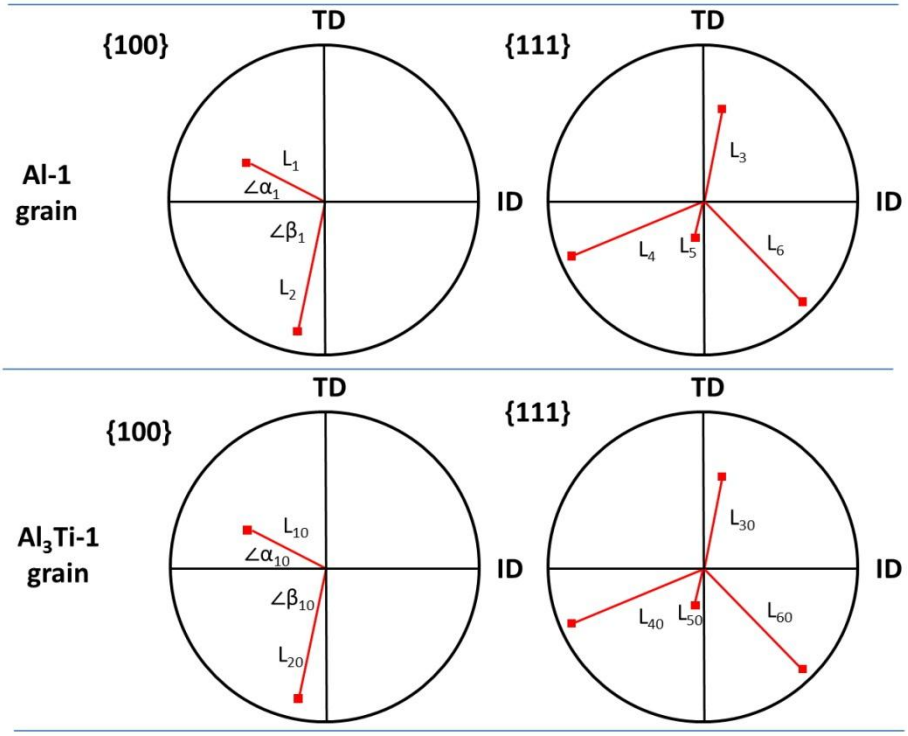

(b)

Figure 6.40 The stereographic projection of the {100} and {111} planes of Al-1 grain (the red dots are the projections of these planes) and the stereographic projection of the {100} and {112} planes of Al_3Ti-1 grain, (a) exported pole figures from HKL CHANNEL5 system (an EBSD post-processing software) (b) simplified images from (a).

Table 6.2 The measured positions of the projection points of the the {100} and {111} planes of the Al-1 grain and Al_3Ti-1 grain

Angle and length		**Angle and length**	
$\angle\alpha_1$	27.05°	$\angle\beta_1$	76.3°
$\angle\alpha_{10}$	26.9°	$\angle\beta_{10}$	76.4°
L_1	0.56	L_2	0.88
L_{10}	0.56	L_{20}	0.88

Note: The radius of the projection round was treated as unit length.

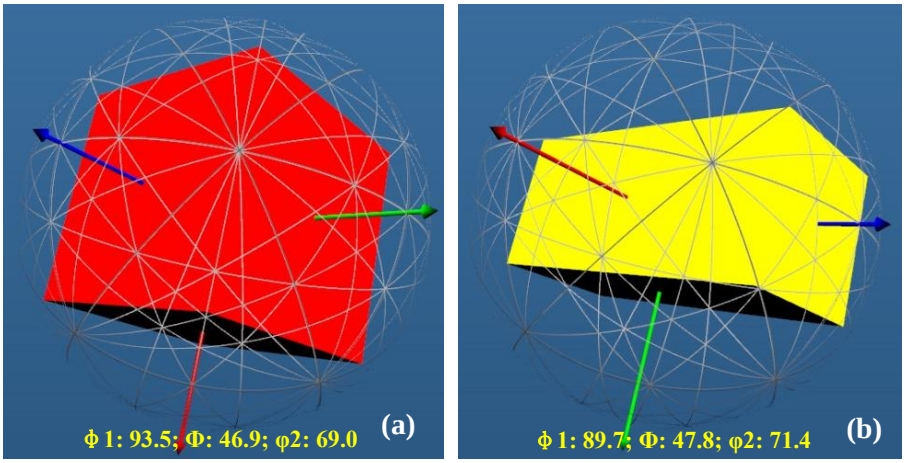

Figure 6.41 The virtually recreated unit cell (orientation) of Al-1 grain (a) and Al_3Ti-1 grain (b) in the sample coordinate system using the measured Euler angles by Aztec software.

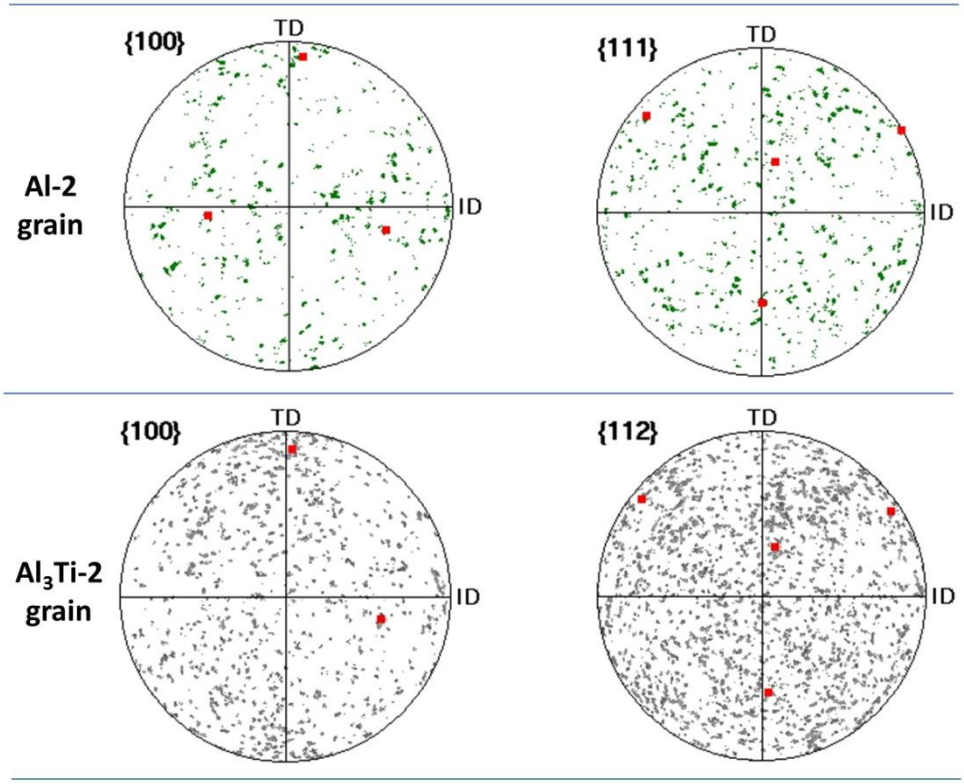

Figure 6.42 The stereographic projection of the {100} and {111} planes of Al-2 grain (the red dots) and the stereographic projection of the {100} and {112} planes of Al_3Ti-2 grain.

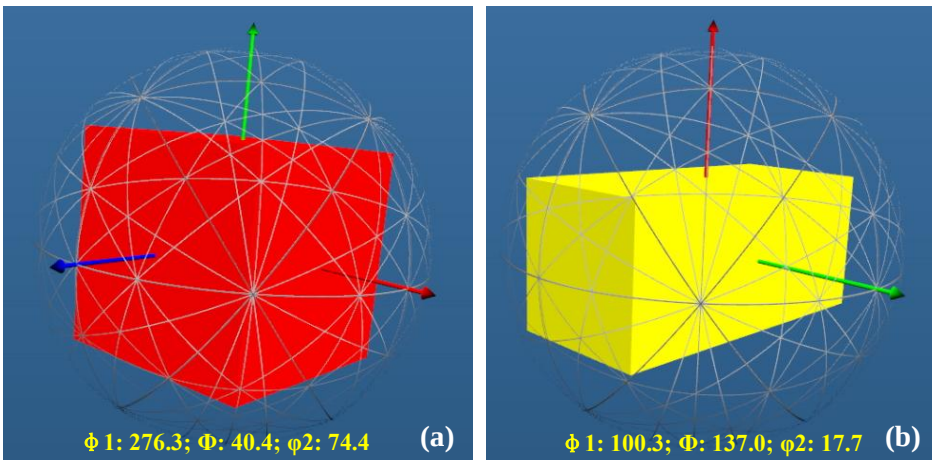

Figure 6.43 The virtually recreated unit cell (orientation) of Al-2 grain (a) and Al_3Ti-2 grain (b) in the sample coordinate system using the measured Euler angles by Aztec software.

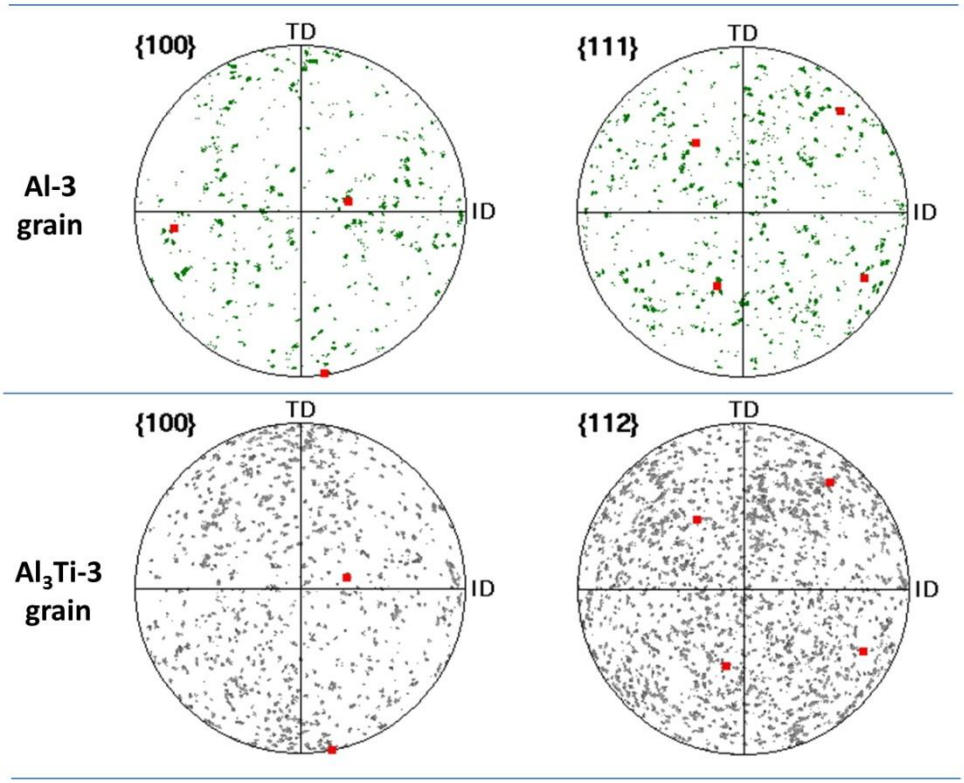

Figure 6.44 The stereographic projection of the {100} and {111} planes of Al-3 grain (the red dots) and the stereographic projection of the {100} and {112} planes of Al_3Ti-3 grain.

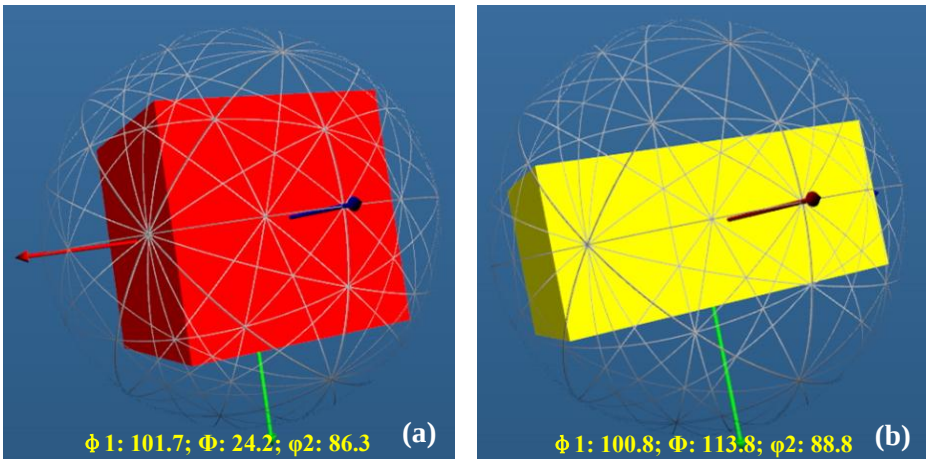

Figure 6.45 The virtually recreated unit cell (orientation) of Al-3 grain (a) and Al_3Ti-3 grain (b) in the sample coordinate system using the measured Euler angles by Aztec software.

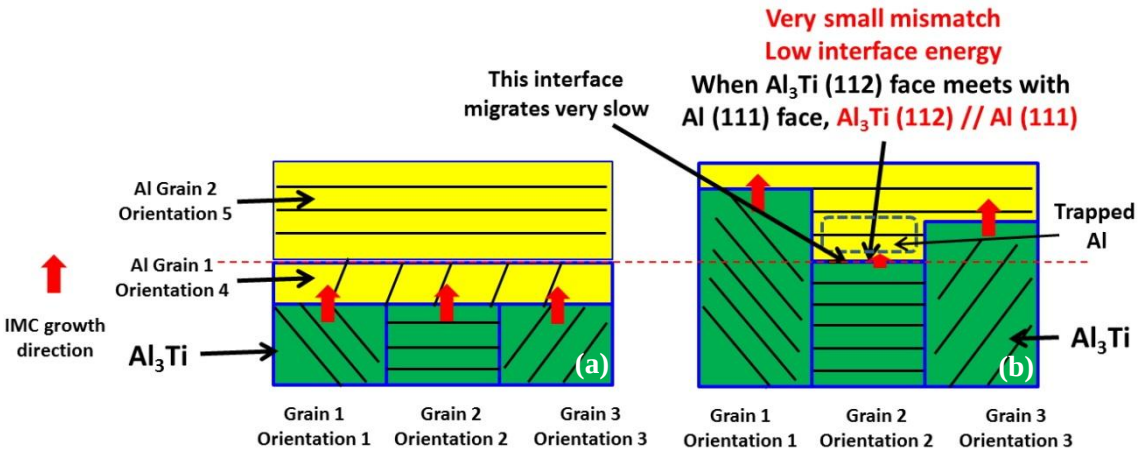

Figure 6.46 Schematic diagram showing the formation mechanism of trapped Al islands, (a) early stage, (b) follow-up stage. (Assumption: The (111) plane of Al Grain 2 is parallel with the (112) plane of Al_3Ti Grain 2, and there is no such parallel relationship between other grains.)

6.3.2 Effect of annealing time and alloying elements on Al islands

6.3.2.1 Al island distribution in IMC layer in annealed CP-Al/CP-Ti joint and annealed CP-Al/Ti6Al4V joint (Effect of annealing time)

As shown in Figure 6.47 and Figure 6.36, the Al islands only exist in the region close to Al, however there is no Al island in the middle region of Al_3Ti layer and in the region close to Ti. This suggests that the early-formed Al islands disappeared with increasing annealing time. The disappearance of early-formed Al islands suggests that though the interfacial reaction on the boundaries of Al islands is slower than that on the growth front of the whole IMC layer, solid state reaction indeed was occurring around the Al islands slowly and with the increase of annealing time the early-formed Al islands are eventually reacted and incorporated into the Al_3Ti layer.

6.3.2.2 Al island distribution in IMC layer in annealed AA2139/CP-Ti joint (Effect of alloying elements from AA2139)

Quite different from the fast IMC layer growth in the CP-Al/CP-Ti joint, the IMC layer grew much slower in annealed AA2139/CP-Ti joint (as compared in Figure

6.2), thus the whole IMC layer thickness is much thinner. It takes 480 h for the IMC layer growing to 8 μm thick at 500 °C, which is extremely slow. (by way of contrast IMC layer thickness between Al and Mg can reach 154 μm after 24 h annealing at 360 °C [170].)

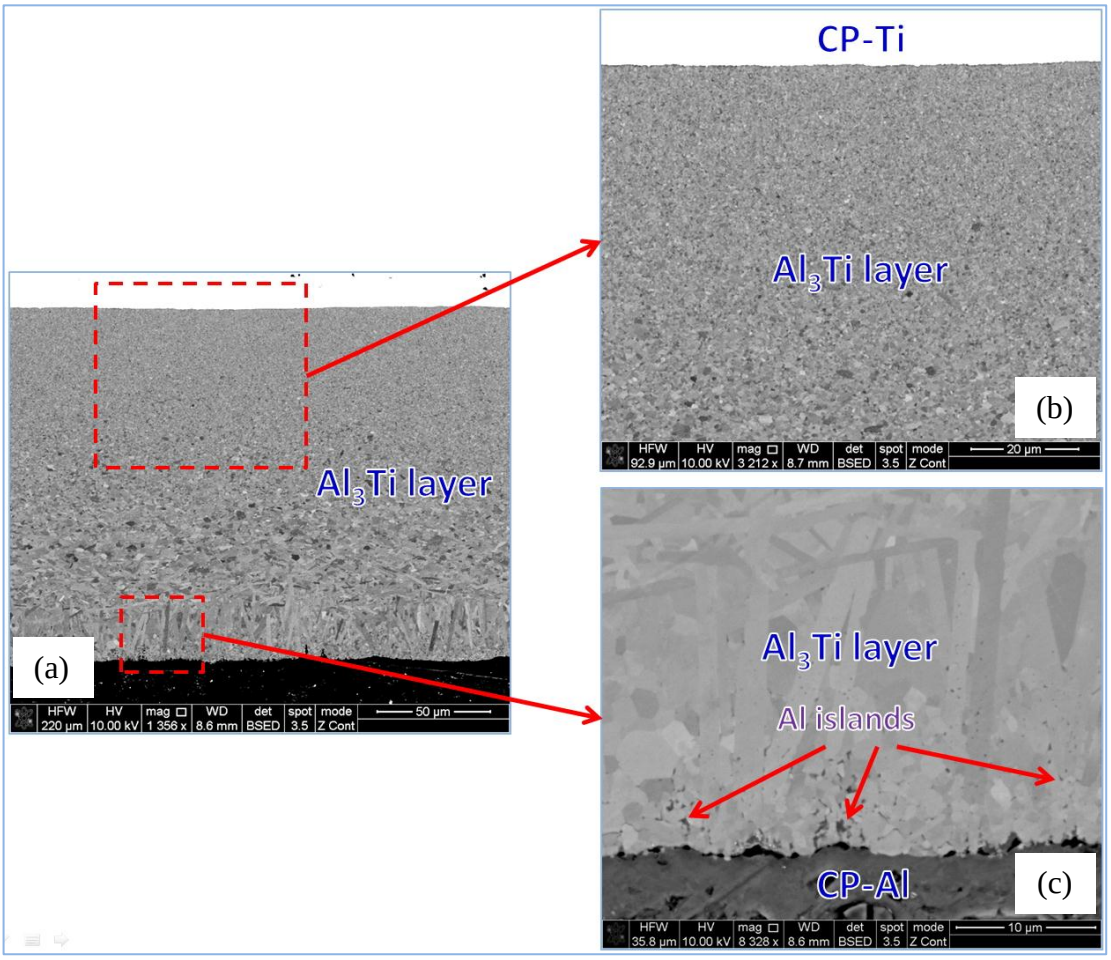

Figure 6.47 Distribution of Al islands in IMC layer, annealed at 600 ℃ for 48 h, (a) low magnification BSE image, (b) high magnification BSE image of the region near the Ti side, (c) high magnification BSE image of the region near the Al side.

Similarly, the distribution of Al islands in IMC layer in annealed AA2139/CP-Ti joint is also quite different. Their distribution is uniform in the thickness direction of the IMC layer, as shown in Figure 6.4, Figure 6.48 and Figure 6.49. This is due to both the very thin IMC layer and the greatly retarded Ti atom diffusion through IMC layer, thought to be due to the presence of Cu and Si in the Al_3Ti layer (as

discussed in Section 6.1.3). Without sufficient Ti atom supply the Al islands cannot be reacted.

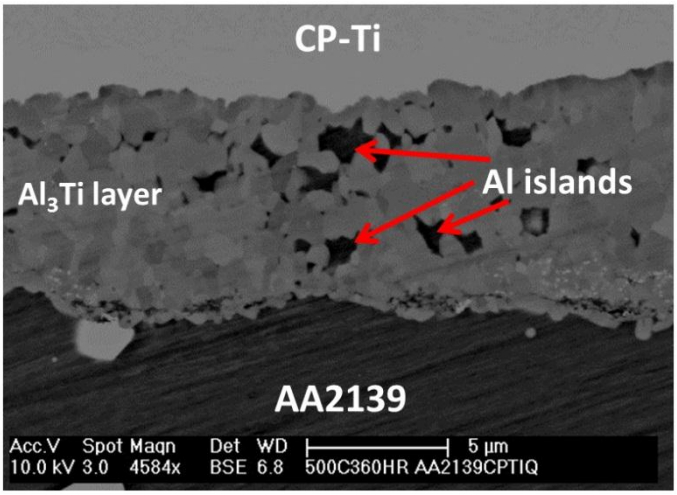

Figure 6.48 Al islands in IMC layer in annealed AA2139/CP-Ti joint (annealed at 500 ℃ for 360 h)

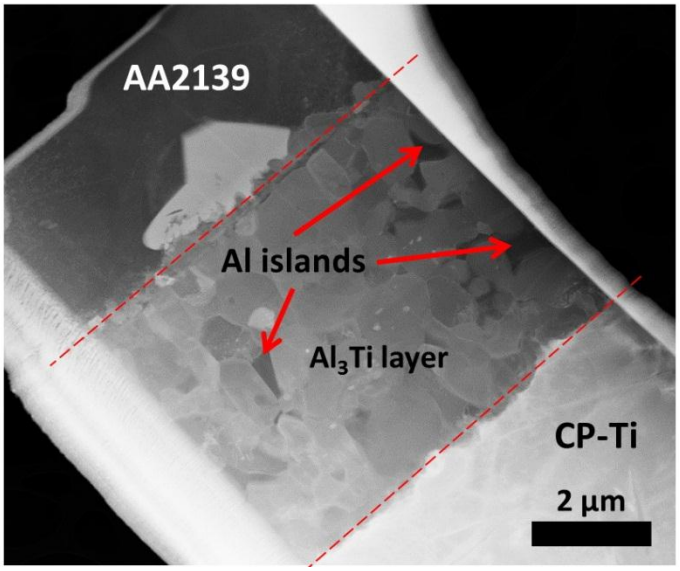

Figure 6.49 Trapped Al islands in the reaction layer in annealed AA2139/CP-Ti joint, TEM-HAADF image (annealed at 500 ℃ for 360 h)

6.3.2.3 Discussion of the possibility of alloying elements segregation on the interface between Al islands and Al_3Ti

Another possible reason for the very persistent existence of the trapped Al islands in the IMC layer (AA2139/CP-Ti), compared with the rapidly disappearing Al

islands in the IMC layer (CP-Al/CP-Ti) and the IMC layer (CP-Al/Ti6Al4V), could be that alloying elements (eg. Cu) segregated at the interface between Al islands and Al_3Ti act as a reaction barrier.

To determine whether there is alloying element segregation on the interface between Al islands and Al_3Ti, STEM-EDS analysis was performed in the region around a trapped Al island, as show in Figure 6.50. It can be seen there is no visible alloying elements segregation on the interface. Only a few Cu-rich particles were observed on the interface, which is common in Al-Cu alloys. This indicates that very persistent existence of the trapped Al islands in the IMC layer (AA2139/CP-Ti) was not be caused by alloying elements segregation, but by the strongly retarded Ti diffusion through the Al_3Ti layer.

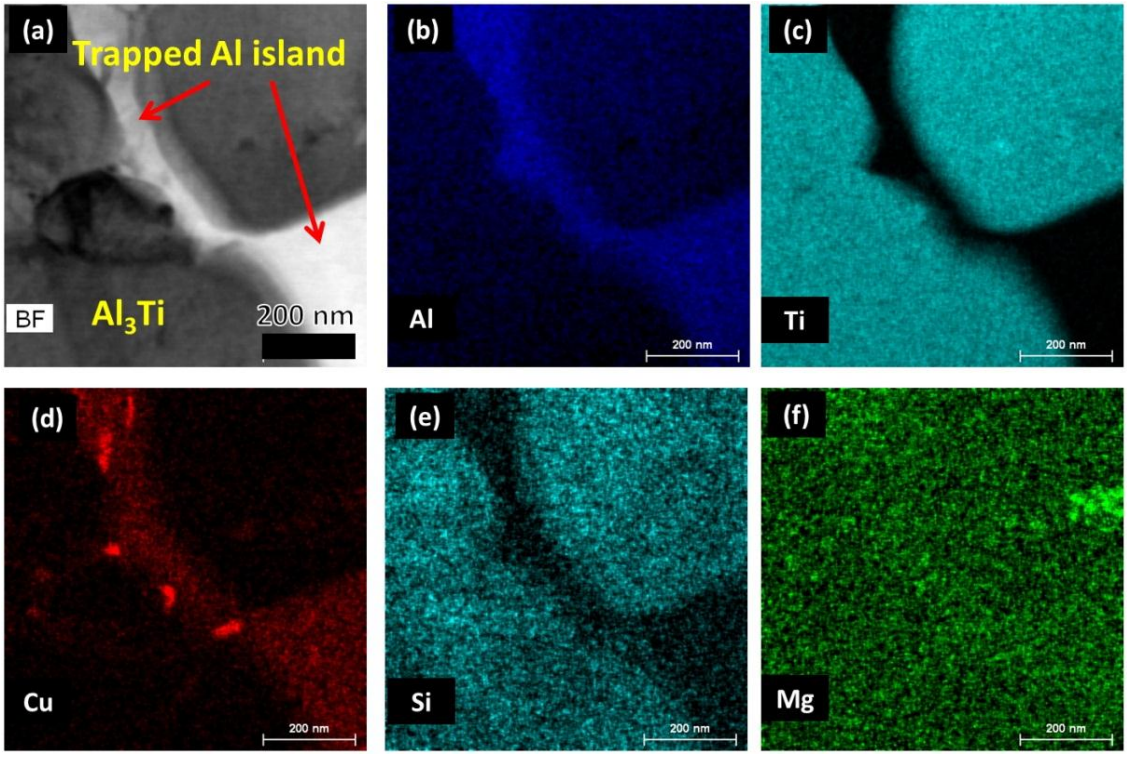

Figure 6.50 Composition maps in the region near a trapped Al island measured by STEM-EDS, (a) TEM bright filed image, (b) Al map, (c) Ti map, (d) Cu map, (e) Si map, (f) Mg map. (annealed at 500 ℃ for 360 h)

6.3.2.4 Discussion of the effect of V on Al islands

As shown in Figure 6.38, both the number and the volume of Al islands in the IMC layer (CP-Al/Ti6Al4V) are much smaller than that in IMC layer (CP-Al/CP-Ti). This suggests that the presence of V reduced the formation and/or survival time of Al islands. As stated in section 6.3.1, the formation mechanism of the Al islands is the very small mismatch between Al (111) plane and Al_3Ti (112) plane. However, the addition of V into Al_3Ti can disturb the crystal structure of Al_3Ti and leads to the change of lattice parameters [96, 97, 224]. The change of lattice parameters of Al_3Ti will result in an increase of mismatch between Al (111) plane and Al_3Ti (112) plane. This may lead to an increase in the rate of Al (111)/Al_3Ti (112) interface migration. In this case, the formation of Al islands would be less likely.

Anisotropic growth effect:

As mentioned in Section 6.3.1, the strongly anisotropic growth of Al_3Ti also could result in the formation of trapped Al islands due to the very slow growth of Al_3Ti grains in the directions normal to the crystal planes with the highest packing density (HPD plane). The very slow growth of Al_3Ti grains in these directions can cause Al grains adjacent to the Al_3Ti HPD planes to become trapped.

As stated in Section 6.2.6, the addition V in Al_3Ti significantly reduced the anisotropic growth of Al_3Ti. Once the the anisotropic growth is retarded, the formation of Al islands would also be reduced. However, according to the fact that there is an orientation relation between Al islands and Al_3Ti (Section 6.3.1), the small mismatch between Al (111) and Al_3Ti (112) should be the dominant

mechanism for the Al island formation, as if only due to anisotropic growth, no orientation relation is expected.

6.3.3 Discussion of the effect of Al islands on IMC layer growth

The presence of Al islands in reaction layer can reduce the fraction of Al_3Ti phase, and then reduce effective volume for Ti atoms to travel through the layer, as trapped Al islands are not a diffusion medium for Ti atoms. Thus, trapped Al islands could retard the reaction layer growth, although given their small overall volume fraction the effect is likely to be a modest one.

6.4 Summary

6.4.1 Summary of the interface reaction in annealed AA2139/CP-Ti joints

1. IMC layer growth in AA2139/CP-Ti joints is much slower than that in CP-Al/CP-Ti joints.

2. There are both Al_3Ti ($D0_{22}$) and trapped Al islands in the reaction layer between AA2139 and CP-Ti.

3. The presence of Cu resulted in a larger average Al_3Ti grain size, which reduced grain boundary fraction and thus could be a factor that slows down the Al_3Ti layer growth.

4. Cu was found to segregate on the Al_3Ti grain boundaries by STEM-EDS, and it the only alloying element that segregates on Al_3Ti grain boundaries. It is thought that Cu segregation can retard the interdiffusion via Al_3Ti grain boundaries.

5. Both Cu and Si segregation to the Al_3Ti/CP-Ti interface was detected by STEM-EDS, which can act as a barrier for diffusion.

6. Si enrichment was observed in the Al_3Ti layer. The strong attraction between Si atom and Ti atom also can retard Ti atom diffusion through the Al_3Ti layer.

7. A double-layer structure within the reaction layer was observed in the region near AA2139. Mg and O enrichment was found on the interface of the double-layer structure, which is expected to mainly composed of old magnesium oxide already existing on the as-welded Al/Ti interface prior to annealing. Thus the formation of the double-layer structure is thought to be due to the trapped stable residual oxide from the surface of AA2139, which cannot be decomposed during the Al-Ti solid state reaction.

8. The precipitates in the AA2139 were decomposed by the growing Al_3Ti layer and did not provide a barrier to interface migration.

6.4.2 Summary of the interface reaction in annealed CP-Al/Ti6Al4V joints

1. At the lower annealing temperature 600 °C, the growth rate of the Al_3Ti layer in CP-Al/ Ti6Al4V weld was slower than that in CP-Al/CP-Ti weld. However, this trend was reversed when annealing temperature rose to 630 °C.

2. The V concentration in the Al_3Ti reaction layer was around 1 at. %. The presence of vanadium greatly retarded the Al_3Ti grain growth at higher annealing temperature (630 °C) and retained more grain boundary area in the Al_3Ti layer. Thus the Al_3Ti layer grew much faster in CP-Al/Ti6Al4V weld.

3. The presence of vanadium may reduce the Al_3Ti grain boundary energy or mobility and thus retard the Al_3Ti grain growth.

4. No vanadium segregation was found on Al/Al_3Ti interface.

5. The anisotropic growth of Al_3Ti was significantly retarded by the solid solution of vanadium, which could be because V reduces the degree of anisotropy in surface energy for Al_3Ti.

6. The presence of V retarded the formation and growth of voids on Al/IMC layer interface at 600 °C.

6.4.3 Summary on the trapped Al islands in IMC layer

1. Trapped islands of Al or Al alloy were discovered in annealed AA2139/CP-Ti joints, CP-Al/CP-Ti joints and CP-Al/Ti6Al4V joints.

2. The formation of the trapped Al islands appears to be due to the low migration rate of interfaces between Al and Al_3Ti that have good matching.

3. The early-formed Al islands can be reacted with increasing annealing time and are removed from the layer.

3. The presence of Cu and Si greatly stabilized the Al islands and thus led to a uniform distribution of Al islands in the thickness direction of the IMC layer.

4. No alloying element segregation was observed on the interface between trapped Al island and Al_3Ti.

5. The presence of V reduced the formation and survival time of Al islands. It is proposed this is due to V increasing the mismatch between the Al (111) plane and Al_3Ti (112) plane and also significantly reducing the anisotropic growth of Al_3Ti.

6.4.4 Summary of factors that could affect the Al_3Ti layer growth

Table 6.3 Summary of factors that could affect the Al_3Ti layer growth

No.	Factors	How (possible mechanisms)
1	Al_3Ti grain size	Affects grain boundary fraction
2	Al_3Ti grain morphology	Affects if the grain boundaries are straighter or more curved and more crossed
3	Residual oxide on Al/Ti interface	Acts as a diffusion barrier
4	Cu segregation on Al_3Ti grain boundary	Retards the interdiffusion via grain boundaries
5	Si segregation on Al_3Ti/Ti interface	Acts as a diffusion barrier
6	Si enrichment in Al_3Ti layer	Retards the interdiffusion in Al_3Ti layer
7	Cu segregation on Al_3Ti/Ti interface	Acts as a diffusion barrier
8	Mg segregation on surface of Al	Acts as a diffusion barrier
9	Vanadium solid solution in Al_3Ti	(1) Retards the interdiffusion in Al_3Ti lattice
		(2) Reduces the Al_3Ti grain size
		(3) Retards the anisotropic growth of Al_3Ti
10	Vanadium in Ti6Al4V	Reduces the concentration gradient of both Al and Ti
11	Annealing temperature	(1) Affects the D_{gb} (diffusion coefficient in grain boundaries) and D_L (diffusion coefficient in lattice)
		(2) Affects decomposition rate of oxide film on titanium
		(3) Affects the Al_3Ti grain size growth rate
12	Annealing time	Affects Al_3Ti grain size

Chapter 7

Conclusions and Future Work

Chapter 7 Conclusions and Future Work

In this thesis, the effect of welding time, natural ageing and welding tip geometry on the mechanical properties of the Al/Ti joints was assessed. The welding thermal cycle was measured by inserting a tiny thermocouple to the centre of the weld. The interfacial structure was investigated in detail using SEM, TEM and high resolution STEM-EDS.

Static heat treatment experiments were performed to understand the growth kinetics of the reaction layer between Al and Ti. In the first stage, to eliminate the influence of alloying elements, the growth behaviour of IMC layer in CP-Al/CP-Ti joint is investigated. The effect of Al_3Ti grain size and the effect of residual oxides on the interface on the IMC layer growth were studied. Then, to determine the effect of alloying elements from both the AA2139 alloy and Ti6Al4V alloy, the IMC layer growth in AA2139/CP-Ti joint and in CP-Al/Ti6Al4V joint were investigated and compared with the IMC layer growth in CP-Al/CP-Ti joint. The behaviour of the alloying elements was analysed using high resolution STEM-EDS. In addition, interestingly small patches of Al were found trapped in the IMC layer; its formation mechanism is discussed. The main findings are summarised here:

Part 1: Interfacial structure and mechanical properties of dissimilar Aluminium/Titanium ultrasonic welding joints

● Both medium strength Al alloy AA6111-T4 and high strength Al alloy AA2139-T8 were successfully to titanium alloy Ti6Al4V by high power ultrasonic spot welding. No obvious IMC layer was observed in both as-welded AA6111-T4/Ti6Al4V joint and AA2139/Ti6Al4V joint by scanning and transmission electron microscopy.

● The peak failure load of Al-Ti welds in a lap shear test reached a high level, 3.5 kN for AA6111-T4/Ti6Al4V joint, the same level as similar Al-Al (AA6111) welds; and 5.6 kN for AA2139/Ti6Al4V joint. The excellent strength of Al-Ti joints compared to that of other dissimilar combinations, e.g. Al-Mg and Al-Fe is attributed to the lack of formation of brittle intermetallic in the Al-Ti case.

● Natural ageing leads to the fracture mode of AA6111/Ti6Al4V USW welds transferring from 'pull-out' mode to 'interfacial failure' for all welding times due to the strength recovery of AA6111 aluminum alloy. This change in fracture mode was accompanied by a decrease in failure energy. All the AA2139/Ti6Al4V joints fractured in an ‘interfacial failure’ mode.

● The peak welding temperatures reached for AA6111/Ti6Al4V joint and AA2139/Ti6Al4V joint were 517 ℃ and 540 ℃, respectively.

● When other things are equal, the lap shear strength and fracture energy of round tip welds are higher than those of rectangular tip welds.

● Enrichment of Mg, O and Si were found on both as-welded AA6111/Ti6Al4V and AA2139/Ti6Al4V interfaces. The observed Mg and O “enrichment” on the Al/Ti interface probably had existed on the surface of AA6111 before ultrasonic welding due to the surface segregation of Mg. The segregated Si distribution varied inversely with that of oxygen and magnesium. The residual oxides and the segregated Si on the Al/Ti interface is thought to be able to act as a barrier for Al_3Ti nucleation and growth.

● The strong chemical attraction (chemical bond) between Ti and Si, i.e. the very great negative chemical mixing enthalpy between Si and Ti ΔH_{Ti-Si}^{mix} (-66 kJ·mol^{-1})

may be the driving force for Si segregation to Al/Ti interface. The residual discontinuous oxides on the Al/Ti weld interface can deteriorate the weld mechanical properties, however the segregated Si atoms on Al/Ti interface are predicted to increase weld strength.

Part 2: The role of grain boundary diffusion and the effect of alloying elements and oxygen on Al_3Ti reaction layer growth

● Al_3Ti phase ($D0_{22}$ structure) was the only Al-Ti intermetallic phase observed in all the reaction layers, which is consistent with most previous investigations. The thickness ratio of Al_3Ti layer growing into Ti side and Al side is very close to 1:3 (in CP-Al/CP-Ti joints), which is consistent with the stoichiometric ratio of Al_3Ti compound.

In CP-Al/CP-Ti joints:

● By comparing the IMC layer growth (in CP-Al/CP-Ti joints) and analysing the grain size evolution at 600 °C and 630 °C, it has been shown that an abnormal (reverse) effect of temperature was observed with a thicker layer formed at lower annealing temperature due to the much faster Al_3Ti grain coarsening at 630 °C, the IMC layer growth at 630 °C became slower than that at 600 °C after a certain annealing time. The quantitative influence of grain size on the effective diffusion coefficient was analysed. Calculations showed that the lattice diffusion make little contribution to the effective diffusion coefficient due to the very high activation energy for lattice diffusion. Grain boundary diffusion therefore dominates for all the annealing conditions and grain sizes studied.

● The comparison of IMC layer microstructure (in CP-Al/CP-Ti joints) at 550 °C and 600 °C showed that there is no significant difference between the Al_3Ti grain size in layers grown at 550 °C and 600 °C. As a result, the difference in effective diffusion coefficient D_{eff} is dominated by the difference in annealing temperature, and growth was faster at the higher temperature, which is normal behaviour.

● A very long incubation stage of Al_3Ti layer growth (in CP-Al/CP-Ti joints) was found in the Al/Ti diffusion couple annealed at 500 °C. This very long incubation stage is probably caused by the oxide layer on titanium, which acts as a diffusion barrier. The length of the incubation stage becomes shorter with increasing annealing temperature probably due to the higher reaction rate between titanium oxides and aluminium at higher temperatures.

● Anisotropic growth of Al_3Ti was suppressed when the annealing temperature was increased from 600 °C to 630 °C.

In AA2139/CP-Ti joints:

● IMC layer growth in AA2139/CP-Ti joints is much slower than that in CP-Al/CP-Ti joints. There are both Al_3Ti ($D0_{22}$) and trapped Al islands in the reaction layer between AA2139 and CP-Ti. The presence of Cu resulted in a larger average Al_3Ti grain size, which reduced grain boundary fraction and thus could be a factor that slows down the Al_3Ti layer growth. Cu was found to segregate on the Al_3Ti grain boundaries by STEM-EDS, and it is the only alloying element that segregates on Al_3Ti grain boundaries. It is thought that Cu segregation can retard the interdiffusion via Al_3Ti grain boundaries. Both Cu and Si segregation on the Al_3Ti/CP-Ti interface was detected by STEM-EDS, which can act as a barrier for diffusion. Si enrichment was observed in the Al_3Ti layer. The strong attraction

between Si atom and Ti atom also could retard Ti atom diffusion through the Al_3Ti layer.

● A double-layer structure within the reaction layer was observed in the region near AA2139, due to the trapped stable residual oxide from the surface of AA2139, which cannot be decomposed during the Al-Ti solid state reaction. The precipitates in the AA2139 were decomposed by the growing Al_3Ti layer and did not provide a barrier to interface migration.

In CP-Al/Ti6Al4V joints:

● At the lower annealing temperature 600 °C, the growth rate of the Al_3Ti layer in CP-Al/ Ti6Al4V weld was slower than that in CP-Al/CP-Ti weld. However, this trend was reversed when annealing temperature rose to 630 °C.

● The V concentration in the Al_3Ti reaction layer was always around 1 at.%. The presence of vanadium greatly retarded the Al_3Ti grain growth at higher annealing temperature (630 °C) and retained more grain boundary area in the Al_3Ti layer. Thus the Al_3Ti layer grew faster in CP-Al/Ti6Al4V weld.

● The presence of vanadium may reduce the Al_3Ti grain boundary energy or mobility and thus retard the Al_3Ti grain growth. No vanadium segregation was found on Al/Al_3Ti interface by STEM-EDS. The anisotropic growth of Al_3Ti was significantly retarded by the solid solution of vanadium, which could be because V reduces the degree of anisotropy in surface energy for Al_3Ti. The presence of V retarded the amount of voids on Al/IMC layer interface at 600 °C.

Trapped Al islands:

● Trapped islands of Al or Al alloy were discovered in annealed AA2139/CP-Ti

joints, CP-Al/CP-Ti joints and CP-Al/Ti6Al4V joints. The formation of the trapped Al islands appears to be due to the low migration rate of interfaces between Al and Al_3Ti that have good matching. The early-formed Al islands can be reacted with increasing annealing time and are removed from the layer.

● The presence of Cu and Si greatly stabilized the Al islands and thus led to a uniform distribution of Al islands in the thickness direction of the IMC layer. No alloying element segregation was observed on the interface between trapped Al island and Al_3Ti. The presence of V reduced the formation and survival time of Al islands. It is proposed this is due to V increasing the mismatch between the Al (111) plane and Al_3Ti (112) plane and also significantly reducing the anisotropic growth of Al_3Ti.

Significance of the present study:

The present study for the first time: (a) observed the no-IMC-layer Al/Ti weld interface; (b) observed Cu segeration on Al_3Ti GBs; (c) quantitatively studied the grain size effect on Al3Ti layer growth kinetics; (d) observed the orientation relationship between trapped Al islands and the adjacent Al3Ti grains; (e) observed that V greatly retarded the anisotropic growth of Al3Ti grains.

The connection between the Chapters (4, 5, 6):

The study of IMC layer growth kinetics of Chapter 5 and Chapter 6 can be used to explain the lack of IMC layer in the as-welded USW joints, because:

(a) The findings in Chapter 5 suggested that the residual oxide film probably strongly retard the Al-Ti reaction at relatively low temperatures.

(b) The findings in Chapter 6 demostrated that the alloying elements, specifically Cu and Si can greatly suppress the IMC layer growth.

Suggestions for future work

On the basis of the present work, a number of topics have been highlighted where further research would be beneficial.

The welding process:

As predicted in Chapter 4, the addition of Si may be able to increase the Al/Ti weld strength, therefore the effect of adding Si on Al surface or Ti surface or on both of them could be experimentally investigated to improve the weld strength and to verify the prediction.

Modelling the IMC layer growth:

As stated in Chapter 5 and Chapter 6, in some cases, the Al_3Ti grain size has been greatly affected by the annealing temperature, annealing time and the alloying elements, and thus the IMC layer growth rate was affected. Calculations in this work have already suggested the strong effect of grain size. A more complete model considering the grain size effect, i.e. grain boundary diffusion effect, could be developed to predict the growth behaviour of IMC layer.

Effect of alloying elements on IMC layer growth:

Due to the industrial application background, the Al alloys used in the present study contain many alloying elements, thus it is difficult to clarify the specific effect of each element. Therefore, it would be interesting to study the IMC layer growth between Al and Ti using high purity binary Al alloys, such as Al-Cu binary

alloy, Al-Si binary alloy and Al-Mg binary alloy to accurately understand the effect of individual alloy elements.

Effect of residual oxides on IMC layer growth:

As stated in Chapter 5, there is a break-away growth behaviour of Al_3Ti layer at low annealing temperature. This is probably caused by the slow oxide decomposition with increasing annealing time. The tentative EDS work in this work has already indicated this point. It would be interesting to quantitatively or semi-quantitatively investigate the oxide change on the diffusion interfaces with increasing annealing time.

References

1. Rendigs, K.H., *Aluminium structures used in aerospace - Status and prospects,* in *Aluminium Alloys: Their Physical and Mechanical Properties, Part 4/Supplement*, J.H. Driver, et al., Editors. 1997. p. 11-23.
2. Song, Z.H., K. Nakata, A.P. Wu, and J.S. Liao, *Interfacial microstructure and mechanical property of Ti6Al4V/A6061 dissimilar joint by direct laser brazing without filler metal and groove.* Materials Science and Engineering a-Structural Materials Properties Microstructure and Processing, 2013. **560**: p. 111-120.
3. Chen, S., L. Li, Y. Chen, and J. Huang, *Joining mechanism of Ti/Al dissimilar alloys during laser welding-brazing process.* Journal of Alloys and Compounds, 2011. **509**(3): p. 891-898.
4. Kreimeyer, M., F. Wagner, and F. Vollertsen, *Laser processing of aluminum-titanium-tailored blanks.* Optics and Lasers in Engineering, 2005. **43**(9): p. 1021-1035.
5. Majumdar, B., R. Galun, A. Weisheit, and B.L. Mordike, *Formation of a crack-free joint between Ti alloy and Al alloy by using a high-power CO2 laser.* Journal of Materials Science, 1997. **32**(23): p. 6191-6200.
6. Song, Z., A. Wu, W. Yao, G. Zou, J. Ren, and Y. Wang, *Influence of laser offset on microstructure and mechanical properties of Ti/Al dissimilar joint by laser welding.* Hanjie Xuebao/Transactions of the China Welding Institution, 2013. **34**(1): p. 105-108.
7. Song, Z., K. Nakata, A. Wu, and J. Liao, *Interfacial microstructure and mechanical property of Ti6Al4V/A6061 dissimilar joint by direct laser brazing without filler metal and groove.* Materials Science and Engineering A, 2013. **560**: p. 111-120.
8. Wei, S., Y. Li, J. Wang, and K. Liu, *Formation of brittle phases during pulsed current gas tungsten arc welding of titanium to aluminum alloys.* Journal of Materials Engineering and Performance, 2014. **23**(4): p. 1451-1457.
9. Ma, Z., C. Wang, H. Yu, J. Yan, and H. Shen, *The microstructure and mechanical properties of fluxless gas tungsten arc welding–brazing joints made between titanium and aluminum alloys.* Materials & Design, 2013. **45**(0): p. 72-79.
10. Sambasiva Rao, A., G. Madhusudhan Reddy, and K.S. Prasad, *Microstructure and tensile properties of dissimilar metal gas tungsten arc welding of aluminium to titanium alloy.* Materials Science and Technology, 2011. **27**(1): p. 65-70.
11. Mishra, R.S. and Z.Y. Ma, *Friction stir welding and processing.* Materials Science and Engineering: R: Reports, 2005. **50**(1–2): p. 1-78.
12. Chen, Y.C. and K. Nakata, *Microstructural characterization and mechanical properties in friction stir welding of aluminum and titanium dissimilar alloys.* Materials & Design, 2009. **30**(3): p. 469-474.
13. Aonuma, M. and K. Nakata, *Dissimilar metal joining of 2024 and 7075 aluminium alloys to titanium alloys by friction stir welding.* Materials Transactions, 2011. **52**(5): p. 948-952.

14. Dressler, U., G. Biallas, and U. Alfaro Mercado, *Friction stir welding of titanium alloy TiAl6V4 to aluminium alloy AA2024-T3.* Materials Science and Engineering A, 2009. **526**(1-2): p. 113-117.
15. Bang, K.S., K.J. Lee, H.S. Bang, and H.S. Bang, *Interfacial Microstructure and Mechanical Properties of Dissimilar Friction Stir Welds between 6061-T6 Aluminum and Ti-6%Al-4%V Alloys.* Materials Transactions, 2011. **52**(5): p. 974-978.
16. Chen, Y., L. Yu, and Q. Ni, *Influence of zinc on the microstructure and brittle phases of friction stir welded joint of Al / Ti dissimilar alloys*, in *Advanced Materials Research*. 2012. p. 439-443.
17. Wei, Y., J. Li, J. Xiong, F. Huang, F. Zhang, and S.H. Raza, *Joining aluminum to titanium alloy by friction stir lap welding with cutting pin.* Materials Characterization, 2012. **71**(0): p. 1-5.
18. Song, Z., K. Nakata, A. Wu, J. Liao, and L. Zhou, *Influence of probe offset distance on interfacial microstructure and mechanical properties of friction stir butt welded joint of Ti6Al4V and A6061 dissimilar alloys.* Materials & Design, 2014. **57**(0): p. 269-278.
19. Oosterkamp, A., L.D. Oosterkamp, and A. Nordeide, *Kissing bond'phenomena in solid-state welds of aluminum alloys.* WELDING JOURNAL-NEW YORK-, 2004. **83**(8): p. 225-S.
20. Kimura, M., S. Nakamura, M. Kusaka, K. Seo, and A. Fuji, *Mechanical properties of friction welded joint between Ti-6Al-4V alloy and Al-Mg alloy (AA5052).* Science and Technology of Welding and Joining, 2005. **10**(6): p. 666-672.
21. *Frictions*. [cited 2015; Available from: http://www.shimizu-kk.co.jp/english/images/frictions.jpg.
22. Katoh, K. and H. Tokisue, *Effect of insert metal on mechanical properties of friction welded 5052 aluminum alloy to pure titanium joint.* Keikinzoku/Journal of Japan Institute of Light Metals, 2004. **54**(10): p. 430-435.
23. Fuji, A., K. Ameyama, and T.H. North, *Influence of silicon in aluminium on the mechanical properties of titanium/aluminium friction joints.* Journal of Materials Science, 1995. **30**(20): p. 5185-5191.
24. Wei, Y., W. Aiping, Z. Guisheng, and R. Jialie, *Formation process of the bonding joint in Ti/Al diffusion bonding.* Materials Science and Engineering: A, 2008. **480**(1–2): p. 456-463.
25. Wei, Y., W. Aiping, Z. Guisheng, and R. Jialie, *5A06/TA2 diffusion bonding with Nb diffusion-retarding layers.* Materials Letters, 2008. **62**(17-18): p. 2836-2839.
26. Jiangwei, R., L. Yajiang, and F. Tao, *Microstructure characteristics in the interface zone of Ti/Al diffusion bonding.* Materials Letters, 2002. **56**(5): p. 647-652.
27. Kenevisi, M.S. and S.M. Mousavi Khoie, *A study on the effect of bonding time on the properties of Al7075 to Ti-6Al-4V diffusion bonded joint.* Materials Letters, 2012. **76**: p. 144-146.
28. Bakavos, D. and P.B. Prangnell, *Mechanisms of joint and microstructure formation in high power ultrasonic spot welding 6111 aluminium automotive sheet.* Materials Science and Engineering: A, 2010. **527**(23): p. 6320-6334.

29. Prangnell, P., F. Haddadi, and Y.C. Chen, *Ultrasonic spot welding of aluminium to steel for automotive applications - microstructure and optimisation.* Materials Science and Technology, 2011. **27**(3): p. 617-624.
30. Panteli, A., Y.C. Chen, D. Strong, X. Zhang, and P.B. Prangnell, *Optimization of Aluminium-to-Magnesium Ultrasonic Spot Welding.* JOM, 2012. **64**(3): p. 414-420.
31. Panteli, A., J. Robson, Y.-C. Chen, and P. Prangnell, *The Effectiveness of Surface Coatings on Preventing Interfacial Reaction During Ultrasonic Welding of Aluminum to Magnesium.* Metallurgical and Materials Transactions A, 2013. **44**(13): p. 5773-5781.
32. Patel, V.K., S.D. Bhole, and D.L. Chen, *Microstructure and mechanical properties of dissimilar welded Mg–Al joints by ultrasonic spot welding technique.* Science and Technology of Welding and Joining, 2012. **17**(3): p. 202-206.
33. Balle, F. and J. Magin, *Solid state joining of aluminium to titanium by high power ultrasonics*, in *Materials Science Forum*. 2014. p. 345-350.
34. Shin, H.S., *Tool geometry effect on the characteristics of dissimilar friction stir spot welded bulk metallic glass to lightweight alloys.* Journal of Alloys and Compounds, 2014. **586**: p. S50-S55.
35. Lin, B.Y. and J.J. Liu, *Effect of Tool Geometry on Fatigue Properties and Fracture Behavior of Friction Stir Spot Welded Aluminum Sheets.* Journal of the Chinese Society of Mechanical Engineers, 2013. **34**(4): p. 277-284.
36. Tozaki, Y., Y. Uematsu, and K. Tokaji, *Effect of tool geometry on microstructure and static strength in friction stir spot welded aluminium alloys.* International Journal of Machine Tools & Manufacture, 2007. **47**(15): p. 2230-2236.
37. Chen, Y.C. and K. Nakata, *Effect of tool geometry on microstructure and mechanical properties of friction stir lap welded magnesium alloy and steel.* Materials & Design, 2009. **30**(9): p. 3913-3919.
38. Jahn, R., R. Cooper, and D. Wilkosz, *The Effect of Anvil Geometry and Welding Energy on Microstructures in Ultrasonic Spot Welds of AA6111-T4.* Metallurgical and Materials Transactions A, 2007. **38**(3): p. 570-583.
39. Watanabe, T., K. Nishihara, and T. Sasaki. *Effect of Weld Tip Geometry on Ultrasonic Welding of Aluminum Alloy*. in *Materials Science Forum*. 2010. Trans Tech Publ.
40. *Aircraft & Aerospace*. [cited 2015; Available from: http://www.aluminum.org/product-markets/aircraft-aerospace.
41. Hale, J., *Boeing 787 from the ground up.* Aero, 2006. **4**: p. 17-24.
42. [cited 2015; Available from: http://modernairliners.com/Boeing787_files/image342.gif.
43. Kaufman, J.G., *Introduction to aluminum alloys and tempers*. 2000: Asm Intl.
44. Gupta, A.K., D.J. Lloyd, and S.A. Court, *Precipitation hardening in Al–Mg–Si alloys with and without excess Si.* Materials Science and Engineering: A, 2001. **316**(1–2): p. 11-17.
45. Quainoo, G.K. and S. Yannacopoulos, *The effect of prestrain on the natural aging and fracture behaviour of AA6111 aluminum.* Journal of Materials Science, 2004. **39**(15): p. 4841-4847.
46. Wang, X., W.J. Poole, S. Esmaeili, D.J. Lloyd, and J.D. Embury, *Precipitation strengthening of the aluminum alloy AA6111.* Metallurgical

and Materials Transactions A: Physical Metallurgy and Materials Science, 2003. **34**(12): p. 2913-2924.
47. Miao, W.F. and D.E. Laughlin, *Effects of Cu content and preaging on precipitation characteristics in aluminum alloy 6022.* Metallurgical and Materials Transactions A: Physical Metallurgy and Materials Science, 2000. **31**(2): p. 361-371.
48. Murayama, M., K. Hono, W. Miao, and D. Laughlin, *The effect of Cu additions on the precipitation kinetics in an Al-Mg-Si alloy with excess Si.* Metallurgical and Materials Transactions A: Physical Metallurgy and Materials Science, 2001. **32**(2): p. 239-246.
49. Dumolt, S.D., D.E. Laughlin, and J.C. Williams, *Formation of a modified β' phase in aluminum alloy 6061.* Scripta Metallurgica, 1984. **18**(12): p. 1347-1350.
50. Lloyd, D.J., D.R. Evans, and A.K. Gupta, *Precipitation reactions and the Differential Scanning Calorimetry response of AA6111 alloy.* Canadian Metallurgical Quarterly, 2000. **39**(4): p. 475-482.
51. Edwards, G.A., K. Stiller, G.L. Dunlop, and M.J. Couper, *The precipitation sequence in Al-Mg-Si alloys.* Acta Materialia, 1998. **46**(11): p. 3893-3904.
52. Thomas, G., *Electron-Transmission Studies of Al-Mg-Si Alloys.* J Inst Metals, 1961. **90**: p. 57-62.
53. Chakrabarti, D.J., B.K. Cheong, and D.E. Laughlin, *Automotive alloys II.* Proc. TMS Annual Meeting, 1998: p. 27-44.
54. Andersen, S.J., H.W. Zandbergen, J. Jansen, C. Træholt, U. Tundal, and O. Reiso, *The crystal structure of the β'' phase in Al-Mg-Si Alloys.* Acta Materialia, 1998. **46**(9): p. 3283-3298.
55. Placzankis, B.E., E.A. Charleton, A.L. Fowler, and U.N.A.W. Center. *Accelerated corrosion and adhesion assessments of Carc prepared aluminum alloy 2139-T8 using three various pretreatment methods and two different primer coatings*. in *DoD Corrosion Conference*. 2009.
56. Polmear, I.J., *Aluminium alloys - A century of age hardening.* Materials Forum, 2004. **28**: p. 1-14.
57. Polmear, I.J. and R.J. Chester, *Abnormal age hardening in an AlCuMg alloy containing silver and lithium.* Scripta Metallurgica, 1989. **23**(7): p. 1213-1217.
58. Cho, A. and B. Bes. *Damage tolerance capability of an Al-Cu-Mg-Ag alloy (2139)*. in *Materials science forum*. 2006. Trans Tech Publ.
59. Ringer, S.P., W. Yeung, B.C. Muddle, and I.J. Polmear, *Precipitate stability in Al Cu Mg Ag alloys aged at high temperatures.* Acta Metallurgica et Materialia, 1994. **42**(5): p. 1715-1725.
60. Lutjering, G. and J. Williams, *Titanium (Engineering materials & processes).* Recherche, 2007. **67**: p. 02.
61. Lütjering, G. and J.C. Williams, *Titanium*. 2007: Springer Science & Business Media.
62. Dragolich, K.S., N.D. DiMatteo, and S.D. Henry, *Fatigue data book: light structural alloys*. 1994: ASM International.
63. Donachie, M.J., *Titanium: a technical guide*. 2000: ASM international.
64. Burgers, W.G., *On the process of transition of the cubic-body-centered modification into the hexagonal-close-packed modification of zirconium.* Physica, 1934. **1**(7–12): p. 561-586.

65. Obasi, G.C., S. Birosca, J. Quinta da Fonseca, and M. Preuss, *Effect of β grain growth on variant selection and texture memory effect during $\alpha \rightarrow \beta \rightarrow \alpha$ phase transformation in Ti‐6 Al–4 V.* Acta Materialia, 2012. **60**(3): p. 1048-1058.
66. Kim, H.G., S.M. Kim, J.Y. Lee, M.R. Choi, S.H. Choe, K.H. Kim, J.S. Ryu, S. Kim, S.Z. Han, W.Y. Kim, and S.H. Lim, *Microstructural evaluation of interfacial intermetallic compounds in Cu wire bonding with Al and Au pads.* Acta Materialia, 2014. **64**: p. 356-366.
67. Meshram, S.D., T. Mohandas, and G.M. Reddy, *Friction welding of dissimilar pure metals.* Journal of Materials Processing Technology, 2007. **184**(1–3): p. 330-337.
68. Tian, Y.h., C.q. Wang, and Y.N. Zhou, *Bonding mechanism of ultrasonic wedge bonding of copper wire on Au/Ni/Cu substrate.* Transactions of Nonferrous Metals Society of China (English Edition), 2008. **18**(1): p. 132-137.
69. Shah, A., H. Gaul, M. Schneider-Ramelow, H. Reichl, M. Mayer, and Y. Zhou, *Ultrasonic friction power during AI wire wedge-wedge bonding.* Journal of Applied Physics, 2009. **106**(1).
70. Lum, I., M. Mayer, and Y. Zhou, *Footprint study of ultrasonic wedge-bonding with aluminum wire on copper substrate.* Journal of Electronic Materials, 2006. **35**(3): p. 433-442.
71. Iwamoto, C., S. Satonaka, A. Yoshida, T. Nishinaka, and K. Yamada, *High Resolution Transmission Electron Microscopy of Aluminum/Mo-Coated Glass Substrate Interface Bonded by Ultrasonic Wire Welding.* Journal of Solid Mechanics and Materials Engineering, 2011. **5**(12): p. 803-809.
72. Seah, M.P., *Grain boundary segregation.* Journal of Physics F: Metal Physics, 1980. **10**(6): p. 1043.
73. Kainuma, R., M. Palm, and G. Inden, *Solid-phase equilibria in the Ti-rich part of the TiAl system.* Intermetallics, 1994. **2**(4): p. 321-332.
74. Oh, J., W. Lee, S.G. Pyo, W. Park, S. Lee, and N.J. Kim, *Microstructural analysis of multilayered titanium aluminide sheets fabricated by hot rolling and heat treatment.* Metallurgical and Materials Transactions A, 2002. **33**(12): p. 3649-3659.
75. Tomashchuk, I., P. Sallamand, E. Cicala, P. Peyre, and D. Grevey, *Direct keyhole laser welding of aluminum alloy AA5754 to titanium alloy Ti6Al4V.* Journal of Materials Processing Technology, 2015. **217**: p. 96-104.
76. Mirjalili, M., M. Soltanieh, K. Matsuura, and M. Ohno, *On the kinetics of TiAl3 intermetallic layer formation in the titanium and aluminum diffusion couple.* Intermetallics, 2013. **32**(0): p. 297-302.
77. Luo, J.G. and V.L. Acoff, *Using cold roll bonding and annealing to process Ti/Al multi-layered composites from elemental foils.* Materials Science and Engineering A, 2004. **379**(1-2): p. 164-172.
78. Xu, L., Y. Cui, Y. Hao, and R. Yang, *Growth of intermetallic layer in multi-laminated Ti/Al diffusion couples.* Materials Science and Engineering: A, 2006. **435**: p. 638-647.
79. Zhao, X.A., F. So, and M.A. Nicolet, *TiAl3 formation by furnace annealing of Ti/Al bilayers and the effect of impurities.* Journal of applied physics, 1988. **63**(8): p. 2800-2807.

80. Goda, D., N. Richards, W. Caley, and M. Chaturvedi, *The effect of processing variables on the structure and chemistry of Ti-aluminide based LMCS.* Materials Science and Engineering: A, 2002. **334**(1): p. 280-290.
81. Van Loo, F. and G. Rieck, *Diffusion in the titanium-aluminium system—I. Interdiffusion between solid Al and Ti or Ti-Al alloys.* Acta Metallurgica, 1973. **21**(1): p. 61-71.
82. Zhang, L., D. Wang, B. Wang, R. Yu, and L. Wei, *Annealing studies of Ti/Al multilayer film by slow positron beam.* Applied surface science, 2007. **253**(17): p. 7309-7312.
83. Shimozaki, T., T. Okino, M. Yamane, Y. Wakamatsu, and M. Onishi. *Effect of diffusion barrier and impurities in titanium on the growth rate of TiAl3 layer*. in *Defect and Diffusion Forum*. 1997. Trans Tech Publ.
84. Tardy, J. and K. Tu, *Solute effect of Cu on interdiffusion in Al 3 Ti compound films.* Physical Review B, 1985. **32**(4): p. 2070.
85. Han, C. and R. Bene, *Variations in interface compound nucleation for Ti - Al ultrathin films on Si substrates.* Applied Physics Letters, 1985. **47**(10): p. 1077-1079.
86. Thuillard, M., L. Tran, and M.-A. Nicolet, *Al 3 Ti formation by diffusion of aluminum through titanium.* Thin Solid Films, 1988. **166**: p. 21-28.
87. Liu, S., H.U. Rongze, D. Zhao, C. Wang, P. Luo, and P.U. Zhongjie, *Bonding characteristics of the intermetallic compound Al3Ti+Cr.* Journal of Materials Science and Technology, 1996. **12**(3): p. 180-184.
88. Westbrook, J.H. and R.L. Fleischer, *Intermetallic Compounds, Structural Applications of*. 2000: Wiley.
89. Yamashita, K., I. Fujimoto, S. Kumai, and A. Sato, *Plastic Deformation of D0 22 Ordered Al 3 Ti in a Centrifugally Cast Al–Al 3 Ti Composite.* Materials Transactions, JIM, 1998. **39**(8): p. 824-833.
90. Ghosh, G., A. van de Walle, and M. Asta, *First-Principles Phase Stability Calculations of Pseudobinary Alloys of (Al, Zn) 3Ti with L12, D022, and D023 Structures.* Journal of phase equilibria and diffusion, 2007. **28**(1): p. 9-22.
91. Udayashankar, N.K., S. Rajasekaran, and J. Nayak, *Oxidation and corrosion resistance of TiAl3 coatings.* Transactions of the Indian Institute of Metals, 2008. **61**(2-3): p. 231-233.
92. Yamaguchi, M., Y. Umakoshi, and T. Yamane, *Plastic deformation of the intermetallic compound Al3Ti.* Philosophical Magazine A, 1987. **55**(3): p. 301-315.
93. Morris, D. and R. Lerf, *Plastic deformation of the intermetallic Al3Ti.* Philosophical Magazine A, 1991. **63**(6): p. 1195-1206.
94. Lu, X., N. Gui, A. Qiu, G. Wu, and C. Li, *Thermodynamic Modeling of the Al-Ti-V Ternary System.* Metallurgical and Materials Transactions A, 2014. **45**(9): p. 4155-4164.
95. Ahmed, T. and H. Flower, *Partial isothermal sections of Ti–Al–V ternary diagram.* Materials science and technology, 1994. **10**(4): p. 272-288.
96. Lee, K.-M., J.-H. Lee, and I.-H. Moon, *Effects of V and Zr addition on lattice parameters of Al 3 Ti phase in mechanically alloyed Al-8wt.% Ti alloys.* Scripta metallurgica et materialia, 1993. **29**(6): p. 737-740.
97. Takahashi, T., K. Iwami, and T. Hasegawa, *Alloying Effect of Vanadium Upon Structure and Strength of σ-Phase Titanium Trialuminide.* MRS Online Proceedings Library, 1996. **460**: p. null-null.

98. Takahashi, T., K. Tominaga, Y. Tsuchida, S. Motizuki, F. Kawai, and T. Hasegawa, *Mechanical properties of L12 modified titanium trialuminides alloyed with chromium, iron and vanadium.* Materials Science and Engineering: A, 2002. **329–331**(0): p. 474-480.
99. Raghavan, V., *Al−Cu−Ti (Aluminum-Copper-Titanium).* Journal of Phase Equilibria and Diffusion, 2006. **27**(2): p. 156-157.
100. Hong, T. and A.J. Freeman, *Effect of ternary additions on the structural stability and electronic structure of intermetallic compounds. Al3Ti + Cu.* Journal of Materials Research, 1991. **6**(2): p. 330-338.
101. Senying, L., H. Rongze, and W. Chongyu, *Electronic and physical properties of the intermetallic compounds Al3Ti+X(X = Mn, Fe, or Cu).* Solid State Communications, 1994. **92**(4): p. 303-307.
102. Frazier, W.E., J.E. Benci, and J.W. Zanter. *Microstructural evaluation of as-cast and melt spun Al3Ti and Al3Ti plus copper*. 1991.
103. Takemoto, T. and I. Okamoto, *Intermetallic compounds formed during brazing of titanium with aluminium filler metals.* Journal of materials science, 1988. **23**(4): p. 1301-1308.
104. Miyazaki, Y., K. Uenishi, and K.F. Kobayashi, *Effect of Ag addition on formation of intermetallic compound Al3Ti by combustion synthesis.* Nippon Kinzoku Gakkaishi/Journal of the Japan Institute of Metals, 2003. **67**(6): p. 302-307.
105. Zhang, F.Y., M.F. Yan, Y. You, C.S. Zhang, and H.T. Chen, *Prediction of elastic and electronic properties of cubic Al18Ti2Mg3 phase coexisting with Al3Ti in Al–Ti–Mg system.* Physica B: Condensed Matter, 2013. **408**(0): p. 68-72.
106. Kerimov, K., S. Dunaev, and E. Sljusarenko, *Investigation of the structure of ternary phases in Al Mg Ti, Al Mg V and Al Mg Cr systems.* Journal of the Less Common Metals, 1987. **133**(2): p. 297-302.
107. Wei, Y., W. Aiping, Z. Guisheng, and R. Jialie, *5A06/TA2 diffusion bonding with Nb diffusion-retarding layers.* Materials Letters, 2008. **62**(17): p. 2836-2839.
108. Mabuchi, H., K.-i. Hirukawa, and Y. Nakayama, *Formation of structural L12 compounds in TiAl3-base alloys containing Mn.* Scripta Metallurgica, 1989. **23**(10): p. 1761-1765.
109. Zhang, S., J.P. Nic, W.W. Milligan, and D.E. Mikkola, *Temperature dependence of the compressive strength of cubic phases formed by alloying Al3Ti with Mn And Cr.* Scripta Metallurgica et Materialia, 1990. **24**(8): p. 1441-1446.
110. Kogachi, M. and A. Kameyama, *Site preference determination in Ll2 ternary intermetallic compounds Al3Ti-X (X=Cr, Mn, Pd).* Scripta Metallurgica et Materialia, 1993. **29**(10): p. 1329-1334.
111. Li, Z., C. Liao, Y. Liu, X. Wang, Y. Wu, M. Zhao, Z. Long, and F. Yin, *700 ℃ Isothermal Section of the Al-Ti-Si Ternary Phase Diagram.* Journal of Phase Equilibria and Diffusion, 2014. **35**(5): p. 564-574.
112. Li, Y., Q. Luo, J.-Y. Zhang, and Q. Li, *Experimental Study of the Al-Rich Corner of the Al-Si-Ti System at 500 ℃*, in *Light Metals 2013*. 2013, John Wiley & Sons, Inc. p. 391-393.
113. Ma, Z., W. Zhao, J. Yan, and D. Li, *Interfacial reaction of intermetallic compounds of ultrasonic-assisted brazed joints between dissimilar alloys of*

Ti-6Al-4V and Al-4Cu-1Mg. Ultrasonics Sonochemistry, 2011. **18**(5): p. 1062-1067.
114. Pang, J., X. Cui, A. Li, G. Fan, L. Geng, Z. Zheng, and Q. Wang, *Effect of solid solution of Si on mechanical properties of TiAl 3 based on the multi-laminated Ti-(SiC P/Al) composite system.* Materials Science and Engineering: A, 2013. **579**: p. 57-63.
115. Zhu, G., Y. Dai, D. Shu, J. Wang, and B. Sun, *Substitution behavior of Si in Al3Ti (D022): a first-principles study.* Journal of Physics: Condensed Matter, 2009. **21**(41): p. 415503.
116. Zhu, G.L., D. Shu, Y.B. Dai, J. Wang, and B.D. Sun, *First principles study on substitution behaviour of Si in TiAl3.* Wuli Xuebao/Acta Physica Sinica, 2009. **58**(SPEC. ISS.): p. S210-S215.
117. Nonaka, K., H. Fujii, and H. Nakajima, *Effect of oxygen in titanium on reaction diffusion between Ti and Al.* Materials Transactions, 2001. **42**(8): p. 1731-1740.
118. Bower, R.W., *Characteristics of aluminum‐titanium electrical contacts on silicon.* Applied Physics Letters, 1973. **23**(2): p. 99-101.
119. Krafcsik, I., J. Gyulai, C.J. Palmström, and J.W. Mayer, *Influence of Cu as an impurity in Al/Ti and Al/W thin‐film reactions.* Applied Physics Letters, 1983. **43**(11): p. 1015-1017.
120. Schubert, E., M. Klassen, I. Zerner, C. Walz, and G. Sepold, *Light-weight structures produced by laser beam joining for future applications in automobile and aerospace industry.* Journal of Materials Processing Technology, 2001. **115**(1): p. 2-8.
121. Qiu, R., C. Iwamoto, and S. Satonaka, *Interfacial microstructure and strength of steel/aluminum alloy joints welded by resistance spot welding with cover plate.* Journal of Materials Processing Technology, 2009. **209**(8): p. 4186-4193.
122. Bozzi, S., A.L. Helbert-Etter, T. Baudin, B. Criqui, and J.G. Kerbiguet, *Intermetallic compounds in Al 6016/IF-steel friction stir spot welds.* Materials Science and Engineering: A, 2010. **527**(16–17): p. 4505-4509.
123. Panteli, A., Y.C. Chen, D. Strong, X.Y. Zhang, and P.B. Prangnell, *Optimization of Aluminium-to-Magnesium Ultrasonic Spot Welding.* Jom, 2012. **64**(3): p. 414-420.
124. Shimozaki, T., T. Okino, M. Yamane, Y. Wakamatsu, and M. Onishi, *Effect of diffusion barrier and impurities in titanium on the growth rate of TiAl3 layer*, in *Defect and Diffusion Forum*. 1997. p. 591-596.
125. van Loo, F.J.J. and G.D. Rieck, *Diffusion in the titanium-aluminium system—II. Interdiffusion in the composition range between 25 and 100 at.% Ti.* Acta Metallurgica, 1973. **21**(1): p. 73-84.
126. Cui, X., G. Fan, L. Geng, Y. Wang, L. Huang, and H.-X. Peng, *Growth kinetics of TiAl3 layer in multi-laminated Ti–(TiB2/Al) composite sheets during annealing treatment.* Materials Science and Engineering: A, 2012. **539**(0): p. 337-343.
127. Mirjalili, M., M. Soltanieh, K. Matsuura, and M. Ohno. *TiAl3 Formation in the Titanium-Aluminum Diffusion Couple*. in *Defect and Diffusion Forum*. 2012. Trans Tech Publ.
128. Wang, Y.-J., G.-J.J. Gao, and S. Ogata, *Atomistic understanding of diffusion kinetics in nanocrystals from molecular dynamics simulations.* Physical Review B, 2013. **88**(11): p. 115413.

129. Mehrer, H., *Diffusion in solids: fundamentals, methods, materials, diffusion-controlled processes*. Vol. 155. 2007: Springer.
130. Barnes, R., *Diffusion of copper along the grain boundaries of nickel.* 1950.
131. Le Claire, A.D., *LII. Grain boundary diffusion in metals.* The London, Edinburgh, and Dublin Philosophical Magazine and Journal of Science, 1951. **42**(328): p. 468-474.
132. Kráľ, J., M. Ferdinandy, D. Liška, and P. Diko, *Formation of TiAl 3 layer on titanium alloys.* Materials Science and Engineering: A, 1991. **140**: p. 479-485.
133. Fu, E., R. Rawlings, and H. McShane, *Reaction synthesis of titanium aluminides.* Journal of materials science, 2001. **36**(23): p. 5537-5542.
134. Mishin, Y. and C. Herzig, *Diffusion in the Ti–Al system.* Acta Materialia, 2000. **48**(3): p. 589-623.
135. D'Heurle, F.M., P. Gas, and J. Philibert, *Diffusion-reaction: The ordered Cu3Au rule and its corollaries.* Solid State Phenomena, 1995. **41**.
136. D'Heurle, F.M., P. Gas, C. Lavoie, and J. Philibert, *Diffusion in intermetallic compounds: The ordered Cu3Au rule, its history.* Zeitschrift fuer Metallkunde/Materials Research and Advanced Techniques, 2004. **95**(10): p. 852-859.
137. Mehrer, H., *Diffusion in intermetallics.* Materials Transactions, JIM, 1996. **37**(6): p. 1259-1280.
138. Heitjans, P. and J. Kärger, *Diffusion in condensed matter: methods, materials, models*. 2006: Springer Science & Business Media.
139. Ikeda, T., H. Kadowaki, and H. Nakajima, *Diffusion of 44Ti and 63Ni in TiAl single crystal.* Acta materialia, 2001. **49**(17): p. 3475-3485.
140. Nose, Y., N. Terashita, T. Ikeda, and H. Nakajima, *Impurity diffusion in γ-TiAl single crystals.* Acta materialia, 2006. **54**(9): p. 2511-2519.
141. Nozaki, K., K. Nagashio, and K. Kuribayashi, *Solidification Behavior of Intermetallic Compounds with Strong Crystallographic Anisotropy.* JASMA, 2008. **25**(3): p. 583-586.
142. John, D.S. and L. Hogan, *Metallography and growth crystallography of Al 3 Ti in Al-Ti alloys up to 5 wt% Ti.* Journal of Crystal Growth, 1979. **46**(3): p. 387-398.
143. Oishi, N., H. Yanagisawa, K. Sasaki, Y. Abe, and M. Kawamura, *Orientational growth of Al(111) caused by interposing Al3Ti layer on a highly oriented TiN(200) film.* Electronics and Communications in Japan (Part II: Electronics), 1998. **81**(9): p. 46-53.
144. Tardy, J. and K.N. Tu, *Solute effect of Cu on interdiffusion in Al3Ti compound films.* Phys Rev B Condens Matter, 1985. **32**(4): p. 2070-2081.
145. LeGoues, F.K., M. Wittmer, T. Kwok, H.C.W. Huang, and P.S. Ho, *The Microstructure of Transition Metal/Al(Cu) Layers.* Journal of The Electrochemical Society, 1987. **134**(4): p. 940-944.
146. Abdel-Hamid, A.A., *Influence of Ta, Zr, V and Mo on the growth morphology of Ti-aluminide crystals.* Zeitschrift fuer Metallkunde/Materials Research and Advanced Techniques, 1991. **82**(5): p. 383-386.
147. Wittmer, M., F. Le Goues, and H.C. Huang, *Effect of Cu on the Kinetics and Microstructure of Al3Ti Formation.* Journal of The Electrochemical Society, 1985. **132**(6): p. 1450-1455.

148. Colgan, E.G. and J.W. Mayer, *Diffusion markers in Al/metal thin-film reactions.* Nuclear Instruments and Methods in Physics Research Section B: Beam Interactions with Materials and Atoms, 1986. **17**(3): p. 242-249.
149. Thuillard, M., L.T. Tran, C.W. Nieh, and M.A. Nicolet, *Thermal reaction of Al/Ti bilayers with contaminated interface.* Journal of Applied Physics, 1989. **65**(6): p. 2553-2556.
150. Nie, X.-y., K.-n. Zhao, H.-x. Li, Q. Du, J.-s. Zhang, and L.-z. Zhuang, *Comparisons of interface microstructure and mechanical behavior between Ti/Al and Ti-6Al-4V/Al bimetallic composites.* China Foundry, 2015(01): p. 1-8.
151. Lv, S., Q. Cui, Y. Huang, and X. Jing, *Influence of Zr addition on TIG welding–brazing of Ti–6Al–4V toAl5A06.* Materials Science and Engineering: A, 2013. **568**(0): p. 150-154.
152. Nahar, R. and N. Devashrayee, *Effect of Si on the reaction kinetics of Ti/AlSi bilayer structures.* Applied physics letters, 1987. **50**(3): p. 130-131.
153. Khursheed, A., *Scanning electron microscope optics and spectrometers*. 2011: World Scientific.
154. Wikipedia. *Principle of EDS*. 2015 [cited 2015 4.21]; Available from: http://en.wikipedia.org/wiki/Energy-dispersive_X-ray_spectroscopy#/media/File:EDX-scheme.svg.
155. Schwartz, A.J. and M. Kumar, *Electron backscatter diffraction in materials science*. 2009: Springer Verlag.
156. Lloyd, G.E., *Atomic number and crystallographic contrast images with the SEM: a review of backscattered electron techniques.* Mineralogical Magazine, 1987. **51**(359): p. 3-19.
157. Prior, D.J., A.P. Boyle, F. Brenker, M.C. Cheadle, A. Day, G. Lopez, L. Peruzzo, G.J. Potts, S. Reddy, and R. Spiess, *The application of electron backscatter diffraction and orientation contrast imaging in the SEM to textural problems in rocks.* American Mineralogist, 1999. **84**: p. 1741-1759.
158. Williams, D.B. and C.B. Carter, *Transmission electron microscopy: a textbook for materials science.* Micron, 1997. **28**(1): p. 75-75.
159. Nellist, P., *Scanning Transmission Electron Microscopy*, in *Science of Microscopy*, P. Hawkes and J.H. Spence, Editors. 2007, Springer New York. p. 65-132.
160. Zürich, E. *Image Modes in TEM - Bright Field Images*. 2015; Available from: http://www.microscopy.ethz.ch/TEM_BF.htm.
161. Browning, N., M. Chisholm, and S. Pennycook, *Atomic-resolution chemical analysis using a scanning transmission electron microscope.* Nature, 1993. **366**(6451): p. 143-146.
162. Karpel, A., G. Gur, Z. Atzmon, and W. Kaplan, *TEM microstructural analysis of As-Bonded Al–Au wire-bonds.* Journal of Materials Science, 2007. **42**(7): p. 2334-2346.
163. FEI. *FEI application note AN0027 07-2010: ChemiSTEM™ technology a revolution in EDX analytics*. Available from: http://www.fei.com.
164. TWI. *Hardness Testing Part 1*. 2015; Available from: http://www.twi-global.com/technical-knowledge/job-knowledge/hardness-testing-part-1-074/.
165. Matsunaga, K., T. Sasaki, N. Shibata, T. Mizoguchi, T. Yamamoto, and Y. Ikuhara, *Bonding nature of metal/oxide incoherent interfaces by first-principles calculations.* Physical Review B, 2006. **74**(12).

166. Iwamoto, C., *Microstructure of Aluminum/Glass Joint Bonded by Ultrasonic Wire Welding.* Metallurgical and Materials Transactions a-Physical Metallurgy and Materials Science, 2014. **45A**(3): p. 1371-1375.
167. Bakavos, D. and P.B. Prangnell, *Mechanisms of joint and microstructure formation in high power ultrasonic spot welding 6111 aluminium automotive sheet.* Materials Science and Engineering a-Structural Materials Properties Microstructure and Processing, 2010. **527**(23): p. 6320-6334.
168. Chen, Y.C., D. Bakavos, A. Gholinia, and P.B. Prangnell, *HAZ development and accelerated post-weld natural ageing in ultrasonic spot welding aluminium 6111-T4 automotive sheet.* Acta Materialia, 2012. **60**(6–7): p. 2816-2828.
169. Panteli, A., J.D. Robson, I. Brough, and P.B. Prangnell, *The effect of high strain rate deformation on intermetallic reaction during ultrasonic welding aluminium to magnesium.* Materials Science and Engineering: A, 2012. **556**(0): p. 31-42.
170. Wang, Y., L. Wang, J. Robson, B.M. Al-Zubaidy, and P. Prangnell, *Coating Design for Controlling β Phase IMC Formation in Dissimilar Al-Mg Metal Welding*, in *Friction Stir Welding and Processing VIII*. 2015, John Wiley & Sons, Inc. p. 171-179.
171. Robson, J., A. Panteli, and P.B. Prangnell, *Modelling intermetallic phase formation in dissimilar metal ultrasonic welding of aluminium and magnesium alloys.* Science and Technology of Welding and Joining, 2012. **17**(6): p. 447-453.
172. Haddadi, F., D. Strong, and P.B. Prangnell, *Effect of Zinc Coatings on Joint Properties and Interfacial Reactions in Aluminum to Steel Ultrasonic Spot Welding.* JOM, 2012. **64**(3): p. 407-413.
173. Zhang, C.Q., J.D. Robson, O. Ciuca, and P.B. Prangnell, *Microstructural characterization and mechanical properties of high power ultrasonic spot welded aluminum alloy AA6111–TiAl6V4 dissimilar joints.* Materials Characterization, 2014. **97**(0): p. 83-91.
174. Jata, K.V., K.K. Sankaran, and J.J. Ruschau, *Friction-stir welding effects on microstructure and fatigue of aluminum alloy 7050-T7451.* Metallurgical and Materials Transactions A: Physical Metallurgy and Materials Science, 2000. **31**(9): p. 2181-2192.
175. Liu, X.-Y., P.P. Ohotnicky, J.B. Adams, C.L. Rohrer, and R.W. Hyland Jr, *Anisotropic surface segregation in Al Mg alloys.* Surface Science, 1997. **373**(2 – 3): p. 357-370.
176. Deng, H., W. Hu, X. Shu, and B. Zhang, *Analytic embedded-atom method approach to studying the surface segregation of Al-Mg alloys.* Applied Surface Science, 2004. **221**(1-4): p. 408-414.
177. Bloch, J., D.J. Bottomley, J.G. Mihaychuk, H.M. van Driel, and R.S. Timsit, *Magnesium surface segregation and its effect on the oxidation rate of the (111) surface of A1-1.45at%Mg.* Surface Science, 1995. **322**(1-3): p. 168-176.
178. Wang, W., P. Liu, and L. Gan, *Research on friction and wear properties of annealed 5052 Al-Mg alloy*, in *Advanced Materials Research*. 2011. p. 157-162.
179. Field, D.J., G.M. Scamans, and E.P. Butler, *HIGH TEMPERATURE OXIDATION OF Al-4. 2 Wt Pct Mg ALLOY.* Metallurgical transactions. A, Physical metallurgy and materials science, 1987. **18 A**(3): p. 463-472.

180. Magin, J. and F. Balle, *Solid state joining of aluminum, titanium and their hybrids by ultrasonic torsion welding.* Materialwissenschaft und Werkstofftechnik, 2014. **45**(12): p. 1072-1083.
181. Caicedo-Martinez, C.E., G.E. Thompson, and E.V. Koroleva, *Nanoscale engineering of aluminium surfaces.* Surface Engineering, 2002. **18**(2): p. 145-150.
182. Takeuchi, A. and A. Inoue, *Calculations of mixing enthalpy and mismatch entropy for ternary amorphous alloys.* Materials Transactions, JIM, 2000. **41**(11): p. 1372-1378.
183. Chen, X.Q., V.T. Witusiewicz, R. Podloucky, P. Rogl, and F. Sommer, *Computational and experimental study of phase stability, cohesive properties, magnetism and electronic structure of TiMn2.* Acta Materialia, 2003. **51**(5): p. 1239-1247.
184. Bian, Z., H. Kato, C. Qin, W. Zhang, and A. Inoue, *Cu–Hf–Ti–Ag–Ta bulk metallic glass composites and their properties.* Acta Materialia, 2005. **53**(7): p. 2037-2048.
185. Association, E.A., *The aluminium automotive manual.* EAA, available at, 2013.
186. Clementi, E., D.L. Raimondi, and W.P. Reinhardt, *Atomic Screening Constants from SCF Functions. II. Atoms with 37 to 86 Electrons.* The Journal of Chemical Physics, 1967. **47**(4): p. 1300-1307.
187. Okamoto, H., *O-Ti (oxygen-titanium).* Journal of Phase Equilibria, 2001. **22**(4): p. 515-515.
188. Wriedt, H.A., *The Al-O (Aluminum-Oxygen) system.* Bulletin of Alloy Phase Diagrams, 1985. **6**(6): p. 548-553.
189. Feng, B., J. Weng, B. Yang, J. Chen, J. Zhao, L. He, S. Qi, and X. Zhang, *Surface characterization of titanium and adsorption of bovine serum albumin.* Materials Characterization, 2002. **49**(2): p. 129-137.
190. Cheng, X. and S.G. Roscoe, *Corrosion behavior of titanium in the presence of calcium phosphate and serum proteins.* Biomaterials, 2005. **26**(35): p. 7350-7356.
191. Pouilleau, J., D. Devilliers, F. Garrido, S. Durand-Vidal, and E. Mahé, *Structure and composition of passive titanium oxide films.* Materials Science and Engineering: B, 1997. **47**(3): p. 235-243.
192. Gemelli, E. and N. Camargo, *Oxidation kinetics of commercially pure titanium.* Matéria (Rio de Janeiro), 2007. **12**(3): p. 525-531.
193. Güleryüz, H. and H. Çimenoğlu, *Effect of thermal oxidation on corrosion and corrosion–wear behaviour of a Ti–6Al–4V alloy.* Biomaterials, 2004. **25**(16): p. 3325-3333.
194. Rodrigues, D.M., A. Loureiro, C. Leitao, R.M. Leal, B.M. Chaparro, and P. Vilaça, *Influence of friction stir welding parameters on the microstructural and mechanical properties of AA 6016-T4 thin welds.* Materials & Design, 2009. **30**(6): p. 1913-1921.
195. Liu, H.J., Y.C. Chen, and J.C. Feng, *Effect of zigzag line on the mechanical properties of friction stir welded joints of an Al–Cu alloy.* Scripta Materialia, 2006. **55**(3): p. 231-234.
196. Hou, X., X. Yang, L. Cui, and G. Zhou, *Influences of joint geometry on defects and mechanical properties of friction stir welded AA6061-T4 T-joints.* Materials & Design, 2014. **53**(0): p. 106-117.

197. Sato, Y.S., H. Takauchi, S.H.C. Park, and H. Kokawa, *Characteristics of the kissing-bond in friction stir welded Al alloy 1050.* Materials Science and Engineering: A, 2005. **405**(1–2): p. 333-338.
198. Smiti, E., P. Jouffrey, and A. Kobylanski, *The influence of carbon and oxygen in the grain boundary on the brittle-ductile transition temperature of tungsten Bi-crystals.* Scripta Metallurgica, 1984. **18**(7): p. 673-676.
199. Choudhury, A., C.L. White, and C.R. Brooks, *The intergranular segregation of boron in Ni3Al: Equilibrium segregation and segregation kinetics.* Acta Metallurgica Et Materialia, 1992. **40**(1): p. 57-68.
200. Lynch, S.P., B.C. Muddle, and T. Pasang, *Mechanisms of brittle intergranular fracture in Al-Li alloys and comparison with other alloys.* Philosophical Magazine a-Physics of Condensed Matter Structure Defects and Mechanical Properties, 2002. **82**(17-18): p. 3361-3373.
201. Choudhury, A., C.L. White, and C.R. Brooks, *The effect of thermal history on intergranular boron segregation and fracture morphology of substoichiometric Ni3Al.* Scripta Metallurgica, 1986. **20**(7): p. 1061-1066.
202. Lozano-Perez, S., M. Schroeder, T. Yamada, T. Terachi, C.A. English, and C.R.M. Grovenor, *Using NanoSIMS to map trace elements in stainless steels from nuclear reactors.* Applied Surface Science, 2008. **255**(4): p. 1541-1543.
203. Lejcek, P., *Grain boundary segregation in metals*. Vol. 136. 2010: Springer Science & Business Media.
204. Heitjans, P. and J. Kärger, *Diffusion in condensed matter*. 2005: Springer.
205. Kabbaj, M., A. Galerie, and M. Caillet, *Composite TiAl//3-TiN Coatings on Titanium.* Journal of the less-common metals, 1985. **108**(1): p. 1-21.
206. Khodabakhshi, F., A.P. Gerlich, A. Simchi, and A.H. Kokabi, *Hot deformation behavior of an aluminum-matrix hybrid nanocomposite fabricated by friction stir processing.* Materials Science and Engineering: A, 2015. **626**(0): p. 458-466.
207. Welham, N.J., *Mechanical activation of the solid-state reaction between Al and TiO2.* Materials Science and Engineering: A, 1998. **255**(1–2): p. 81-89.
208. Ying, D.Y. and D.L. Zhang, *Solid-state reactions between Cu and Al during mechanical alloying and heat treatment.* Journal of Alloys and Compounds, 2000. **311**(2): p. 275-282.
209. Ma, Z.Y. and S.C. Tjong, *In Situ ceramic particle-reinforced aluminum matrix composites fabricated by reaction pressing in the TiO2 (Ti)-Al-B (B2O3) systems.* Metallurgical and Materials Transactions A, 1997. **28**(9): p. 1931-1942.
210. Zhang, Q., B.L. Xiao, W.G. Wang, and Z.Y. Ma, *Reactive mechanism and mechanical properties of in situ composites fabricated from an Al–TiO2 system by friction stir processing.* Acta Materialia, 2012. **60**(20): p. 7090-7103.
211. Hamajima, T., K. Ameyama, and A. Fuji, *Microstructural change of weld interface in Ti/Al friction weld during heat treatment.* Zairyo/Journal of the Society of Materials Science, Japan, 1995. **44**(505): p. 1224-1230.
212. Dietrich, D., N. Grittner, T. Mehner, D. Nickel, M. Schaper, H.J. Maier, and T. Lampke, *Microstructural evolution in the bonding zones of co-extruded aluminium/titanium.* Journal of Materials Science, 2014. **49**(6): p. 2442-2455.

213. Liu, C.T., R.W. Cahn, and G. Sauthoff, *Ordered intermetallics: physical metallurgy and mechanical behaviour*. Vol. 213. 2012: Springer Science & Business Media.
214. Murray, J.L., *The Mg−Ti (Magnesium-Titanium) system.* Bulletin of Alloy Phase Diagrams, 1986. **7**(3): p. 245-248.
215. Weimin, W., F. Zhengyi, W. Hao, and Y. Runzhang, *Chemistry reaction processes during combustion synthesis of B2O3–TiO2–Mg system.* Journal of Materials Processing Technology, 2002. **128**(1–3): p. 162-168.
216. Park, J.-Y., I.-H. Kim, Y.-I. Jung, H.-G. Kim, D.-J. Park, and B.-K. Choi, *High temperature steam oxidation of Al3Ti-based alloys for the oxidation-resistant surface layer on Zr fuel claddings.* Journal of Nuclear Materials, 2013. **437**(1–3): p. 75-80.
217. Grewal, G. and S. Ankem, *Solubility of vanadium in α and β titanium.* Metallurgical and Materials Transactions A, 1989. **20**(2): p. 334-337.
218. Murray, J., *The Ti−V (Titanium-Vanadium) system.* Bulletin of Alloy Phase Diagrams, 1981. **2**(1): p. 48-55.
219. Murray, J.L., *Al-V (aluminum-vanadium).* Bulletin of Alloy Phase Diagrams, 1989. **10**(4): p. 351-357.
220. Tiffin, D.A., W.S. Brennan, D. Soza, P.L. Smith, A. White, and T.Z. Hossain, *Thin titanium film as self-regulating filter for silicon migration into aluminum metal lines*. 2001, Google Patents.
221. Rivero, C., O. Bostrom, P. Gergaud, O. Thomas, P. Boivin, and A. Mazuelas, *In situ study of strain evolution during thin film Ti/Al(Si,Cu) reaction using synchrotron radiation.* Microelectronic Engineering, 2002. **64**(1-4): p. 81-89.
222. Besser, P.R., J.E. Sanchez, and R. Alvis, *The Effect of Si ON TiAl3 Formation EV Ti/Al Alloy Bilayers.* MRS Online Proceedings Library, 1994. **355**: p. null-null.
223. Yu, J. and J.Y. Kim, *Effects of residual S on Kirkendall void formation at Cu/Sn–3.5Ag solder joints.* Acta Materialia, 2008. **56**(19): p. 5514-5523.
224. Lee, H.M., *Design of Al3(Ti,V,Zr) systems through phase stability calculations*, in *High Temperature Aluminides and Intermetallics*, S.H. Whang, D.P. Pope, and C.T. Liu, Editors. 1992, Elsevier: Oxford. p. 26-30.